



# **Fabrication and characterisation of tellurite planar waveguides**

**Khu Tri Vu**

January 2012

A thesis submitted for the degree of Doctor of Philosophy of the  
Australian National University

Laser Physics Centre  
Research School of Physics and Engineering  
College of Physical and Mathematical Sciences  
The Australian National University





# Declaration

The contents of this thesis are the result of original research and have not been submitted for a higher degree to any other university or institution. This thesis is entirely my own work, unless explicitly stated otherwise.



Khu Tri Vu  
23..January 2012

## **Acknowledgment**

There has been so much help from everyone who I know and have met during the course of this work that I would like to thank deeply. Although I am trying to name some people that I can think of at the moment of writing, there are many others who I might fail to mention and for this I apologise.

First of all I would like to say thank you to my supervisors, Dr. Steve Madden and Prof. Barry Luther-Davies. They have done their best for me throughout this time. Dr. Steve Madden has been inspiring and given me all of the guidance that I needed all the way. Prof. Barry Luther-Davies has always been the point of contact whenever I needed help. His expertise in every field makes all problems become simple. I also acknowledge the help of Prof. Andrei Rode, Prof. Neil Manson with thoughtful advice.

I would like to specially thank other members of Laser Physics Centre with whom I have shared many ideas, joy and, sometimes, frustration. I express my deepest gratitude to Dr. Duk-Yong Choi, Dr. Douglas Bulla, Mr Craig Macleod, Mr John Bottega, Ms Anita Smith, Mr Sukhanta Debbarma, Ms Belinda Barbour, Ms Sonia Padrum and specially Mrs Maryla Krolikowska. I also thank all of the administrative and technical support staff at the Research School of Physics and Engineering for their assistance at various times.

I am also grateful for the contribution of all other student members at the Laser Physics Centre and at the Research School of Physics and Engineering. They also made the student life so much more enjoyable.

I specially thank Ian McKerracher, Dr. Fouad Karouta and Dr. Kaushal Vora for help with sputtering and other fabrication facilities. I would like also thank Prof. Rob Elliman and Dr. Avi Shalav for helping with RBS and photoluminescence measurements. The electron beam characterisations such as SEMs and EDXAs have all been carried out with help from staff at the Australian National University Electron Microscopy Unit. I express my deepest appreciation to Dr. Frank Brink for helping me all the time. The mass spectrometer measurements were performed by Dr. Charlotte Alan at the Research School of Earth Sciences. I thank her for all of the help.

This project is funded by the Australian Research Council under Discovery Project Grand DP070333 with Dr. Steve Madden is the chief investigator. I also have had the privilege of working with and being partially supported by the Centre for Ultra-high bandwidth Devices for Optical Systems (CUDOS). My study was only possible with financial support from the Australian Government Department of Education, Science and Training with the International Postgraduate Research Scholarship (IPRS) and the Australian National University PhD scholarship. I am, therefore, very grateful to all these organisations.

I also thank all members of the Vietnamese Society in Canberra (ACTVOSA) and the Vietnamese Embassy in Canberra for providing a home away from home. I express my thanks to members of University House and Graduate House for providing a friendly living environment for the duration we stayed there.

Most of all, this is tribute to my family who are always my love and encouragement at any moment. They are always my motivation for every thing. I would like to thank my wife, Uyen Nguyen, for being a patient, devoted and unconditional companion. My life has been so much more joyful with the arrival of our son, Minh Vu. For that, saying “thank” is just not enough.

## **Abstract**

Tellurite glasses, which contain tellurium dioxide ( $\text{TeO}_2$ ) as the main component, have some remarkable optical properties which are well recognised and exploited in the bulk optics and fibre fields. They include a high acousto-optic figure of merit, wide mid infrared transparency, the highest optical nonlinearity amongst oxides, and excellent rare earth hosting, etc. Despite these attractive properties, until now, no one has succeeded in fabricating low loss planar waveguides in these materials.

This work develops high quality optical planar waveguides in  $\text{TeO}_2$  for the first time. The project investigates the materials science for optical  $\text{TeO}_2$  films and discovers an appropriate waveguide fabrication method. The thin films have been fabricated by reactive radio frequency magnetron sputtering using a Tellurium target in an oxygen and argon atmosphere. Propagation losses at 1550nm in the planar films are 0.1dB/cm or lower in stoichiometric composition. The properties of films have been also found to be stable with thermal annealing up to 300°C. Plasma etching of tellurite glasses has been systematically studied. High quality etching of  $\text{TeO}_2$  and chalcogenide glass films has been demonstrated with a Methane/Hydrogen/Argon gas mixture. As a result, a fabrication recipe which produces low loss (0.1dB/cm) planar waveguides has been discovered. The nonlinear coefficient of the sputtered  $\text{TeO}_2$  has been characterised by self-phase modulation (SPM) experiments and the nonlinear coefficient  $n_2$  has been measured to be  $65 \times 10^{-20} \text{ m}^2 \text{ W}^{-1}$ , around 25 times that of silica. Significant signal conversion, -4dB, has achieved with large bandwidth of 30nm in the four-wave mixing (FWM) experiment pumped at 1550nm in a slightly normal dispersion waveguide. Erbium doped Tellurium oxide thin films have also been fabricated by co-sputtering of Erbium and Tellurium targets into an Oxygen and Argon atmosphere. The obtained films have been found to have good properties for Erbium doped waveguide amplifiers. The Erbium concentration can be controlled within the range of interest with Erbium/Tellurium ratios ranging from 0.1% to 3% or more. The 1.5 $\mu\text{m}$  photoluminescence properties of the films are excellent with effective bandwidth of more than 60nm and intrinsic lifetime of order of 3ms. Despite the fact that there was OH contamination in the films, single mode Erbium doped waveguide amplifiers with

high internal gain have been successfully obtained. The 1480nm pumped amplifier achieved internal gain from below 1520nm to beyond 1600nm. The peak gain of 2.8dB/cm and 40nm 3dB gain bandwidth have been accomplished. These results are a major stepping stone towards “system-on-chip” optical applications for telecom and mid infrared optics given the multifunctional nature of tellurite materials.

# List of publications

Part of this thesis has been presented in the following publications:

## Peer reviewed

1. **K. Vu** and S. Madden, "Erbium doped Tellurium dioxide planar waveguide amplifiers with 2.8dB/cm internal gain", *Group IV photonics*, London, (2011).
2. **K. Vu** and S. Madden, "Erbium doped Tellurium dioxide planar waveguide amplifiers with 2.8dB/cm internal gain", *Conference on Lasers and Electro-Optics Pacific Rim (CLEO PAC RIM)*, Sydney, (2011).
3. **K. Vu** and S. Madden, "Passive and active amorphous Tellurium dioxide thin film waveguides for integrated photonics", *The 9th International Meeting of Pacific Rim Ceramic Societies (PacRim 9)*, (2011).
4. **K. Vu** and S. Madden, "High gain Erbium doped Tellurium oxide waveguide amplifier", The European Conference on Lasers and Electro-Optics and the XII<sup>th</sup> European Quantum Electronics Conference (CLEO/Europe-EQEC), (2011).
5. **K. Vu** and S. Madden, "Reactive ion etching of tellurite and chalcogenide waveguide using Hydrogen, Methane and Argon", *Journal of Vacuum Science & Technology A* 29, 011024 (2011).
6. **K. Vu** and S. Madden, "2.8dB/cm Internal gain tellurium dioxide Er doped waveguide amplifiers" Australian Institute of Physics Congress and Australian Conference on Optical Fibre Technology (AIP/ACOFT), (2010).
7. **K. Vu** and S. Madden, "Tellurium dioxide Erbium doped planar rib waveguide amplifiers with net gain and 2.8dB/cm internal gain", *Optics Express* 18, (2010).
8. S. Madden and **K. Vu**, "Very low loss reactively ion etched Tellurium Dioxide planar rib waveguides for linear and non-linear optics", *Optics Express* 17, 17645 (2009).
9. **K. Vu** and S. Madden, "Low loss nonlinear planar tellurite waveguides", *Proceedings of Australasian Conference on Optics Lasers and Spectroscopy and the Australian Conference on Optical Fibre Technology in association with the International Workshop on Dissipative Solitons (ACOLS/ACOFT)*, (2009).
10. B. Luther-Davies, A. Prasad, X. Gai, **K. Vu**, S. Madden, D.-Y. Choi, D. Bulla and R. Wang, "Ge<sub>11.5</sub>As<sub>24</sub>Se<sub>64.5</sub> glass: a new material for the fabrication of highly nonlinear (gamma=33000W-1km-1) dispersion engineered waveguides", *Proceedings of Optical Society of America Optics and Photonics Congress/Integrated Photonics and Nanophotonics Research and Applications (IPNRA)*, (2009).
11. B. Luther-Davie, A. Prasad, S. Madden, D.-Y. Choi, D. Bulla, X. Gai and **K. Vu**, "Supercontinuum generation and four wave mixing in Ge<sub>11</sub>As<sub>22</sub>Se<sub>67</sub> rib waveguides with a nonlinear parameter >26000W-1km-1", *Proceedings of*

*European Conference on Lasers and Electro-Optics and the European Quantum Electronics Conference (CLEO/EQEC)*, (2009).

12. **K. Vu**, S. Madden and B. Luther-Davies, "Stoichiometric low loss Tellurium oxide thin films and waveguide", *Conference on Lasers and Electro-Optics (CLEO09)*, Baltimore, CTuEE3. (2009).
13. **K. Vu**, S. Madden, B. Luther-Davies and D. Bulla; "Stoichiometric low loss Tellurium oxide thin films for phonic applications"; Conference of the Opto-Electronics and Communications Conference and the Australian Conference On Optical Fibre Technology, (OECC/ACOFT), Sydney, ThF-3, (2008).

## Other

1. **K. Vu** and S. Madden, "Method for etching Chalcogen containing glass", Australian Pattern, logged, (2009).
2. **K. Vu** and S. Madden, "Tellurium Oxide based Erbium doped waveguide amplifier", *Centre for Ultra-high bandwidth Devices for Optical Systems (CUDOS) workshop*, (2010).
3. **K. Vu** and S. Madden, "High Gain Single Mode Er Doped Tellurium Dioxide Waveguide Amplifier", *Centre for Ultra-high bandwidth Devices for Optical Systems (CUDOS) workshop*, (2011).
4. A. Prasad, **K. Vu**, T. Han, A. Minovich and S. Beavan, "Bridging the Gap", *Optics and Photonics News*, Vol. 19, No. 12, (2008).

# Table of contents

**Declaration-----ii**

**Acknowledgment -----iii**

**Abstract-----v**

**List of publications -----vii**

**Table of contents-----ix**

**Chapter 1: Introduction ----- 1**

    1.1 General background ----- 1

    1.2 Tellurite planar waveguides ----- 9

    1.3 Outline of this work -----10

**Chapter 2: Tellurite glass properties and applications----- 13**

    2.1 Tellurium and Tellurium dioxide: a brief introduction-----13

    2.2 Tellurite glasses -----17

    2.3 Optical properties and applications of tellurite glass -----21

    2.4 Development of tellurite and Tellurium oxide waveguide fabrication-----35

    2.5 Conclusion -----39

**Chapter 3: Reactive sputtering deposition of optical Tellurium oxide films ----- 41**

    3.1 Tellurite glass and Tellurium oxide thin film development -----41

    3.2 Magnetron reactive RF sputtering deposition -----45

    3.3 Experimental measurements of refractive index and thickness of thin films-----48

    3.4 Deposition and characterisation of Tellurium oxide films fabricated by reactive RF magnetron sputtering -----49

    3.5 Raman spectra -----56

    3.6 Effect of annealing -----58

    3.7 Thin film propagation loss -----59

    3.8 Conclusion -----61

**Chapter 4: Fabrication of high quality Tellurium oxide rib waveguides ----- 63**

    4.1 Plasma etching technology-----63

    4.2 Plasma etching study of Tellurium oxide and chalcogenide glasses -----68

    4.3 Etching of Tellurium oxide with ICP machine-----89

    4.4 Conclusion -----93



**Chapter 5: Characterisation of TeO<sub>2</sub> waveguides----- 94**

5.1 Waveguide geometry and modelling method -----94

5.2 Dispersion properties----- 104

5.3 Waveguide attenuation measurements----- 111

5.4 Self phase modulation ----- 120

5.5 Four-wave mixing: ultra-fast wavelength conversion ----- 126

5.6 Conclusion ----- 133

**Chapter 6: Erbium doped Tellurium oxide films-----134**

6.1 Properties of rare earth doped glasses ----- 134

6.2 Rate equations for photoluminescence study ----- 147

6.3 Effect of OH quenching centre concentration on lifetime ----- 151

6.4 Fabrication of Er doped Tellurium oxide by sputtering----- 152

6.5 Characterisation of Er doped Tellurium oxide films ----- 154

6.6 Conclusion ----- 167

**Chapter 7: Erbium doped Tellurium oxide waveguide amplifiers -----169**

7.1 Development of Er doped planar waveguide amplifier----- 169

7.2 Development of Er doped tellurite devices----- 173

7.3 EDTWA fabrication with co-sputtering and ICP etching ----- 176

7.4 EDTWA characterisation ----- 183

7.5 Conclusion ----- 196

**Chapter 8: Conclusions and recommendations-----198**

8.1 Conclusions ----- 198

8.2 Recommendations for future work ----- 199

**Bibliography-----202**

# ***Chapter 1:***

## ***Introduction***

### ***1.1 General background***

#### **1.1.1 Integrated optics**

Since the 1980s, electronics has been slowly supplemented by and in some cases even replaced by optics, in telecommunications systems in particular. The appeal of optical techniques originally stemmed from the wide bandwidth available and the ultra low attenuation possible in optical fibres compared to the best available from the coaxial cables required to carry high data rate signals. The advent of the optical amplifier accelerated this process and led to the replacement of repeaters with all optical amplifier devices. New fields of application such as astronomy, biological/chemical and other sensing devices, consumer electronics, on chip and intra-chip connections etc. have emerged since the original telecoms based drive towards integration [1-3] and the field has matured to the point that integrated optics devices are routinely deployed. The appeal and possibilities of integrated optics are essentially the same as integrated electronics, namely that bulk components can be eliminated and multiple functionalities can be integrated on one stable robust, mass producible, low cost device. However, progress has been much slower than in the electronic domain and a number of key functionalities remain to be integrated together due to materials limitations.

The basic concept in optical integrated circuits is the same as that in optical fibres: the confinement of light. Light confines within high refractive index regions of the guiding structure. In a channel waveguide, light propagates within a region embedded in a planar substrate or within a portion of a film deposited upon a planar substrate. The channel has refractive greater than that of the substrate/surrounds. The thin film type optical circuit aims to perform multiple functions by integrating laser light sources, functional components such as switches/modulators/filters/amplifiers, interconnecting waveguides, and detectors all on single substrate. Through integration,

more compact, stable and functional optical systems can be achieved. The key components are slab (2-D) waveguides or channel (3-D) waveguides. [4].

There are a number of basic properties of integrated optical devices that make them attractive [1]:

- **Good confinement:** Wider choice of materials enabled by not needing to draw fibres allows guided modes to be confined to very small mode areas ( $<1\mu\text{m}^2$ ) if desired to enhance active or nonlinear optical effects and enable very tight bend radii (down to  $\sim 2\mu\text{m}$  in silicon [5]). Multimaterial integration also allows modes to be expanded as desired for low interactions or coupling to standard optical fibres.
- **Stable alignment:** a key performance factor in optical systems is the stability of alignment between the various optical components. Integrated photonic devices are by definition free of internal alignment issues as everything is monolithically integrated. Also with the application of simple design principles, the devices can be stable against vibrations and thermal changes.
- **Fast operation:** The small size of the control electrodes in integrated photonic devices implies low capacitance which allows fast switching speeds and high modulation bandwidth in electro-optic devices.
- **Effective acousto-optic interactions:** devices using acousto-optic interactions such as surface acoustic wave (SAW) switches and filters can operate very effectively because of the SAW and optical waveguide mode overlap strongly.
- **Compact and low weight:** The use of single substrate with an area of several centimetre square for integrating photonic components makes the optical devices very compact and very light weight.
- **Low cost:** The fabrication of integrated optics devices can leverage the techniques routinely employed in the semiconductor industry enabling true low cost mass production.
- **System on a chip opportunity** – realisation of a whole optical system on a single chip, integrating a wide range of functionalities together to achieve devices that are not possible with fibre or bulk optics alone

To attain the desired goal of low cost high functionality system on a chip devices there are a number of functions and capabilities that have to be attained in a planar geometry that can be compatibly integrated together. Ideally any given materials system would provide as many capabilities as possible, for instance including:

- On chip laser source (CW and mode locked) capability
- Optical amplification where desired on the chip
- Large third order optical nonlinearity where desired on the chip
- Large second order nonlinearity where desired on the chip
- Accousto-optic effects for widely tunable filters
- Tight bending capability
- Means to interface to standard optical fibre
- Wide transmission range
- Stable photosensitivity for performance tuning and Bragg grating devices
- Light detection capability

So a key challenge is to find materials systems that can satisfy as many as possible of the above capacities, and that are compatible with integrating other technologies to supply those that it cannot. Established integrated optics technologies meet this list of desirable criteria to varying degrees, but not sufficiently that there are no opportunities for alternate materials, and it is this opportunity that inspired the work reported in this thesis.

### 1.1.2 Established materials for integrated optical devices

While the range of optical materials that can be used to fabricate optical devices is large, ranging from glasses, dielectrics such as silicon dioxide, silicon nitride, or silicon oxynitride, dielectric crystals (e.g. lithium niobate), semiconductors (silicon, indium phosphide), polymers, etc.[6] each material has some advantages and disadvantages over the others, and varying levels of maturity in individual technologies have been attained. Despite the fact that these materials categories have been extensively studied, there are still a limited number of functionalities can be obtained from any single material. A brief review of the most available technologies will now be given with a summary of their known capabilities and shortcomings. Table 1.1 summaries the refractive indices and waveguide refractive index contrast of these key materials

(contrast defined to a demonstrated top cladding other than air). Higher index contrast leads to smaller waveguides (better nonlinear or active device performance) and more compact optical circuits.

Table 1.1: Basic optical properties of key established materials [6].

<i>Materials</i>	<i>Refractive index</i>	<i>Channel/rib waveguide index contrast</i>
Silica	1.44-1.47	0-2%
Silicon	3.47	60%
Polymers	1.3-1.7	0-30%
Lithium niobate	2.1-2.2	0-0.5%
Semiconductors (e.g. InP, GaAs)	3.1-3.4	0-14%
Chalcogenides (e.g. As <sub>2</sub> S <sub>3</sub> )	2.5-3.3	60%
Silicon oxynitride (SiO <sub>x</sub> N <sub>y</sub> )	1.44-2.0	0-30%

Silica on Silicon technology is the most widely used and best established planar technology. It involves growing silica layers on silicon substrates mainly by plasma enhanced chemical vapour deposition (PECVD) or flame hydrolysis, followed by plasma etching to form waveguides [7-9]. The core material is usually raised in refractive index from pure silica by doping with germanium, index contrasts of up to 3% being commonly attained. The silica on silicon platform has been used to produce lasers, amplifiers, couplers, array waveguide grating (AWG) multi/demultiplexers, filters, and millisecond response time thermo-optic based switches and attenuations [6, 10, 11]. Commercial products on silica platforms have been available for many years now. However, silica based waveguides have low refractive index leading to low integration density, low Kerr nonlinear coefficient and no second order nonlinear coefficient. Silica cannot be used for wavelength conversion or other desired nonlinear effects with device lengths that can feasibly be integrated on a chip. Furthermore, silica is not a very good host of rare earth ions. The maximum concentration before the ions cluster is very low. For instance, silica can only contain ~1000ppm of Erbium before clustering starts and quenching effects dominate over radiative process [12]. This leads to very low gain per unit length of the device. Whilst silica will remain the workhorse of the passive planar integrated optics industry for some time to come, it is not the ideal

materials platform for system on-a-chip type devices, and additionally has no mid infrared (MIR) transparency.

Silicon on insulator (SOI) planar waveguide technology has been developed in the last few years with co-integration with high speed electronics and leveraging the existing worldwide silicon foundry capacity and capability in mind. Silicon on insulator has been used to produce couplers, filters, switches, microring and other types of resonator, photonic crystals, etc. There have also been a wide variety of nonlinear optical experiments in SOI waveguides [5, 13-17], though silicon is not the ideal material for this due to the two photon absorption it displays at 1550nm on account of its  $\sim 1100\text{nm}$  band edge. Additionally there are demonstrations of modulators running at up to 50GHz [18], silicon based lasers by wafer bonding active III-V layers [19, 20], high speed waveguide detectors based on Germanium selective area growth [21, 22], and recently some commercial products have become available, e.g. Luxtera [23]. Silicon is additionally transparent to 5-6 $\mu\text{m}$  offering some useful MIR capabilities. Thus silicon has demonstrated a wide range of capabilities and is an “accessible” technology due to the massive infrastructure investments in silicon processing. However many of the techniques that enables some of these capabilities (e.g. wafer bonded III-V gain, selective area Ge growth, etc) are not standard CMOS technologies and will therefore not be low cost readily available methods. Additionally silicon nanowire waveguides typically employed for this technology are very small (200x400nm is typical) meaning very high end lithographic tools are required, losses are high (the record for a nanowire device is  $\sim 2\text{dB/cm}$  propagation loss at 1550nm [24-26]) and the extremely high index contrast makes devices sensitive to phase errors much harder to make (e.g. AWG multiplexers). Further silicon accousto-optic devices have not been demonstrated, taper type structures have to be employed for efficient fibre coupling. Silicon technology is very expensive unless there is a mass market such as consumer electronics to reduce the cost per unit product; however this scenario is not yet anywhere in sight.

Polymers can use fast turnaround spin-and-expose techniques for low cost fabrication. Some polymers however are not photosensitive and require photo-resist assisted patterning and plasma etching reducing this advantage. One of the advantages of polymers is the tunability of the refractive index difference between the core and the

cladding enabling high index contrast and high density, and the sheer range of functional groups than can be incorporated for second and third order nonlinearity, gain, etc. Furthermore, polymers can often be used in unconventional techniques such as moulding, stamping, and embossing permitting rapid, low cost fabrication. Polymers have been used to produce interconnects, lasers, amplifiers, detectors, modulators, polarization controllers, couplers, filters, switches and attenuators [27-32]. Polymers generally contain CH or O-H bonds which have vibration overtone absorption in the S-C-L band, overcoming this loss for broadband telecom type applications requires other compromises (e.g. fluorination) that can deactivate some of the other desirable active effects. Polymer passive and active devices are commercially available (e.g. Gemfire makes VOA arrays [33], Gigoptix markets 40-100GHz modulators [34]), But two key challenges remain for polymers. Firstly, polymers usually exhibit large temperature dependence of key properties (e.g. refractive index) and excepting a very few classes of materials (acrylates and polysiloxanes) often exhibit poor stability in harsh environmental conditions [28]. Secondly, there is no one polymer that can support the full range of effects. All of the active functionalities in particular listed above were attained in very specific and very different optimised materials. Whilst polymers offer the ultimate toolbox and the promise of great things, much work remains to realise a true single material capable platform.

Lithium niobate has been studied extensively for more than three decades because of its good second order nonlinear coefficient, electro-optic coefficient and acousto-optic coefficient. It is readily available commercially and is currently the material of choice for external modulators, periodical poled crystal for waveguide conversion. Titanium diffusion, nickel diffusion and proton exchange are generally used to fabricate of waveguides in  $\text{LiNbO}_3$ . The lithium niobate platform has been used to produce lasers, amplifiers, modulators, polarization controllers, couplers, wavelength convertors, filters and switches [35-39]. There has however been no report of low loss rib channel waveguide in this material. The waveguide critical bending radius remain high, therefore, the devices are not yet compact. The third order nonlinearity  $n_2$  in  $\text{LiNbO}_3$  is only order of 5 times of silica, therefore, it is not suitable for Kerr nonlinear applications [40-42]. Additionally the fact that the material is a relatively fragile single

crystal makes capabilities such as integration of pump diodes or detectors quite challenging from both the thermal and bonding perspectives.

Semiconductors such as indium phosphide and gallium arsenide are also well investigated and can be used to produce both active and passive optical devices [43-49]. These semiconductors are usually grown by epitaxial methods. The integration of active component with passive components is typically achieved by epitaxy of different material compositions. They have been used to produce laser, SOAs, detectors, modulators, couplers, filters, and switches. In many regards, the indium phosphide waveguide system is the one which has currently achieved the most impressive results in terms of system level integration, with companies such as Infinera now selling 10x10 GB/s transceiver chips and other researchers demonstrating chips with 240 active and passive components integrated [49, 50]. Cost remains a concern for the InP system as does scalability into the MIR or to a wide range of emission wavelengths. Widely tunable filters are also problematic.

More recently, chalcogenides, which contain one or more of the chalcogen elements S, Se or Te compounded with network forming elements such as Ge, Si, P, As, Sb, have been fabricated and used for low loss and highly nonlinear waveguides [51-56]. Chalcogenides have high third order nonlinearity, therefore, very high nonlinear interaction with even CW laser beams. This allows effective wavelength conversion in four-wave mixing or supercontinuum generation. They have high acousto-optic coefficients, can be good hosts for rare earth dopants at a range of wavelengths, and are transparent across the whole MIR band. Chalcogenides also hold the record for poled second order nonlinearity at 9 pm/V with larger numbers likely possible. There are also chalcogenide solar cells indicating the potential for light detection, but no demonstrations of integrated waveguide photodiodes. On the other hand, they are soft glass and have low glass transition temperature glasses. Also, chalcogenides have two-photon absorption, even much lower than silicon, which is still unsuitable for a number of applications involving high optical power. Chalcogenide glasses have great potential in nonlinear signal processing and integrated optics but the long term stability for real world application have yet to be demonstrated.

Silicon oxynitride ( $\text{SiO}_x\text{N}_y$ ) and silicon nitride ( $\text{Si}_3\text{N}_4$ ) have also been studied extensively for optical integrated circuits [57-72]. This class of material has some



properties that are similar to tellurite glass such as refractive index of 2, transmission window from UV to Mid-IR. Silicon oxynitride planar waveguides are generally fabricated by low pressure chemical vapour deposition [63] or thermal chemical vapour deposition [71], or plasma enhanced chemical vapour deposition (PECVD) [60, 63-65] and reactive ion etching (RIE) [60, 63, 68]. There are also several high temperature annealing processes before the low stress and low loss waveguide can be fully obtained. The index of the material varies between 1.45 of  $\text{SiO}_2$  to 2.0 of  $\text{Si}_3\text{N}_4$ . This material allows monolithic integration into current silicon technology using current CMOS techniques. There has been some progress in passive devices with this class of material. For instance, waveguide with loss of less than 0.1dB/cm has been demonstrated and that leads to the successful fabrication of ring cavity with quality factor of  $3 \times 10^6$  [63]. However, there are number of shortcomings that make silicon oxynitride a less attractive candidate for optical integrated optics. There is still significant absorption loss at 1500nm due to the N-H bond [72], which is inherent in all processing steps. The films and waveguides are generally under stress due to high processing temperature. The nonlinearity of silicon nitride film was reported to be around 10 times of silica [57]. The rare earth ions hosting capability of silicon oxynitride is still unclear [58, 59]. Silicon oxynitride thin film has been poled to achieve only small  $\chi^{(2)}$  of 0.23 [73].

So far, there no single material platform has been able to realise all the required components on one platform to achieve a truly integrated circuit. This is because, that material has to satisfy some strict optical, mechanical, chemical properties etc. Multifunction optical circuits often require hybridisation to utilise the different strengths of different materials. Even the ease of hybridisation is an important attribute of a materials system. The search for materials with more diverse functionality that minimise the need for complex fabrication is continuing.

Tellurite glasses have been known for a while to provide some excellent properties. This project will concentrate on demonstration of tellurite glass planar technology in a range of components from passive waveguide to nonlinear conversion and active amplifiers.

## 1.2 Tellurite planar waveguides

Tellurite glasses are a broad class of multi-component oxide glasses containing predominantly Tellurium dioxide ( $\text{TeO}_2$ ). Tellurite glasses are promising for a wide range of applications of generating mid-infrared light for sensing, spectroscopy, telecommunications. Important optical properties of tellurite include: having refractive index at around 2.1, being a very good hosts for rare earth ions (Erbium, Thulium etc. which can be used for laser amplifiers), having high Raman gain coefficient (30-60 times higher than silica) and Raman shift at about double that of silica [74]. At refractive index of 2.1, the single mode waveguide can be obtained with relatively large cross-section leading to lower susceptibility to fabrication errors. This also allows efficient coupling between different components or from an external fibre. Furthermore, the critical bending radii remain relative low allowing high density integration. The propagation loss can be lower than more tightly confined waveguides in silicon or chalcogenides. Interestingly, tellurite glasses can be poled to achieve second order nonlinearities with coefficient comparable with those of crystalline materials [75]. This property can be used for electro-optic devices or frequency conversion via parametric mixing. Tellurite glasses have also been recognised for its third order nonlinearity as having the largest coefficient between oxide based glasses [76]. Because they have band edge at very short wavelength, 300-400nm, they also can handle very high optical intensity without the multi-photon absorption and photo darkening that affect most of current materials currently used for thin film optical applications.

In comparison with other optical glasses such as silica, fluoride and chalcogenide, tellurite has some excellent competitive properties. Table 1.2 summaries important properties of the mentioned glasses and indicates several advantages of tellurites over the others. For instance, the refractive indices of tellurites are much higher than silica and fluoride but not as high as chalcogenide. This makes it possible to make small mode area tightly bendable clad waveguides that cannot be made in low index materials whilst easing single mode device fabrication by allowing core sizes in the region where high end lithography tools are not required, and at the same time allowing greater surface roughness thus easing the etch criteria. The nonlinearity of tellurite materials is 30-60 times that of silica, which whilst less than the maximum value in chalcogenides of  $\sim 500\times$  silica is still large enough to make compact nonlinear

planar devices. The mechanical properties of tellurites are also superior to those of fluoride and chalcogenide glasses. Those are just a few of the advantages of tellurites over other well-known optical materials.

Table 1.2 Basics properties of tellurite in context with other optical glasses [77]

<i>Property</i>	<i>Tellurite</i>	<i>Silica</i>	<i>Fluoride</i>	<i>Chalcogenide</i>
Refractive index	1.8-2.3	1.46	1.5	2.5-3
Nonlinear refractive index ( $n_2$ , $\text{m}^2/\text{W}$ )	$30\text{-}60 \times 10^{-20}$	$1\text{-}3 \times 10^{-20}$	$\sim 10^{-21}$	$300\text{-}1000 \times 10^{-20}$
Highest phonon energy ( $\text{cm}^{-1}$ )	$\sim 800$	$\sim 1000$	$\sim 500$	$\sim 300$
Bandgap (eV)	$\sim 3$	$\sim 10$	$\sim 10$	1-3
Acousto-optical FoM ( $10^{-15} \text{s}^3/\text{kg}$ )	24, 750	8	-	164
Glass transition ( $T_g$ , C)	300-450	$\sim 1000$	$\sim 300$	110-280
Thermal expansion ( $10^{-7} \text{ }^\circ\text{C}$ )	120-170	$\sim 5$	$\sim 150$	$\sim 140$
Solubility in water	$< 10^{-2}$	$< 10^{-3}$	Soluble	$< 10^{-4}$
Mohs Hardness	2	6	1	1

Despite of all of their excellent properties, the detailed investigations in thin film and waveguide formats have not yet been conducted in the literature. Although there is some previous research on tellurite glass devices, they are mainly aimed at making optical fibres and as hosts for rare earth ion based amplifiers. There are tellurite fibre amplifier products available on the market. Only small amount of research [78-83] has experimentally examined tellurite as materials for planar waveguides but non considered non-linear optical devices. This work will target the understanding of the materials science, processing technology, and optical science of Tellurite materials for integrated planar waveguides. This project is to thoroughly characterise and optimise the materials; the deposition technology; the waveguide fabrication approach; and performance of passive and active planar tellurite waveguides.

### 1.3 Outline of this work

This work mainly concentrates on fabricating and characterising Tellurium dioxide planar waveguides. The aim is to provide a platform for a future integrated system

based largely on a single highly functional material. The remainder of the thesis is organised as follows:

**Chapter 2** introduces comprehensively the important properties of Tellurium oxide and tellurite glasses as excellent choices for a wide range of optical applications. Basic structural, physical and chemical properties of tellurite glasses are reviewed. Then, important optical properties such as refractive index, chromatic dispersion, nonlinearity, Raman properties are discussed. The applications of tellurite glasses in bulk, and optical fibre forms are introduced. The properties of tellurite glasses outlined in this chapter will be referred to in the later chapters. It is the foundation of the work for the development of thin film and waveguide using Tellurium oxide and tellurite glasses.

**Chapter 3** reports the use of reactive RF sputtering to fabricate as deposited films with the required stoichiometry and optical propagation losses below 0.1dB/cm, low enough to enable high quality integrated optics devices. A wide range of sputtering parameters was explored using the design of experiment (DOE) method to obtain the desired stoichiometry, high index, and low loss planar waveguides. The obtained films from these series of runs had O/Te ratios ranging from 1 to 3.5. The refractive index variation and planar waveguide propagation losses at 1550nm are reported as a function of oxygen content over a wide range. The bandgap, Raman spectra, and effects of annealing against stoichiometry are reported and it is shown that there are compositions which are completely thermally stable.

**Chapter 4** studies the reactive plasma etching properties of Tellurium dioxide. A high quality etching process using Hydrogen, Methane and Argon was demonstrated. Plasma etching of  $\text{TeO}_2$  using standard parallel plate Reactive Ion Etching (RIE) and toroidal winding Inductively Coupled Plasma (ICP) machines are covered in detail. The quality of etching in the two systems was slightly different but the outcome of this study was recipes for etching high optical quality  $\text{TeO}_2$  waveguides. The etch process is also shown to be highly suitable for chalcogenide glass thin films which may be of importance in applications such as phase change memory, nonlinear integrated optics, etc.

**Chapter 5** characterises the linear and nonlinear properties of RIE etched  $\text{TeO}_2$  waveguides. First, modal simulations were performed to obtain some important properties of the waveguides such as effective indices, dispersion, mode area, etc. Then,

the attenuation of the fabricated waveguides was measured by several techniques including non-destructive mode overlap estimation and destructive cutback methods. Nonlinear experiments were also performed. The self-phase modulation simulation gave the nonlinear refractive index of sputtered  $\text{TeO}_2$  at  $65 \times 10^{-20} \text{ m}^2 \text{ W}^{-1}$ , which is around  $\sim 25$  times that of silica. The four-wave mixing experiments also gave significant signal conversion to idler when pumped at  $1.550 \mu\text{m}$  in  $3 \mu\text{m}$  wide waveguide.

**Chapter 6** develops Erbium doped co-sputtered Tellurium Oxide films. The films were fabricated by reactive radio-frequency magnetron sputtering. Erbium was incorporated directly into the films by co-sputtering of an Erbium metal target on a separate gun. Fabrication and characterization processes and properties of Erbium doped thin films are described in detail. The main task was to deal with experimental measurement of the lifetime of thin films. The lifetime of  $1.5 \mu\text{m}$  radiation was found to not only depend on the Erbium concentration, Oxygen content of the film but to heavily depend on OH contamination.

**Chapter 7** details the production of Erbium doped Tellurium oxide waveguide amplifiers fabricated by co-sputtering. Waveguides were fabricated using standard lithography and reactive ion etching with Hydrogen/Methane/Argon gas mixture. The obtained low loss waveguides were pumped at  $1480 \text{ nm}$  to obtain signal gain from  $1520$  to  $1630 \text{ nm}$ . An amplifier with peak gain of  $14 \text{ dB}$  over  $5 \text{ cm}$  length was achieved. The gain was achieved over  $1520 \text{ nm}$  to beyond  $1600 \text{ nm}$  when bidirectionally pumped with a total of  $250 \text{ mW}$  at  $1475 \text{ nm}$ . The simulation of the performance of the amplifier shows very good agreement with the experimental data. The results show that rare earth tellurite waveguides have great potential for use in integrated nonlinear optics as loss compensators or as CW lasers or short pulse lasers.

**Chapter 8** summarises the main challenges, achievements of the work then suggests future work to further advance the field of tellurite planar waveguide.

## **Chapter 2:**

# ***Tellurite glass properties and applications***

This chapter reviews important properties of Tellurium dioxide and tellurite glasses as choices for a wide range of optical applications. First, basic structural, physical and chemical properties of tellurite glasses are reviewed. Then, important optical properties such as refractive index, chromatic dispersion, nonlinearity, Raman properties are discussed. The applications of tellurite glasses in bulk and optical fibre forms are introduced. The properties of tellurite glasses outlined in this chapter are important for the work in the later chapters.

## ***2.1 Tellurium and Tellurium dioxide: a brief introduction***

### **2.1.1 Tellurium and Tellurium dioxide**

Tellurium is one of the rarest elements on Earth with an abundance of only 1 part per billion by weight on crustal rocks [84]. The reason for its scarcity is due to the formation of volatile forms of Tellurium hydride which meant most Tellurium escaped Earth during its formation. Pure Tellurium in crystalline form is a p-type semiconductor.  $Te_{127}^{52}$  has the electron configuration of  $[Kr] 4d^{10}, 5s^2, p^4$ . It has oxidation states of 4, -2 and 6. It readily reacts to form different oxide, hydride or halide compounds [85].

Tellurium oxide can exist in three forms depending on the oxidation, temperature and pressure. The most stable form of Tellurium oxide is Tellurium dioxide ( $TeO_2$ ). The other less stable forms are Tellurium monoxide ( $TeO$ ), Tellurium trioxide ( $TeO_3$ ) and Tellurium pentoxide ( $Te_2O_5$ ) [86].  $TeO$  can be detected when  $TeSO_3$  is heated to 180-230°C. However, the existence of  $TeO$  in solid form is doubtful.  $TeO_3$  is reported to exist in two phases:  $\alpha$ , and  $\beta$  [86].  $\alpha$ - $TeO_3$ , coloured bright yellow, is formed by thermal decomposition of orthotelluric acid  $H_6TeO_6$  in air at 300-320°C,  $\beta$ - $TeO_3$  is formed by heating the orthotelluric acid with a trace of sulphuric acid in a

sealed tube.  $\text{Te}_2\text{O}_5$  is formed by heating orthotelluric acid  $\text{H}_6\text{TeO}_6$  or  $\alpha\text{-TeO}_3$  at  $406^\circ\text{C}$  for 25hr, and is stable at room temperature [86].

The most stable form of Tellurium oxide,  $\text{TeO}_2$ , occurs naturally as the mineral tellurite or paratellurite with two different crystal structures.  $\text{TeO}_2$  can be prepared by a number of methods including: burning of Tellurium in air, reaction with nitric or sulphuric acids, thermal decomposition of orthotelluric acid or its anhydride (Tellurium trioxide), oxidation of Tellurium dichloride by liquid  $\text{N}_2\text{O}_4$  and the oxidation of Tellurium in water or sodium hydroxide solution with oxygen at 60atm at  $150^\circ\text{C}$  [86]. A most convenient method is the reaction of nitric acid on Tellurium [86]. The basic Tellurium nitrate is formed which is then thermally decomposed into Tellurium dioxide with 80% yield. Tellurium dioxide has a melting point and boiling point of  $733^\circ\text{C}$  and  $1245^\circ\text{C}$ , respectively [85]. These temperatures are very attractive for fabrication as they are high enough for stable device operation yet low enough for convenient processing.

### 2.1.2 Tellurium dioxide crystal states

Tellurium dioxide traditionally exists in two polymorphous forms, paratellurite or  $\alpha\text{-TeO}_2$ , first described by Leciejewicz, 1961 [87], and tellurite or  $\beta\text{-TeO}_2$ , first described by Beyer in 1967 [88]. In both structures, Tellurium atoms have four neighbouring oxygen atoms forming a basic trigonal bipyramid  $\text{TeO}_4$  structural unit as shown in Figure 2.1. In this trigonal bipyramid, the two equatorial oxygen atoms are separated from the Te atom by a distance shorter than the two axial oxygen atoms as shown on Figure 2.1 a). The distances of Te atom to the axial and equatorial O atoms are 2.1 Å and 1.9Å, respectively. The distance between the two axial oxygen atoms is 3.0 Å while the distance between the two equatorial atoms is 4.1Å [89, 90].

The  $\alpha\text{-TeO}_2$  and  $\beta\text{-TeO}_2$  nomenclatures describe the frameworks of the  $\text{TeO}_4$  units, where they are linked by a highly asymmetric bridge  $\text{Te}_{\text{-ax}}\text{O}_{\text{eq}}\text{-Te}$ . In the  $\alpha\text{-TeO}_2$  structure, the  $\text{TeO}_4$  units share the corners forming a three-dimensional network as illustrated in Figure 2.1 b). In  $\beta\text{-TeO}_2$  the units share the corners and edges forming a two-dimensional network of sheets as shown in Figure 2.1 c).

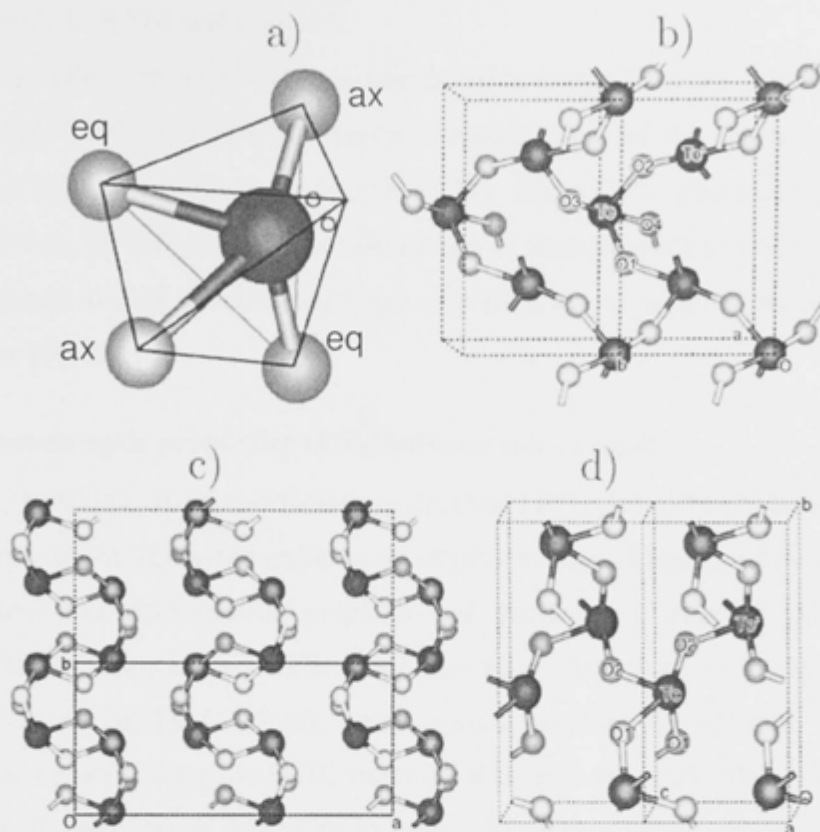


Figure 2.1: a) Structure model for  $\text{TeO}_4$  trigonal bipyramid unit (large atom are Te and smaller atoms are O); b), c) and d) are lattice projection on xy plane of  $\alpha$ ,  $\beta$  and  $\gamma$ - $\text{TeO}_2$ , respectively [90].

Single paratellurite ( $\alpha$ - $\text{TeO}_2$ ) crystals can be grown by the Czochralski method [91-93], or Bridgman technique [94, 95]. The crystal belongs to the tetragonal system with lattice parameters of  $a=b=4.81\text{\AA}$  and  $c=7.61\text{\AA}$ . The tellurite ( $\beta$ - $\text{TeO}_2$ ) crystals have orthorhombic symmetry with eight formula units per unit cell. The dimension of the unit cell are  $a=12.0\text{\AA}$ ,  $b=5.46\text{\AA}$  and  $c=5.61\text{\AA}$  [90, 96].

Recently, some authors [89, 97] reported the existence of two more forms of Tellurium oxide:  $\gamma$ - and  $\delta$ - $\text{TeO}_2$ . The  $\gamma$ - $\text{TeO}_2$ , as shown in Figure 2.1d) represents a new structural type different from the  $\alpha$ - and  $\beta$ -phases and  $\delta$ -phase seems to exist as a superposition of domains of  $\alpha$ -,  $\beta$ - and  $\gamma$ -phases. The Raman spectrum of  $\delta$ -phase suggests that it is an intermediate structure between the crystalline and glass states [98-101]. The  $\gamma$ - $\text{TeO}_2$  can be obtained by slowly heating, up to  $390^\circ\text{C}$ , pure  $\text{TeO}_2$  glass and



then annealing it for 24h at this temperature. The crystal forms an orthorhombic cell with  $a=4.90\text{\AA}$ ,  $b=8.57\text{\AA}$  and  $c=4.35\text{\AA}$ .

In  $\gamma\text{-TeO}_2$ , one Te-O bond is substantially longer than the other three and by breaking this bond in a three-dimensional visualization of the network, a chainlike structure is formed as shown in Figure 2.1 d). The  $\gamma\text{-TeO}_2$  phase can be seen as a polymeric form of  $\text{TeO}_3$  units. From the results of Raman spectra of  $\text{TeO}_2$  glass, it has been suggested that the chainlike structure of  $\gamma\text{-TeO}_2$  would represent the main structure of the glass [90, 101].

### 2.1.3 Accousto-optic properties of Tellurium oxide crystals

Arlt *et al.*, 1968 [91, 102], and Uchida *et al.*, 1969 [103] and 1971 [104] first suggested the potential use of Tellurium oxide as an ultrasonic-light deflector while analysing the piezoelectric and photoelastic properties of paratellurite crystals. Single crystal paratellurite,  $\alpha\text{-TeO}_2$ , is an excellent acousto-optic (AO) material. It has a high AO figure of merit (defined below), good optical rotation of  $87^\circ/\text{mm}$ , and a slow propagation velocity along the [110] direction of 616m/s [94, 105, 106].

The figure of merit,  $M_2$ , of an accousto-optical material is defined as:

$$M_2 = \frac{n^6 P^2}{\rho v} \quad (2.1)$$

where  $n$  is the refractive index,  $P$  is the photoelastic constant,  $\rho$  is the density and  $v$  is the sound velocity [88].

The figure of merit of  $\alpha\text{-TeO}_2$  is around  $750 \times 10^{-15} \text{s}^3/\text{kg}$  for circular polarisation or  $34 \times 10^{-15} \text{s}^3/\text{kg}$  for random polarisation [107, 108]. These numbers are significantly larger than those of quartz at  $2.2 \times 10^{-15} \text{s}^3/\text{kg}$  or lithium niobate at  $15 \times 10^{-15} \text{s}^3/\text{kg}$ . Due to the high figure merit of  $\text{TeO}_2$ , the drive power required to achieve high efficiency is very low. This property makes  $\text{TeO}_2$  crystals widely used in accousto-optical modulators [107-110].

## 2.2 Tellurite glasses

### 2.2.1 Basic properties

Amorphous  $\text{TeO}_2$  and tellurite glasses exhibit a range of unique properties which give them great potential in a wide range applications such as near and mid-infrared devices, new laser hosts, Raman amplifiers [88], etc. Although the physical properties and structure of crystalline solids are now relatively well understood, this is not yet the case for amorphous materials including bulk glasses, fibres and especially thin films [88].

The stability and other excellent optical properties of Tellurium dioxide crystal materials gave incentive to produce glassy Tellurium dioxide based fibres and waveguides. Brady [111, 112] reported the first tellurite glass. Brady reported that  $\text{TeO}_2$  forms a glass when fused with a small amount of  $\text{Li}_2\text{O}$ . The molten glass of 98.15%  $\text{TeO}_2$  and 1.84%  $\text{Li}_2\text{O}$  by weight was poured onto a flat steel surface, and cooled rapidly. To achieve glassy product, the ratio of  $\text{TeO}_2$  units over  $\text{Li}_2\text{O}$  was 10:1.

Since  $\text{TeO}_2$  is a conditional glass former, it requires special procedures to obtain pure  $\text{TeO}_2$  glass. It has been obtained by melting a small amount of crystalline  $\beta\text{-TeO}_2$  powder in Pt-5% Au crucible at  $800^\circ\text{C}$  for 20min. Then, the melt was rapidly quenched down to  $-11^\circ\text{C}$  by dropping the bottom of the crucible into a freezing mixture consisting of ice, ethanol and NaCl [113, 114]. Transparent  $\text{TeO}_2$  glass, confirmed to be amorphous by X-ray powder diffraction, was obtained. Akagi *et al.*, 1999 [115] prepared  $x\text{K}_2\text{O}-(100-x)\text{TeO}_2$  ( $x=5, 10, 15, 20$  and  $30$  mol%) glasses using a roller-quenching technique. The mixtures were melted at  $700\text{-}900^\circ\text{C}$  for 1h in a platinum crucible. The resultant liquid was poured into twin rollers rotating at 3000rpm to yield amorphous thin flakes. The estimated cooling rate was between  $10^5\text{-}10^6$  K/s.

A large number of modifiers can be added to  $\text{TeO}_2$  to form glasses [116]. The most studied tellurite glasses are for use in tellurite optical fibres [77]. Tellurite glasses with BaO or  $\text{WO}_3$  modifiers were found to have good durability and rare earth solubility. Glasses with alkali oxides have poor chemical durability to water.  $\text{ZnO-TeO}_2$  glass has a short wavelength UV edge and good durability but low rare earth solubility, but the addition of sodium oxide to  $\text{ZnO-TeO}_2$  glasses significantly improves the rare earth solubility without affecting the other two properties. It was later observed that  $\text{Na}_2\text{O}$  could be replaced by other monovalent ions, such as  $\text{Li}_2\text{O}$ ,  $\text{K}_2\text{O}$ ,  $\text{Rb}_2\text{O}$ ,  $\text{Cs}_2\text{O}$ , or  $\text{Ag}_2\text{O}$ ,

without deteriorating the UV edge, chemical durability, and rare earth solubility [77]. Thus, for the  $R_2O$ -ZnO- $TeO_2$  system, R can be Li, Na, K, Rb, Cs, or Ag or combinations thereof. Also, the relative amounts of these constituents can be varied over a wide range without seriously affecting glass stability. Therefore, a wide range of compositions can be achieved to match specific needs in the  $R_2O$ -ZnO- $TeO_2$  family. Furthermore, these compositions also give better loss characteristics in fibres [117].

Optical properties of tellurites can also be modified at will with addition of different elements [88]. For instance, Na, Li, K or Rb can be added to lower the refractive index from 2.1 down to 1.7. Addition of F or I based dopants can extend the mid infrared transmission. Ba and Li can improve the UV transmission. Specially, the nonlinearity can also be tailored to increase  $\sim 2$ - $3\times$  by adding W, Nb, Ti or to reduce by up to  $\sim 0.3$  by adding La, Mb, K, Li comparing to that of  $TeO_2$ .

### 2.2.2 Structure

Because of the high technological potential of tellurite glasses, their basic structures have been studied intensively by X-ray [111, 112, 118], electron energy loss spectroscopy [119], neutron diffraction [114, 118, 120, 121], nuclear magnetic resonance [89, 118, 122-127], Raman studies [76, 89, 99, 101, 123, 124, 126, 127] and by *ab initio* cluster calculation [90, 98, 99, 101, 114, 123, 128-131].

Brady [111, 112] first undertook a detailed study of the structure of Tellurium dioxide based glass by radial distribution of electrons using X-ray analysis. Brady found that there are two well-resolved primary peaks, one at about  $1.95\text{\AA}$  and the other at about  $2.75\text{\AA}$ ; and two other well-resolved peaks are  $3.63\text{\AA}$  and  $4.38\text{\AA}$ . The first two peaks correspond to the two sets of equatorial and axial Te-O bonds. The later two peaks overlap, their extracted distances correspond to the two preferred sets of Te-Te distance.

The presence of the two peaks at equivalent distances and with the same nearest neighbour numbers as in the crystal strongly suggests that the basic unit that forms the crystalline structures is preserved and relatively unchanged when the crystalline materials are transformed into glass. This finding agrees with the experimental results on  $SiO_2$  glasses, where the same form of tetrahedral  $SiO_4$  unit is present in all the known crystalline forms and glassy states [132]. These tetrahedral blocks are assembled in

different ways to accomplish various states. The angle of the Si-O-Si bond is varied slightly. There are however fundamental differences between glass formation in  $\text{SiO}_2$  and  $\text{TeO}_2$ . It is simple to prepare  $\text{SiO}_2$  glass from the pure material because the mechanism of glass formation is a simple distortion of one of the corner of the tetrahedral Si-O-Si angle. The essential difference between a glass and a crystal is found in the fact that although the essentially the same local order exists in each, the glass lacks the regularly repeating long range order of the crystal [132].

In crystalline  $\text{TeO}_2$ , four basic units share three edges. A major breakdown of the structure is necessary to break one edge in  $\text{TeO}_2$  to obtain a corner-sharing structure for the glass. Brady [111, 112] first observed that it is necessary to add a modifier M such as  $\text{Na}_2\text{O}$  or  $\text{Li}_2\text{O}$  to  $\text{TeO}_2$  before the material solidifies into a glass and attempts to melt the pure material and quickly quench it to a glass were unsuccessful because the melted material quickly crystallised. The minimum mole ratio of  $\text{Li}_2\text{O}$  to  $\text{TeO}_2$  actually required is approximately 1:10. This number was in agreement with theoretical calculations for the ratio required to break all shared edges in the  $\text{TeO}_2$  crystalline structure.

Detailed studies of the structure of pure  $\text{TeO}_2$  and alkali tellurite glasses using neutron diffraction, NMR, X-ray diffraction and *ab initio* molecular orbital calculations [114, 118, 120, 121, 125] concluded that the  $\text{TeO}_4$  units are in fact transformed in  $\text{TeO}_3$  units in glassy networks [76, 89, 98, 114, 118, 120, 121, 123, 125]. The experimental radial distribution functions along with the calculated results demonstrated that the basic structural units of tellurite glasses change from highly strained  $\text{TeO}_4$  trigonal bipyramids (tbp) to more regular  $\text{TeO}_3$  trigonal pyramids (tp) with increasing modifier content (see Figure 2.2). It has also been shown that the  $\text{TeO}_3$  trigonal pyramids do not exist in the form of isolated units in the glass network but interact with each other to form inter-trigonal Te...O linkages. The present results suggested that nonbridging oxygen (NBO) atoms in tellurite glasses do not exist in their "pure" form; that is, all the NBO atoms in  $\text{TeO}_3$  trigonal bipyramids will interact with the first- and/or second-neighbour Te atoms, resulting in a three-dimensional continuous random network even in tellurite glasses with over 30 mol% of alkali oxides.

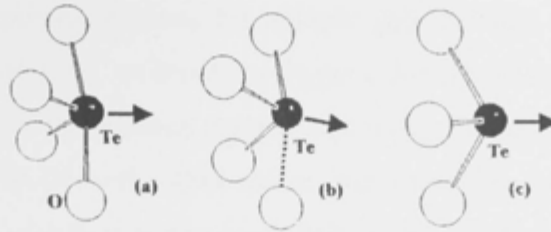


Figure 2.2: Transition from the  $\text{TeO}_4$  to  $\text{TeO}_3$  unit structure [76].

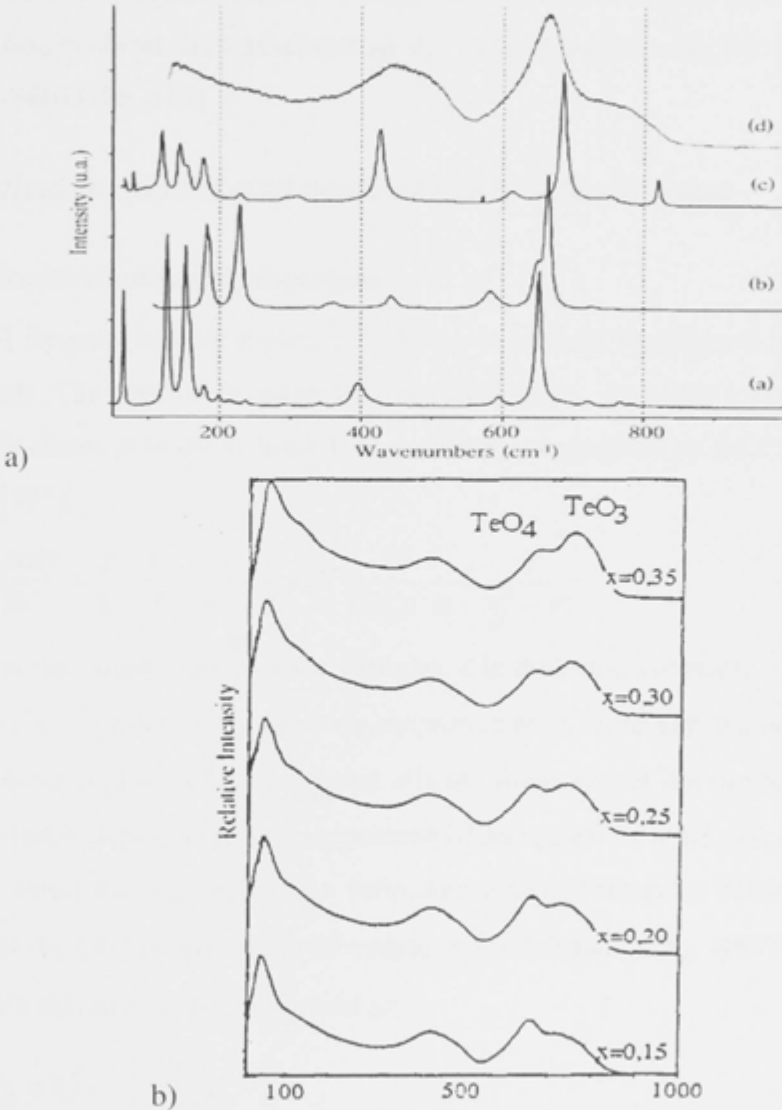


Figure 2.3 a) Raman spectra of various phase of  $\text{TeO}_2$ : a)  $\alpha$ - $\text{TeO}_2$ , b)  $\beta$ - $\text{TeO}_2$ , c)  $\gamma$ - $\text{TeO}_2$  and glassy  $\text{TeO}_2$  [89, 133]; b) Raman spectra of  $x\text{ZnO}+(1-x)\text{TeO}_2$  for  $x=0.15$  to 0.35 [134].

The Raman spectra obtained for tellurite glasses have three Raman bands at around 770, 670 and 460  $\text{cm}^{-1}$  as shown in Figure 2.3a). These bands are ascribed to the stretching mode of the  $\text{TeO}_3$  trigonal pyramid (tp) units containing terminal Te-O bonds such as  $\text{Te}=\text{O}$  and  $\text{Te}-\text{O}^-$  with NBO atoms, the stretching mode of  $\text{TeO}_4$  trigonal bipyramid (tbp) units with bridging oxygen (BO) atoms and the bending mode of  $\text{Te}-\text{O}-\text{Te}$  or  $\text{O}-\text{Te}-\text{O}$  linkages, respectively. The amplitude of the 770 $\text{cm}^{-1}$  band becomes larger, and the amplitudes of the 670 and 470 $\text{cm}^{-1}$  bands become smaller as the modifier content increases (Figure 2.3b). It is suggested that these results show the addition of modifier brings about the conversion of the  $\text{TeO}_4$  tbp units with BO into the  $\text{TeO}_3$  tp units with NBO [98, 115].

## 2.3 Optical properties and applications of tellurite glass

### 2.3.1 Refractive index and dispersion

At optical frequencies, the dielectric constant is entirely determined by the electronic polarisation. The relation between the refractive index, dielectric constant, number of polarisable atoms  $N$  in the volume  $V$  of the solid, is expressed by the Clausius-Mossotti equation [135]:

$$\frac{4\pi\alpha N}{3V} = \frac{\epsilon - 1}{\epsilon + 2} = \frac{n^2 - 1}{n^2 + 2} = N \frac{e^2}{12\epsilon_0\pi^2 m} \sum \frac{f_i}{\nu_i^2 - \nu^2} \quad (2.2)$$

where  $\alpha$  is the polarisability of the material,  $\epsilon$  is dielectric constant,  $n$  is the refractive index ( $\epsilon=n^2$ ),  $e$  is electron charge,  $m$  is electron mass,  $f_i$  represents the oscillator strength,  $\nu_i$  is the electron plasma frequency and  $\nu$  is the frequency of the incident photons. The refractive index depends on the composition of an optical material, the more polarisable the outer electrons, the higher the refractive index. The molar refractive index, the measure of the total polarisability of a mole of the substance,  $R_M = 4\pi N_A \alpha / 3$ ,  $N_A$  is the Avogadro's number, is also expressed as:

$$R_M = \left( \frac{n^2 - 1}{n^2 + 2} \right) \left( \frac{M}{\rho} \right) \quad (2.3)$$

where  $\rho$  is the density of the material and  $M$  is the molecular mass. The above equation is known as Lorentz-Lorenz equation. It can also be written in the form:

$$n = \left( \frac{2\rho R_M + M}{M - \rho R_M} \right)^{1/2} \quad (2.4).$$

The molar refraction  $R_M$  and index of refraction  $n$  depend on the polarisability of the materials.

The measured refractive indices for the tellurite glasses are higher than those of fluoride glass, silicate glass, phosphate glass, and close to those of chalcogenide glass. To understand how tellurite glasses have high refractive index, the number of polarisable units per volume  $N/V$ , the electronic polarisability of the ion,  $\alpha_{\text{ionic}}$ , must be considered. The values of  $n$  for  $\text{TeO}_2$  vary from  $n_{\text{glass}}=2.2$  to  $n_{\text{cryst.}}=2.37$  due to the density variation from  $\rho_{\text{glass}}=5.1\text{g/cm}^3$  to  $\rho_{\text{cryst.}}=5.99\text{g/cm}^3$  [135]. The atom density decreases from  $6.78 \times 10^{22} \text{ cm}^{-3}$  for  $\text{TeO}_2$  crystal to  $5.77 \times 10^{22} \text{ cm}^{-3}$  for glass [135]. The polarisability has been decreased from  $7.37 \times 10^{-24} \text{ cm}^3$  to  $6.96 \times 10^{-24} \text{ cm}^3$  or  $\alpha_{\text{crys.}}/\alpha_{\text{glass}}=1.1$ . The ratio between the density, dielectric constant and static polarisability of  $\text{TeO}_2$  crystal to  $\text{TeO}_2$  glass is in range from 1.18 to 1.27. Therefore, tellurite glasses have a lower refractive index than the crystal due to low electronic polarisability and lower density. El-Mallawany, 1992 [135] has calculated the refractive indices and various electronic properties of binary and ternary glasses. The indices are in the range from 2.01 to 2.15 depending on the exact composition.

The refractive indices of the materials are also dependent on the frequency or wavelength of the electromagnetic wave travelling within the medium. This gives rise to refractive dispersion often described by Sellmeier equations. The Sellmeier equation of the refractive index of binary tellurite ( $x\text{M}_m\text{O}_n-(100-x)\text{TeO}_2$ , where  $\text{M}_m\text{O}_n$  was network modifier) have been studied in details by Ghosh, 1995 [136]. The single oscillator model is described as:

$$n^2 = 1.0 + \frac{B}{1 - C/\lambda^2} \quad (2.5)$$

where  $n$  is the refractive index,  $B$  and  $C$  are constants,  $\lambda$  is the wavelength in micrometers.  $C$  also is the average electronic absorption bandgap. For pure  $\text{TeO}_2$ :  $B$  and  $C$  are approximately 3.46539,  $3.27652 \times 10^{-2} (\mu\text{m}^2)$ , respectively [136]. This model is not usually accurately representing the refractive indices.

A two pole Sellmeier equation represents the dispersion of tellurite materials much more accurately than single pole Sellmeier equations [136]:

$$n^2 = A + \frac{B}{1 - C/\lambda^2} + \frac{D}{1 - E/\lambda^2} \quad (2.6).$$

For pure  $\text{TeO}_2$  glass, the values of  $A$ ,  $B$ ,  $C$ ,  $D$  and  $E$  are 3.5483034, 0.9783726,  $8.2669346 \times 10^{-2} (\mu\text{m}^2)$ , 6.6510879 and  $225 (\mu\text{m}^2)$ .

A more common method used for dispersion assessment is the dispersion coefficient around the wavelength of interest. From the curve of refractive index versus wavelength, the dispersion coefficient can be calculated by using the expression [137]:

$$D = -\frac{\lambda}{c} \frac{d^2 n(\lambda)}{d\lambda^2} \quad (2.7).$$

Figure 2.4 shows the material dispersion coefficient for pure  $\text{TeO}_2$  glass with refractive index represented by the above two pole Sellmeier Equation (2.6) [136]. The zero dispersion wavelengths for tellurite glasses are typically around  $2.2\mu\text{m}$  whereas it is at  $1.3\mu\text{m}$  for  $\text{SiO}_2$ . At  $1.5\mu\text{m}$ , the dispersion coefficient of bulk tellurite glass is approximately  $-100\text{ps/nm/km}$  depending on exact composition. The dispersion of tellurite at  $1550\text{nm}$  is much smaller than most other nonlinear optical materials such as chalcogenide glasses. However, the dispersion can be engineered in waveguiding structure to shift the zero dispersion wavelength to  $1.5\mu\text{m}$  such as with the use of microstructured fibres [138-140]. This dispersion engineering will be applied to Tellurium oxide waveguides in the Chapter 5.

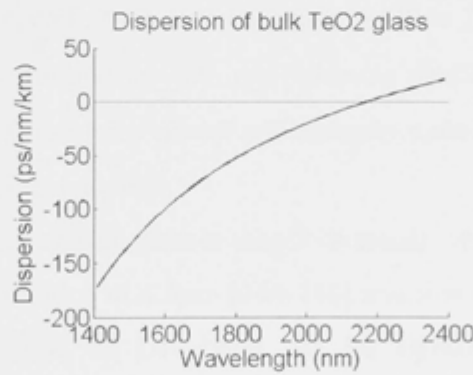


Figure 2.4: Dispersion coefficient of bulk a tellurite glass using dispersion with two pole Sellmeier equation [136].



### 2.3.2 Optical loss and bandgap

The absorption coefficient  $\alpha_a$  can be determined using the relation:

$$\alpha_a = \left(\frac{1}{d}\right) \ln\left(\frac{I_0}{I}\right) \quad (2.8)$$

where  $d$  is the length of propagation,  $I$  and  $I_0$  are the intensity of the transmitted and incident beam, respectively. For semiconductor materials in the high absorption region, the absorption coefficient  $\alpha_a(\omega)$  can be represented by the Davis-Mott model [141, 142]:

$$\begin{aligned} \alpha_a(\omega) &= \frac{A(\hbar\omega - E_{opt})^n}{\hbar\omega} & \text{for } \hbar\omega > E_{opt} \\ \alpha_a(\omega) &= 0 & \text{for } \hbar\omega < E_{opt} \end{aligned} \quad (2.9)$$

where  $A$  is a constant,  $E_{opt}$  is the optical bandgap,  $\omega$  is angular frequency. The value of  $n$  depends on the nature of the transition; whether it is allowed ( $n=1/2$ ) or forbidden ( $n=2/3$ ). From the above formula, when the value of  $\alpha_a(\omega)$  is measured against the frequency or wavelength, the plot of  $(\alpha\hbar\omega)^{1/n}$  against  $\hbar\omega$  when extrapolated to zero gives the value of the bandgap  $E_{opt}=E_{gap}$ . The bandgap energy for tellurite glasses are in order of 2.5eV to 4eV. Pure  $\text{TeO}_2$  has a band gap energy of 3.79eV [88], which corresponds to a wavelength of 330nm.

On the mid-IR edge of tellurites, the cut off wavelengths for thin sample (1mm) are around 5 to 7 $\mu\text{m}$  depending on the exact composition [143]. For instance,  $\text{WO}_3\text{-TeO}_2$  has mid-IR transmission at 5.5  $\mu\text{m}$  whereas  $\text{BaCl}_2\text{-BaO-TeO}_2$  has mid-IR transmission at 6.7 $\mu\text{m}$ . These long cut off wavelengths make tellurite glasses excellent UV to Mid-IR transmissive materials.

Tellurite glasses are oxide glasses therefore usually contain OH bonds. The OH bond has fundamental vibration at 3.3 $\mu\text{m}$  [144-148] and first overtone at 1.48 $\mu\text{m}$  [148]. However, the concentration of OH bond can be significantly reduced with the incorporation of halogen element contain components such as  $\text{BaF}_2$  [149].

### 2.3.3 Nonlinear optical properties

When an intense light beam interacts with materials, the intensity of the response polarisation is nonlinear with the electric field. The resulting polarisation of the material can be given by:

$$P = \epsilon_0 (\chi^{(1)} \cdot E + \chi^{(2)} : EE + \chi^{(3)} : EEE + \dots) \quad (2.10)$$

where  $\chi^{(i)} (i=1,2,3\dots)$  is the  $j^{\text{th}}$  order susceptibility. In general,  $\chi^{(3)}$  is a tensor of rank  $j+1$ . The first term expresses the linear polarisability and  $\chi^{(1)}$  generates the linear refractive index,  $n$ , of the material. The second-order  $\chi^{(2)}$  is responsible for such nonlinear effects as second-harmonic generation and sum-frequency generation.  $\chi^{(2)}$  is always equal to zero in centrosymmetric materials such as un-poled amorphous glasses. The third term represents the nonlinear polarisability or hyperpolarisability.  $\chi^{(3)}$  is at the origin of the variation of the refractive index,  $\Delta n$ , with the intensity,  $I = \epsilon_0 c n |E|^2 / 2$ , of the electromagnetic field, the coefficient of proportionality,  $n_2$ , being called the nonlinear index. In the simplest form, the refractive index can be written as the following [137]:

$$n(\omega, |E|^2) = n(\omega) + n_2 I \quad (2.11)$$

where  $n(\omega)$  is the linear part. The nonlinear index is related to the nonlinear polarisability,  $\chi^{(3)}$  by:

$$n_2 = \frac{3}{2n^2 c \epsilon_0} \chi^{(3)} \quad (2.12)$$

The third-order susceptibility is responsible for phenomena such as third harmonic generation, nonlinear refraction, self phase modulation, cross-phase modulation, four-wave mixing, etc.

Several models have been proposed to predict the nonlinear refractive index  $n_2$  from the dispersion of the linear refractive index at photon energies lower than the resonant energy. The simplest formula is given by Miller [150]:

$$n_2 \approx (n-1)^4 \quad (2.13)$$

which means higher linear refractive index is corresponding to higher nonlinear coefficient. Miller's rule reflects the general trend very well for a wide range of materials [151]. Figure 2.5 shows a summary of nonlinear refractive index against linear refractive index for different types of glasses and Miller's rule. In general, Miller's rule reflects the data relatively well.

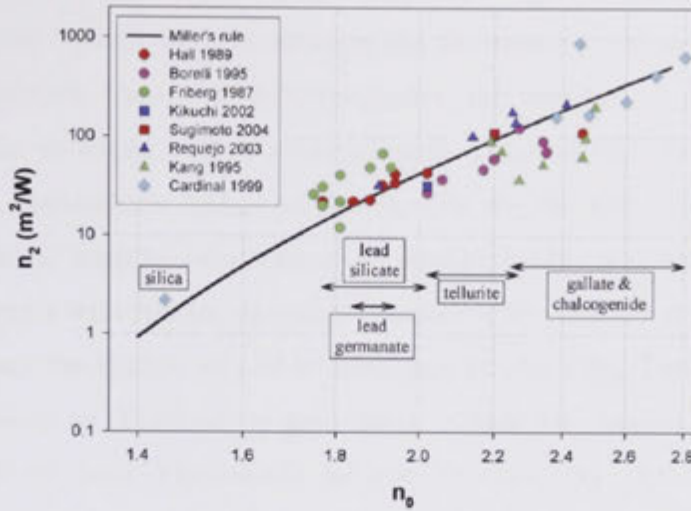


Figure 2.5: Nonlinear index ( $n_2$ ) versus linear index ( $n_0$ ) for a range of glasses and Miller's rule (black line). Source Ref. [151].

The major contributions to the total nonlinear refractive index are [152]:

$$n_2 = n_2(\text{electronic}) + n_2(\text{nuclear}) + n_2(\text{electrostrictive}) + n_2(\text{thermal}) \quad (2.14).$$

The electronic component is due to the deformation of the electron orbits and exhibits a nearly instantaneous (typically femtosecond) response. The nuclear term is on the time scale of nuclear motions, about 1ps. The electrostrictive effect is due to the refractive index variation resulting from the strain induced by electric field of the laser. The final term is the thermal effect produced by refractive index change by local heating from absorption at the laser frequency. The latter two are much slower than the former two therefore their contributions are generally ignored [152]. For tellurite oxide glasses, the nuclear contribution to the nonlinear index of refraction is about 20% compared to 10% in lead silicate glass [153].

*Ab initio* calculation of the molecular orbital's energy for  $TeO_4^{4-}$  trigonal bipyramid and  $TeO_3^{2-}$  trigonal pyramid show that, for both clusters, the highest occupied orbital is of the anti-bonding type and essentially combines the 5s atomic orbital of tellurium and 2p of atomic orbital of oxygen [154, 155]. A large part of this orbital is localized on the Tellurium atom and is oriented toward the external side of the cluster. This orbital can be correlated with the Lewis  $5s^2$  free pair of Tellurium. The corresponding electrons are highly polarisable and therefore responsible for macroscopic high linear and nonlinear indices.

The nonlinear indices of tellurite glasses are the highest found for oxide glasses. The values depend on both the concentration and the nature of the modifier introduced into the glassy matrix. Usually in tellurite glasses, the introduction of a modifier ion changes the basic structural  $\text{TeO}_4$  disphenoid entity progressively into a  $\text{TeO}_3$  trigonal pyramid via an intermediate  $\text{TeO}_{3+1}$  polyhedron [76, 89, 98, 114, 118, 120, 121, 123, 125]. This evolution leads to a decrease of the nonlinear refractive index  $n_2$ . However, addition of elements with similar electronic structure with a second lone pair such as Tl or Bi can increase the nonlinearity of tellurite glasses [76, 156]. This is related to the hyperpolarisability of Thallium oxygen units, which has been evidenced by the structural study of both Thallium(I) tellurite crystals and glasses of the same composition. Nonlinearity of thallium tellurite oxide of  $n_2=9 \times 10^{-19} \text{ m}^2/\text{W}$ , which is around 40 times higher than that of silica glass, is highest in oxide glasses. Others [157, 158] have also reported compositions with similar nonlinearity, for example,  $(100-x)\text{TeO}_2-10\text{ZnO}-10\text{Nb}_2\text{O}_5-x\text{MoO}_3$  ( $x=0, 2, 4, 6, 8$  and  $10$ ).

### 2.3.4 Second order nonlinear effects

It has been observed that with poling by laser irradiation or the application of an external voltage at elevated temperatures, that glassy materials are capable of generating second harmonic light, ie  $\chi^2$  effects are present in apparent defiance of the need to break centrosymmetry for such effects. Second harmonic generation was initially observed in Ge-doped silica glass fibres [159, 160] and thermo-electrically poled silica glass fibre [161]. This led to a number of investigations in optical second-order nonlinearity of silica-based glasses [162-165] and tellurite glass [75, 166-175]. Because tellurite glasses have very large optical third-order nonlinear susceptibility, they also have significant potential as second order materials when poled. Tellurites have high linear refractive index which leads to large third-order nonlinear optical susceptibility  $\chi^{(3)}$  according to Miller's rule. Because second order nonlinearity,  $\chi^{(2)}$ , is proportional to  $\chi^{(3)}$  in an electric-field-induced SHG, a material with a large  $\chi^{(3)}$  is an excellent candidate for poling for high second-order nonlinearity according to the relation [176]:

$$\chi^{(2)} = 3\chi^{(3)}E_{DC} \quad (2.15)$$

where,  $E_{DC}$  is the internal DC electric field.

Of previous results, that of Fujiwara *et al.*, 1997 [165] who obtained  $\chi^{(2)} = 6.8 \text{ pm/V}$  for Ge doped silica glass with UV poling stands out. Whilst it is believed to be a real result the exact means by which it was obtained and how to repeat it are unknown. The electron beam irradiation of lead silicate glass produced second-order nonlinear susceptibility of  $4 \text{ pm/V}$  [177] with the field being directly built in by the charged particles and the ionisation they produce on their damage tracks, and figures of up to  $1 \text{ pm/V}$  have been reported in silica by various means. Tanaka *et al.*, 2000 [75] obtained comparable second-order nonlinear susceptibility of  $2.1 \text{ pm/V}$  in Tungsten tellurite glass ( $20\text{WO}_3\text{-}80\text{TeO}_2$ ) using thermo-electrical poling. Taniquchi *et al.*, 2001 [170] first demonstrated the electrical poling of RF sputtered pure  $\text{TeO}_2$  thin film with second-order nonlinear susceptibility of  $1.35 \text{ pm/V}$ . Kassab *et al.*, 2007 [178] reported second order optical susceptibilities in optically poled 2%wt. Erbium doped tellurite ( $\text{TeO}_2\text{-GeO}_2\text{-PbO}$ ) glass near the melting temperature with second-order nonlinearity of  $3.6 \text{ pm/V}$ . The introduction of rare earth ions enhances the second-order optical effects as well as second order-optical effects because of increase in third order susceptibilities. Whilst the results obtained so far have been only modestly above those in silica glass, the 30x larger third order nonlinearity promises much and makes tellurites of serious interest as second order materials.

### 2.3.5 Tellurite fibre and supercontinuum generation

Tellurite glass fibres have been demonstrated in two formats to date: conventional step-index and microstructured fibres such as holey fibre (HF) or photonic bandgap fibre (PBF). Tellurite glass is classified as one of the soft glasses. Conventional step-index fibres are all solid while the microstructured fibres consisted of air holes surrounded by the material. HF [138, 140, 179, 180] has a solid core surrounded by a cladding region defined by array of holes extending along the fibre length. This fibre is similar to conventional fibre where the guiding mechanism is due to total internal reflection due to higher refractive index in the core than the cladding. This design can maintain single mode operation even with a very large core making it possible to carry high intensity with low nonlinear effects. In PBF, the hollow core is surrounded by holes confined by thin walls of material. With carefully designed parameters, these fibres can have

tailored properties that are suitable for number of linear and nonlinear applications [151].

Tellurite fibre fabrication technology has become mature in the last few years. Like the majority of soft-glasses, tellurite microstructured fibre preforms are produced by extrusion. This technique allows for the fabrication of preforms with millimetre-scale featured directly from bulk glass [151]. Another technique for tellurite glass fibre fabrication is by moulding [117, 179]. Small mode area ( $3.5\mu\text{m}^2$ ) HF with loss at order 2dB/m has been made from dehydrated tellurite glasses [117]. This fibre had a nonlinear coefficient  $\gamma$  of around  $700\text{W}^{-1}\text{km}^{-1}$  and zero dispersion around the  $1.5\mu\text{m}$  region. Recently, Qin *et al.*, 2010 [139] reported fibre with a core diameter of  $4.2\mu\text{m}$  with loss as low as 0.18dB/m at 1550nm. Larger core HF fibres have been also fabricated with very low loss such as the one by Kumar *et al.*, 2003 [140] with loss of 2.3dB/m at 1055nm. Feng *et al.*, 2008 [179] reported a very large core single mode HF with mode area of  $3000\mu\text{m}^2$ .

Because tellurite fibres can have high nonlinearity coefficients, low dispersion, and a wide transmission window, they can be used to efficiently generate very wideband supercontinuum (SC) from visible to the mid infrared beyond  $3\mu\text{m}$ . There have been a number of reported IR supercontinuum generation experiments in compact tellurite fibres [139, 180-186]. As the bulk tellurite glasses have zero dispersion wavelengths at around  $2\mu\text{m}$ , the zero dispersion wavelengths can be easily shifted down to the 1- $1.5\mu\text{m}$  region where most of the pump lasers are readily available. SC generation in fibres can be achieved in small core HF [181, 184], large mode HF [179, 180, 185, 187]. Liao, 2009 [186] reported SC generation using a 1064nm source to generate wideband light from 800nm to  $1.6\mu\text{m}$ . The author also reported SC generation from  $1.5\mu\text{m}$  to  $2.4\mu\text{m}$  when the fibre was pumped with a 1557nm source [183]. Similarly, Domachuk *et al.*, 2008 [180] generated SC from 600nm to beyond 5000nm in an 8mm length HF tellurite fibre. Surprisingly, SC generation is not only possible in very small core HF, but also in very large core holey tellurite fibre with a mode area of  $3000\mu\text{m}^2$  pumped at  $2.15\mu\text{m}$  [179]. The generation of SC in tellurite fibre can be relatively easy with the use of tapered fibre with core from  $4.2\mu\text{m}$  to  $1.2\mu\text{m}$  as reported recently [139]. Visible-to-mid-IR SC generation from tellurite fibres is a very promising

source for a wide variety of applications from instruments, biological sensing, to defence.

**2.3.6 Rare earth doped tellurite glasses**

Since tellurites have a low maximum phonon energy of 600-800cm<sup>-1</sup> and high rare earth solubility, rare earth doped tellurite glasses have been extensively studied. Tellurite glasses have a very wide transparency range (330nm to 5µm), relatively low phonon cut-off energies, and good corrosion resistance and mechanical stability. They have high refractive indices, which in turn can result in increased radiative transition rates for rare earth ions [188]. A large number of rare earth ions can be incorporated into tellurite glasses to produce a wide range of possible laser transitions from the visible to beyond 3µm. Some transitions are not possible in other glass. For instance, Pr doped tellurites [189] have photoluminescence at 1.3µm due to the low phonon cut-off energy. This photoluminescence is complete quenched in higher phonon energy glasses such as silica.

Table 2.1: Optical parameters of Er<sup>3+</sup> in a range of popular rare earth host materials reproduced from [188, 190] with updated/additional details from the cited references.

<i>Glass hosts</i>	<i>Index at 1.5 µm</i>	<i>Peak emission cross-section cm<sup>2</sup></i>	<i>Emission FWHM bandwidth nm</i>	<i>Lifetime ms</i>	<i>Maximum Er concentration</i>	<i>Max phonon energy cm<sup>-1</sup></i>
Silica	~1.5	7x10 <sup>-21</sup>	20	12	0.1% at.	1200
Alumina	~1.7	6x10 <sup>-21</sup>	55[191]	8	>1.4% at. [192]	1000 [193]
Aluminosilicate	~1.6	6x10 <sup>-21</sup>	43	10	500ppm	1100
Phosphosilicate	~1.6	6x10 <sup>-21</sup>	27	10	2.5% at	1200
Tellurite	~2.1	13x10 <sup>-21</sup> [194]	80	4	>5% mol [147], 10 <sup>21</sup> cm <sup>-3</sup> [195]	700
Chalcogenide	~2.4-3	15x10 <sup>-21</sup>	45	2.5	2%at.	400
[196]						
ZBLAN[197]	1.5	4.2x10 <sup>-21</sup>	82	9	4%mol.	500



Amongst rare earth materials, Erbium has been most widely studied because the 1.5 $\mu\text{m}$  emission falls within the low loss window of fibre for long distance telecommunication. Table 2.1 summaries properties of Er doped tellurites in comparison with other major materials for Er doped amplifiers. Apart from the comparative advantages in terms of peak emission, bandwidth, solubility and phonon energy outlined in the Table 2.1, a study by Hu *et al.*, 2001 [194] on highly Erbium doped tellurite glasses shows excellent figures for upconversion coefficients and excited state absorption rates. In particular, the  $^4\text{I}_{13/2} \rightarrow ^4\text{I}_{9/2}$  cooperative upconversion coefficients of  $2.74 \times 10^{-18} \text{ cm}^3 \text{ s}^{-1}$  were found to be more than an order of magnitude lower than that in phosphosilicate hosts ( $9.0 \times 10^{-17} \text{ cm}^3 \text{ s}^{-1}$ ) and comparable to that in silica ( $3.0 \times 10^{-18} \text{ cm}^3 \text{ s}^{-1}$ ). Another comparison of tellurite glasses (75mol%  $\text{TeO}_2$ ) with binary fluorides ( $\text{AlF}$ ,  $\text{ZrF}$ , etc.) as host materials for Erbium suggested that both co-operative upconversion and excited state absorption are reduced in the tellurite host [198].

Measurements on Erbium doped material have shown that high concentrations of optically active Erbium can be incorporated without clustering (at least 5 at%), and emission cross-sections at 1535 nm of up to  $1.3 \times 10^{-20} \text{ cm}^2$  are achievable [194, 199]. Er doped  $\text{TiO}_2\text{-TeO}_2\text{-Al}_2\text{O}_3$  has been reported with a concentration as high as  $10^{21} \text{ cm}^{-3}$  and a lifetime of 2ms with more than 50% quantum efficiency and  $8 \times 10^{-12} \text{ cm}^2$  stimulated emission cross section [195].

Ce-Er or Eu-Er codoped tellurite glass can reduce excited absorption and increase efficiency of the transition rate between the metastable state and the ground state for pumping at 980nm by reducing the population at the pump level quickly [200-202]. Because the energy gap between  $^4\text{I}_{11/2}$  and  $^4\text{I}_{13/2}$  of  $\text{Er}^{3+}$  is resonantly matched with the gap between  $^2\text{F}_{7/2}$  and  $^2\text{F}_{4/2}$  in  $\text{Ce}^{3+}$  or  $^7\text{F}_0\text{-}^7\text{F}_4$  in  $\text{Eu}^{3+}$ , the population at the pump level  $^4\text{I}_{11/2}$  is rapidly decayed to the metastable state reducing the ESA absorption of the pump significantly [203].

In some instances, tellurite glasses can be used as efficient hosts for upconversion processes for laser emission in the visible using near IR pumping. The co-doping of Er-Yb [204] or Er-Yb-Nd codoped tellurite system [205] can improve the upconversion processes when pumped at 800nm. Yb doping also helps the pump absorption at 980nm through the energy transfer between Yb and Er.



Beside Er as a dopant, rare earth doped tellurite glasses with other emission lines such as  $1.47\mu\text{m}$ ,  $1.3\mu\text{m}$ ,  $1\mu\text{m}$ ,  $1.9\mu\text{m}$  and  $2.8\mu\text{m}$  have also been studied. Tellurites have been investigated as hosts for Thulium for application in optical amplifiers in the  $1.4\mu\text{m}$  region because of their low phonon cut-off energies [74, 201, 206-211]. Also, the system allows very efficient pumping using the 800nm line of  $\text{Tm}^{3+}$  because of its hypersensitivity [210]. The performance of  $\text{Tm}^{3+}$  in tellurite is much superior to that in ZBLAN glasses [210].

Although  $\text{Tm}^{3+}$  concentrations must remain low in order to reduce cross-relaxation and OH quenching,  $\text{Tm}^{3+}$ -tellurites codoped with Holmium show sufficiently high quantum efficiencies to be considered for amplifiers [208, 211, 212]. Wang 1994 [212] reported  $\text{Tm}^{3+}$  and  $\text{Tm}^{3+}$ - $\text{Ho}^{3+}$  for emission at  $1.47\mu\text{m}$ ,  $1.88\mu\text{m}$  and  $2.8\mu\text{m}$  in tellurite glasses. The upper limit for  $\text{Tm}_2\text{O}_3$  concentration without quenching is 0.4wt% for  $1.47\mu\text{m}$  emission. By adding a cladding layer doped with Neodymium, the competitive  $\text{Tm}^{3+}$  emission at 800 nm can be effectively quenched by coupling to the  $\text{Nd}^{3+}$  absorption band [208].

Co-doping of Er and Tm in tellurite glasses results in ultra-high bandwidth fluorescence emission systems and therefore the potential for much wider bandwidth amplifiers than exist today. Huang *et al.*, 2004 [213] reported broadband emission from  $1.35\mu\text{m}$  to  $1.6\mu\text{m}$  (160nm FWHM bandwidth) in  $\text{Er}^{3+}$ - $\text{Tm}^{3+}$  codoped tellurite glass.

Emission at  $1.3\mu\text{m}$  in tellurite glasses can be achieved by two routes. The first is by doping with Nd [74]; the second is by doping with Pr [214, 215]. Tellurites with low phonon energy generally provide high fluorescence quantum efficiency therefore it is possible to measure  $1.3\mu\text{m}$  fluorescence from  $^1\text{G}_4$  to  $^3\text{H}_5$  transition of  $\text{Pr}^{3+}$  whereas it is impossible to obtain this emission in silica-based glass because the level  $^1\text{G}_4$  is next to  $^3\text{F}_4$ , which can be quenched by emission of three photons in silica-based glass but 5 phonons in tellurite glasses [214]. Man, 1999 [189] reported  $\text{Pr}^{3+}$  doped zinc-tellurite glasses emitting  $1.33\mu\text{m}$  with bandwidth of 100nm and lifetime of 24 $\mu\text{s}$  and quantum efficiency of 2.6% pumped at 488nm or 980nm.

Nd doped tellurite glasses for laser and amplifier at  $1\mu\text{m}$  have been studied and demonstrated [74, 214, 216]. Wang *et al.*, 1994 [216] was the first to demonstrate operation of a single mode  $\text{Nd}^{3+}$  doped tellurite glass fibre laser at 1061nm pumped at

818nm with a slope efficiency of 23% to prove the possibility of using tellurite as a low phonon host.

Another milestone in rare earth doped tellurite glasses is the achievement of 2 $\mu$ m emission of Tm and Ho [212]. Tm<sup>3+</sup> and Tm<sup>3+</sup>-Ho<sup>3+</sup> doped tellurite can fluoresce at 1.47  $\mu$ m, 1.88 $\mu$ m and 2.8  $\mu$ m. The upper limit for Tm<sub>2</sub>O<sub>3</sub> concentration without quenching is 0.4%wt. for 1.47 $\mu$ m emission. Tsang *et al.*, 2008 [217] demonstrated a Yb<sup>3+</sup>-Tm<sup>3+</sup>-Ho<sup>3+</sup> triply-doped tellurite fibre laser pumped at 1.1 $\mu$ m giving 25% slope efficiency for 2.1 $\mu$ m emission. Recently, Richards *et al.*, 2010 [218] obtained Q switched operation at 2 $\mu$ m in a fibre laser doped with Tm<sup>3+</sup> (1.8 $\mu$ m emission) and Ho<sup>3+</sup> (2.0 $\mu$ m emission) pumped at 800nm.

The presence of OH in tellurite glass can have detrimental effect on the performance of the device due to quenching of number of levels such as 1.4-1.6 $\mu$ m of Er<sup>3+</sup> [144-147, 219] and 2 $\mu$ m of Tm<sup>3+</sup> and Ho<sup>3+</sup> [211, 220]. The solution to overcome this effect is to reduce the OH contamination using highest quality materials [117], preparing and storing samples in dry conditions and dehydration after glass fabrication using dry oxygen bubbling [146, 219, 221] and halogenation of tellurite glasses [144, 220].

### 2.3.7 Erbium doped fibre amplifier

The Er doped tellurite fibre amplifier (EDTFA) has been intensively studied for use in the telecommunication window at 1.5 $\mu$ m [117]. High gain Erbium doped tellurite fibre amplifiers (EDTFA) were first demonstrated by NTT labs in 1997 [199]. An 85cm long Er doped tellurite fibre was pumped with 130mW of 975nm and provided a small signal gain of 16dB. The slope efficiency was 0.29dB/mW. After further investigation, the authors found that the gain per unit length in fibre for Er doped tellurite fibre is five times larger than that for Er doped Silica fibre with almost the same fibre parameters. With the help of a fibre-grating-type gain equalizer, it was possible to achieve gain of more than 25dB and noise figure of less than 6dB over a wavelength range from 1561 to 1611nm [117, 222-224] well beyond what silica based devices can achieve. Higher gain (over 25dB) and lower noise (less 5dB) EDTFA have been obtained for pumping at both 980nm [225] and 1480nm [226].

Devices with gain-flattened bandwidths of up to 80 nm have been reported [222, 223, 227]. A hybrid fibre amplifier using a combination of a tellurite EDFA and a  $\text{Tm}^{3+}$ -doped fibre was reported, exhibiting a gain bandwidth of 113 nm [222, 223].

EDTFAs have been demonstrated in wavelength-division-multiplexing transmission systems in the C- and L- band [228, 229]. The system employing EDFAs has a number advantages over the system employing silica based amplifiers, such as transmission capacity and higher gain from the shorter length of fibre amplifier [229]. It has been shown that EDFAs provide the highest capacity in broadband system compared to common Er doped fibre materials such as aluminum-phosphate-silicate, zinc-sodium-germanate-silicate [227, 230].

### 2.3.8 Raman amplifiers

Tellurite fibre Raman amplifiers (FRAs) have been used in multi-wavelength pumping experiments to achieve ultra-wideband amplification [231]. The gain-bandwidth expansion that can be achieved by this scheme is determined by the magnitude of the Stokes shift. The maximum shift for FRA using silica fibre is 100nm while the shift for tellurite is at least 170nm at 1.5 $\mu\text{m}$ . The Raman gain coefficient is about as high as 30 times larger in tellurite than silica. These features indicate that tellurite devices are more promising than silica for making ultra-wideband FRA with much shorter device length and fewer pumps. Mori *et al.*, 2001 [232] demonstrated the first wideband tellurite based RFA with 160nm bandwidth (1490nm to 1650nm) with gain over 10dB and noise figure below 10dB. It required only 4 different wavelength laser diodes to pump a 250m length of tellurite fibre. The tellurite FRA has been used in a large capacity wavelength demultiplexing (WDM) system with 313 channels of 10 Gb/s. Error-free operation across a 124nm band was achieved as the widest seamless application ever reported [231, 233].

Gain flattening in tellurite RFA, apart from large number of pump wavelengths, can be achieved by using hybrid system of tellurite and silica fibre [117, 232, 234] or using complex tellurite glass with flat Raman gain spectrum [235, 236]. Some compositions of tellurite glasses can also increase the Raman shift limit to even  $1000\text{cm}^{-1}$  (or 284nm shift when pumped at 1550nm) such as in  $\text{WO}_3$  rich tellurites [236-241] or/and  $\text{PO}_4$  rich tellurites [239, 241, 242] or  $\text{Ti}_2\text{O}$  rich tellurites [243]. These

compositions also exhibit much higher gain coefficients with peak as high as 30-60 times that of silica [236, 243]. With this development in tellurite glass technology, better ultra-broadband tellurite Raman amplifiers are on the horizon and the capacity limits on a single strand of optical fibre can be further extended.

### 2.3.9 Summary

From the above discussions, it is clear that tellurite glasses offer a rich range of functionalities for integrated optical devices potentially all of which can be integrated together to form much of a system-on-a-chip. Passive devices with high refractive index, small mode areas, broad transmission windows from UV to Mid-IR and high nonlinearity are certainly possible. Also, the possibility for wavelength conversion via supercontinuum in short devices, four-wave mixing etc. is another advantage. Active devices such as Raman amplifiers, lasers or rare earth doped amplifiers and lasers provide loss compensation or on board laser sources. Despite all this promise there have been no demonstrations of even low loss planar waveguides in tellurite glasses, and as discussed in the next section this is what is preventing the field developing. This project will be the stepping stone for the development of tellurite glass planar integrated optical platform.

## 2.4 *Development of tellurite and Tellurium oxide waveguide fabrication*

There are various methods to make 2D waveguides but they can essentially be divided into two main categories [244]:

- a) **Direct patterning processes** where the pattern is directly written on the substrate using a focused laser, electron, or ion beam to produce a refractive index change. This is often performed on bulk glass substrates due to the inherently 2-D confinement produced, but photosensitive thin films for example have also been used.
- b) **Masking processes** where the circuit is first written on the substrate (which may include a core layer) as a mask layer by photolithography. Then either an additive step (eg lift off using the mask to add the core) or a modification process (etching away unwanted parts of the core

layer, or raising the index of the core layer/substrate by ion exchange, diffusion, UV or ion beam to provide a 2D core) is used.

Each of the techniques has advantages and disadvantages. For instance, direct patterning usually results in low index contrast leading to low confinement of the mode. Therefore, mode areas are usually large and the waveguides cannot be bent sharply. However, the direct patterning method allows the use of an optimised bulk glass with known good properties. Masking processes followed by etching on the other hand provide strong confinement for the mode leading to mode area of only a few square micrometers. Long waveguide structures can also generally be coiled compactly in a very small area yielding small devices, or alternately the opportunity to integrate multiple amplifiers on one chip. However, masked processes usually involve more fabrication steps, making fabrication more challenging, longer and generally requiring more sophisticated facilities. Furthermore, fabricated thin films generally have different properties from the bulk requiring extensive film characterisation and further treatments, such as thermal annealing, are sometimes needed in order to make the films bulk-like.

#### 2.4.1 UV, femtosecond and ion direct writing

The first reports of direct writing used a 244nm laser to form single mode channel waveguide in tellurite glasses ( $\text{TeO}_2\text{-ZnO-Na}_2\text{O-xGeO}_2$ ,  $x=0, 10, 20\%$ ) [78, 79]. Refractive index change of  $1.5 \times 10^{-3}$  was reported with a waveguide dimension of around  $10\mu\text{m}$  diameter. However, the total insertion loss for a 1cm waveguide was 8dB including coupling losses, though the waveguide mode field appeared to be a reasonable match for single mode fibre and so most of this loss would be considered propagation loss. The mechanism of formation of the waveguides is not completely understood, however, it has been concluded that it does not relate to the photosensitivity of Germanium but a local densification of the glass most likely caused by localised heating of the glass as the 244nm radiation is well above the bandgap of the glass and therefore very strongly absorbed.

An alternative method of direct laser writing is using femtosecond pulsed lasers at a wavelength below the band gap. Tokuda *et al.*, 2003 [81] reported guiding of a He-Ne laser beam in fs-pulse direct write tracks in niobium tellurite glasses ( $x\text{Nb}_2\text{O}_5\text{.(1-}$

x)TeO<sub>2</sub>, x=5, 15, 23). The permanent index change was  $9 \times 10^{-3}$ . The author suggested that the change in index was due to the breaking of Te-O bonds which caused re-arrangement of glass structure. Sundaram *et al.*, 2003 [245] experimented with tightly focused femtosecond laser pulses in tellurite glasses (10Na<sub>2</sub>O-90TeO<sub>2</sub> doped with 2 mol% La<sub>2</sub>O<sub>3</sub> and 1 mol% Al<sub>2</sub>O<sub>3</sub>). There was no structural change observed when comparing the bulk regions and laser-written regions. There was no structural change evident even in the microexplosion regime. Righini *et al.*, 2005 [246] used 50-fs pulses with a repetition rate of 1kHz at 800nm to modify refractive indices in tungsten-tellurite and zinc-tellurite glass samples. The pulse energy used was in the range of 0.1-1μJ and at writing speeds of 20 or 100μm/s. The refractive index change was detectable but unfortunately, the induced refractive index change was negative and so conventional waveguiding was not possible.

Improvements of this technique have been recently reported [247]. Direct writing in Erbium doped tellurite (TeO<sub>2</sub>-P<sub>2</sub>O<sub>5</sub>, Al<sub>2</sub>O<sub>3</sub>, La<sub>2</sub>O<sub>3</sub> and Er<sub>2</sub>O<sub>3</sub>) glasses produced waveguides with estimated losses below 2dB/cm. The glass was modified using 45 fs-pulses at 806nm with 1kHz repetition rate. The addition of phosphate seems to favour waveguide formation. The best reported results so far in direct writing of tellurite waveguides were reported in 2008 [248]. Tellurite based Erbium doped active waveguides fabricated by femtosecond laser pulses were produced in a glass composition of 10ZnO-10Na<sub>2</sub>O-80TeO<sub>2</sub> doped with 0.5wt% Er<sub>2</sub>O<sub>3</sub> or ion concentration  $7 \times 10^{-19}$  ions/cm<sup>3</sup>. An index change of  $1 \times 10^{-3}$  at 633nm was achieved in waveguide length of 2.5cm. Waveguide loss was estimated to be ~1.35dB/cm.

An analogy to direct laser writing, ion irradiation, has also been used to fabricate tellurite waveguide [249, 250]. A 24μm gap created by two 75μm thick silicon covers was used to gate the N<sup>+</sup> ions. The N<sup>+</sup> ions had an energy of 1.5MeV and penetrated 1.5μm into the tungsten sodium tellurite (WNT) glass. Despite the fact the introduction of N<sup>+</sup> into the sample induces a negative density change due the volume expansion of the implanted region, there is light confinement via a barrier structure formed by ionisation processes induced by the implanted N<sup>+</sup> ions. No losses or index changes were reported.

Despite their flexibility in terms of the geometry of the formed waveguide and 3-D structure capability, direct writing techniques are restricted to low index contrast.

The modes are generally large and compact devices are not easily obtained due to bending loss. Low loss waveguides have yet to be accomplished.

#### 2.4.2 Ion-exchange

Ion-exchange techniques have long been known to produce high quality waveguides in phosphosilicate glasses [251, 252]. Therefore, it was a natural extension to apply the same methodology to tellurite glasses [83, 253-255]. All reported ion exchange in tellurites were performed by Ag-Na exchange at elevated temperature ( $\sim 300^\circ\text{C}$ ) and in planar slab waveguide form. Index changes of up to 0.2, diffusion depths of up to  $4\mu\text{m}$  and propagation loss of 3.7dB/cm have been reported [254, 255]. Severe surface degradation was reported with exchange temperatures of  $330^\circ\text{C}$  and above. Because all the obtained waveguides from ion-exchange have been in slab planar forms there is no direct comparison with other techniques outlined here for channel waveguides.

#### 2.4.3 Physical sputter etching

Lanata, *at al.* 2008 [256] and Pietralunga, *at al.* 2008 [257] chose dry etching methods for  $\text{TeO}_2$  using Ar sputter etching. They made this choice to avoid the micromasking effects observed in reactive ion etching of  $\text{TeO}_2$  when halogen-containing gas mixtures are used from non volatile Fluoride or Chloride compounds of Tellurium. The waveguide obtained had a width of  $4.5\mu\text{m}$  with a refractive index of 2.05. The authors claimed that the roughness was negligible with this etching method. However, the propagation loss was estimated to be 6.3dB/cm and 11.4dB/cm for TE and TM modes at  $1.55\mu\text{m}$ , respectively. Certainly, this was a novel approach to  $\text{TeO}_2$  etching but the propagation losses were an order of magnitude too high for any useful functional optical devices.

#### 2.4.4 Wet etching

O'Donnell 2007 [258] studied the possibility of wet etching tellurite glasses using a number of solutions including NaOH,  $\text{H}_2\text{SO}_4$ , HCl, HF and  $\text{H}_2\text{O}$ . It was found that tellurites react very quickly with these solutions. NaOH,  $\text{H}_2\text{SO}_4$  and HCl are poor etchants due to severe hydrolysis on the glasses leaving very poor surfaces. HF leaves relatively clean etched surfaces, however, subsequent IR spectroscopy studies showed that there was large amount of OH bonds formed inducing high IR loss.



### 2.4.5 Fibre-on-glass

Benson *et al.*, 2005 [259] suggested the fibre-on-glass (FOG) method to fabricate waveguiding structures on substrates. The FOG method is to thermally bond high quality fibre onto glass substrates. This method can be used to obtain high contrast waveguides without the roughness due to etching in conventional fabrication. Rivera *et al.*, 2007 [260] used this technique to demonstrate the applicability to tellurite fibre on tellurite substrates. However, in this demonstration, a 100 $\mu\text{m}$  thick rod was used as a fibre core leading to a highly multimode structure, and it is not clear how this can be used to make more complex waveguide devices.

### 2.4.6 Summary

The results reported so far have not yet come close to achieving planar tellurite waveguide with losses low enough to be useable in real world integrated devices. It was clear at the outset of the project that attaining low loss waveguides would be of fundamental importance to the field and so this was considered initially to be the major aim of the project. The availability of facilities for film deposition by sputtering or ultrafast pulsed laser deposition, and high quality UV lithography and plasma etching at the ANU allowed us to seriously consider the subtractive approach using thin film, lithography and plasma etching, and to investigate this route thoroughly for the first time.

## 2.5 Conclusion

The excellent optical properties of tellurite are well known and extensively exploited in the fields of acousto-optic devices, fibre based optical amplification, and non-linear optical processing. However, planar tellurite devices have, until now, proven to be rather problematic. There have been a number of reports of planar waveguides fabricated in tellurite glasses using techniques such as UV direct write, femtosecond laser direct write, ion exchange, ion implanting, and sputter etching. Whilst some of these methods have realized small channel waveguides, propagation losses were high (lowest reported loss of 1.3dB/cm) and there are no reports of losses even approaching 0.2dB/cm, the allowable values for useful linear or non-linear optical integrated devices. The best reported result using plasma etching was 6.3dB/cm. Hence, to date no high



quality fabrication process has yet been demonstrated for tellurite materials for planar integrated optics.

## **Chapter 3:**

# ***Reactive sputtering deposition of optical Tellurium oxide films***

This chapter reports the use of reactive radio frequency (RF) sputtering to fabricate as deposited films with the required stoichiometry and optical propagation losses below 0.1dB/cm, low enough to enable high quality integrated optics devices. In doing so, a wide range of sputtering parameters was explored using the design of experiment (DOE) method to obtain the desired stoichiometry, high index, and low loss planar waveguides. The obtained films from these series of runs had O/Te ratios ranging from 1 to 3.5. The refractive index variation and planar waveguide propagation losses at 1550nm are reported as a function of oxygen content over this wide range. The bandgap, Raman spectra, and effects of annealing against stoichiometry are also reported and evidence provided that there are compositions which are completely thermally stable.

### ***3.1 Tellurite glass and Tellurium oxide thin film development***

Thin films of amorphous tellurite glasses and Tellurium oxide have been produced by several methods including glass blowing [142, 261-263], chemical and sol-gel [264-267], large dose ion implantation [268], thermal evaporation [269-271], plasma-activated reactive, bias-assisted deposition (PARBAD) [272, 273], reactive radio frequency sputtering using pure Tellurium [274-281]; and pulsed laser deposition [282-284]. Despite this variety of fabrication methods, the previous works on tellurite thin films have not reported low propagation losses at 1550nm for useful functional planar applications. The latest achievements from some of the mentioned technologies are now summarised.

#### **3.1.1 Glass blowing**

Tellurite glass thin films can be achieved by a glass blowing technique. A number of binary tellurite glass such as  $V_2O_5$ - $TeO_2$  [261],  $Cu$ - $TeO_2$  [262],  $BaO$ - $TeO_2$  [263] and  $MoO_3$ - $V_2O_5$ - $TeO_2$  [142] obtained from this technique have been reported. The glasses

were melted at temperature around 700-900°C in air before being blown into films. Thicknesses of a few micrometers can be achieved. The obtained films have amorphous characteristics. This is an interesting method to achieve thin films for characterization but it remains to be demonstrated that the thin films can be transferred onto a planar substrate to make practical integrated devices.

### 3.1.2 Sol-gel

Sol-gel and related chemical processing routes are attractive options for thin film fabrication as they utilise only spin on coatings and thermal processing and so can be performed quickly on relatively low cost equipment. It can be used to make thin film coatings, waveguides, and other planar devices [264-267]. To obtain tellurite glass films, tellurium alkoxide compounds,  $\text{Te}(\text{OR})_n$ , where R is normally a simple organic alkyl group, are used as precursors. Challenges with these compounds are their tendency to form precipitates rather than gels. In addition, there are a number of other precursors such as telluric acid  $\text{Te}(\text{OH})_6$  or Tellurium (VI) methoxide  $\text{Te}(\text{OCH}_3)_6$  which can be employed in chemical processing routes for tellurites. There are significant challenges in producing low loss optical thin films with sol-gel. Transparent films with reasonable mechanical and optical properties could only be obtained via heat treatment to densify the films and eliminate residual OH and other contaminants [265, 285]. However, devitrification can appear in sol-gel tellurite films at temperatures above 290°C. Hodgson *et al.* 2006 [265] concluded that it is impossible to obtain pure and dense  $\text{TeO}_2$  thin films via the sol-gel route. Only multicomponent glasses such as 10 $\text{TiO}_2$ -90 $\text{TeO}_2$  can be made into thin films with properties similar to the bulk after high temperature thermal treatment. [265, 285]. The refractive index of the obtained film at 679nm was 2.19, which was close to that of the bulk sample of the same composition which measured 2.13 at 633nm. Additionally, this is not a suitable technique for rare earth ion doping (e.g.  $\text{Er}^{3+}$ ) as the significant levels of OH contaminant present quenches the 1.5 $\mu\text{m}$  Er emission lifetime very effectively. So far, there has been no report of propagation loss in tellurite thin films fabricated by sol-gel method.

### 3.1.3 Thermal evaporation

Thermally evaporated tellurite films can be achieved via electron beam heating or electrical heating. Takenaga *et al.*, 1983 [286] first reported  $\text{TeO}_x$  ( $x < 2$ ) thin film by

thermal evaporation of Te and  $\text{TeO}_2$  powder for optical memory disk applications due to its sensitivity to laser diodes and excellent stability for archival recording. When pure  $\text{TeO}_2$  is used as the source to produce films, the stoichiometry of the films is known to not only depend on the source temperature but also strongly on the substrate temperature [287, 288]. Films produced by resistive heating of the  $\text{TeO}_2$  were wholly amorphous when the substrate was kept at room temperature [288]. Thermal evaporation is relatively easy to apply to  $\text{TeO}_2$  films, due to the low melting temperature of  $\text{TeO}_2$  around  $650^\circ\text{C}$ . However, the stoichiometry of the films is hard to maintain as the initial materials can decompose, phase separate, or reduce during the deposition. There has been no report of propagation loss in tellurite films produced by this technique.

### 3.1.4 Laser deposition

Most tellurite glasses are multicomponent because of the need for inclusion of network modifiers to make them glassy. Stoichiometry transfer is critical as the glass properties change with composition. Maintaining the amorphous state to the films to reduce scattering loss is also important. Obtaining films with properties that are the same as the bulk glass is a difficult task in most fabrication methods. Laser deposition techniques are known to fulfil many of these requirements. Laser deposition of films has so far been demonstrated by two types of laser: UV pulsed lasers such as excimer lasers at 193 or 248nm with typically nanosecond pulses [282-284, 289, 290] or ultrafast lasers such as Ti-Sapphire femtosecond pulsed lasers at 800nm [291]. The two laser ablation mechanisms are significantly different. The absorption of the radiation by the material differs between the long pulse UV excimer laser and the NIR femtosecond pulse [292, 293]. The energy absorption is linear in the former and nonlinear in the latter. In the femtosecond regime, the ablation is a result of multiphoton ionizations followed by avalanche ionization which evaporates the materials from the target.

Most reported results using laser deposition are for complex glasses with rare earth doping. Earlier experiments suggested that the films were nearly stoichiometric with respect to the target when the substrate was kept at room temperature and the chamber was filled with Oxygen at around 5Pa [282-284]. The lowest thin film loss was 0.8dB/cm at 633nm. Very recently, Irannejad *et al.*, 2010 [289, 290] have reported

phospho-tellurite glass thin films deposited on silica substrates using an ArF laser at 193nm with 20ns pulse width and  $3.2\text{J}/\text{cm}^2$  fluence. The deposited films had refractive indices and stoichiometries close to that of the bulk. The films obtained had propagation losses in range of 0.13-0.75dB/cm at 633nm despite the fact the films were in microstructure form with a particle size of 50nm. Still, obtaining large-area uniform films from this technique remains a challenge [284].

### 3.1.5 Plasma technique

Reactive RF sputtering of Tellurium in Oxygen and Argon has been reported to be the most promising method to produce  $\text{TeO}_2$  thin films [274-281]. The stoichiometry of the deposited films can be controlled precisely by adjusting sputtering power, chamber pressure, gas flows and Oxygen content in the sputtering chamber [276-281]. Totally amorphous stoichiometric thin films are generally obtained relatively easily by sputtering [276]. Suitable sputtering tools and conditions lead to high energy species creating denser as deposited films eliminating the need for thermal annealing. The optical quality of the films depends on all deposition parameters, and the production of high optical quality films requires optimization of more parameters than just Oxygen flow.

Since the report of RF sputtered Tellurium oxide films in 1992 [294], most works on plasma deposition of  $\text{TeO}_2$  use the Oxygen flow percentage to tune the stoichiometric properties of the films. Di Giulio *et al.*, 1993 [275] reported the properties of sub-stoichiometric oxide films with O/Te ratio in the range of 1.0-2.0. These films are very lossy due to the presence of excess Tellurium. They also tend to exhibit crystallization when subjected to post deposition thermal treatments. Recently, more work has been done on targeting stoichiometric and oxygen rich films, which have O/Te ratio ranging from 2.0 to 3.0 [278, 279, 281]. It has been proved that stoichiometric amorphous  $\text{TeO}_2$  thin films can be consistently obtained by room temperature RF sputtering [276], but increasing the substrate temperature (usually desirable in thin film manufacture to promote adhesion and obtain a more bulk like film) can result in crystallization and increases in grain sizes, and therefore higher optical loss. Nayak *et al.*, 2003 [278] reported losses of 2.2dB/cm in as deposited films and 0.26dB/cm in films annealed at 200°C. Whilst the losses in the annealed film were almost at the level

required for planar devices, annealing is undesirable in planar devices as it often leads to restructuring of the film at the anneal temperature which results in frozen in stress on cooling due to the different thermal expansion coefficient of the substrate. Ideally, as-deposited films would be amorphous, stable, and low loss straight from sputtering at room temperature without any further heat treatment. However, low optical losses in as deposited thin films have not been reported previously.

One of the priorities of this project is to obtain low loss tellurite films. Therefore, the RF magnetron sputtering route was chosen because of the many advantages over other techniques as outlined above. Ultrafast pulsed laser deposition may also be a viable route, but funding and time restrictions and the need to develop means to generate DUV Ultrafast pulses at multi-Watt powers meant the resources to explore this route were unavailable.

### 3.2 Magnetron reactive RF sputtering deposition

#### 3.2.1 Sputtering principle

Sputtering is one of the most versatile deposition techniques for fabricating device-quality films [295]. Sputtering processes give particulate free films on large substrates and provide films with good adhesion, homogeneity and high control of film thickness [296]. It involves creating plasma (usually with an inert gas such as argon) by applying a voltage between a cathode (target holder) and anode (gun shield, rest of vacuum chamber). The target is consequently subjected to bombardment by high energy ions. The target surface ejects atoms or atom clusters which diffuse away finally depositing a thin film on the substrate by condensation. Sputtering is normally performed at a pressure of  $10^{-3}$ - $10^{-2}$  Torr due to the need to support the plasma, although there are means to enable lower pressure plasmas than this (e.g. low pressure ion sources) which provides greater mean free paths for the sputtered material.

There are two modes of powering the sputtering guns. In DC sputtering mode, a direct voltage is applied between the cathode and the anode. This process is restricted to conducting targets, such as Al or In. In RF sputtering, which is suitable for both conducting and insulating targets, a high frequency generator (usually at 13.56MHz as assigned by the FCC) is connected between the electrodes. The use of magnets, as in

magnetron sputtering, is particularly useful to confine the plasma increasing its density near the target surface producing high deposition rates and low substrate temperature.

RF sputtering allows all materials whether metal or insulator to be used as targets. Low pressure (5-15mTorr) can be used. Oscillating electrons at high frequencies cause increased collision with the gas contributing to enhanced ionization. Unlike DC, electrons do not reach the anode surface since both electrodes in an RF discharge are at negative potential with respect to the plasma [295] and so electrons are reflected back and forth between the electrodes and cause ionization. RF sputtering is possible because the target self-biases to a negative potential due the mobility difference between electrons and ions [297].

The sputtering rate can be improved for all materials via the use of magnetrons in RF sputtering guns. The efficient use of electrons to promote ionization of the gas in the sputtering chamber is possible with the assistance of a magnetic field. Application of an axial magnetic field in a planar diode glow discharge system increases the path length of the electron because electrons follow longer helical path orbits before they reach the anode. In addition, the magnetic field helps the electrons to stay away from the walls of the sputtering chamber, therefore, reducing the losses of electrons due to recombination process at the walls. Magnetrons greatly enhance the capability of the sputtering process by increasing the ionization efficiency. Magnetron sputtering achieves high deposition rates [297].

With magnetron sputtering, the target surface erodes unevenly due to the magnetic field which leads to the formation of a racetrack. The racetrack region sputters preferentially whereas the rest of the target barely erodes. Special designs of magnetic and electric field configuration and target shapes are necessary to assure uniform erosion of targets. The electron bombardment of substrates is virtually eliminated in a magnetron source.

The principle advantage of the magnetron configuration is the formation of dense plasma near the cathode at low pressure (2-40mTorr) [297]. This means ions can be accelerated from the plasma to the cathode without loss of energy due to physical or exchange collisions. The result is an increase in the average kinetic energy of the sputtered atoms and an increase in the probability of atoms from the cathode to the substrate.

In the case of reactive sputtering of metallic targets, the deposition rate and structure properties of transparent films strongly depend on the reactive gas content in the sputtering chamber. The sputtering rate at low partial pressure tends to be high but suddenly drops to a much lower rate when the partial pressure increases above a particular level. At a low partial pressure, metal is sputtered from the target and the oxidation reaction takes place only on the substrate. At higher partial pressures, oxidation of the target face occurs and the sputtering rate drops rapidly since oxides sputter generally much more slowly than pure metals [296].

The reactive gas pressure, the flow rate of gases and sputtering rate determine whether the compound formation occurs at the target or at the substrate. The stoichiometry of the film depends on the rate of arrival of sputtered atoms at the substrate compared to the arrival rate of gas atoms from the reactive gas. The removal of compounds that may have formed at the target surface occurs much slower than the removal rate of the material from the target. Therefore, when reactive gases such as Oxygen, Nitrogen are introduced into the chamber, the sputtering rate can be significantly reduced. Higher RF power or lower pressure can be used to compensate for the reduction.

### 3.2.2 Sputtered film composition

Considering the example of sputtering a Te target in partially Oxygen-fill plasma, it is known that the oxidation rate of the Te atoms is directly related to the ratio of the number of  $O_2$  molecules striking the substrate surface to the number of Te atoms getting onto the surface of the substrate. The flux of  $O_2$  molecules striking a unit area of the substrate surface is [298]:

$$n(O_2) = \frac{1}{4} n v_{av} = \frac{1}{4} \frac{P(O_2)}{kT_s} \sqrt{\frac{8kT_s}{\pi m}} = 1.07 \times 10^{11} \times \frac{P(O_2)}{\sqrt{mT_s}} \quad (3.1)$$

where  $v_{av}$  is the average velocity of  $O_2$  molecule,  $P(O_2)$  is the partial pressure of  $O_2$  in the chamber,  $T_s$  is the temperature of the sputtering,  $k$  is Boltzmann constant, and  $m$  is molecular mass of  $O_2$ .

The flux of Te atoms getting to the substrate surface per second is:



$$n(\text{Te}) = \frac{\rho R N_A}{M_{\text{TeO}_x}} \quad (3.2)$$

where  $\rho$  is the density of the film and  $R$  is the deposition rate of the  $\text{TeO}_x$  film,  $N_A$  is Avogadro's number,  $M_{\text{TeO}_x}$  is the molar mass of the  $\text{TeO}_x$ . Alternatively, the flux of Te atoms getting to the substrate surface per second can also be calculated from the sputtering rate of the target as:

$$n(\text{Te}) = N_s \delta / S \quad (3.3)$$

where  $N_s$  is the sputtering rate of the target, and  $\delta$  is the efficiency of the atoms getting from the target to the substrate,  $S$  is the substrate area.  $N_s$  is approximately proportional to the RF power for a fixed gas mix, and  $\delta$  is determined by the geometry of the substrate and the gun. It also depends on the pressure of the chamber as this determines the mean free path.

From the Equation (3.1-3.3), the ratio of  $n(\text{O}_2)$  to  $n(\text{Te})$  is:

$$\frac{n(\text{O}_2)}{n(\text{Te})} = 1.07 \times 10^{11} \times \frac{P(\text{O}_2) M_{\text{TeO}_x}}{\sqrt{m T_s} \rho N_A R} = 1.07 \times 10^{11} \times \frac{P(\text{O}_2) S}{\sqrt{m T_s} N_s \delta} \quad (3.4).$$

The ratio of  $n(\text{O}_2)$  to  $n(\text{Te})$  will increase with the increase of oxygen pressure in the sputtering gas and decrease of the sputtering rate of the Te target. The composition of  $\text{TeO}_x$  films are determined by the parameter  $P(\text{O}_2)/R$  or  $P(\text{O}_2)/N_s$ .

### 3.3 Experimental measurements of refractive index and thickness of thin films

A dual angle spectroscopic reflectometer (SCI Filmtek 4000 [299]) was used to measure the refractive indices and thicknesses of the films. The wavelengths of the spectrum is from 450nm to 1650nm. The reflectometer uses the normal incidence and polarized 70 degree reflection data to calculate the properties of the measured films. An appropriate model of refractive are selected for the parameters to be solved. For optical thin films Tauc + Lorenz model, which is a generation of the Lorentz Oscillator model, are selected.

### 3.4 Deposition and characterisation of Tellurium oxide films fabricated by reactive RF magnetron sputtering

All depositions were performed on an AJA International ATC 2400-V sputtering system equipped with A330 guns. The targets used were pure ( $>99.95\%$ ) Te powder pressed in to a 3" plate bonded to a copper cup for good heat dispersion and were commercially sourced to AJA international. The RF magnetron sputtering chamber had a load lock and was usually pumped to base pressures below  $3 \times 10^{-7}$  mTorr. The RF gun was cooled with water at  $20^{\circ}\text{C}$ . The rotating substrate holder was placed at a distance of  $\sim 10\text{cm}$  from the target and the substrate was not actively cooled. The schematic of the gun-substrate relative position is on Figure 3.1.

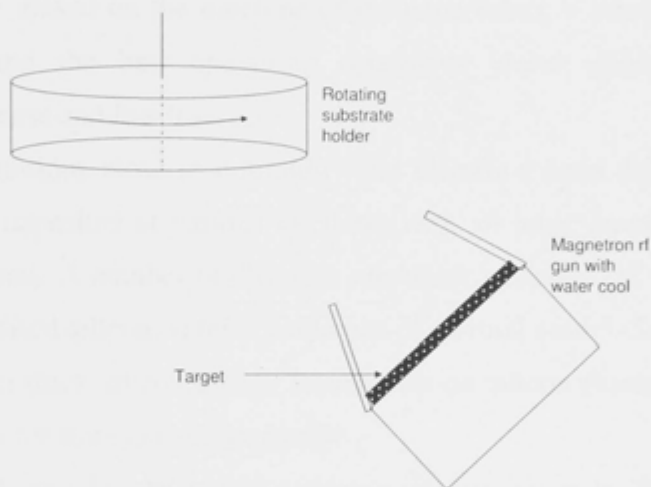


Figure 3.1: Sputtering gun and substrate configuration

It has been reported that the properties of reactively sputtered  $\text{TeO}_x$  films are influenced by the running parameters such as RF power, pressure of the gas mix, ratio of gases ( $\text{Ar}/\text{O}_2$ ), substrate temperature etc. [274, 276]. Thus there are number of variables to optimise the condition of the  $\text{TeO}_x$  films.

The effects of several sputtering parameters were investigated to obtain suitable thin films. The sputtering parameters that were investigated were: chamber pressure (2.0mTorr to 20mTorr), RF power (120W to 360W), and percentage of Oxygen in the gas mix (20% to 80%). The total flow of  $\text{O}_2$  and Ar was kept at 15sccm (standard cubic centimetre per minute or  $\text{cm}^3/\text{min}$  at standard room temperature and atmospheric pressure). This flow was chosen as it was the maximum possible whilst allowing

chamber pressures across the whole desired range (limited by the turbomolecular pump's pumping speed). The thin films produced from this investigation had thickness in the range 500nm to 2µm. Since there were 3 varying parameters and several optimization targets, the design of experiment (DOE) method was employed using software ("D.O.E Fusion" from S-Matrix or "Essential Regression and Experimental Design" written by D. Steppan, J. Werner, and R. Yeater, available from <http://www.jowerner.homepage.t-online.de/>, last visited on 12 May 2010), to screen the experimental conditions to achieve the desired properties. In the initial experiments, the refractive indices of the films were used as a response function to map out its dependence on the various sputtering parameters such as O<sub>2</sub>/Ar content, pressure and sputtering power. Based on the outcome of the experiment, a smaller set of runs was performed to find the best sputtering conditions under which the films were stoichiometric, dense and low loss.

Once conditions close to optimum were identified from the DOE, a series of TeO<sub>x</sub> films was deposited at various O<sub>2</sub> flows with all other parameters fixed at the optimum conditions. A number of different substrates were used in each run including 4" thermally oxidised silicon wafers (2 microns of thermal oxide), Silicon pieces, silica slides and 200nm thick silicon nitride membranes on silicon (back etched to make a very thin window for Raman measurements).

The DOE data for the initial screening experiment is in Table 3.1. The first column is the order of the run, the second to fourth are the values of chamber pressure (mTorr), RF gun power (as % of 600W) and O<sub>2</sub> flow (as % of 15sccm) as produced using the DOE software. The fourth column is the measured refractive index at 1550nm. The experimental data is then fitted with the relationship:

$$y = b_0 + b_1P_r + b_2P + b_3O_f + b_4P_rP_r + b_5P_rP + b_6P_rO_f + b_7PP + b_8PO_f + b_9O_fO_f \tag{3.5}$$

where  $b_n$  are fitting coefficients,  $P_r$  is the pressure (mTorr),  $P$  is power in percentage of 600W, and  $O_f$  is the flow of Oxygen in sccm. The values of  $b_n$  are in Table 3.2. The predicted value of index and the residuals of the fitting are the sixth and seventh column on Table 3.1. The values indicate relatively good fitting. Figures 3.1-3.3 show contour plots of the predicted refractive index against the conditions.

Table 3.1: Series of depositions to screen the sputtering conditions effects on optical properties.

Case	Pressure	Power	O2	Index	Predicted Index	Residuals
1	2	20	20	2.69	2.64	0.05
2	15	40	50	2.07	2.09	-0.02
3	15	40	20	2.09	2.09	0.00
4	5.25	35	35	2.08	2.04	0.04
5	5.25	35	35	2.09	2.04	0.05
6	11.75	25	65	1.87	1.80	0.07
7	8.5	30	50	1.92	1.89	0.03
8	15	40	20	2.08	2.09	-0.01
9	2	30	80	1.97	2.01	-0.04
10	2	30	80	1.97	2.01	-0.04
11	8.5	30	50	1.91	1.89	0.02
12	5.25	35	65	1.95	1.98	-0.03
13	2	20	20	2.62	2.64	-0.02
14	15	20	50	1.87	1.91	-0.04
15	8	30.75	33.75	1.91	1.95	-0.04
16	6	30.5	42.5	1.92	1.98	-0.06
17	2	31	60	2.30	2.07	0.23
18	6	30	60	1.89	1.93	-0.04
19	10	30	25	2.01	1.92	0.09
20	5	30	30	2.08	2.06	0.01
21	4	30	25	2.11	2.12	-0.01
22	6	30	25	2.05	2.04	0.01
23	4	30	40	1.96	2.07	-0.11
24	3	30	40	1.99	2.11	-0.12
25	8	30	20	1.97	1.99	-0.02

Table 3.2. Values of fitting parameters for the refractive index in Table 3.1.

Coefficients	Average	Std Error
b0	5.215	0.779
b1	-0.103	0.04913
b2	-0.160	0.06605
b3	-0.01125	0.01491
b4	0.00142	0.00225
b5	0.00156	0.000993
b6	0.000121	0.000450
b7	0.00223	0.00117
b8	0.000228	0.000361
b9	4.31E-06	8.8E-05

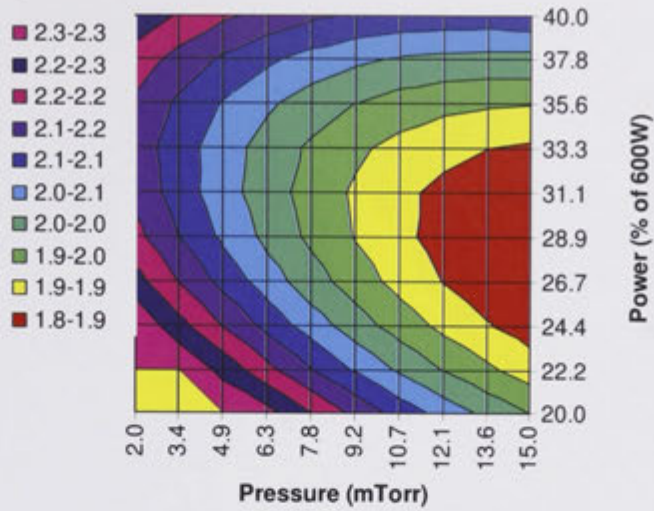


Figure 3.2: Contour plot of fitted refractive index vs power and pressure at oxygen flow of 42% (of 15sccm).

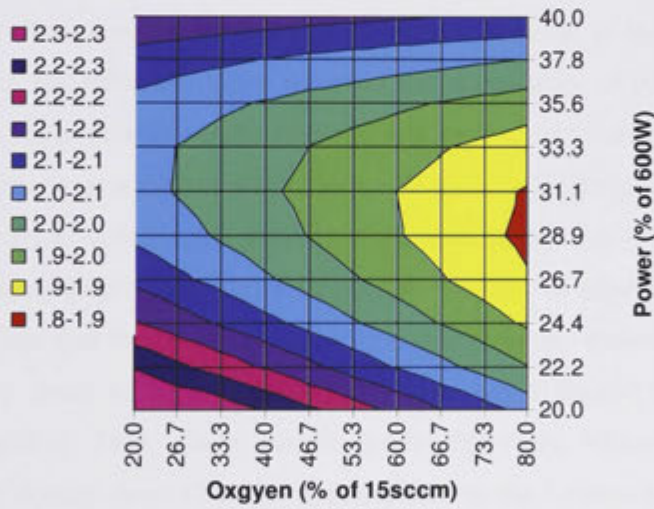


Figure 3.3: Contour plot of fitted refractive index vs power and Oxygen flow at pressure of 7mTorr.

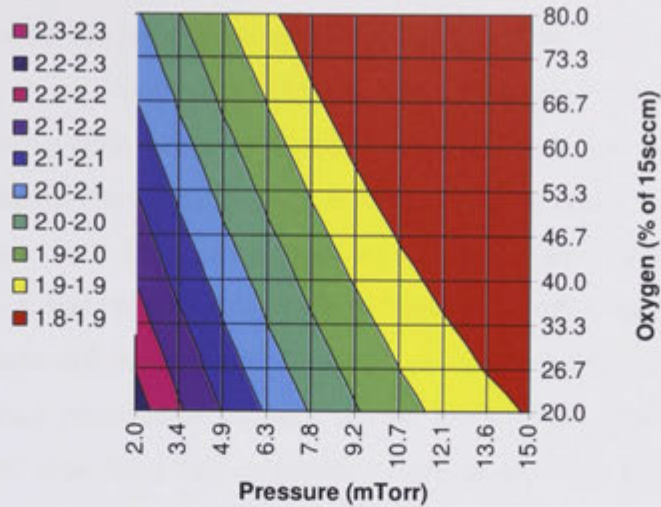


Figure 3.4: Contour plot of fitted refractive index vs pressure and Oxygen flow at power of 30.5 (% of 600W).

There are some notable trends in those contour plots in Figure 3.1. First of all, the indices are increased with a decrease of pressure. Secondly, as the Oxygen partial pressure increases, the refractive index reduces. The dependence of index on power is slightly different. It is inverse saddle like. At low power, the index is high, then at middle value, it reaches a minimum before increases again at higher power.

Highest refractive index is however not the main target. For optical application, lowest optical propagation loss is also an important criterion. In order to achieve this, it is generally the case that the films should be stoichiometric and densely packed. Since non-stoichiometry leads to higher porosity, the first target should be films with a composition equalling  $\text{TeO}_2$ . Once stoichiometric films are achieved, the highest packing factor or density should be then targeted. Due to the Lorentz-Lorenz equations (Equation 2.4 from Chapter 2) [300], then for stoichiometric films the higher the refractive index the higher density.

The refractive index of Tellurite glasses at 1550nm is around 2.1 as quoted in the previous Chapter 2. Therefore, it is expected that, high quality Tellurium oxide thin films should have refractive index in this vicinity. From the DOE results in Figures 3.2 to 3.4, the areas corresponding to refractive index of 2.0-2.1 are around 5mTorr pressure, O2 flow of 40 % (of 15sccm) and power of 25% (of 600W).



Figure 3.5 summarizes the dependence of the refractive indices at  $1.55\mu\text{m}$  of the sputtered films against the ratio of Oxygen to Tellurium in the films as determined by energy dispersive X-ray analysis (EDXA). Each data point corresponds to one sputtering run. As a wide range of sputtering parameters was used during film deposition the obtained films had a range of optical and physical properties. The as-deposited amorphous  $\text{TeO}_x$  films were classified into three types: Tellurium rich ( $x < 2$ ); stoichiometric ( $x \sim 2$ ); and Oxygen rich ( $x > 2$ ). Tellurium rich films were produced when there was an Oxygen deficiency in the chamber, or a high flux of Tellurium from the target. This condition occurred at high RF power, low Oxygen flow or low chamber pressure. Tellurium rich films had excessive levels of metallic Te atoms and were therefore highly absorbing. These films had an effective band edge high up in the red or infrared and refractive indices at  $1.55\mu\text{m}$  greater than 2.1. Oxygen rich films on the other hand were highly transmissive down to  $\sim 350\text{nm}$ , had low absorption in the infrared as well as lower density and refractive index at  $1.55\mu\text{m}$  below 2.0. These films were produced when the sputtering power was low, or the Oxygen flow or chamber pressure were high. Stoichiometric films were obtained when the balance of all three parameters was maintained which corresponded to 5mTorr pressure; 150W RF power; 6.75sccm Oxygen flow (45%) and 8.25sccm Argon flow (55%).

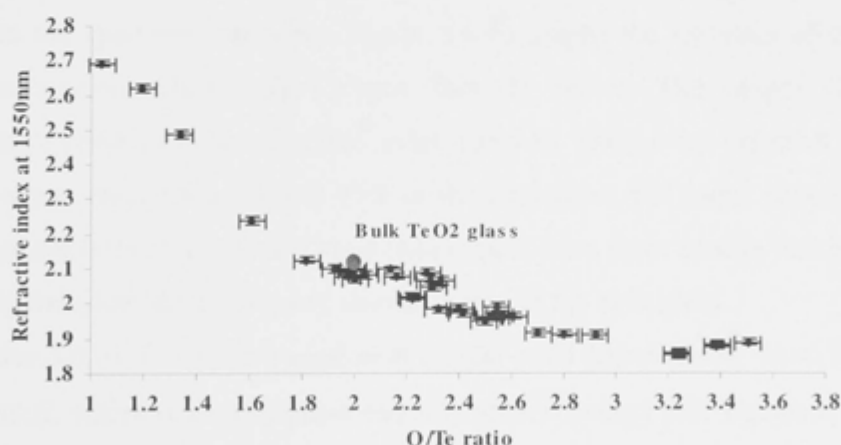


Figure 3.5: Dependence of refractive indices at 1550nm on composition. The index also depends on the sputtering conditions. The dots with error bars are data points; the large dot is represents bulk  $\text{TeO}_2$  glass.

The results of Figure 3.5 represent a much wider range of compositions and refractive indices than reported by previous work [279]. The graph shows that the refractive indices of films around  $\text{TeO}_2$  composition are very close to bulk  $\text{TeO}_2$ . At an O/Te ratio of 2.0, the film refractive indices are as high as 2.08 compared to bulk amorphous  $\text{TeO}_2$  glass of 2.12 [88]. Furthermore, the slope of the composition/index relationship appears to flatten in the vicinity of the stoichiometric point, with a plateau in the refractive index between about 1.9 and 2.2 O/Te. The refractive indices remain almost constant for O/Te higher than 2.6. This is slightly different to the results from [279] which reported a constant index of around 1.98 (at 1500nm) for O/Te ratios between 2.3 and 2.6. The thin films obtained here have higher refractive indices and are therefore denser than previously reported according to the Lorentz-Lorenz relation [300].

Furthermore, the refractive index does not only depend on the stoichiometric coordination but also the sputtering conditions. The cluster around the O/Te ratio of 2.2-2.4 on Figure 3.5 clearly shows a significant range of refractive indices for the same stoichiometries. Higher index films were usually obtained with lower Oxygen flow, therefore, higher deposition rate. This indicates that higher deposition rate increases the density of the films leading to higher refractive indices.

Figure 3.6 a) shows the dependence of the O/Te ratio against the flow of Oxygen into the sputtering chamber. Figure 3.6 b) graphs the variation of film index against composition when only Oxygen flow is varied. The graphs show that stoichiometric, close to bulk refractive index films of  $\text{TeO}_2$  were obtained when the oxygen flow percentage was around 45% of the total flow. The index difference from bulk was around 0.04 at 1550nm. One would expect from these results that the optical properties of the films should be very similar to that of the bulk glass.

Figure 3.6 c) shows the variation of optical band gaps inferred from Tauc plots of  $(\alpha E)^{1/2}$  vs  $E$ , where  $\alpha$  is absorption and  $E$  is photon energy (see Equation 2.9). The band gaps reach a maximum of 3.7eV at stoichiometric composition. This is closely approaching the value of bulk  $\text{TeO}_2$  glass of 3.79eV [88]. With Te rich films, the optical band gaps decrease very rapidly due to metallic absorption. On the other hand Oxygen rich films retain relatively high optical band gaps.



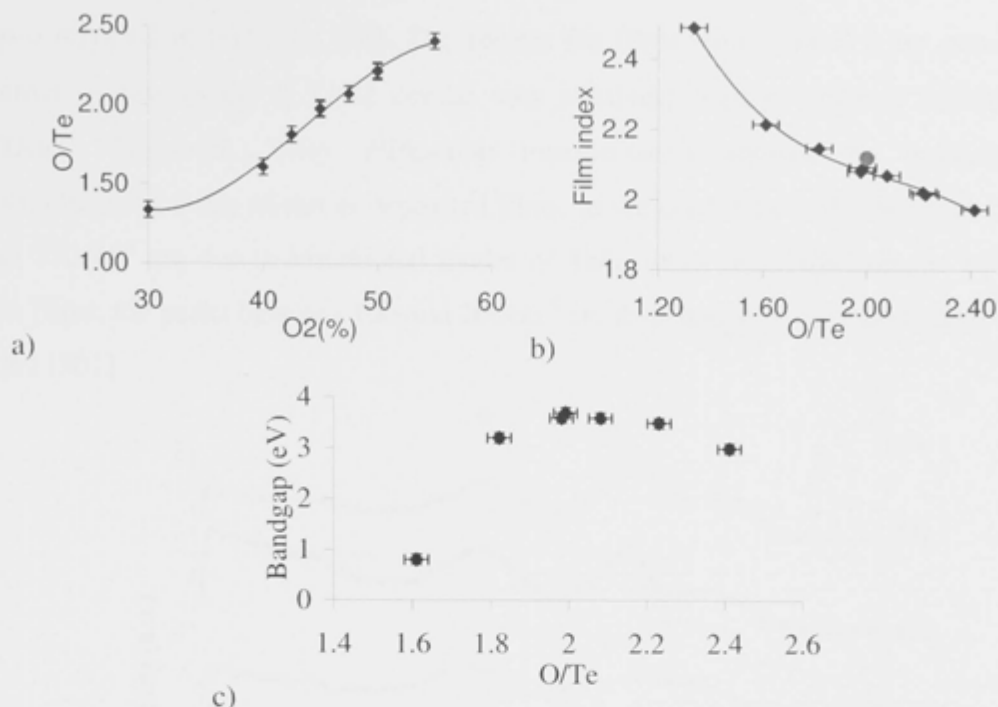


Figure 3.6: a) Film composition vs Oxygen flow around the optimum point, the horizontal line representing stoichiometric composition  $O/Ti=2$ , the solid curve is a polynomial fit of 3rd order b) film index at 1550nm vs composition for films deposited around the optimum conditions, the single dot represents bulk  $TeO_2$  glass index, the solid curve is a polynomial fitting of 3rd order; c) Variation of optical band gaps with composition.

### 3.5 Raman spectra

The Raman spectra measurement was performed on a home made instrument. The Raman spectra were obtained using a backscatter configuration with a pump laser at 808nm. Since the Tellurium oxide films for this characterization were deposited on very thin Silicon Nitride membranes, the substrate background signal was effectively suppressed leaving only the unobscured Raman signal from the Tellurium oxide film.

The Raman spectra of the films with various  $O/Ti$  compositions are shown in Figure 3.7. The figure also contains a spectrum from a  $TeO_2$  crystal for comparison. There are some significant trends in the result. For thin films with  $O/Ti \geq 2$ , there are three broadened peaks at  $770cm^{-1}$  (stretching vibration of  $Te=O$ ),  $660cm^{-1}$  (coupled symmetric vibration along  $Te-O-Te$  axes),  $450cm^{-1}$  (symmetric and bending vibration of

Te-O-Te linkage at corner sharing sites). The spectra for this case are in agreement with those reported in literature [88]. The spectra for films with  $O/Te \leq 2$  are remarkably similar to that of the  $\alpha$ -TeO<sub>2</sub> crystal with relatively narrow peaks at  $660\text{cm}^{-1}$  and  $400\text{cm}^{-1}$ . However, X-ray diffraction measurements showed no indication of crystallization in any of the as deposited films. In the crystal case, the two peaks at  $150$  and  $120\text{cm}^{-1}$  are due to vibrational modes of TeO<sub>4</sub> units [90]. However, in Tellurium rich films, the peaks between  $100$  and  $200\text{cm}^{-1}$  are dominated by the vibrations of Te-Te bond [301].

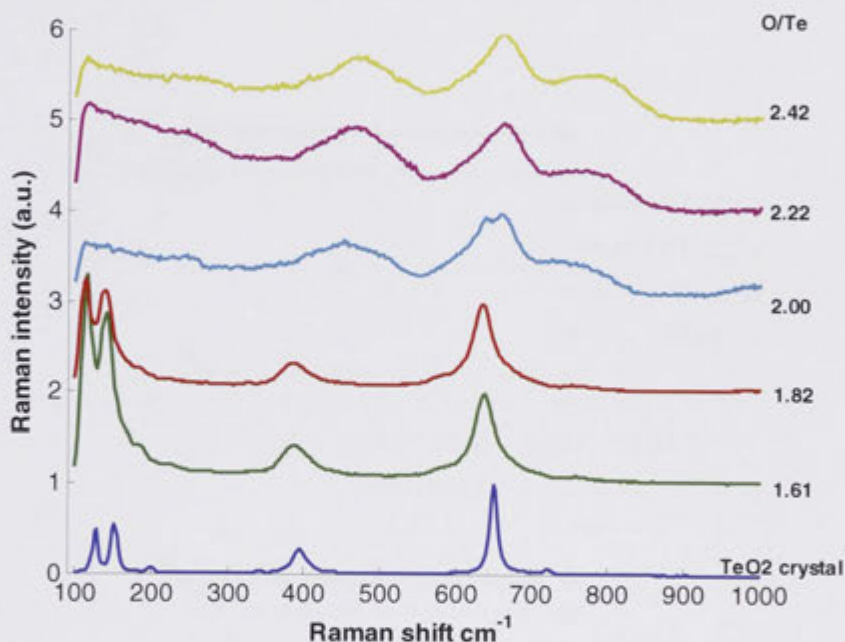


Figure 3.7: Raman spectra of TeO<sub>x</sub> thin films, x value is on the right side of the graph. The curves have been normalized based on the main peaks between  $600$ - $700\text{cm}^{-1}$  and shifted upward by 1 unit consecutively.

In a pure TeO<sub>2</sub> crystal and in Te rich films, TeO<sub>4</sub> bi-pyramid structures and Te-Te bonds dominate. TeO<sub>4</sub> units are linked by corner or edge sharing Oxygen atoms resulting in very similar Raman spectra. With the additional of Oxygen, the TeO<sub>4</sub> trigonal bipyramid units evolve into TeO<sub>3</sub> trigonal pyramid resulting in non-bridging Oxygen in Te=O bonds with strong stretching vibration at  $770\text{cm}^{-1}$  as shown in Figure 2.3 in Chapter 2 [89, 98, 302].

3.6 Effect of annealing

In general thin films deposited onto cold substrates are expected to be far from a minimum entropy state immediately after deposition, and therefore perhaps vulnerable to refractive index drift over time at even room temperature. Hence thermal annealing is often used to “relax” the films and remove any possible index drift. Films with various O/Te compositions from 1.2 to 3.2 were annealed in an Oxygen atmosphere. The surfaces of films were observed with optical microscopy during the annealing process. Refractive indices of the films were also monitored.

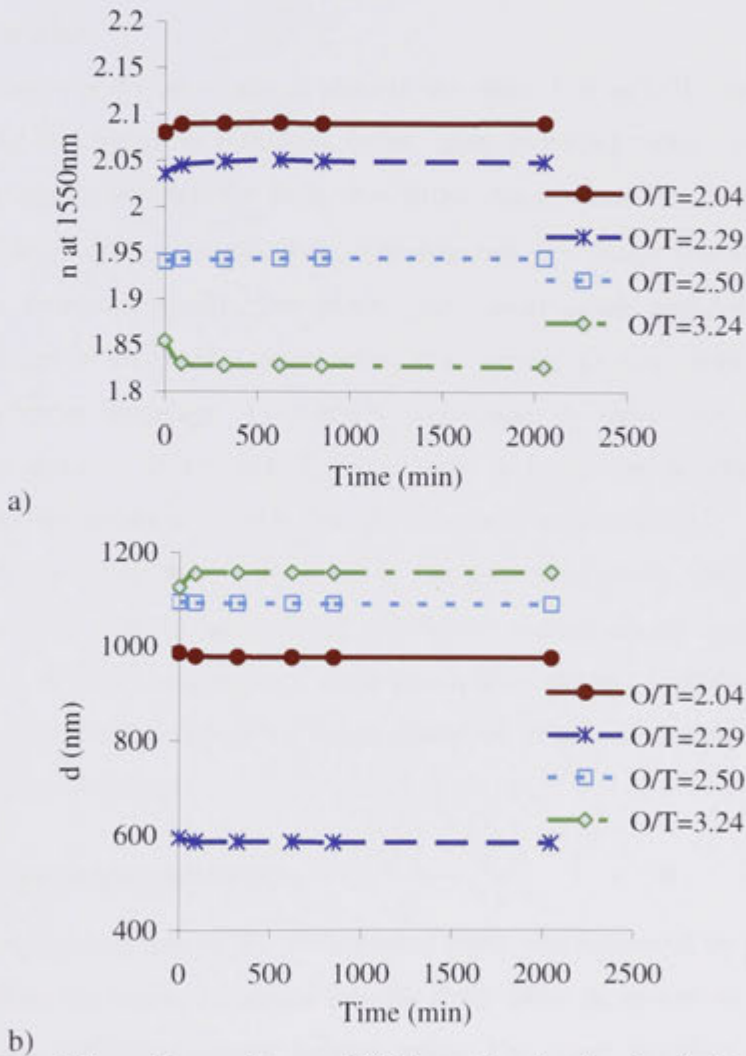


Figure 3.8: Effect of annealing at 200°C on the a) refractive indices and b) thicknesses of samples at different compositions.

It has been reported that annealed Te rich amorphous films contained crystalline Te metal with subsequent crystallization of  $\text{TeO}_2$  at higher temperatures [269, 286]. A number of Te rich films from this work annealed at  $200^\circ\text{C}$  indeed showed crystallization as evidenced by XRD patterns, but this was not visible with optical microscopy.

In order to observe the behaviours of films with excess Oxygen during annealing, a set of  $\text{TeO}_x$  thin films on Silicon substrate that had O/Te ratios of 2.04, 2.29, 2.5 and 3.24 were annealed in an air-filled oven for durations of more than 33 hours. The refractive indices and thicknesses were measured at different times and are shown on Figure 3.8 a) and b).

There are significant trends evident in the plots. For an O/Te ratio of 2.5 there was essentially no change in refractive index upon annealing, which is an interesting result not previously reported for  $\text{TeO}_2$  thin films. Away from this composition, small index shifts ( $\Delta n < 3 \times 10^{-2}$ ) occurred upon annealing but the change was complete within  $\sim 100$  minutes. Increases in refractive index upon annealing are generally explained by the rearrangement of atoms to a more relaxed, lower energy state with higher density and film thickness shrinkage. Conversely, decreases in index can occur when a compressively strained film relaxes by expansion to lower the density and therefore refractive index according to Lorentz-Lorenz relation (Equation 2.3).

EDXA measurements at the end of the annealing study showed unchanged overall composition. Furthermore, X-ray diffraction measurements suggested that the films annealed at  $200^\circ\text{C}$  maintained their amorphous phase. Therefore the changes observed were not brought about by either oxidation or crystallization, but by density changes from film shrinkage.

### 3.7 Thin film propagation loss

The optical propagation loss of the as deposited films was measured by prism coupling [303, 304], where the beam is coupled into the  $\text{TeO}_x$  films deposited on a  $2\mu\text{m}$  thermal oxide layer on a 100mm diameter Silicon wafer. The prism coupling technique was used to couple the light into each of the modes in turn and both polarisations of the propagation mode. An external cavity tunable laser at 1550nm was used along with an EDFA to boost the power for this experiment. As the laser beam propagated in the  $\text{TeO}_x$



layer, light scattered. A cooled InGaAs CCD camera was used to image the streak of light propagating along the path. Image processing software written in Labview captured the image and analysed the scattering streak to extract the propagation loss. The light streak image was cropped and integrated in the transverse direction. The data was then plotted against distance on a semi log scale, and a variable degree of rejection of data lying away from the best fit line was used to eliminate discrete scattering centres. The reduced data set was then subjected to the same fit/reject procedure to leave a data set with minimised discrete scattering to which a best fit line was used where the slope of the straight fitting line is the loss per length (dB/cm). Figure 3.9 shows an example of the front panel of the software. A critical assumption is that the films are homogenous throughout the wafer and the lens vignetting is negligible.

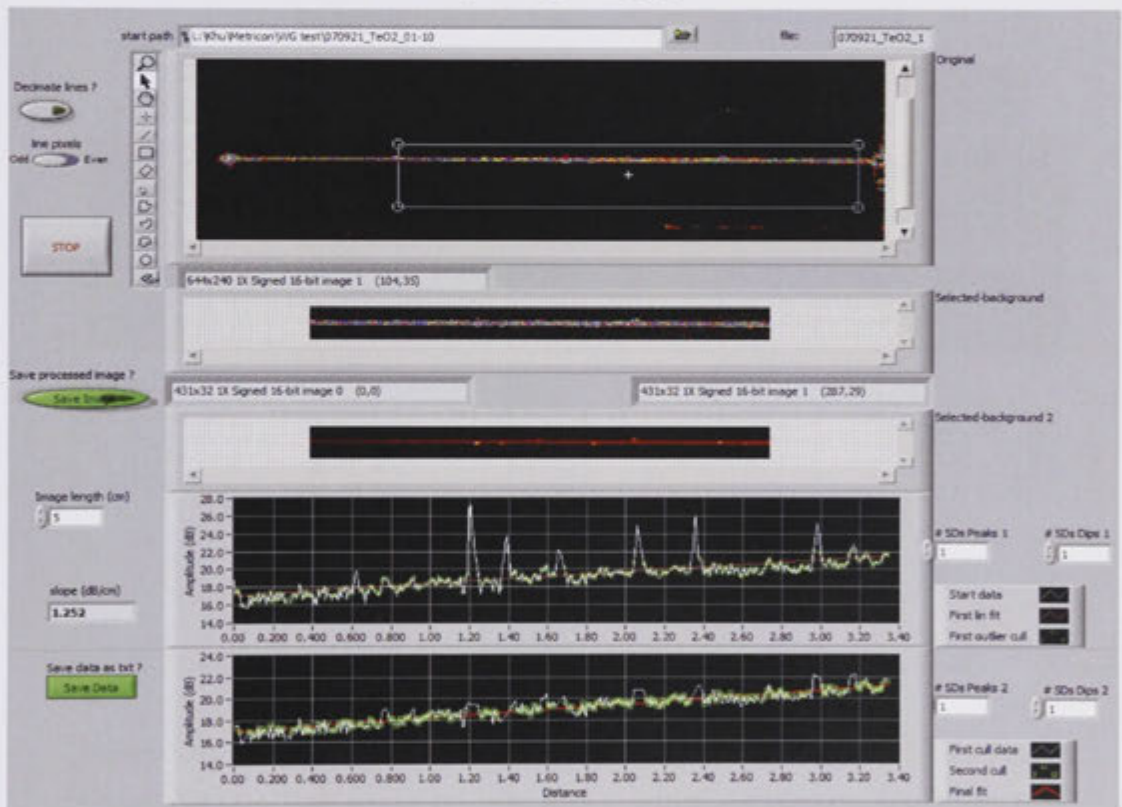


Figure 3.9: Front panel of the Labview software to calculate propagation loss of thin film

The propagation losses at 1550nm were determined from observation of the light streaks from a set of as-deposited  $\text{TeO}_x$  thin films on thermally oxidized silicon substrates with film thickness of around  $1.5\mu\text{m}$  and composition O/Te ratios of 1.6 to

2.4. The results are shown in Figure 3.10. The minimum loss observed was less than 0.1dB/cm at 1550nm, which is the first time such low losses have been reported in this material and is even more remarkable given that this is an as-deposited Tellurium Oxide film. As argued above, an excessive level of Te in the films,  $x < 2$ , is expected to produce high losses and this is indeed observed. However, the loss curve dips to a minimum right at the stoichiometric point before gradually increasing as the Oxygen content increases. There are two possible explanations for the increase in the loss. Firstly, the Oxygen rich thin films are relatively more porous and inhomogeneous than the stoichiometric  $\text{TeO}_2$  films. This leads to a potential increase in scattering loss in Oxygen rich films [300]. The losses of Oxygen rich films would be expected to be lower when they are annealed to lower porosity [278].

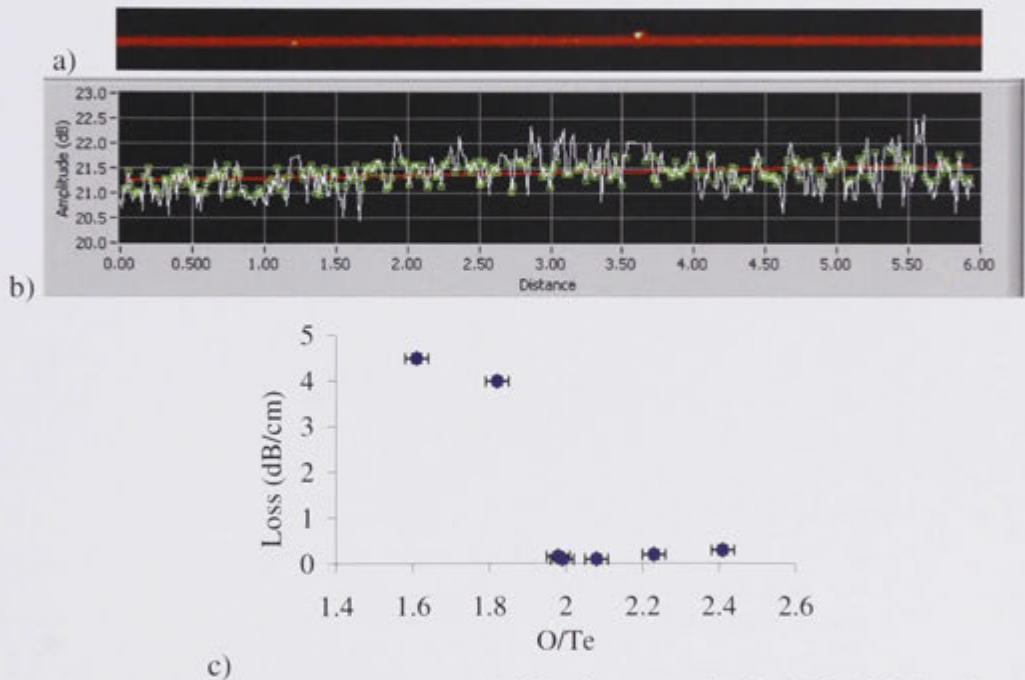


Figure 3.10: a) light streak image acquired by the camera, in the  $\text{O/Te}=2.0$  film for a length of 6cm, light propagates from right to left; b) data analysis with fitting to obtain a slope of less than 0.1dB/cm; c) propagation loss at various  $\text{O/Te}$  ratios.

### 3.8 Conclusion

This chapter has reported the fabrication method for high quality Tellurium dioxide thin films. A pure Tellurium target was used in a reactive RF sputtering system and

Tellurium oxide films were formed in Argon and Oxygen plasma chamber. Using a DOE study, the optimum conditions for film deposition were obtained. Propagation losses at 1550nm of light in the planar films were as low at 0.1dB/cm in stoichiometric films. Other properties of the films have also been studied. It was found that the films are robust to annealing even at 300C. Therefore, reactive RF sputtering is a suitable technique for Tellurium dioxide film fabrication for planar devices.

## **Chapter 4:**

# ***Fabrication of high quality Tellurium oxide rib waveguides***

Detailed studies on the reactive plasma etching properties of Tellurium dioxide are reported in this chapter. A high quality etching process using Hydrogen, Methane and Argon is demonstrated. Plasma etching of  $\text{TeO}_2$  using standard parallel plate Reactive Ion Etching (RIE) and toroidal winding Inductively Coupled Plasma (ICP) machines are covered in detail. The quality of etching in the two systems is slightly different but the outcome of this study was recipes for etching high optical quality  $\text{TeO}_2$  waveguides. The etch process is also shown to be highly suitable for chalcogenide glass thin films which may be of importance in other additional applications such as phase change memory.

## ***4.1 Plasma etching technology***

### **4.1.1 Introduction to plasma etching**

Plasma etching (also commonly referred to as dry etching) is the most widely used technique for pattern transfer in semiconductor electronic and optoelectronic devices. It is a crucial process in very large scale integrated circuits which may consist of billions of individual devices. It is also an extremely important technique for fabricating optical quality devices. The key advantages of this technique over wet liquid based etching techniques include high anisotropy, waste management, profile control, and precise etching control and monitoring [305, 306].

Plasma etching can occur in two ways. The first is by physical sputtering through high energy ion bombardment. This is not a widely used technique as the etching rate tends to be slow, selectivity to the mask is limited (essentially the ratio of the sputtering rates of mask to etched material), corner mask erosion often leads to non-vertical profiles, and the re-deposition of sputtered material often leads to high surface roughness.



The second more frequently used method is reactive ion etching (RIE), which was pioneered by Hosokawa *et al.*, in 1974 [307]. The etch gas mixture is chosen so that ions and radicals are formed in the plasma that chemically react with the substrate to form volatile products which are then pumped away. At the same time, physical sputtering also occurs due to the acceleration of ions in the plasma toward the substrate and more importantly this enhances the etch rate on horizontal surfaces leading to anisotropy of the etch rate and hence the possibility to etch vertical structures. The presence of ions in the chamber also acts not only as a physical bombardment process but also help the generation of radicals [305].

Plasma etching is a highly favourable method for the fabrication of tellurite and chalcogenide devices due the extreme chemical reactivity of these materials to aqueous bases which makes precise and smooth wet etching problematic [258, 308]. Plasma etching has been shown to be capable of generating extremely smooth sidewalls, as required for example for air clad silicon nanowire devices where the sidewall roughness allowable is around the nm rms level [5, 14]. In optical waveguide fabrications, the etching induced roughness is very critical to determine the quality of the etching process. The propagation loss is proportional to the product of squared of the interface roughness and squared of the refractive index difference between the core and cladding [5, 14, 309, 310]. Therefore, high index waveguides required to have the interface roughness as low as possible to avoid the additional loss introduced by etching. Given the excellent results in silicon and chalcogenides, it was considered appropriate to investigate the etching of tellurite waveguides with plasma etching rather than other fabrication methods.

Etching rate, selectivity to the mask material, anisotropy, and uniformity are some of the most important factors in plasma processing. High etching rate and high uniformity across large diameter wafers are necessary to ensure that all of the devices fabricated have similar characteristics. Tuning the process chemistry and machine configuration can enhance all the above properties. For example, the etch rate is essentially proportional to the number of reactive ions present in the plasma. High density plasma sources such as ICP systems, discussed in a moment, produce sufficient ions and reactive species to meet high throughput commercial demands even on relatively slow etching materials such as silica [306]. For deep feature etching, etch

anisotropy and high selectivity between the material being etched and the mask are required, and this is generally decided by gas selection.

Isotropic or anisotropic etching can be defined quantitatively by the degree of isotropic etching of  $IE = d_H/d_V$ , where  $d_H$  is the horizontal undercut and  $d_V$  is the vertical etched depth as shown on Figure 4.1. The degree of anisotropic etching then is  $1/IE$ . Isotropic etching in a plasma results from purely chemical gasification reactions between the etchant species and a substrate which have no preferred orientation and so will undercut and etch masked feature. The plasma plays little role other than to create the etchants [311].

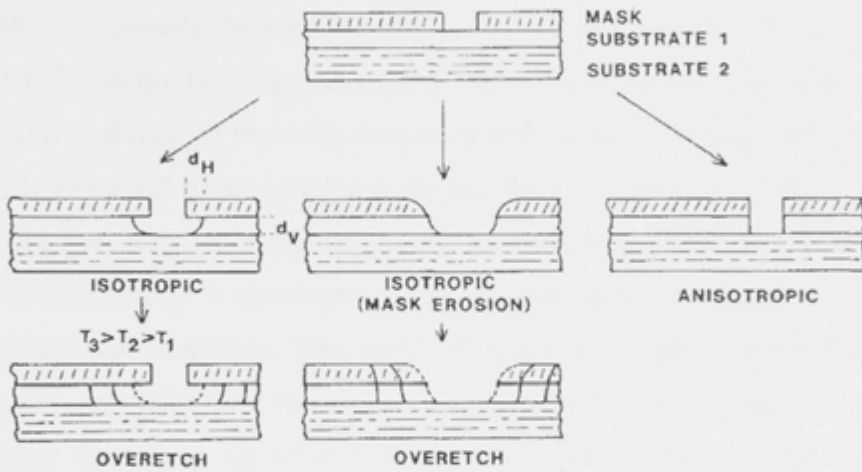


Figure 4.1: Isotropic and anisotropic etching profile taken from Ref. [311].

The profile of the etched feature depends generally on the anisotropy of the etch which is in turn determined by the interactions between the etching and any deposition processes that may occur simultaneously, and also by the ratio of free radicals to ions and the ion energy and mean free path in the plasma. Species sputtered from the target can be deposited back on the wafer, especially on the side-walls. Etching and deposition rates depend in a complex manner on various factor such as materials present and the geometry of the features being etching [306]. Since anisotropy is enhanced by processes that depend on ion bombardment and selectivity is improved by processes that depend on chemical reactions, an optimum process is often a balance between anisotropy and selectivity. All processing parameters such as gas composition, flow rate, pressure, power density and wafer temperature, play important roles. The induction power

determines the generation rate of radicals and ions in the plasma. Electron collisions transfer the energy from the RF field to the reactive gases and fragment the molecules into atoms, radicals and ions that perform the deposition or etching process. An increase in power density leads to an increase in density of radicals and ions hence an increase in etch rate. Lowering the pressure and increasing the power density will increase the energy of ions bombarding the surface hence improving anisotropy but decreasing selectivity.

#### **4.1.2 Machine configurations**

There are a number of configurations for plasma etching machines. A typical standard RIE machine is normally driven at 13.6MHz and pressure less than 100mT. There are two parallel electrodes, typically the smaller below the larger one carries the sample to be etched and is driven by the radio-frequency (RF) field via a coupling capacitor, the larger one is grounded. Upon striking a plasma, there is a dark space above the driven electrode, the ions are accelerated across this area and land on the sample in a vertical direction. A DC voltage is developed across this dark space, its magnitude depending on the pressure and frequency. This rectification occurs because the electrons, having very low mass, can follow the variation of a high-frequency field whilst the ions having much heavier mass, may not be able to. Generally, only a small portion of the gas molecules are ionized in a parallel plate RIE chamber, but the proportion can be increased by increasing RF power. Increasing the power however also increases the ion energy as they are directly coupled, at the expense of substrate heating, increased energetic bombardment, etc. Enhanced RIE methods were developed where the ion density can be decoupled from the ion energy with the aid of additional fields.

There are several enhanced plasma sources, such as, magnetically enhanced reactive ion etching (MERIE), electron cyclotron resonance (ECR), helicon, helical resonator and inductively/coupled plasma (ICP/TCP) [306]. MERIE has additional electromagnetic coils which produce a rotating magnetic field that improves ionization efficiency and minimizes plasma losses to the walls, hence enhancing the etch rate. However, etch rate uniformity using MERIE may be low because of nonuniformities in the magnetic field. ECR sources generate high plasma densities using 2.45GHz microwave power by confining electrons in magnetic field cusps

provided by twelve equally spaced permanent magnets. The complexity of ECR systems prompted the development of simpler high density plasma sources. The helicon source is made up of an upper antenna section and a lower confinement section. RF power is inductively coupled into the plasma via an antenna which is wrapped around the upper chamber. Four solenoid magnets are used to control the magnetic field. The helical resonator consists of a helical coil wrapped around a quartz/ceramic tube. RF power is inductively coupled into the plasma through the coil. The ICP etching machine also has a RF coil wrapped around the chamber and generates the plasma through inductive coupling but the ions are extracted by another RF field (see Figure 4.2). This configuration allows much higher ion density to be generated above the substrate and for independent control of the ion energy [312, 313].

At the time of this project, there were RIE and ICP plasma systems at the Australian National University. Therefore, only these two systems were used in the etching studies of Tellurium oxide and chalcogenide films.

#### 4.1.3 Gas selection

The choice of gases for etching materials is very important in RIE. The gases are required to be reactive with the compounds to be etched resulting in chemical species that are volatile in vacuum at achievable temperatures, and also often to provide polymerizing species that provide sidewall passivation to achieve highly anisotropic etching. The gas mixture and process conditions must also allow the sidewall polymer to remain on the sidewalls preventing them from being etched whilst simultaneously removing it from the flat surfaces (usually by sputtering) to allow etching to proceed there. The most common ingredients for etching glassy and semiconductor materials are halogen-containing gases such as  $\text{Cl}_2$ ,  $\text{HBr}$ ,  $\text{CF}_4$ ,  $\text{CHF}_3$ ,  $\text{CH}_3\text{F}$  [306, 311, 313, 314]. Fluorine is commonly used to etch Silicon and Silicon compounds while Chlorine is used with Ga, Al and As containing III-V compounds. Methane and Hydrogen are also frequently used to etch a number of important II-VI [315, 316], III-V [317-319], and IV-VI [320] compounds. The idea in this instance is to form hydrides and metal-organic compounds.  $\text{CH}_4$  contributes to the etching process in two ways. The first is to form volatile metallo-organic compounds. The second is to create active radicals  $\text{C}_n\text{H}_m$  and ions  $\text{C}_n\text{H}_m^+$  such as  $\text{CH}_3$ ,  $\text{CH}_2^+$  [321, 322] to act as polymer precursors for sidewall

polymerization and passivation. Additives and dilutants such as Argon [319] or Nitrogen [323] are also often used to help the plasma etching process. They provide additional ions which help to stabilise the plasma and prevent over polymerization at the etched surface.

Thus, there are a number of features in the selection of the etch gas mix that have to be balanced to attain the desired etch rate, selectivity, and anisotropy. With the availability of Ar, O<sub>2</sub>, CHF<sub>3</sub>, CH<sub>4</sub> and H<sub>2</sub> in the RIE and ICP plasma etching systems and the versatility of these gases, the etching study was conducted around them.

## ***4.2 Plasma etching study of Tellurium oxide and chalcogenide glasses***

As discussed so far, the properties of tellurites are well known and extensively exploited in the fields of acousto-optic devices,[103] fibre based optical amplification,[74, 215, 324, 325] and non-linear optical processing [78, 180, 322]. However, planar tellurite devices have, until now, proven to be rather problematic. There have been a number of reports[78, 79, 81, 83, 247, 248, 253, 257, 326, 327] of planar waveguides fabricated in tellurite glasses using techniques such as UV direct writing, [78, 79] femtosecond laser direct writing, [81, 247, 248] ion exchange, [83, 253, 326] ion implantation, [327] and sputter etching [257]. Whilst some of these methods have realized small channel waveguides, propagation losses were high (lowest reported loss of 1.3dB/cm[78]) and there are no reports of losses even approaching 0.5dB/cm, about the highest allowable value for useful linear or non-linear optical integrated devices. The best reported result using plasma etching was 6.3dB/cm[257]. Hence, to date no high quality plasma etching process has been demonstrated for tellurite materials.

### **4.2.1 Equipment: ICP and RIE plasma systems**

All of the etching work was performed on either an ICP system (PlasmaLab 100 from Oxford Instruments) or a parallel plate RIE system (PlasmaLab 80 from Oxford Instruments). The schematic configurations of both machines are shown on Figure 4.2. The ICP system had an exchange chamber and sample chamber which were pumped separately. The chamber pressure was maintained by a turbomolecular pump (Alcatel ACT1000T) with 900L/s pumping speed in conjunction with a position controlled gate valve acting as an automatic pressure controller. The base pressure was around  $\sim 2 \times 10^{-6}$  Torr and the system can pump up to 100sccm of gas and still maintain 8mT pressure.

The maximum permissible operating pressure is 100mT but in practise the system had problems stabilising that high pressure. Etch gas flows were controlled by individual thermal mass flow controllers (MFCs). The induction coils that surrounded the source tube were driven at 13.56MHz by a separate 3kW RF power source. The wafer was held in place by a mechanical clamp and Helium was used as a heat transfer medium between the wafer and the lower electrode. The lower electrode itself was water cooled and could be temperature controlled between 10°C and 90°C. The etch rate of transparent thin films was monitored by an in-situ laser interferometer operating at 677nm. At the beginning of this work, there were only O<sub>2</sub>, Ar, CHF<sub>3</sub> and CF<sub>4</sub> gases connected to the ICP system.

The RIE system was qualitatively similar to the ICP system in design and implementation, but lacked in-situ etching rate monitoring and wafer cooling. The RIE, however, had CH<sub>4</sub> and H<sub>2</sub> gases available at the beginning of the project. Therefore, it was used as the main machine for the etching studies in this project.

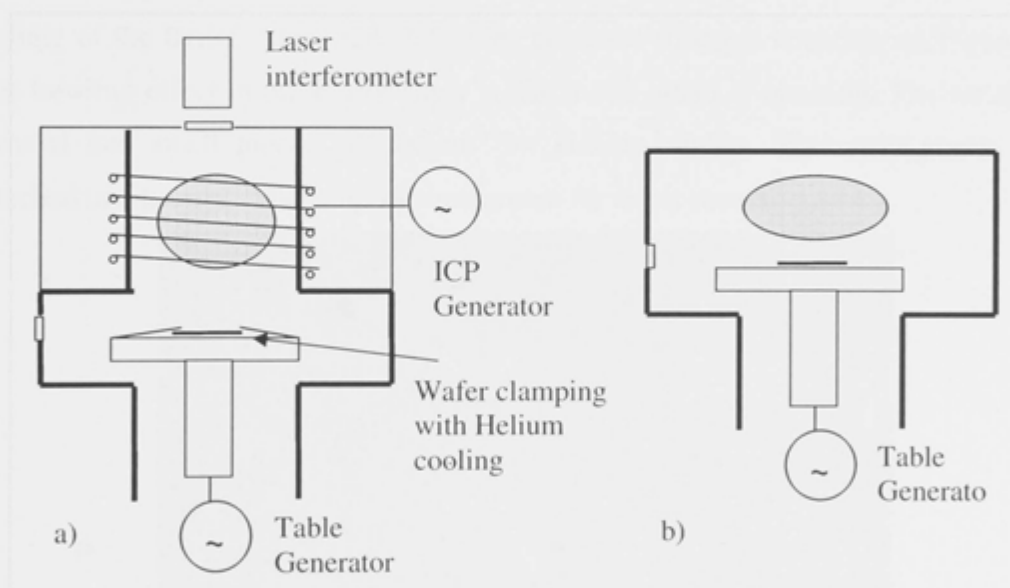


Figure 4.2: Configuration of a) ICP and b) RIE plasma etching systems

#### 4.2.2 TeO<sub>2</sub> film preparation and photolithography

Pure TeO<sub>2</sub> films were deposited using reactive sputtering of Tellurium metal in an Argon/Oxygen mixture as described in Chapter 3. The optimum sputtering conditions for the stoichiometric state were with a pressure of 5mTorr, an Oxygen flow of 6.4sccm, an Argon flow of 8.6sccm, and an RF power of 150W. Films were deposited at 1.8μm

thickness on <100> oriented 100mm silicon wafers with 2 $\mu$ m of thermal oxide as a bottom cladding. The refractive index of the as deposited films was measured to be 2.08 (within 0.03 of that of bulk amorphous TeO<sub>2</sub>) at 1550nm. An etch mask was then patterned using standard I-line contact photolithography methods utilizing ~0.9 $\mu$ m thick Clariant AZ 701 MiR photoresist and ~150nm thick Brewer Science XHRiC-16 bottom anti reflective coating (BARC). The BARC layer also crucially acted as a protective layer during the photoresist development process to avoid wet etching of the film [256-258]. Nominal waveguide widths were 1, 2, 3 and 4 $\mu$ m. Photoresist coating and development was carried out in an SVG 8600 series track to ensure repeatability, and resist exposure was undertaken in a Karl Suss MA-6 with 350W mercury arc lamp filtered to provide just the 365nm i-line emission. Before etching the TeO<sub>2</sub> structures, the BARC layer was removed by exposing the wafer to an Oxygen plasma using the ICP system set at 200W ICP power, 20W forward power, 10mTorr pressure and 30sccm Oxygen gas flow. This was known from previous work to result in vertical etching of the BARC film [328, 329]. The achieved structure is shown on Figure 4.3. The bowling effect in the BARC layer is due to the effect of cleaving. The wafer was cleaved into small pieces of ~1x1cm<sup>2</sup> for etching studies. The small pieces were attached to silicon wafers using vacuum grease for better thermal contact.

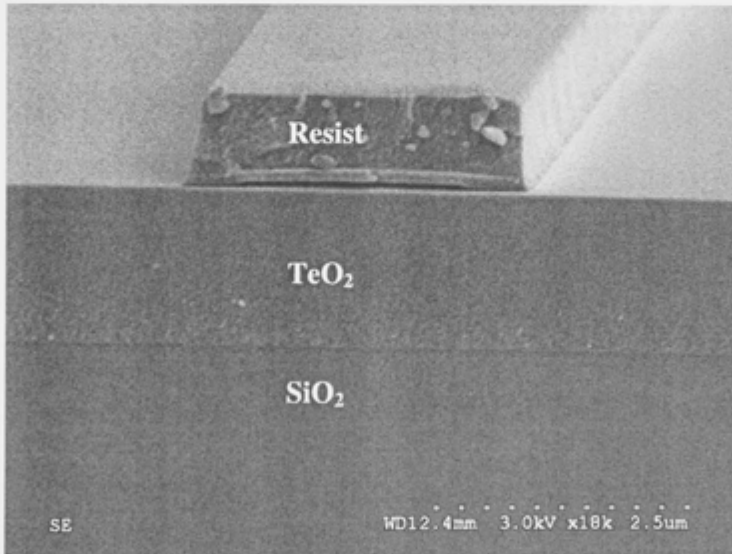


Figure 4.3: SEM image of a lithographed photoresist mask on top of a thin layer of BARC above a TeO<sub>2</sub> film on thermal oxide.

4.2.3 Physical etching in Ar plasma

The first attempt to etch  $\text{TeO}_2$  was with a non-reactive Argon sputter etching process, motivated by the fact that it is simple and has been reported to give relatively low surface roughness on Tellurium oxide waveguides [248]. The operating condition of the ICP was as laid out in Table 4.1. An etched depth of 800nm was achieved in around 13mins. The waveguide profile exhibited relatively vertical sidewalls with trenches on both sides due to ion reflections off the sloped sidewalls (Figure 4.4). This profile is typical of physically etched waveguides [313]. The physical sputtering process occurs purely through momentum transfer where the atoms on the film surface are knocked out by the impinging flux of ions. The process left the side walls of the waveguide very rough under even in low resolution electron microscopic imaging. The level of sidewall roughness was considered far too high for low loss propagation in an optical waveguide given the large index contrast of Tellurium oxide, and so attention was turned to reactive processes where control of the sidewall morphology could be attempted.

Table 4.1 Ar plasma etching of  $\text{TeO}_2$  waveguide in ICP machine

<i>Parameter</i>	<i>Values</i>
Pressure	5mTorr
Ar Flow	100sccm
ICP power	500W
Table power	200W
Rate	60nm/min



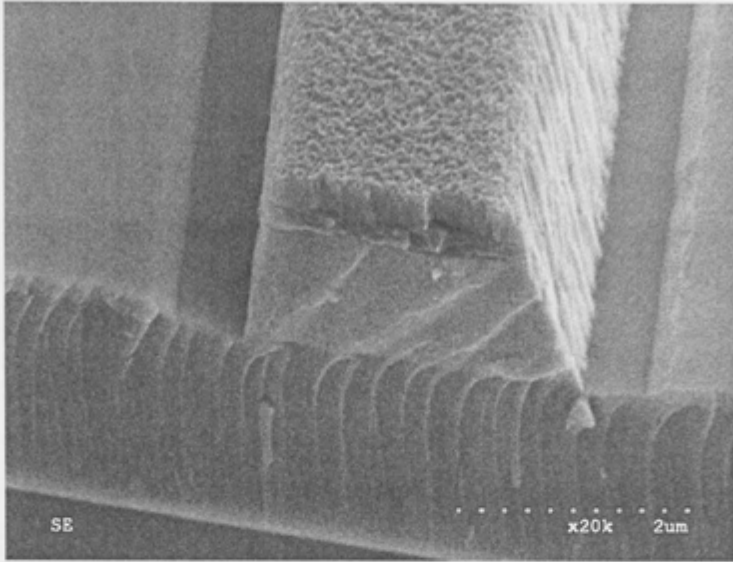


Figure 4.4: SEM image of etched TeO<sub>x</sub> waveguide using dry physical etching with Ar plasma

#### 4.2.4 CHF<sub>3</sub> based etching of TeO<sub>2</sub>

Halogen containing gases such as CHF<sub>3</sub> and CF<sub>4</sub> have been used for etching a number of materials [306], and of particular relevance to the current study have demonstrated low loss waveguiding in silica [330], silicon nitride [306] and even in high index contrast chalcogenide glass waveguides [328]. Plasmas from these gases produce active fluorocarbon and Fluorine radicals. The Fluorine radical reacts with many compounds to form volatile products [85]. The CF<sub>x</sub> (x=1,2,3) fluorocarbon radicals, especially CF<sub>2</sub>, form polymer which is deposited on the sidewalls to passivate the waveguide structure producing vertical sidewalls [331]. Therefore, etching of a TeO<sub>2</sub> film was attempted using the standard oxide etch recipe for the ICP system using a gas mix of CHF<sub>3</sub> and Ar with the conditions tabulated in Table 4.2. This recipe produces smooth sidewalls with a positive slope angle exceeding 80 degrees in silica, with an etch rate of about 35nm/min [330]. The etch rate monitor indicated the etch rate at typically between 50-60nm/min with Tellurium dioxide.

The SEM image of the etched surface after 15mins is shown in Figure 4.5. Beside the clear visibility of a two layer structure of TeO<sub>2</sub> underneath and the photoresist layer on top, the side walls of the waveguide structure are vertical and smooth but badly corrugated. There are also regions far from the waveguide with

significant columnar growth. The structure has the appearance that something has grown on the outside of the mask and the etched waveguide. Considering the fluoride compounds of Tellurium, Tellurium hexafluoride- $\text{TeF}_6$  is a volatile compound, but Tellurium tetrafluoride- $\text{TeF}_4$ , which has melting point and boiling point at  $129^\circ\text{C}$  and  $195^\circ\text{C}$  [85], respectively, is not volatile at the set table temperature of  $20^\circ\text{C}$ . This results in re-deposition and micromasking making the side walls rough and forming columns on the surface. Other halogen compounds of Tellurium also have melting points at elevated temperature. In the particular case of  $\text{TeF}_4$ , it might have been possible to overcome the lack of inherent volatility by raising the table temperature to the maximum  $90^\circ\text{C}$ , but this also comes at a price in terms of increased chemical (ie isotropic) etching. In the light of this, the inherent unsuitability of other halogen based plasmas, and the corrosive nature of halogen based etchants and their environmental unfriendliness, a move to another etch chemistry was decided upon.

Table 4.2 Ar and  $\text{CHF}_3$  plasma etching of  $\text{TeO}_2$  waveguide.

<i>Parameter</i>	<i>Values</i>
Pressure	30mTorr
Ar Flow	50sccm
$\text{CHF}_3$ flow	50sccm
ICP power	0W
FW power	200W
Rate	55nm/min

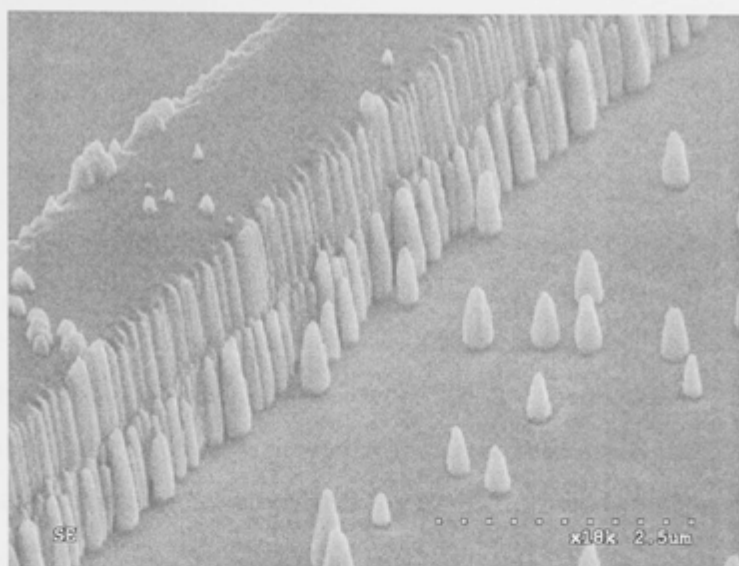
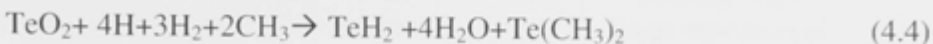
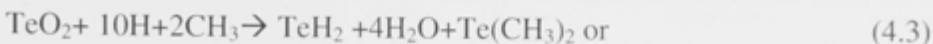


Figure 4.5: SEM image of TeO<sub>2</sub> waveguide after etching by CHF<sub>3</sub> and Ar plasma

#### 4.2.5 H<sub>2</sub>/CH<sub>4</sub>/Ar plasma etching of TeO<sub>2</sub>

The idea behind H<sub>2</sub> and CH<sub>4</sub> based etching is to form volatile hydrides and metallo-organic compounds. The exhaust products of RIE using H<sub>2</sub> and CH<sub>4</sub> are easier to handle, less toxic, less corrosive and more environmentally friendly than halocarbon gases, once scrubbed likely by combustion. Hydrogen/Methane gas mixes have been used for a range of semiconducting compounds such as groups III-V [317-319], II-VI [315, 316, 332], IV-VI [320] and Oxides [333]. CH<sub>4</sub> contributes to the etching process in two ways. The first is to form volatile metal-organic compounds. The second is to create active radicals C<sub>n</sub>H<sub>m</sub> and ions C<sub>n</sub>H<sub>m</sub><sup>+</sup> such as CH<sub>3</sub>, CH<sub>2</sub><sup>+</sup> [321, 322, 334]. These very active species can also react with each other to form polymers and help to passivate the sidewalls of the masked areas and increase the selectivity and anisotropy of the etching process. The combination of Tellurium oxide with highly reactive hydrogen and methane radicals form all volatile compounds under vacuum and plasma such as Tellurium hydride-TeH<sub>2</sub> [335], dimethyl tellurite-Te(CH<sub>3</sub>)<sub>2</sub> [85] and water. Some of the possible chemical reactions between the film and the plasma are [318, 320]:



The reactions (4.1)-(4.4) are just a small sample of the possible reactions that can occur on the surface of the films due to the fact that there a large number of radical species of Hydrogen and Methane generated in the plasma. Argon is added to the mix to stabilize the plasma as it can add more electrons to the plasma mix [305]. The Argon ions are also accelerated under the bias electric field toward the film to clean up polymers on the etched horizontal surfaces.

#### 4.2.6 Design of experiment: screening

Since there are a nontrivial number of RIE parameters that can be varied, the design of experiments (DOE) method was used to screen the etch characteristics of the  $\text{TeO}_2$  in  $\text{H}_2$ ,  $\text{CH}_4$ , and Ar plasma and to determine the best condition. The linear Plackett-Burman design [336] was applied to 5 factors, namely pressure, Ar flow,  $\text{H}_2$  flow,  $\text{CH}_4$  flow and RF power. Table 4.3 shows the detailed parameters of 14 randomized runs including 2 repeats for consistency monitoring. The etching runs were performed using an Oxford PlasmaLab 80 RIE system. The lower and upper limits used for the variables were 15/30mTorr for pressure, 30/60sccm for Ar flow, 10/30sccm for  $\text{H}_2$  flow, 5/20sccm for  $\text{CH}_4$  flow and 200/300W for RF power. The limits were chosen based on the constraints of pumping speed and the plasma operating condition. Each sample of around 1cm x 1cm was etched for 3 minutes in a separate run.

Table 4.3: Experiment design for TeO<sub>2</sub> etching using RIE with H<sub>2</sub>, CH<sub>4</sub>, and Ar. The response 0-3 corresponds to from bad to very good etch.

Exp. #	Press. ,mTorr	Ar, sccm	H <sub>2</sub> , sccm	CH <sub>4</sub> , sccm	Power, W	DC bias voltage (V)	Observation	Response
1	30	60	30	5	300	185	Rough, damaged	0
2	30	30	10	5	300	196	Rough, resist damaged	1
3	30	60	10	20	300	192	Polymer build up	0
4	15	60	30	5	300	179	Etched, resist damaged	2
5	22.5	45	20	12.5	250	165	polymer build up	1
6	22.5	45	20	12.5	250	166	Polymer build up	0
7	30	30	30	20	200	139	polymer build up	1
8	30	30	30	5	200	143	Good etch	3
9	15	60	30	20	200	140	Etched, resist damaged	1
10	30	60	10	20	200	150	Polymer build up	0
11	15	30	30	20	300	174	Etched, resist damaged	2
12	15	30	10	20	300	181	Polymer build up	1
13	15	30	10	5	200	149	Etched, resist damaged	1
14	15	60	10	5	200	152	Etched, polymer build up	1

A scanning electron microscope (SEM), Hitachi S4300, was used to observe the profile and the morphology of the etched waveguides. Quantitative responses were scored based on the observation of the SEM images as follows: 0 for no etching or a lot of polymerization, 1 for rough etching, 2 for better etching and 3 for very good etching. Some SEM images of the waveguides with the etching conditions of Table 4.3 are shown on Figure 4.6. Clearly, the quality of the etching processes varied significantly between different conditions. The results a-d respectively show badly damaged photoresist with rough etching, damaged resist with some etching, a lot of polymer build up with no etching and good photoresist remaining with good etched surfaces. The response of the etching quality varies nonlinearly significantly with different parameters. The last column shows the values of the responses for each etching condition. However, the applied DoE only works with linear formalism. The regression fitting can be written as:

$$Response=b_0+b_1*Press,m+b_2*Ar,sccm+b_3*H_2,sccm+b_4*CH_4,sccm+b_5*power,W \tag{4.5}$$

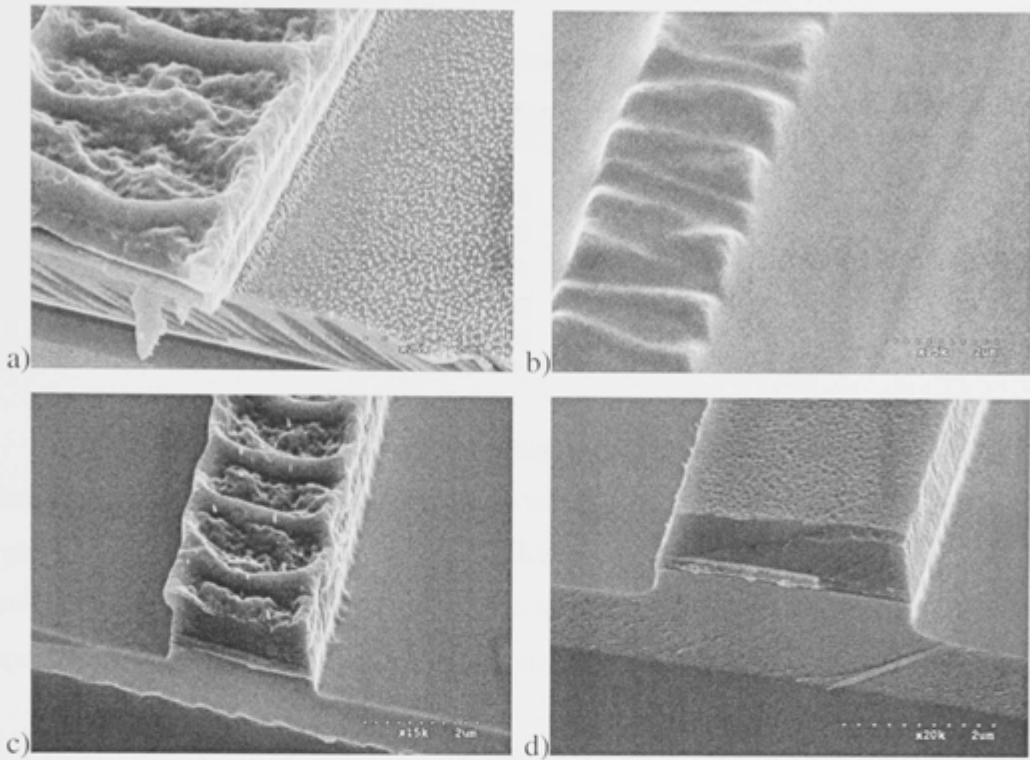


Figure 4.6: Some SEMs of the DOE screening runs; from a) to d) corresponding to Experiment 2, 3, 4 and 8 on Table 4.3, respectively; a) and c) show significant photoresist damage and some degree of  $\text{TeO}_2$  etching; b) shows polymer build up; and d) shows good etch.

The fitting coefficients  $b_n$  ( $n=0..5$ ) and their standard errors are shown in Table 4.4. They indicate that the best etching conditions correspond to lower pressure, lower Ar flow, higher  $\text{H}_2$  flow, lower  $\text{CH}_4$  flow and lower power. The screening design only uses a linear approximation, therefore, there are some limitations. The pressure cannot be too low as the plasma will stop. It is also limited by the capability of the turbomolecular pump. Too low  $\text{CH}_4$  flow will produce no polymer and hence no sidewall passivation resulting in very fast etching and large undercutting the waveguides. Furthermore, the lower limit RF power is also capped because the plasma can only be maintained when the power is above a certain limit. Too low RF power also results in very low etching rate. Therefore, the screening DOE test gives only a rough picture of the dependence of etching quality against the tested parameters within the tested range and extrapolation cannot be relied upon.

Table 4.4: Statistical analysis for the linear screening of the Table 4.3

<i>Coefficient</i>	<i>Average Value</i>	<i>Standard Error</i>
$b_0$	3.0	1.5
$b_1$	-0.033	0.028
$b_2$	-0.027	0.014
$b_3$	0.042	0.021
$b_4$	-0.033	0.028
$b_5$	-0.002	0.004

The response function is highly nonlinear, therefore, linear fitting is not entirely suitable as indicated by the standard errors in Table 4.4. Despite that, the coarse screening of the RIE parameters indicated that a suitable condition might correspond to 30mT pressure, 30sccm Ar, 30sccm H<sub>2</sub>, 5sccm CH<sub>4</sub>, and 200W RF. However, since the response was qualitative further investigation was required.

4.2.7 Design of experiment: fine tuning

Further investigation of the etching conditions around experiment 8 on Table 4.3 was undertaken. Since the largest coefficients in Table 4.4 are those of the CH<sub>4</sub> flow and pressure, two sets of samples with dimension of around 1cm by 1cm were etched: one with varying CH<sub>4</sub> flow from 3sccm to 10sccm while keeping all other parameters fixed as on Table 4.5 (5mins etching time, 30mTorr pressure, 30sccm Ar, 30sccm H<sub>2</sub>, and 200W RF power); another set with varying pressure from 20mTorr to 80mTorr while keeping all other parameters fixed as on Table 4.6 (5mins etching time, 30sccm Ar, 30sccm H<sub>2</sub>, 5sccm CH<sub>4</sub>, and 200W RF power). The etched samples were then imaged using the Hitachi S4300 electron microscope.

Figure 4.7 shows the SEM images of the etched samples for varying CH<sub>4</sub> flows. In all cases, the etched surfaces are clean and smooth. The differences in the four images are in the etched thickness and the amount of undercut. The waveguide in Figure 4.7 b) corresponds to 5sccm CH<sub>4</sub> flow and shows no undercut. The SEM images of the etched samples for varying power input to the sample table are shown on Figure 4.8. One obvious trend from these images is that the degree of isotropic etching increases with the chamber pressure. Furthermore, the roughness both on the horizontal area and sidewalls appears increased.

Table 4.5: Fine tuning of etching study with RIE machine, varying CH<sub>4</sub> flow

Parameters	Values
Pressure (mTorr)	30
Ar flow (sccm)	30
H2 flow (sccm)	30
CH4 flow (sccm)	3, 5, 7, 10
Power (W)	200

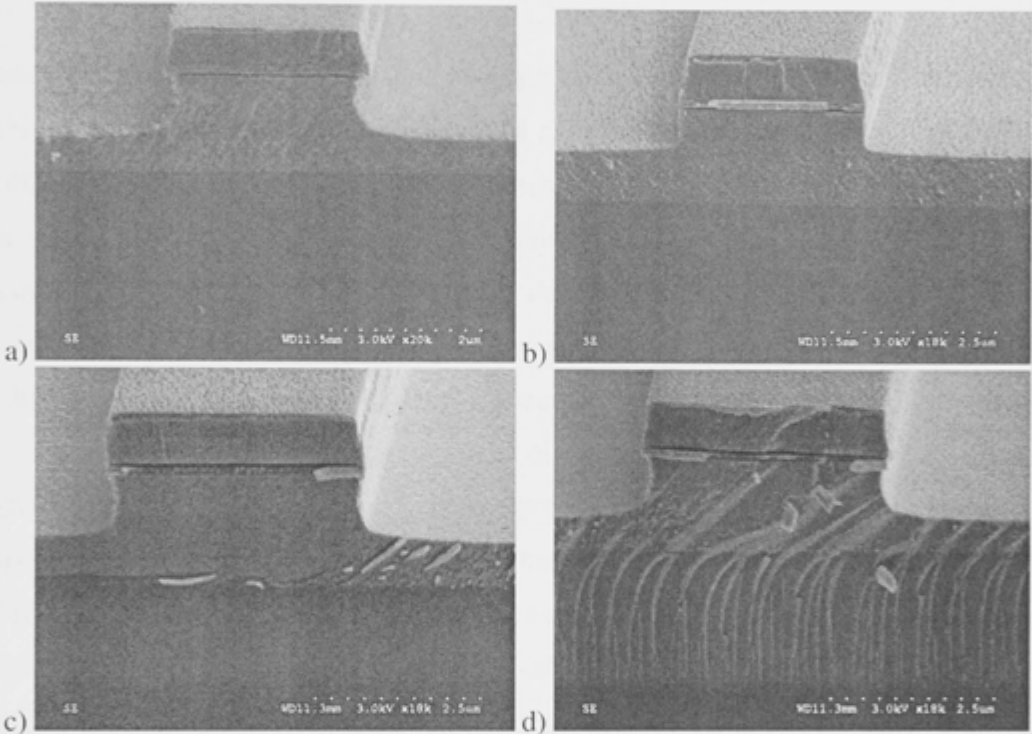


Figure 4.7: Effect of varying CH<sub>4</sub> flow on the etched profile. The etching parameters (as on Table 4.5) were: 5mins etching time, 30mTorr pressure, 30sccm Ar flow, 30sccm H<sub>2</sub> flow, and 200W RF power. The flows of CH<sub>4</sub> were varied: a) 3, b) 5, c) 7, d) 10sccm. The sample d) has bad cleaving and produce chipping on the facet.

The TeO<sub>2</sub> film etch rate, photoresist etch rate and degree of isotropic etching ( $IE=d_l/d_v$ ) were chosen as the response functions. These response functions are plotted in Figure 4.9. Since CH<sub>4</sub> can form polymer which not only passivates the vertical side walls but even builds up on the photoresist layer, then the photoresist etching rate can become slightly negative with large amounts of CH<sub>4</sub> in the chamber leading to negative selectivity as shown on Figure 4.9 a) and c). The TeO<sub>2</sub> etching rate was generally



greater than 100nm/min for all conditions. There were dips in the etching rate and undercut with varying  $\text{CH}_4$  flow. The optimum point for low isotropic etching was with 5sccm  $\text{CH}_4$  flow. With increasing chamber pressure, the etching rate increased but the isotropic etching got worse. The optimum operating pressure was at 30mTorr. It therefore can be concluded that the best profile has been obtained with etching condition of 30mTorr pressure, 30sccm Ar, 30sccm  $\text{H}_2$ , 5sccm  $\text{CH}_4$ , and 200W RF power.

The reactive etching mechanism is a complex process that involves the interaction of the plasma with the substrate and the chamber setting. However, the etching mechanism of a particular material can be deduced from its etching rate and profile dependence on the process parameters. As the pressure increases, the etching rate of the  $\text{TeO}_2$  surface increases monotonically but at the same time, the etching becomes more isotropic. An increase in the gas pressure without power increase normally leads to an increase in the radical density but a decrease in the ion density [328]. This means that the predominant etchant in the chamber are radicals.

One the other hand, the dependence of etching rate and profile on  $\text{CH}_4$  flow are highly nonlinear with a minimum in their representing curves as on Figure 4.9 a) and b). This etch rate dependence on  $\text{CH}_4$  flow has also been seen previously [337]. The sidewall becomes vertical with the  $\text{CH}_4$  flow at 5sccm indicating highly anisotropic etching. This is an indication that the side wall is well passivated while the flat surface is still etched away at a reduced rate. The precursors from the  $\text{CH}_4$  initial gas have now become the polymer on the side wall and the proportion of  $\text{CH}_x$  radicals as etchant are reduced. At low  $\text{CH}_4$  flows, the density of hydrogen radicals and ions are higher leading to higher etching rate. At high  $\text{CH}_4$  flows, the  $\text{CH}_x$  radicals' density increases to compensate for the decrease in hydrogen radicals and maintain a higher etch rate.

Table 4.6: Fine tuning of etching study with RIE machine, varying processing pressure

Parameters	Values
Pressure (mTorr)	20, 30, 50, 80
Ar flow (sccm)	30
H2 flow (sccm)	30
CH4 flow (sccm)	5
Power (W)	200

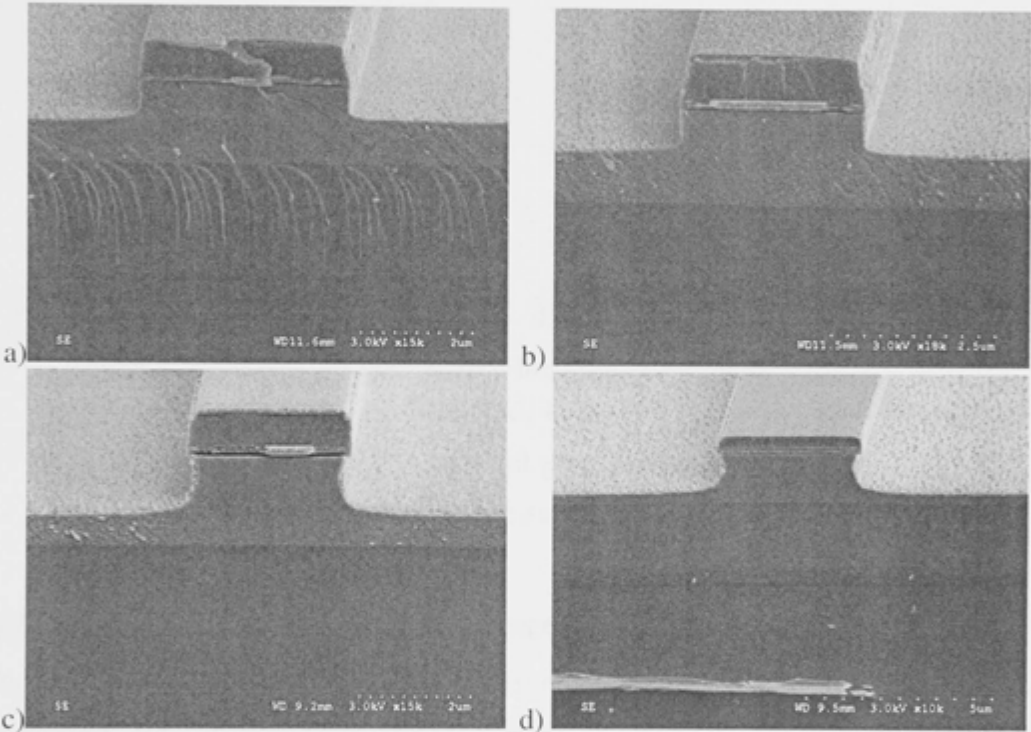


Figure 4.8: Effect of varying pressure on the etched profile. The etching parameters (as in Table 4.6) were: 5mins etching time, 5sccm CH<sub>4</sub> flow, 30sccm Ar flow, 30sccm H<sub>2</sub> flow, and 200W RF power. The pressure was varied: a) 20, b) 30, c) 50, d) 80sccm. The sample a) had bad cleaving and produced chipping on the facet.

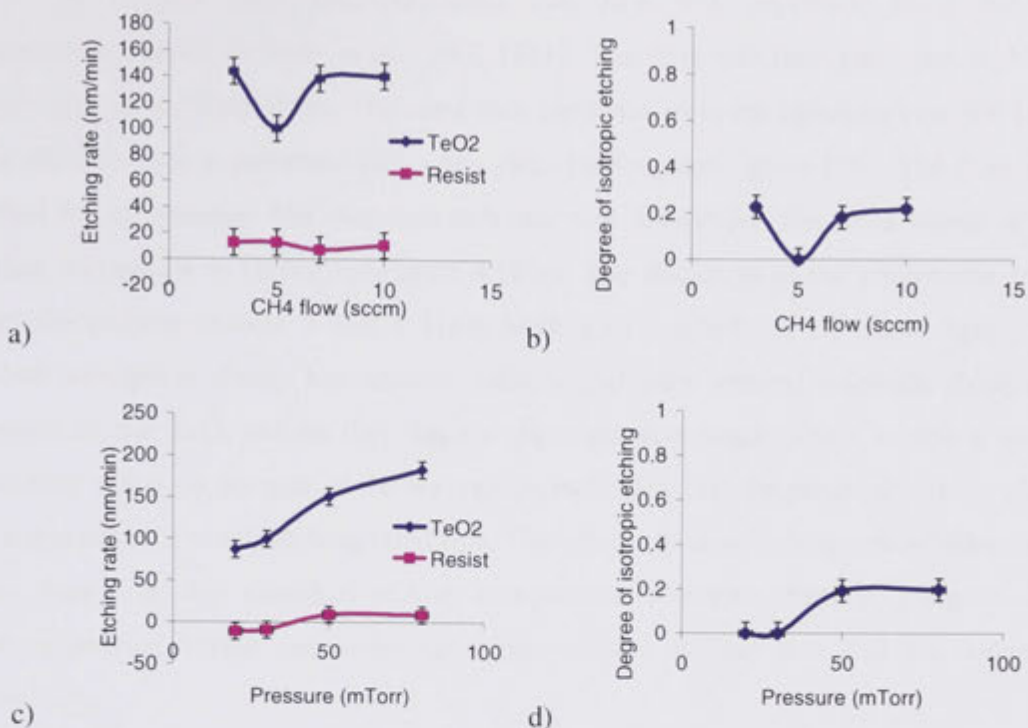


Figure 4.9: Response functions against the varied parameters; a) etching rates of TeO<sub>2</sub> and photoresist at various CH<sub>4</sub> flows b) degree of isotropic etching at various CH<sub>4</sub> flows c) etching rates of TeO<sub>2</sub> and photoresist at various pressures and d) degree of isotropic etching at various pressures.

#### 4.2.8 H<sub>2</sub>/CH<sub>4</sub>/Ar plasma etching of chalcogenide glasses

Chalcogenide glasses contain Chalcogen elements (S, Se or Te) as substantial components typically covalently bonded to network forming elements such as Ge, As, Sb, or Si. These glasses have significant applications ranging from non-volatile random access memories [338] to integrated nonlinear optical devices [53, 339] due to their high optical nonlinearity. Chalcogenides have a unique set of properties among optical glasses that make them an excellent choice for mid-infrared technology and nonlinear optics. The current etching technology to make devices from these materials uses halocarbon gases such as CHF<sub>3</sub> [329] or CF<sub>4</sub>. [340]. Halogen containing gases are considered increasingly harmful to the environment. Therefore, an alternative option which uses more friendly and easier to handle gases would be a big advantage for large scale industrial applications involving these materials.

A  $1.80\mu\text{m}$  thick  $\text{Ge}_{11.5}\text{As}_{21.5}\text{Se}_{67}$  thin film was deposited using thermal evaporation similar to Jarvis *et al.*, 2007 [341]. The film was then patterned with the same steps as the  $\text{TeO}_2$  films. The same etch condition as in the optimum case for  $\text{TeO}_2$  was used to etch a patterned  $\text{Ge}_{11.5}\text{As}_{21.5}\text{Se}_{67}$  chalcogenide glass film. The film was etched for 25 minutes. The observed etch rate was  $40\text{nm}/\text{min}$ . The SEM image of the etched waveguide is shown on Figure 4.10 a). The thickness of the photoresist layer after the etching process is still  $0.41\mu\text{m}$  leading to a selectivity of  $1/2.5$ . Again, the etched waveguide clearly has smooth surfaces and quite vertical sidewalls though in contrast to the  $\text{TeO}_2$  results they have a slight positive angle. There is also a slight trenching effect on the side of the waveguide indicating that the physical etching plays an important role at this etching condition. The relatively slow etching rate of  $40\text{nm}/\text{min}$  also shows the low chemical etching component. Therefore, further change to the current etching recipe can potentially improve the etching rate and the sidewall verticality.

In contrast to the above result, a patterned sample of thermally evaporated  $\text{As}_2\text{S}_3$  film etched with the same recipe resulted in very rough surface (Figure 4.10 b). The etch rate in this case was  $\sim 120\text{nm}/\text{min}$ , which is significantly higher than etching rate of  $\text{Ge}_{11.5}\text{As}_{21.5}\text{Se}_{67}$ . It is suspected that the rapid formation of  $\text{H}_2\text{S}$  may have resulted in poor surface morphology or there is a non-volatile As metallo-organic compound. Further study by changing the key parameters such as reduction of Hydrogen content to slow down the etching rate might lead to better quality etched surfaces.

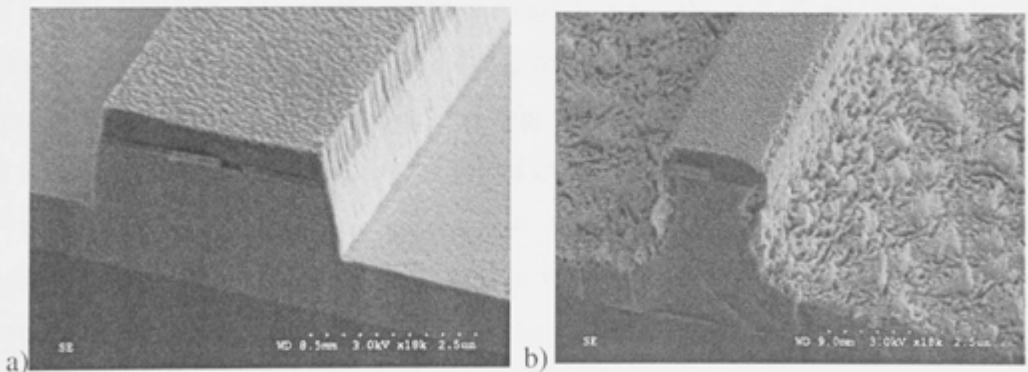


Figure 4.10: a)  $\text{Ge}_{11.5}\text{As}_{21.5}\text{Se}_{67}$  and b)  $\text{As}_2\text{S}_3$  glass thin films using RIE with  $\text{H}_2/\text{CH}_4/\text{Ar}$  plasma mix.

### 4.2.9 Etching of full wafers of TeO<sub>2</sub>

The above studies were performed on small sample sizes of around  $\sim 1\text{cm}^2$ . However, when a full 4" wafer is etched, there is loading effect due to the significant depletion of the etching species due to the consumption during the etching process. Mogab *et al.*, 1977 [342] analysed the relationship between the etch rate,  $R$ , and area,  $A$ , of wafer loaded and found the expression [343]:

$$R = \frac{B\tau G}{1 + KB\tau A} \quad (4.6)$$

where  $G$  is the generation rate of active species,  $B$  is the reaction rate constant,  $\tau$  is the lifetime of the active species in the absence of etchable material,  $K$  is a constant for a given material and reactor geometry and  $A$  is the surface area of the etchable material. For a large wafer, the Equation (4.6) approximately becomes  $R = G / KA$ . The etch rate varies inversely with the wafer loading area  $A$ .

Therefore, it was expected that the etch rate would be significantly lower when a full wafer was being etched. To quantify this change, a patterned full wafer was etched using the optimum recipes from the previous section. Since there was no in situ etching rate monitor in the Oxford PlasmaLab 80, the etch rate was measured from the pre and post etch thicknesses. After 16mins, the etched depth was 750nm, giving an etch rate of 47nm/min. This value is about half of the value of the small sample etch rate. Therefore, for practical applications, where the etching depth is in order of a few hundred nanometres, the etching duration is still only a few minutes.

The SEM images of an etched waveguide from the full 4" wafer are shown in Figure 4.11. Figure 4.11a is as-etched TeO<sub>2</sub> whereas Figure 4.11b is after the exposure to the Oxygen plasma to remove polymers/photoresist. There are a number of features that are different to the small samples etched in Figures 4.6, 4.7 and 4.8 above.

Firstly, the photoresist has become significantly thinner. This leads to the sidewall being divided into two parts, a near vertical section and a curve section above it. This structure is a clear indication that the photoresist has been attacked whereas it was barely etched when the samples were small. This effect can be explained by the fact that it is an oxide film that is being etched. The etching of large areas of oxides can give rise to the release of sufficient numbers of oxygen radicals [311] that the photoresist is

attacked by them during the etch. The selectivity has now been reduced significantly to roughly 1:1.

Secondly, post etch the etched surface appears to have a large number of submicron particles sitting on the surface. The nature of these is uncertain but they were clearly removed after the Oxygen plasma. Despite those differences, the fabricated waveguides still have very high surface quality that should be suitable for low propagation loss optical waveguides.

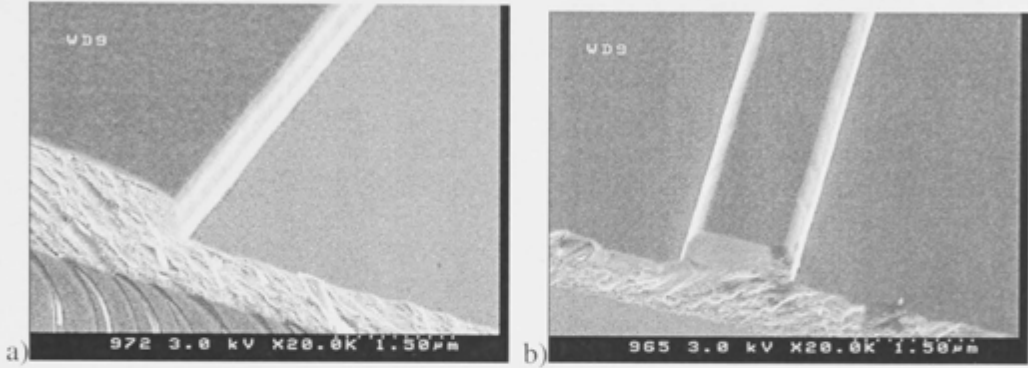


Figure 4.11: Etching of  $\text{TeO}_2$  wafer with 30mTorr pressure, 30sccm Ar, 30sccm  $\text{H}_2$ , 5sccm  $\text{CH}_4$ , and 200W RF power a) before Oxygen plasma, b) after Oxygen plasma.

#### 4.2.10 Etched surface characteristics

##### a) Surface roughness

After the  $\text{TeO}_2$  etching process, the photoresist was removed by a standard Oxygen plasma (50sccm  $\text{O}_2$  flow, 200W forward table power, 500W ICP power, and 30mTorr chamber pressure). The etched surfaces were then imaged using two different techniques to determine the nanoscale properties: atomic force microscopy (AFM) and optical white light interferometry. A Veeco Nanoscope IIIa AFM was first used to scan the etched surface. Due to the low hardness of  $\text{TeO}_2$  surfaces, the tapping mode was utilized. In this mode, the cantilever was driven at a frequency near one of the cantilever tips mechanical resonances at  $\sim 313\text{kHz}$ . As the cantilever is scanned across the sample surface, the interaction of the sample with it varies with the surface topography. Because the cantilever is oscillating at its mechanical resonance, the oscillation amplitude changes with sample surface topography. The measured root mean square



(RMS) roughness of an etched surface using this equipment was 0.8nm calculated over a scanned area of  $25\mu\text{m}^2$  as shown on Figure 12 b). This is a relatively small increase of the roughness from the un-etched sample which had a measured RMS roughness of 0.3nm as shown on Figure 4.12 a). It is also clear that the spatial frequency components of the roughness are lower for the etched surface appearing to be moved from around  $0.5\mu\text{m}$  to the 1-2 $\mu\text{m}$  range.

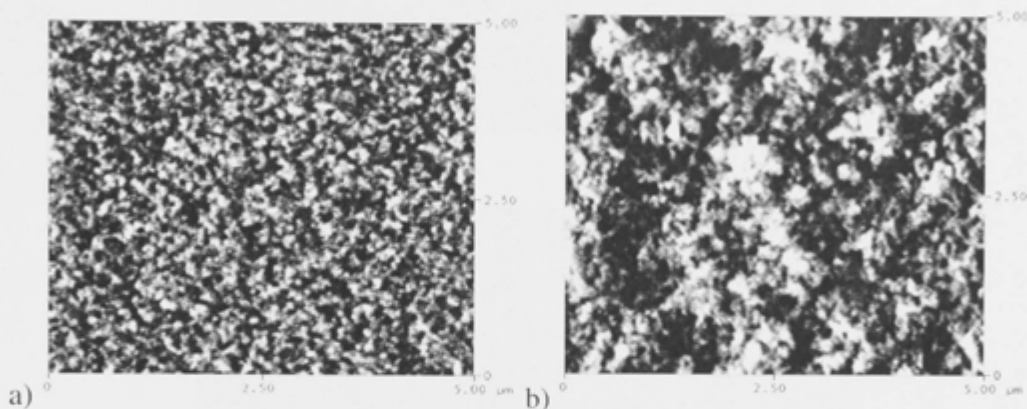


Figure 4.12: AFM images of an a) un-etched surface RMS roughness of 0.3nm, z range 5nm and b) etched surface RMS roughness of 0.8nm, z range 11nm.

The alternative measurement was an optical interferometric profiler model Wyko NT9100 from Veeco. This technique is a noncontact, non-destructive measurement of surface profile using interference of broadband light and special objectives with built in reference mirrors [344]. In this technique, a LED light source is split into two paths, one arm is used to probe the sample surface, one arm goes to a reference surface. The reflected beams are then combined to form an interference pattern. Due to the low coherence length of broadband light, interference is only obtained when the two paths are very nearly equal, typically within  $\pm 10\mu\text{m}$  which provides immediate height profiling capabilities. By monitoring the interference pattern as the objective lens is scanned in vertical direction, the surface profile is calculated to sub nanometre accuracy by fitting the interferogram. Figure 4.13 shows the result of a scan of the un-etched and etched  $\text{TeO}_2$  surface. The scan area was  $40 \times 50\mu\text{m}^2$  with resolution of  $0.5\mu\text{m}$ . The RMS roughness was measured to be 0.8nm for etched surface compared to 0.3nm for un-etched surface. The two techniques are in good agreement with each other, and clearly there is insignificant attack of any grain structure in the film

or any other chemical roughening effect which implies the etched sidewalls should also be smooth barring lithography limitations.

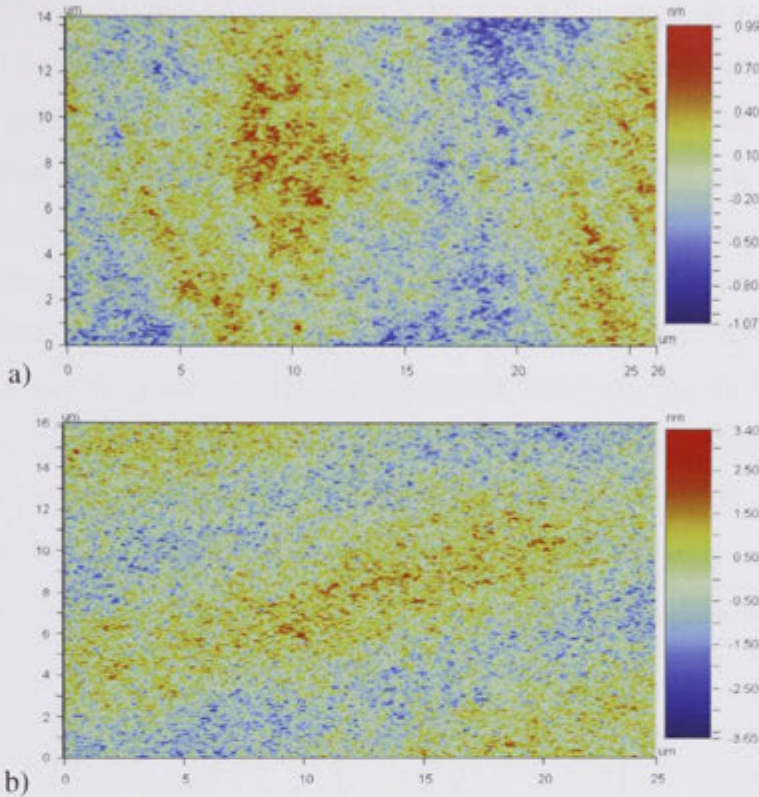


Figure 4.13: Optical profiler images of an a) unetched surface (RMS=0.3nm) and b) etched surface (RMS=0.8nm) magnifications X50 objective, X2 eye piece.

#### ***b) X-ray photoelectron spectroscopy***

The etched surface was further studied under X-ray photoelectron spectroscopy (XPS). XPS involves irradiation of a sample under high vacuum by X-rays of known energy. This causes the photo-ejection of electrons from atoms near the surface. The emitted electrons have a kinetic energy  $E_k$ , which is given by:  $E_k = h\nu - E_b - \Phi$ , where  $h\nu$  is the photon energy,  $E_b$  is the binding energy relative to the Fermi level of the solid,  $\Phi$  is the work function and  $E_b$  is the binding energy of the electrons. XPS may involve the concurrent emission of photoelectrons and Auger electrons. XPS can probe the first few nanometres (~5-10nm) of the surface and give a significant amount of information such as identification of all elements (except H and He), molecular environment, bonding structures, depth profile (destructive measurement).



Two samples, one un-etched, the other etched, in the same condition under  $\text{H}_2/\text{CH}_3/\text{Ar}$  plasma as the previous section, were analysed. The film has composition O/Te of  $2.20 \pm 0.05$  measured by EDXA and RBS. The XPS composition analysis gives the films with the composition O/Te of  $2.14 \pm 0.05$ . The XPS spectrum of Tellurium has the strongest peaks due to the 3d orbital. In general, binding energies decrease with formal oxidation state; for example, those reported for elemental Te  $3d_{5/2}$  range is around 573.3 [286, 345] and  $3d_{3/2}$  is at 583.5 eV [286, 346] while values reported in the literature for  $3d_{5/2}$  Tellurium oxides are 575.8-576.5 eV for  $\text{TeO}_2$ , 576.1 eV for  $\text{TeO}_3$ , and 577.1 eV for  $\text{Te(OH)}_6$  and the value for  $3d_{3/2}$  for Tellurium oxide are 586.4 eV for  $\text{TeO}_2$ , 587.7 for  $\text{TeO}_3$  and 587.1 for  $\text{Te(OH)}_6$  [281, 286, 298, 346-348]. The Te 3d spectrum of the as-deposited (un-etched) sample is shown on Figure 4.14 a). It comprises a single doublet, with the  $3d_{5/2}$  component at 576.8 eV and  $3d_{3/2}$  component at 587.3 eV. It is confirmed that the Te atoms are all in binding states with Oxygen.

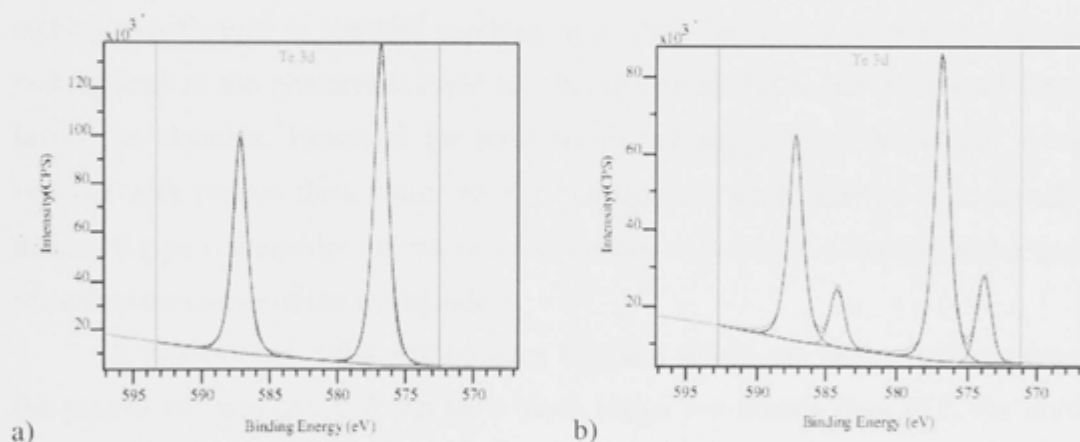


Figure 4.14: Te 3d XPS spectra of a) un-etched b) etched surfaces

The Te 3d spectra of etched sample contain a second doublet at lower binding energy and of lower intensity (Figure 4.14 b). The  $3d_{5/2}$  components of these are at 576.9 and 573.8 eV. The  $3d_{3/2}$  components are at 587.3 and 584.2 eV. The etched surface therefore contained both Te in pure form (Te-Te bond) and Te in oxide form ( $\text{TeO}_2$  or  $\text{TeO}_3$ ). The relative contribution of the minor components to the overall area under the Te 3d spectrum is 21%. From the composition analysis, the Oxygen over total amount of Te ratio was 4.3. This indicates that the etched surface contains large amount of Oxygen. However, from the measurement, it is not conclusive which form the Oxygen is in, water, bonded Oxygen atoms or trapped  $\text{O}_2$ . Despite this, the composition changes are confined to the surface of order of few nanometres, the affected layer can be

removed easily through a short Oxygen plasma etch. Thus the surfaces created by the etch process appear to be suitable for waveguide applications, and perhaps could even be functionalised in the future through OH groupings.

### 4.3 Etching of Tellurium oxide with ICP machine

At the latter stages of the project, the ICP machine had Methane and Hydrogen gas lines added to it. Therefore, the etching process for Tellurium oxide with Methane/Hydrogen/Ar was studied using ICP. As Equation 4.6 indicated, the etching rate and therefore etching process occurring inside an ICP machine is different from that inside the RIE machine due to the differences in chamber geometry, configuration of the plasma, and the sample cooling arrangements. In order to determine if this leads to a difference in the optical quality of the etched waveguide, ICP etching using some of the parameters from the successful RIE processes was trialled. From the full wafer etching experiments in the RIE machine, it is clear that products of oxide thin film etching lead to the photoresist layer also being etched due to the present of Oxygen inside the chamber. However, for most waveguide applications this is not a major concern with micron thick resists as the etch depth is usually below  $1\mu\text{m}$  for rib or nanowire type waveguides, therefore, resist erosion may not be a limiting factor except in cutting the corner of the waveguide.

A fundamental difference between RIE and ICP is the ion density control and the plasma location. As ICP can have much higher ion density than RIE, the etching rate can be much higher if needed. Another difference is in the location of the plasma centre (schematic in Figure 4.2). One of the obviously different characteristics of the two plasmas in the RIE and ICP is that the bias voltage in RIE is only around half of that in the ICP. The plasma in an ICP machine is located high above the sample therefore it can have higher degree of anisotropy at a given power and pressure.

In the first instance, the same parameters that gave the best etching results using the RIE chamber were used as a starting point. The best etching conditions were with 30mTorr pressure, 30sccm Ar, 30sccm  $\text{H}_2$ , 5sccm  $\text{CH}_4$ , and 200W RF power. Initially small samples  $\sim 1\text{cm}^2$  were trialled. For the first series of experiments, the  $\text{CH}_4$  flows were varied from 3sccm to 10sccm whilst keeping all other parameters constant (see Table 4.7). Also, the ICP power was still set to zero because the etching rate was

already sufficiently high. A second series of experiments was run varying the chamber pressure in the range 10mTorr to 30mTorr (see Table 4.8) with a CH<sub>4</sub> flow of 10sccm. A lower pressure limit of 10mTorr was chosen because this is just within the limit of the pump capability at the selected gas flows. Similar response functions of etching rates and anisotropy were chosen to the RIE study. Figure 4.15 shows SEM images at three conditions of a) 3sccm CH<sub>4</sub> flow at 30 mTorr pressure b) 10sccm CH<sub>4</sub> flow at 30mT pressure c) 10mTorr pressure at 10sccm CH<sub>4</sub>. It is clear from the inspection that all conditions give high quality etched surfaces and all obtained profiles were undercut to some degree.

Table 4.7: Fine tuning etching study with ICP machine, varying CH<sub>4</sub> flow

<i>Parameters</i>	<i>Values</i>
Pressure	30mTorr
Ar flow	30sccm
H2 flow	30sccm
CH4 flow	<b>3, 5, 7, 10sccm</b>
FW Power	200W
ICP power	0W

Table 4.8: Fine tuning etching study with ICP machine, varying pressure

<i>Parameters</i>	<i>Values</i>
Pressure	<b>10, 20, 30mTorr</b>
Ar flow	30sccm
H2 flow	30sccm
CH4 flow	10sccm
FW Power	200W
ICP Power	0W

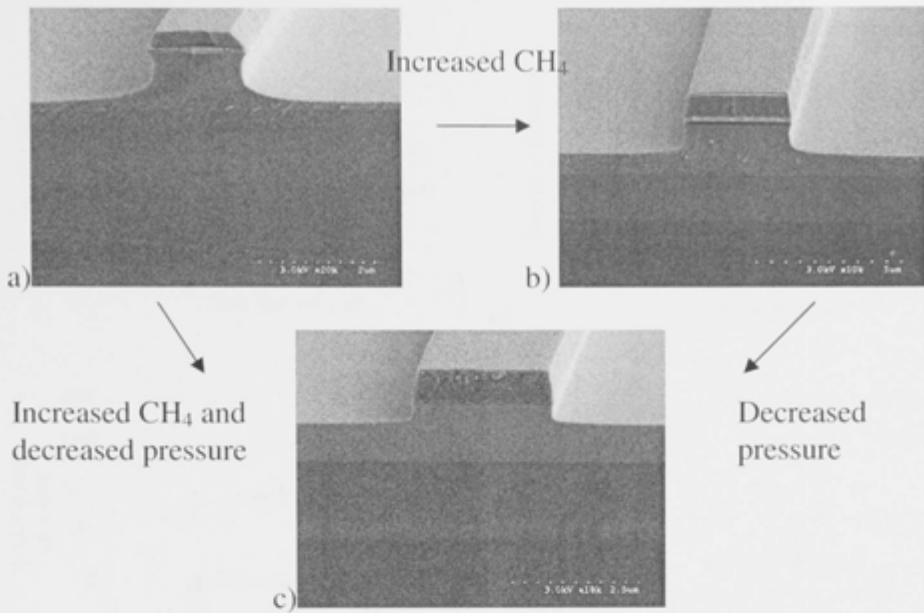


Figure 4.15: Some SEM images of ICP DOE results a) 3sccm CH<sub>4</sub> flow at 30mT pressure b) 10sccm CH<sub>4</sub> flow at 30mT pressure c) 10mTorr pressure at 10sccm CH<sub>4</sub>.

The response functions at various CH<sub>4</sub> and pressures are shown on Figure 4.16 a) to d). While there are some similarities between these results and the RIE (Figure 4.9), the ICP etch behaviour was slightly different to the RIE machine. At the sample setting of 10sccm CH<sub>4</sub>, 30mTorr pressure, the ICP etching rate is 150nm/min while the RIE was at 100nm/min. As the pressure increases, the TeO<sub>2</sub> etching rate raise sharply as was the case with the RIE. The TeO<sub>2</sub> etch rate doubles for a rise from 10mTorr to 30sccm. This is perhaps to be expected as there are more ions and radicals in the chamber as the pressure increases. As more CH<sub>4</sub> was added to the chamber, the TeO<sub>2</sub> etching rate reduced slightly, but remained relatively high (more than 150nm/min) indicating sufficient ion bombardment was occurring to clear the polymer deposition on horizontal surfaces or the CH<sub>x</sub> radicals are the main etchants.

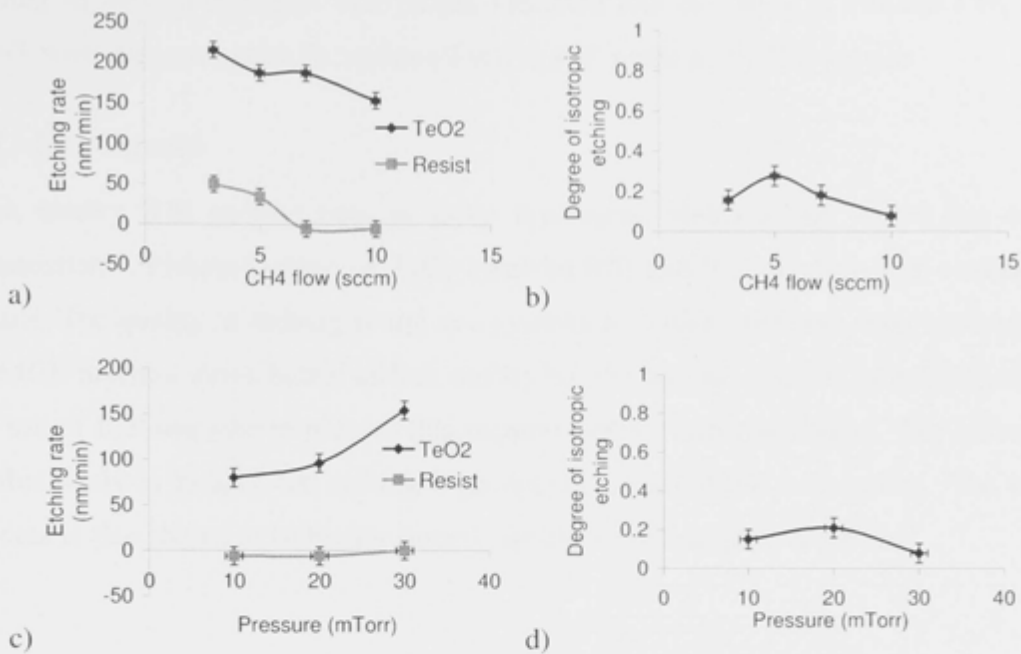


Figure 4.16: ICP DOE results a) TeO<sub>2</sub> and resist etch rate vs. CH<sub>4</sub> flow at 30mT pressure b) Etch Anisotropy vs. CH<sub>4</sub> flow at 30mT pressure c) TeO<sub>2</sub> at resist etch rate vs. pressure at 10sccm CH<sub>4</sub> flow and d) Etch anisotropy vs. pressure at 10sccm CH<sub>4</sub> flow. Polymer build up on top of the mask leads to negative photoresist etching rate.

The etch rate of photo resist follows the etch rate of TeO<sub>2</sub>. This is due to the fact that Oxygen from the film has now formed active species to etch the resist away. With a very high rate of Oxygen coming into the plasma from the film, the Oxygen species are not removed fast enough by the pump. At high TeO<sub>2</sub> rates, the ratio of Oxygen species over other gases is high therefore the photoresist etching rate increases.

The etch anisotropy was relatively good under all conditions tested. Both trials showed a local minimum in the anisotropy with the highest anisotropy coming at the highest trailed CH<sub>4</sub> flow and pressure. The local minimum is believed to result from a trade off between two processes in each case, namely the polymerization process/TeO<sub>2</sub> etch rate for the CH<sub>4</sub> based study, and the ion directionality/polymerization process for the pressure study. At low CH<sub>4</sub> flow, anisotropy is high due to the high TeO<sub>2</sub> etch rate. At high CH<sub>4</sub> flow, the anisotropy is increased again because of increasing passivation due to polymer formation. Similarly with low pressure, anisotropy is enhanced due to increased directionality of active species whilst at high pressure, the etch rate is higher

leading to more anisotropy. The results indicated that operating at 10sccm  $\text{CH}_4$  and 30mT were the best option for etching  $\text{TeO}_2$  in RIE mode in the ICP system.

#### **4.4 Conclusion**

High quality RIE etching process using Hydrogen, Methane and Argon has been demonstrated. Plasma etching of  $\text{TeO}_2$  involved RIE and ICP machines are studied in details. The quality of etching in the two systems is slightly different from each other. The RIE machine gives better surface quality but the lack of etch rate monitor leads to the use of ICP machine in process that requires precise etch rate control. The outcome of this study is recipes for etching high optical quality  $\text{TeO}_2$  waveguides. The etch process is also shown to be highly suitable for chalcogenide glass thin films.

# **Chapter 5:**

## **Characterisation of $\text{TeO}_2$**

### **waveguides**

This chapter investigates the linear and nonlinear properties of  $\text{TeO}_2$  waveguides fabricated by RIE. First, modal simulations were performed to obtain some important properties of the waveguides such as effective indices, dispersion, mode area, etc. Then, the attenuation of the fabricated waveguides was measured by several techniques including non-destructive mode overlap estimation and destructive cutback methods. Nonlinear experiments were also performed. The self-phase modulation simulation of the experiment gave the nonlinear refractive index of sputtered  $\text{TeO}_2$  at  $65 \times 10^{-20} \text{ m}^2 \text{ W}^{-1}$ , which is  $\sim 25$  times that of silica. A four-wave mixing experiment also gave significant signal conversion to idler when pumped at  $1.55 \mu\text{m}$  in a  $3 \mu\text{m}$  wide waveguide.

#### **5.1 Waveguide geometry and modelling method**

##### **5.1.1 Waveguide geometry**

The basic element of integrated photonic technology is the optical waveguide. Waveguiding can be achieved by using a number of configurations to guide light in a particular direction. In this work, the main purpose is to fabricate high quality rib waveguides through a top down approach using thin film deposition, lithography, and plasma etching. Rib waveguides are the most commonly used geometry for semiconductor optical waveguides and for many dielectric nonlinear optical waveguides [1]. Rib geometry waveguides are important elements in integrated optics as they allow for potentially single moded operation with waveguides several microns wide in structures with high index contrast. The high index core is defined by a width  $W$ , etched depth  $h$  and total height  $H$  as shown on Figure 5.1. In this geometry, the confinement is due to total internal reflection not only from the upper and lower interface but also at the effective lateral boundaries.



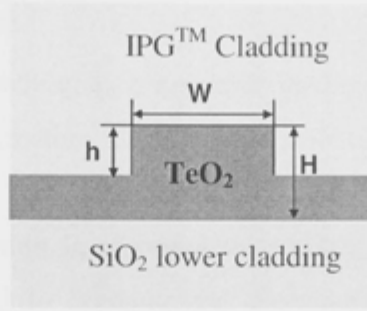


Figure 5.1: Ridge waveguide of Tellurium Oxide with SiO<sub>2</sub> lower cladding and air or inorganic polymer glass IPG™ upper cladding

### 5.1.2 Maxwell equation

Assuming that the light is propagating in a purely dielectric medium (no conductivity, no magnetic effects, isotropic and linear), then Maxwell's equations can be reduced to [1]:

$$\begin{aligned}\nabla \times E &= -\eta_0 \frac{\partial H}{\partial t} \\ \nabla \times H &= \epsilon_0 n^2 \frac{\partial E}{\partial t}\end{aligned}\tag{5.1}$$

where  $E$  and  $H$  are the electric and magnetic fields respectively,  $\mu_0$  is the free space permeability,  $\epsilon_0$  is the permittivity of the free space and  $n$  is the refractive index of the medium where the light propagates. If the medium is optically inhomogeneous its properties are position-dependent,  $n=n(r)$ . The wave equations for  $E$  and  $H$  can be derived as [1].:

$$\begin{aligned}\nabla^2 E + \nabla \left( \frac{1}{n^2} \nabla n^2 E \right) - \epsilon_0 \mu_0 n^2 \frac{\partial^2 E}{\partial t^2} &= 0 \\ \nabla^2 H + \frac{1}{n^2} \nabla n^2 \times (\nabla \times H) - \epsilon_0 \mu_0 n^2 \frac{\partial^2 H}{\partial t^2} &= 0\end{aligned}\tag{5.2}$$

These two full vectorial equations generally describe the all coupled components of electric and magnetic fields. Each component cannot be reduced to a scalar equation. Furthermore, because of non cylindrical symmetry, the optical mode of the waveguide cannot be solved analytically. Instead, numerical techniques must be used to solve for the eigenvalues of the eigenmode equation which describes the modes of propagation of the waveguide.

### 5.1.3 Simulation techniques

Optical waveguide mode solving is a key task in the area of integrated optics. The modal analysis gives information such as the number of modes supported by the structure, the propagation constants, modal intensity distribution and via overlap integrals, the modal excitation in response to a given input field. There are several techniques commonly used to compute the electromagnetic modes of waveguides including finite element methods, mode-matching techniques, methods of lines, beam propagation method and finite difference methods [349].

Mode solvers may be classified as scalar wave equation solvers and vector wave equation solvers, with semi-vectorial being considered as a part scalar method. For many waveguides, the refractive index varies by only a small fraction across the waveguide cross-section. The index at the core where the light propagation occurs is only slightly higher than that of the cladding region. These types of waveguides are classified as weakly-guiding waveguides. Modal analysis can be then greatly simplified for these waveguides by replacing the full-vector eigenmode equation with a simple scalar equation for single field component.

For high index contrast waveguides, the full vector finite difference (FDM) and finite element (FEM) methods are the best known and most accurate [137, 349]. The FEM is particularly useful when analysing inhomogeneous core (graded-index) planar waveguides whereas FDM is easier to implement and can be used to effectively simulate wave propagation in homogenous core (step-index) waveguides.

#### a) The finite difference method

From Maxwell's equations, the wave equation in a uniform region can be reduced to [349]:

$$\nabla^2 E + k_0^2 \epsilon_r E = 0 \quad (5.3)$$

where the time harmonic variation of  $\omega$  is included in  $k_0^2$  which is equal to  $\omega^2 \epsilon_0 \mu_0$  and  $\epsilon_r(x,y)$  is a function describing the relative dielectric constant over the cross-section of the waveguide.

In the finite difference method, the domain of the analysis is discretised into a rectangular grid of points, which might be of constant or variable spacing. A scalar formulation for a quasi-TE mode may be written in term of  $E_x$  or the  $H_z$  component. The

advantage of the  $H_z$  component analysis is that no boundary conditions are required to be set on any of the dielectric interfaces since it is continuous across them. A vector formulation involves both  $E_x$  and  $E_y$  or  $H_z$  and  $E_z$  and the two components of the wave equation have to be solved simultaneously [350].

### b) The finite elements method

The finite-element method uses a variational formulation for solution of waveguide problems. For dielectric waveguides, the usual approach is to use all three components of the  $H$  or the  $E$  vector. The advantage of using the three components of  $H$  is that no boundary conditions need to be set except at the exterior boundary. From Maxwell's equations [349]:

$$\nabla \times \epsilon_r^{-1} (\nabla \times H) = k_0^2 H \quad (5.4)$$

leads to a functional of form:

$$F = \int_S [(\nabla \times H)^* \cdot \epsilon_r^{-1} (\nabla \times H) - k_0^2 H \cdot H^*] dx dy \quad (5.5)$$

In the finite element method, an approximate function is used as a trial function for an expansion of  $H$ . If the trial function coefficients are  $a_i$ , then it is required that  $\partial F / \partial a_i = 0$ . The trial function must span the whole domain and satisfy the exterior boundary conditions. The full-wave three-vector method may suffer from the appearance of spurious, nonphysical modes in its solution [351]. There are a number of schemes to overcome this difficulty such as one proposed by Abid *et al.*, 1993 [351].

#### 5.1.4 Effective mode area and mode overlap calculation

Once the modal properties of the waveguide are available from the modal calculation, several important parameters can be evaluated. Effective mode area is important for nonlinear optics calculations and active devices as it influences the strength of interaction of light with the waveguide structure and the material. The mode area is often evaluated using the expression [137]:

$$A = \frac{\left| \int \int_{-\infty}^{\infty} |E(x, y)|^2 dx dy \right|^2}{\int \int_{-\infty}^{\infty} |E(x, y)|^4 dx dy} = \frac{\left| \int \int_{-\infty}^{\infty} I(x, y) dx dy \right|^2}{\int \int_{-\infty}^{\infty} |I(x, y)|^2 dx dy} \quad (5.6)$$

where  $E(x, y)$  is the electric field amplitude,  $I(x, y)$  is the intensity profile. This evaluation

of mode overlap is accurate for scalar scenarios, which is a good approximation for low index contrast waveguides such as optical fibres. For a Gaussian beam,  $A_{eff} = \pi\omega^2$ ,  $\omega$  is the mode radius at  $1/e^2$  in intensity. However, a full vector variant should be used for the case of high index contrast and tightly confined structures such as nanowires [352].

The mode overlap calculation estimates the amount of light launched into or collected out of the waveguide by another structure with its own defined mode field. This parameter can be modelled using an overlap integral or by the beam propagation method [353]. The beam propagation method takes much longer to calculate so the overlap integral is usually used as a quick and easy method to estimate this coupling parameter.

Assuming the fields are approximated to be scalar quantities, the coupling efficiency  $C$  can be expressed by the overlap integral between the fields  $E_w$  of the waveguide mode and  $E_f$  of the external field [354]:

$$C = \frac{\left| \iint_{-\infty}^{\infty} E_w(x, y) E_f^*(x, y) dx dy \right|^2}{\iint_{-\infty}^{\infty} |E_w(x, y)|^2 dx dy \cdot \iint_{-\infty}^{\infty} |E_f(x, y)|^2 dx dy} \quad (5.7)$$

Again, this calculation is only applicable for scalar approximation, the full vector versions are significantly complicated. With the full vector version, all components of the field need to be taken into account as well as the number of modes that are bound [353].

### 5.1.5 Tellurium oxide waveguide

Very high quality  $\text{TeO}_2$  waveguides were successfully fabricated by  $\text{CH}_4/\text{H}_2/\text{Ar}$  plasma using an RIE etcher as described in Chapter 4, Section 4.2. A full 4" (100mm) wafer of  $\text{TeO}_2$  (coded  $\text{TeO}_2\text{-12}$ ) with thickness of  $1.81\mu\text{m}$  was patterned and etched. The etched waveguide had a  $0.8\mu\text{m}$  etch depth. Post etch resist removal was accomplished by an oxygen plasma strip. The waveguides were then clad with a  $15\mu\text{m}$  thick film of UV cured inorganic polymer glass (RPO Pty Ltd, IPG<sup>TM</sup>) which has a refractive index of 1.51 at 1550nm. End facets were then prepared on the waveguides by hand cleaving the silicon substrate with a diamond scribe. The resulting waveguide chips were approximately 6cm wide and 7.8cm long.

The refractive index and the thickness of the  $\text{TeO}_2$  film were measured using a spectroscopic dual angle reflectometer (SCI Filmtek 4000 [299]) in the range from 450nm to 1650nm. The thickness it reported was  $1.81\mu\text{m}$  and the refractive index at 1550nm was 2.082, which is around 0.03 less than the value of pure  $\text{TeO}_2$  glass [88, 135].

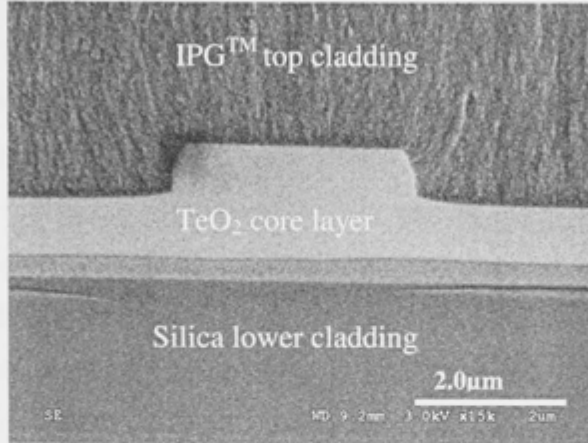


Figure 5.2: SEM micrograph of cleaved waveguide in the  $1.8\mu\text{m}$  thick Tellurium oxide film (the apparent layer between  $\text{TeO}_2$  and silica is due to cleaving effect, it's part of the  $\text{TeO}_2$  layer).

Figure 5.2 shows an SEM micrograph of the end facet of a finished waveguide. The nominal widths of the waveguide sets were  $4\mu\text{m}$ ,  $3\mu\text{m}$ ,  $2\mu\text{m}$  and  $1\mu\text{m}$ . However, due to the variations in lithography and etching, those widths became  $3.5\mu\text{m}$ ,  $2.5\mu\text{m}$ ,  $1.5\mu\text{m}$  and  $\sim 0.5\mu\text{m}$  measured under the optical microscope.

Simulations were performed using Matlab finite different code written by Fallahkhair *et al.*, 2008 [355], the Rsoft - FemSim package, and C2V Olympios generic FD software. The Matlab finite different mode solver is a full-vector simulation based on the transverse magnetic field components. It is versatile and reprogrammable to allow custom properties to be calculated. The C2V Olympios and Rsoft- FemSim are both commercial tools, widely used to simulate planar waveguide and integrated optics. The optical mode solver module in Olympios and the Matlab code both use the finite difference method (generic full vector) whereas FemSim utilizes the finite element method to calculate the optical eigenmodes within a waveguide.

In most instances, the full vector finite difference discretisation method was employed for calculating the electromagnetic modes of isotropic, homogeneous optical

waveguides with transverse, non-diagonal anisotropy. This technique was implemented using Matlab, as this allowed us a degree of customization and integrated post processing, unavailable with the commercial applications.

### 5.1.6 Mode properties

Figure 5.3 shows the profile of the TE<sub>0</sub> and TM<sub>0</sub> calculated by the FD method implemented in Matlab. The modelled waveguide used a grid size of 30nm and calculation window of 8 $\mu$ m in horizontal direction and 5 $\mu$ m in the vertical direction. A summary of the modal properties is tabulated in Table 5.1. The two modes show high confinement with effective mode areas of 4.1 $\mu$ m<sup>2</sup> and 3.8 $\mu$ m<sup>2</sup> for the nominally 4 $\mu$ m waveguide, respectively. The index of the TM<sub>0</sub>s are lower than that of the TE<sub>0</sub>s, however, the TM<sub>0</sub>s are more confined than the TE<sub>0</sub>s. Also, the calculation of the overlap to a Gaussian beam with 1/e<sup>2</sup> diameter of 2.5 $\mu$ m shows only slight difference between TE<sub>0</sub>s and TM<sub>0</sub>s. This will lead to lower polarization dependent total insertion loss (PDL).

Table 5.1: Mode properties of TeO<sub>2</sub>-12 waveguides with film thickness of 1.81 $\mu$ m, etched depth of 0.74 $\mu$ m. The overlap calculation is with a Gaussian beam with 1/e<sup>2</sup> diameter of 2.5 $\mu$ m.

Nominal width ( $\mu$ m)	Measured width ( $\mu$ m)	TE <sub>0</sub>			TM <sub>0</sub>		
		Index	Area ( $\mu$ m <sup>2</sup> )	Overlap (dB)	Index	Area ( $\mu$ m <sup>2</sup> )	Overlap (dB)
4	3.5	2.0397	4.1	0.70	2.0343	3.8	0.75
3	2.5	2.0337	3.7	0.62	2.0285	3.0	0.65
2	1.5	2.0197	2.7	0.85	2.0139	2.3	0.85
1	~0.5	1.9991	4.5	2.50	1.9805	3.0	1.61

At wavelength of 1.55 $\mu$ m, beside the two TE<sub>0</sub> and TM<sub>0</sub> modes, there are higher order modes present in the nominal 4 $\mu$ m and 3 $\mu$ m waveguides, also supporting TE<sub>1</sub> and TM<sub>1</sub> modes (Figure 5.4). The 2 $\mu$ m waveguides are single mode with only TE<sub>0</sub> and TM<sub>0</sub> modes, but the 1 $\mu$ m only supports the weakly bounded fundamental modes. Therefore, for applications that require high quality mode control, the 2 $\mu$ m width waveguides are the most suitable ones. While the 1 $\mu$ m are also single moded they would likely suffer from higher loss due to the lower confinement and thus the higher electric field of the modes at the waveguide sidewalls.

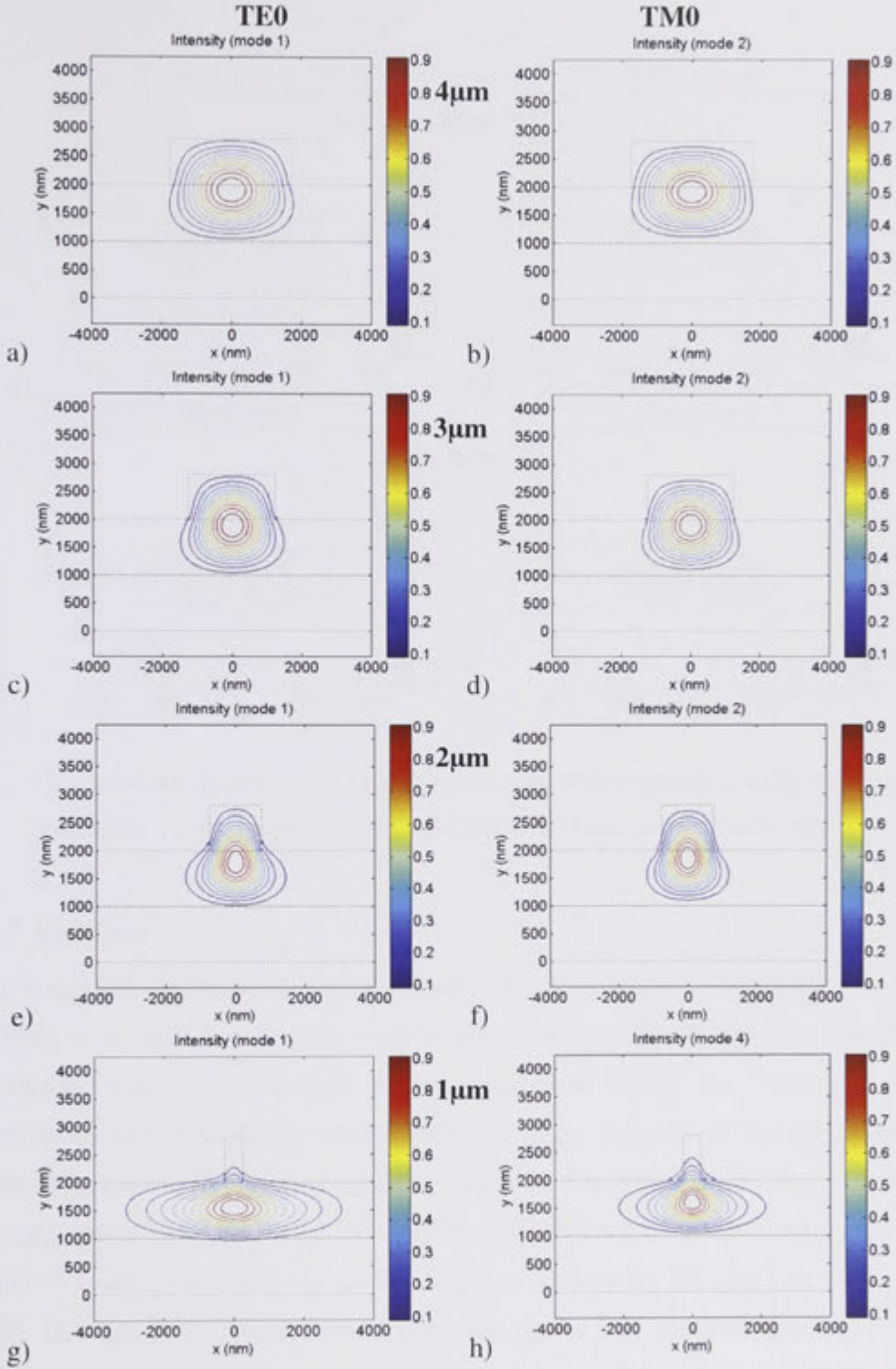


Figure 5.3: Mode profile of TE<sub>0</sub> (left images) and TM<sub>0</sub> (right images) for 4 μm, 3 μm, 2 μm and 1 μm width TeO<sub>2</sub> waveguide with 1.81 μm thick and 0.74 μm etched (TeO<sub>2\_12</sub>).



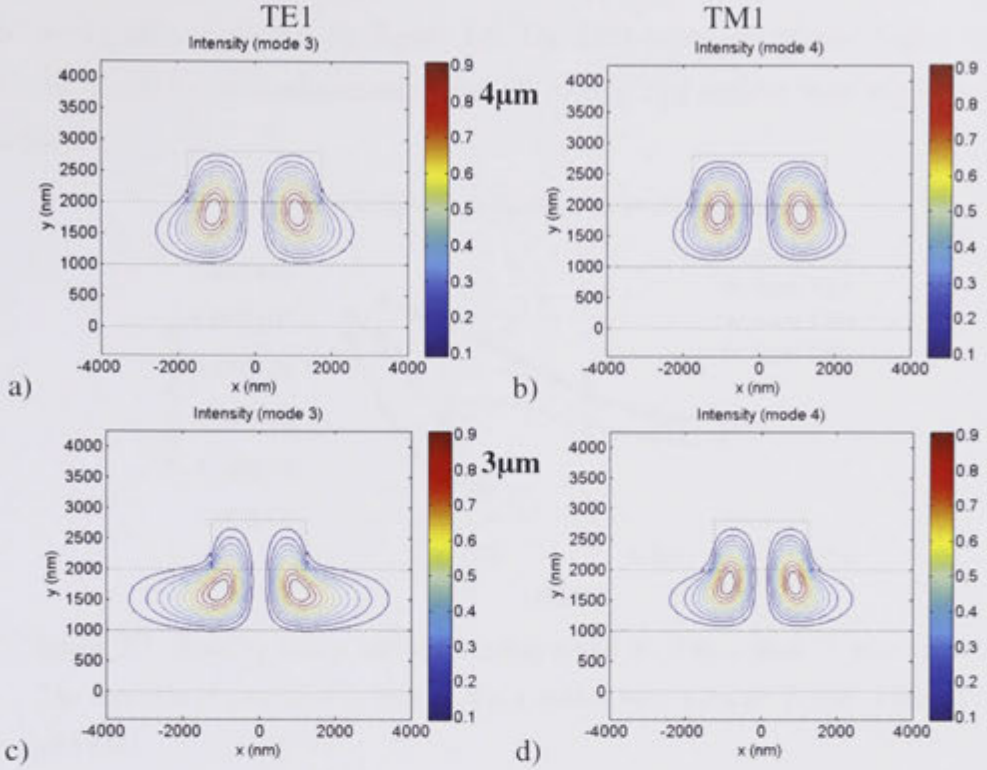


Figure 5.4: Mode profile of TE1 (left images) and TM1 (right images) for 4 $\mu\text{m}$  and 3 $\mu\text{m}$  width  $\text{TeO}_2$  waveguide with 1.8 $\mu\text{m}$  thick and 0.8 $\mu\text{m}$  etched ( $\text{TeO}_2_{12}$ ).

### 5.1.7 Bend loss

The waveguide design must also be suitable for use in integrated structures where tight bending is required (e.g. compact long length amplifier coil). Therefore, a bending loss simulation was also performed to determine how tightly the Tellurium dioxide waveguides could be bent without inducing large amounts of radiative loss. The bending loss was calculated using C2V Olympios. The loss was calculated against the bending radius for a 4 $\mu\text{m}$  wide waveguide with 1.81 $\mu\text{m}$  thick film, 0.74 $\mu\text{m}$  etch depth. Figure 5.5 shows the results of the bending loss per turn for the first four modes, TE0, TM0, TE1 and TM1. Clearly, the fundamental modes TE0 and TM0 are very robust to bend with no loss at bends as tight as 400 $\mu\text{m}$ . The next first order mode TE1 and TM1 can suffer significant bending loss around 700 $\mu\text{m}$  bend radius. Therefore, for any bend less than this order, the waveguides will experience significant degradation in propagation loss especially if significant mode coupling or conversion is present. The

bend loss behaviours of the fundamental modes are very similar in 4 $\mu\text{m}$ , 3 $\mu\text{m}$  and 2 $\mu\text{m}$  wide waveguides as shown on Figure 5.6. The TE0 losses are always higher than the TM0 due to the lower confinement of the TE modes. The critical bend radius is around 400-500 $\mu\text{m}$ .

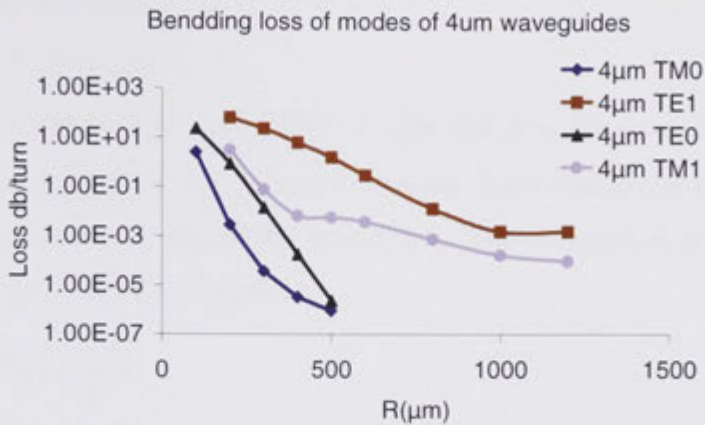


Figure 5.5: Bending loss at various bending radius for 1.8 $\mu\text{m}$  thick, 0.8 $\mu\text{m}$  etched. The loss axis is measured in dB/turn. Four modes were simulated, TE0, TM0, TE1 and TM1.

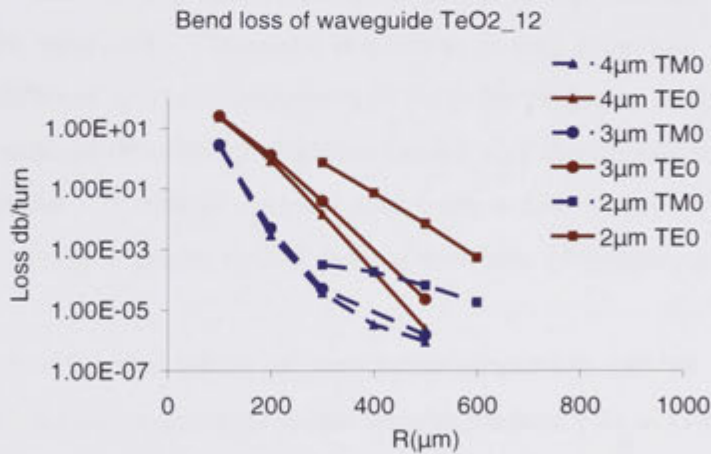


Figure 5.6: Bending loss of the fundamental mode at various bending radius of 4 $\mu\text{m}$ , 3 $\mu\text{m}$  and 2 $\mu\text{m}$  waveguides with 1.81 $\mu\text{m}$  thick, 0.74 $\mu\text{m}$  etched. The loss axis is measured in dB/turn.

These values are purely based on bending induced radiation loss. The effects of sidewall roughness and microbending have not been considered. Therefore, in reality, the critical radii may be larger.

## 5.2 Dispersion properties

### 5.2.1 Introduction

A propagating mode in a waveguide has amplitude and phase variation along the propagation direction as follows:

$$A(x, y, z) = A(x, y)e^{i\beta z} \quad (5.8)$$

where  $A(x, y, z)$  is the complex amplitude of light and  $\beta$  is the (complex) propagation constant. If  $\beta$  is complex, the real part represents the phase change per unit distance and the imaginary part relates to the optical gain or loss. The propagation constant is related to the effective index and wavelength as:

$$\beta = \frac{\omega n_{\text{eff}}}{c} = \frac{2\pi n_{\text{eff}}}{\lambda} \quad (5.9)$$

where  $n_{\text{eff}}$  is the effective index of the propagating mode at wavelength  $\lambda$ .

The propagation constant depends on the wavelength or optical frequency of light through changes in the field distribution between core and cladding with wavelength and changes of the waveguide material's refractive index with wavelength. The relation between these properties determines the group velocity and chromatic dispersion of the waveguide. Chromatic dispersion is very important for short pulse propagation as different spectral components of the pulse propagate at different velocity. The dispersion induced broadening of pulses can be very detrimental to the quality of the signal transmitted in optical systems over even a few metres at TB/s rates for example and in nonlinear planar optical devices with tens of picoseconds or less pulse widths.

Mathematically, the effect of waveguide dispersion can be approximately expanded by a Taylor series about the centre angular frequency  $\omega_0$  as [137]:

$$\beta(\omega) = \frac{\omega n_{\text{eff}}(\omega)}{c} = \beta_0 + \beta_1(\omega - \omega_0) + \frac{1}{2}\beta_2(\omega - \omega_0)^2 + \dots \quad (5.10)$$

where

$$\beta_m = \left( \frac{d^m \beta}{d\omega^m} \right)_{\omega=\omega_0} \quad (m = 0, 1, 2, \dots). \quad (5.11)$$

Therefore,  $\beta_1$  and  $\beta_2$  can be calculated from the effective index of the mode as follows:

$$\beta_1 = \frac{1}{v_g} = \frac{n_g}{c} = \frac{1}{c} \left( n_{\text{eff}} + \omega \frac{dn_{\text{eff}}}{d\omega} \right) \quad (5.12)$$

$$\text{and } \beta_2 = \frac{d\beta_1}{d\omega} = \frac{1}{c} \left( 2 \frac{dn_{\text{eff}}}{d\omega} + \omega \frac{d^2 n_{\text{eff}}}{d\omega^2} \right) \quad (5.13)$$

where  $n_g$  is the group index and  $v_g$  is the group velocity. While the phase of each component of the pulse spectrum travels at the phase velocity, the envelope of the optical pulse moves at group velocity. The parameter  $\beta_2$  represents dispersion of the group velocity and is responsible for pulse broadening. This is known as group-velocity dispersion (GVD) and  $\beta_2$  is GVD parameter. The GVD parameter  $\beta_2$  can be positive (normal dispersion), negative (anomalous dispersion) or zero (zero-dispersion).

The dispersion of a guiding structure depends on the both of the material dispersion and the waveguide dispersion. Material dispersion arises because of the Kramers-Kronig relationship linking absorption to refractive index, and all real materials have absorptions. In optical communications, the GVD parameter is usually represented by  $D$  in ps/(nm.km) units and is equal to the sum of material dispersion and waveguide dispersion. It can be written as [137]:

$$D = \frac{d\beta_1}{d\lambda} = -\frac{2\pi c}{\lambda^2} \beta_2 = -\frac{\lambda}{c} \frac{d^2 n_{\text{eff}}}{d\lambda^2} \quad (5.14)$$

The GVD parameter can be tailored to suit different applications by a process referred to as dispersion engineering. Since, the GVD has two components, one from the material dispersion and one from the waveguide design, the two can be played off against each other to achieve a desired dispersion figure. Operation at or close to the zero-dispersion wavelength (ZDWL),  $\lambda_D$ , is preferred in number of nonlinear optics applications such as supercontinuum generation (SCG) and four wave mixing (FWM). Even though the ZDWL is at around  $\lambda_D$ , the dispersion does not vanish at  $\lambda = \lambda_D$ . Pulse propagation around this wavelength is governed by the cubic term (or third-order dispersion parameter  $\beta_3$ ) and other higher order dispersion parameters.

One example of dispersion engineering in optical fibre is the use of double clad (depressed clad) or quadruple-clad fibres. Conventional step index single mode silica fibres have ZDWL at 1.3 $\mu\text{m}$ . With double clad, the zero dispersion can be red-shifted to 1.5 $\mu\text{m}$ . while quadruple-claddings can flatten the dispersion to as low as 1ps/km.nm over a wide wavelength range [137]. In planar waveguide geometry, the dispersion of

the waveguide can most easily be engineered by varying the thickness of the films, etch depth or cladding materials.

### 5.2.2 Simulation of dispersion

The refractive index of a  $\text{TeO}_2$  film coded  $\text{TeO}_2_{12}$  was measured using the SCI Filmtek 4000 in the range from 450nm to 1650nm. The refractive index against wavelength is plotted on Figure 5.7a and the dispersion parameter  $D$  was calculated for the 1550nm region using the Equation (5.14). The refractive index around 1550nm is relatively flat leading to a quite low (for a high index glass) material dispersion of around -150ps/km.nm (see Figure 5.7b). The Abbe number for this film was calculated as 17, which is in good agreement with reported range of 15-20 [88, 356].

The calculation is then extended to the dispersion of different modes (TE0, TM0, TE1 and TM1) in three different waveguide nominal widths of 2 $\mu\text{m}$ , 3 $\mu\text{m}$  and 4 $\mu\text{m}$ . This exercise is a part of a dispersion engineering process to design a waveguide with ZDWL at around 1550nm. Figure 5.8 shows the results of the calculations. Here, the first 4 modes are corresponding to TE0, TM0, TE1 and TM1. However, it is also necessary to note that modes 3 and 4 are not of primary interest because they are usually not excited at the launch point at the beginning of the waveguide due to the use of a Gaussian beam. These modes might, however, be excited by the propagation of the low order modes due to the presence of roughness and scattering centres.

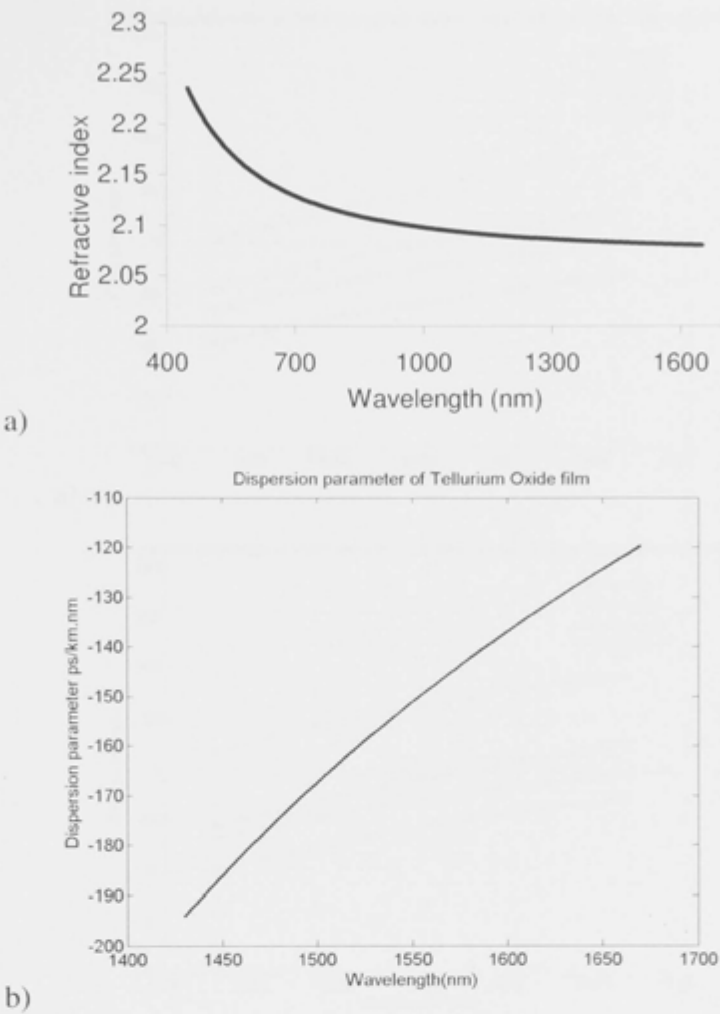


Figure 5.7: Dispersion parameter of the films a) refractive index of the film vs wavelength and b) dispersion parameters around 1550nm region.



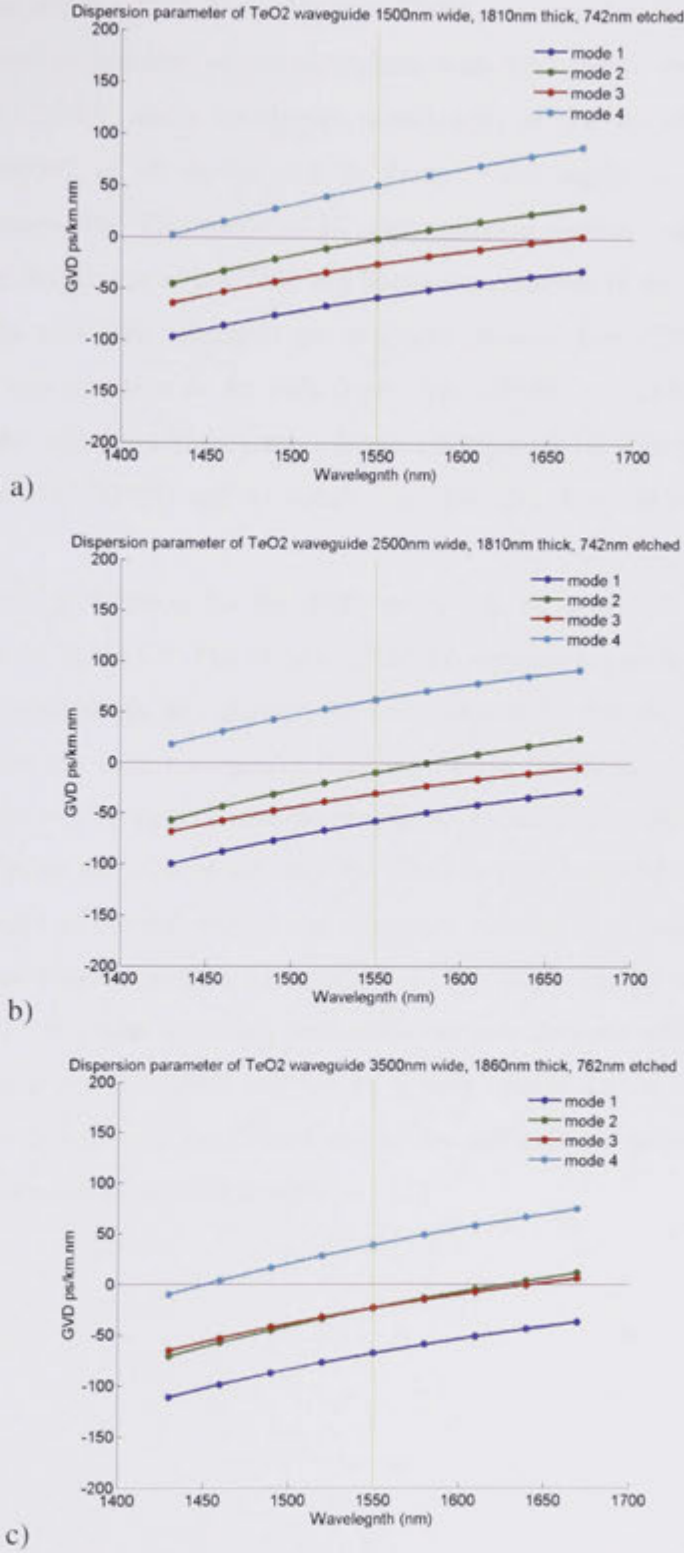


Figure 5.8: Dispersion calculation of modes in TeO<sub>2</sub> waveguide (mode 1-4 are corresponding to TE<sub>0</sub>, TM<sub>0</sub>, TE<sub>1</sub>, TM<sub>1</sub>, respectively)



A range of designs can achieve 1550nm ZDWL waveguides. Figure 5.9 plots the ZDWL for different dimensions of the waveguide with 50% etched depth. The general trend is that the ZDWL shifts to shorter wavelength as the thickness of the film decreases. The ZDWL of all modes shift to shorter wavelengths as the width of the waveguide decreases. The TE<sub>0</sub> mode of all waveguides is normally dispersive around 1.5 $\mu$ m, whilst the dispersion of the TM<sub>0</sub> can become anomalous in this region when the waveguide widths and film thickness are properly chosen. The ZDWLs for various waveguides are also sensitive to the etch depth. The ZDWLs of TM<sub>0</sub> shift to shorter wavelengths as the etch depth increases as shown on Figure 5.10. The etch depth can be used to fine tune the ZDWL and to compensate for film deposition and fabrication variations.

The ZDWL at 1550nm for the TM<sub>0</sub> mode can be achieved with the critical dimensions listed in Table 5.2. The trend is clear for waveguides with width of 2-4 $\mu$ m. The smaller the waveguide, the thinner the films should be for the ZDWL to be at 1550nm. However, the 1 $\mu$ m waveguides does not follow the trend as its mode is very close to cut off. As will be shown, loss measurements indicated that the 1 $\mu$ m waveguide only weakly supports the TE<sub>0</sub> mode, and the TM<sub>0</sub> is very lossy because its index is lower than the index of the slab modes and therefore, couples to an outgoing slab mode at an angle where phase matching is satisfied [357]. High quality waveguides with thickness of order 1.6-1.8 $\mu$ m are easily achievable because they are relatively large. The variation in etching and thickness will not be a very critical factor. The accuracy of these calculations is yet to be confirmed due to the difficulty in accessing dispersion measurement set ups for such short devices.

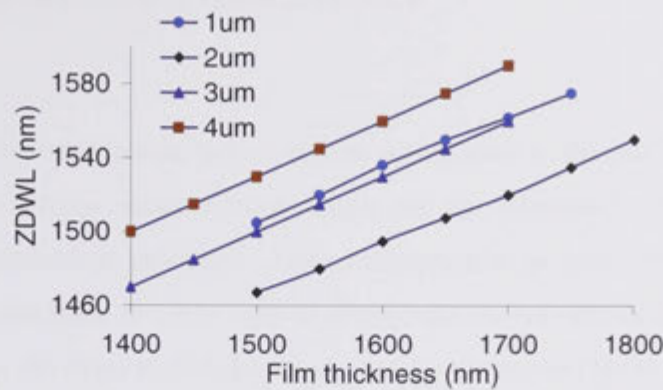


Figure 5.9: ZDWL of TM0 for different 1-4μm waveguides against different film thicknesses with 50% etch depth, TM0 in 1μm might be very lossy due to its refractive index being close to the slab modes.

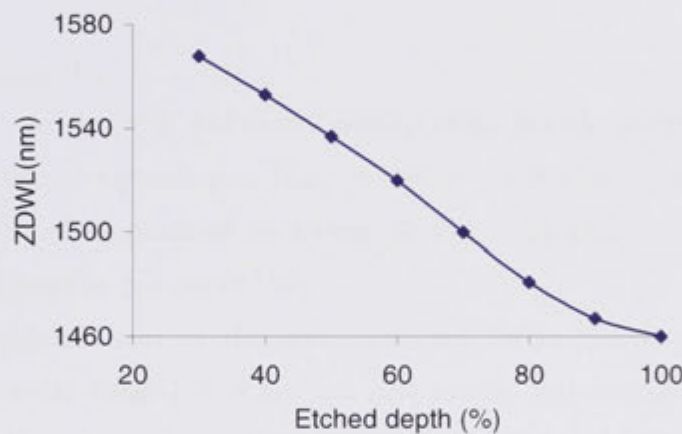


Figure 5.10: ZDWL of TM0 mode for 1810nm thick, 1500nm wide waveguides at different etch depths

Table 5.2: Waveguide dimensions to achieve ZDWL at 1.55μm for TeO<sub>2</sub> rib waveguide with 50% etch depth.

Waveguide width (μm)	Film Thickness(nm)
4	1575
3	1675
2	1800
1	1650

### 5.3 Waveguide attenuation measurements

#### 5.3.1 Principle

One of the most important properties of optical waveguides is the propagation loss. It is the single most obvious measurement parameter to determine the quality of the deposition and fabrication processes. Loss measurement is generally undertaken by launching light (laser lines or white light sources) into the waveguide and collecting the transmitted light at the other end of the waveguide as shown on Figure 5.11. In the work reported here, the input and the outputs are fibre coupled using tapered fibre lenses with a  $2.5\mu\text{m } 1/e^2$  spot diameter due to the small sizes of the waveguides. The total loss also included the coupling loss into the waveguide, Fabry-Perrot cavity losses within the chips due to the relatively high reflectivity facets and coupling loss at the output of the waveguide:

$$L_t = L_{in} + L_{cavity} + L_{out} \quad (5.15)$$

where  $L_{in}$  and  $L_{out}$  are the input and output overlap of the launching/collecting fibre lens fields and the mode at input/output;  $L_{cavity}$  is due to standing wave inside waveguide with the reflectivity of the facets of the waveguide and the propagation loss between the two end faces included in this cavity loss.

The propagation loss of the waveguide can be measured in several ways: conventional cut back, Fabry-Perrot method, side scatter, and overlap calculation. The conventional cut back method involves measuring the waveguide total loss at different lengths. As the length changes, the only loss component that should change is the propagation loss. Therefore, a plot of the total insertion loss against the length will give the propagation loss per unit length. This method relies on the consistency of the alignment and cleaving of the input and output ends to maintain over all accuracy. Also, there is a limit on how low a propagation loss can be measured by this technique. If the propagation loss is very low, the fluctuation in the total insertion loss might be larger than the total propagation loss itself leading to a very substantial uncertainty of the propagation loss per unit length.

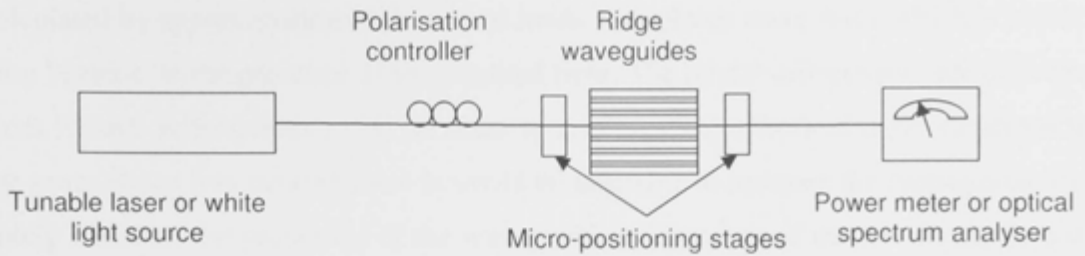


Figure 5.11: Loss measurement experimental set up.

The alternatives to cutback are non-destructive methods including the Fabry-Perot, side scatter, and overlap coupling calculation. The side scatter method involves imaging the light scattered out of the waveguide and plotting its intensity versus distance to derive the waveguide attenuation. However for losses below  $\sim 0.3\text{dB/cm}$  in rib waveguides it is very difficult to implement reliably due to signal to noise limitations caused by waveguide inhomogeneities, scattering of uncoupled light off other structures on the chip, and noise in the camera/digitisation.

The Fabry-Perot method depends on measuring the finesse of the cavity formed between the end facets of the waveguide and uses calculation based on the expected mirror reflectivities to extract the propagation loss. The overlap calculation uses measurement of the total insertion loss from which the calculated coupling of the launch/receive beam to the mode at the input/output are subtracted along with the calculated reflective/cavity losses leaving the remainder as the propagation loss. Both of these techniques are dependent on the quality of the cleaving such that the facets behave as a perfect end faces.

Both techniques are convenient and non destructive, but potentially less deterministic than the conventional cutback method. However, the overlap technique usually gives an upper limit on the waveguide propagation loss as the coupling losses are under-estimated because of imperfect cleaving. The facets are often not perpendicular to the waveguide nor perfectly flat. The maximum launch efficiency depends not only on the angle of the cleave to the waveguide but also the launch beam direction relative to the waveguide [354]. Since the cleaving of the fabricated wafers was done by diamond tip scribe, the control of the angle of the end facets is relatively poor. The roughness of the facets also plays an important roles as it determines the reflectivity of the mode [358]. Furthermore, the Fresnel reflectivities are usually

calculated by approximation of the modal fields with planar wave form, which is not the case because of the presence of longitudinal field. The modal reflectivities are different from Fresnel reflectivities [359]. In order to minimize the effects of these variations to the propagation loss measurement it would be desirable to estimate the propagation loss solely based on the properties of the waveguide, independent of the launch conditions. The FP technique offers this advantage over the cutback method, but instead substitutes uncertainty about the quality of the end facet and its precise reflectivity.

### 5.3.2 Fabry-Perot method

The Fabry-Perot method relies on the fact that the waveguide with two reflective ends is a Fabry-Perot cavity. In the ideal case when the end faces are symmetric with no scattering loss and perpendicular to the waveguide, the transmittance  $P_t$  at the output varies periodically with the optical phase difference between the successive waves in the cavity as [360]:

$$\frac{P_t}{P_0} = C \frac{(1-R)^2 \cdot e^{-\alpha L}}{(1-R \cdot e^{-\alpha L})^2 + 4R \cdot e^{-\alpha L} \cdot \sin^2(\beta L)} \quad (5.16)$$

where  $C$  is the coupling efficiency to and from the cavity,  $P_0$  is the incident power,  $\beta$  is the propagation constant in the waveguide,  $\alpha$  is the intensity attenuation coefficient and  $R$  is the facet reflectivity.  $R$  may under some circumstances be approximated using the Fresnel reflectivity for smooth waveguide end facets perpendicular to the waveguides axis, and is expressed as:

$$R = \left( \frac{n_{eff} - n_0}{n_{eff} + n_0} \right)^2 \quad (5.17)$$

where  $n_{eff}$  is the effective refractive index of the waveguide mode,  $n_0$  is the refractive index of the adjacent medium (often air,  $n_0=1$ ).

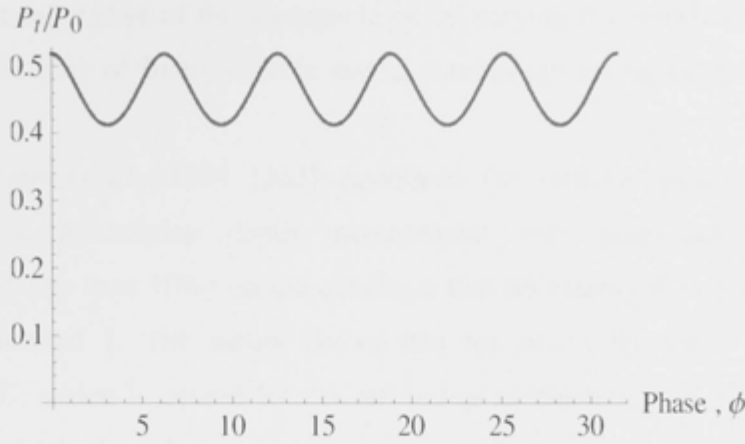


Figure 5.12: A calculated transmittance of a Fabry-Perot cavity with end face reflectivity  $R=0.1$ , length of  $L=5\text{cm}$  and loss of  $\alpha=0.5\text{db/cm}$ .

The loss coefficient is related to the maximum and minimum output intensity as shown on Figure 5.12 and separately corresponding to  $\phi = 2\beta L = 0$  or multiples of  $2\pi$  and  $\phi = \pi$  or  $\pi + n\pi$  by [361]:

$$\frac{P_{\max}}{P_0} = C \frac{(1-R)^2 \cdot e^{-\alpha L}}{(1 - R \cdot e^{-\alpha L})^2} \quad (5.18)$$

$$\frac{P_{\min}}{P_0} = C \frac{(1-R)^2 \cdot e^{-\alpha L}}{(1 + R \cdot e^{-\alpha L})^2} \quad (5.19)$$

Therefore, it can be deduced that

$$r = \left( \frac{1 + R \cdot e^{-\alpha L}}{1 - R \cdot e^{-\alpha L}} \right)^2 \quad (5.20)$$

Or

$$\alpha L = \ln \left( R \frac{\sqrt{r} - 1}{\sqrt{r} + 1} \right) \quad (5.21)$$

where  $r = P_{\max}/P_{\min}$  is the modulation ratio.

From Equation (5.21) above, if the transmitted power has been obtained by experimentally sweeping the waveguide cavity through cycles of  $n2\pi$ , the normalized attenuation  $G = \exp(-\alpha L)$  can be estimated without the knowledge of the coupling efficiency, provided the coupling efficiency does not change during the measurement. The phase difference can be changed by varying the optical path length, for instance, by

changing the temperature of the waveguide or by varying the wavelength of the light. With the availability of finely tunable lasers, wavelength tuning seems to be a better solution.

Tittelbach *et al.*, 1993 [362] calculated the relative mean errors for this technique. The modulation depth measurement only gives acceptable results (uncertainty of less than 10%) on the condition that reflectivity  $R$  is greater than 0.15 and  $\alpha L$  is around 1. The author shows that for  $\alpha L \geq 1$  the error increases with attenuation  $\alpha L$ , which is caused by the increasing modulation ratio  $r$  and decreasing finesse. For  $\alpha L < 1$ , the relative error increases with decreasing attenuation  $\alpha L$  due mainly to the proportionality  $1/\alpha L$  and to the increasing relative errors in the  $P_{min}$ . The maximum facet reflectivity for a tellurite waveguide is around 0.11 and therefore the Fabry-Perot resonance technique is not quite suitable for attenuation measurements. Furthermore, there are some other systematic errors that can lower the measurement accuracy of the attenuation  $\alpha L$ . One problem is the evaluation of the facet reflectivity  $R$  which in reality can be significantly different from the value calculated in Equation (5.17) due to roughness of the end face as well as the off-normal orientation to the waveguide [354, 358, 359].

For the case with a reflectivity of around 0.1 (corresponding to  $n_{eff}=2$  with  $n_o=1$ ), the lowest relative mean error is around  $\pm 12\%$  at  $\alpha L \sim 1$ . This loss corresponds to the value of  $\sim 4\text{dB}$  over the length. For a 5cm long waveguide the propagation loss should be around  $\sim 1\text{dB/cm}$ . For very low loss waveguides such as the ones fabricated in this project, this simple FP method is not a suitable way of measuring propagation loss. Furthermore, optical waveguides often exhibit mode coupling either between the different polarizations or between different mode orders. The FP fringes are generally not of a simple pattern leading to higher uncertainties.

### 5.3.3 Fabry-Perot cutback

The critical effect of the value of reflectivity  $R$  of the end face in FP loss measurement technique can be removed by eliminating it from the calculation by using the FP cutback method. We can obtain the following expression from Equation (5.21):

$$-\ln\left(\frac{\sqrt{r}-1}{\sqrt{r}+1}\right) = \alpha L + \ln\left(\frac{1}{R}\right) \quad (5.22)$$



Therefore, an alternative is to use simple FP measurement with several different lengths of waveguide, ideally all on one chip with common shared cleaved facets so there is no variation in the facet reflectivity with length. By plotting the value  $y = -4.43 \ln[(\sqrt{r} - 1)/(\sqrt{r} + 1)]$  with respect to length  $x=L(\text{cm})$ , one can deduce the loss  $\alpha(\text{dB/cm})$  from the slope of the curve and the reflectivity  $R$  from the intercept  $b$  ( $R = \exp(-b/4.43)$ ) of the curve to  $L=0$ .

### 5.3.4 Conventional average power cutback

As noted above, the basis of the conventional cut back is that only the propagation loss term is varied as the length varies. However in terms of average power transmission, strictly speaking the chip is a Fabry-Perot cavity with loss inside the cavity and therefore the potential for resonant enhancement. The correct way to perform the measurement is to use a broadband source and a detector or a tunable laser swept over many fringes of the cavity with time averaging of the detected signal. Under these circumstances, the propagation loss component should strictly be the integration of function described by Equation (5.16) over a complete cycle of  $n\pi$ . The result of the integration has no simple analytical form. It must be numerically calculated or it can be approximately estimated. The average power can be evaluated by setting the phase to the centre between the minimum and maximum transmission, i.e.  $\phi = \pi/2 + n\pi$  which results in:

$$\frac{P_{\text{average}}}{P_0} \approx C \frac{(1-R)^2 e^{-\alpha L}}{1 + (R \cdot e^{-\alpha L})^2} \quad (5.23)$$

Alternatively, average power transmission can also be approximated as the average of the maximum and the minimum transmission values, i.e.:

$$\frac{P_{\text{average}}}{P_0} \approx C \frac{(1-R)^2 e^{-\alpha L} (1 + (R e^{-\alpha L})^2)}{(1 - (R \cdot e^{-\alpha L})^2)^2} \quad (5.24)$$

Both of the above equations can be further reduced if  $(R \cdot e^{-\alpha L})^2$  is considered to be negligible compared to 1. This is usually the case as  $R \sim 0.1$  and  $e^{-\alpha L} < 1$ . Under this condition:

$$\frac{P_{\text{average}}}{P_0} \approx C(1-R)^2 e^{-\alpha L} \quad (5.25)$$

Physically speaking, this is simply the transmission formula taking into account the coupling efficiency to and from the waveguide, transmission of the two facets and the propagation loss.

### 5.3.5 Experiment

#### *a) Direct estimation of very low propagation loss waveguide*

A simple approach to estimate the propagation loss is to measure the total insertion loss and subtract the theoretical estimation of all other losses such as mode coupling and reflectivity. The Equation (5.25) is the basis of this technique. This technique is still dependent on the end facet quality, the accuracy of the alignment, and the accuracy of the modelling used to determine the mode mismatch loss. However, this technique has the valuable advantage of being non-destructive and provides an upper limit of the waveguide propagation losses since most errors will cause the coupling losses to be under-estimated.

The measurement of the loss can be done by single laser or a broadband source such as the set up in Figure 5.11. Wideband measurements were made using a fibre coupled Mercury arc lamp and optical spectrum analyser operated with a 10nm resolution bandwidth to smooth out the chip Fabry-Perot resonances. Figure 5.13 shows the insertion loss data after normalization through the fibre tapered lens for a typical 4 $\mu$ m wide waveguide of 7.8cm length from 1000-1700nm measured with the arc lamp source. Normalization spectra were recorded before and after the measurement to eliminate source drift, and there was a measurement uncertainty of about 0.2dB from fibre connector insertion repeatability induced during the alignment procedures. The minimum observed insertion loss in Figure 5.13 was 2.8dB at 1400nm including all coupling, overlap, and reflective losses, and the insertion loss at 1550nm was 3.5dB. The laser based measurement verified that from the OSA at 1550nm to within 0.05dB.

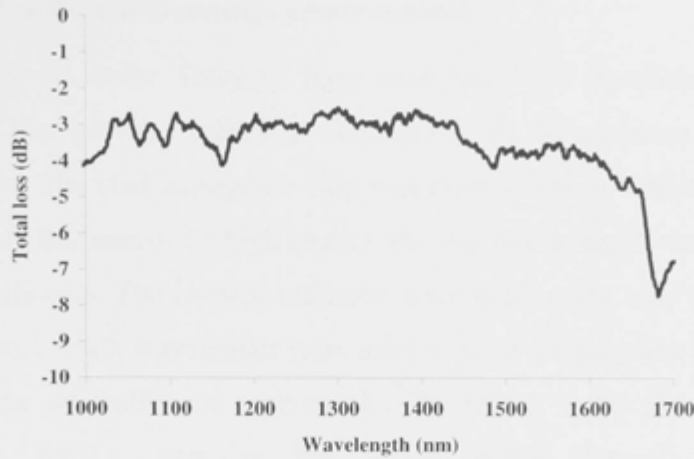


Figure 5.13: Broadband total insertion loss of a 4μm waveguide from chip TeO<sub>2</sub>\_12.

The non flat nature of the response is believed to be attributable to mode coupling and beating phenomena which generate wavelength dependent coupling effects as the waveguides support 3 modes at 1550nm (more at shorter wavelengths) and the input fibres become multimode below ~1250nm. Also clear from Figure 5.13 are that there are some absorption dips in the spectrum; one centred at 1166nm, one band from 1450nm to about 1610nm, and one strong dip centred at 1680nm. The 1680nm dip is related to strong C-H overtone absorption in the top IPG cladding of the waveguide, and the other two bands likely result from OH absorption in the tellurite film (further details will be discussed in Chapter 6).

The modal calculations give the Gaussian to waveguide mode coupling of 0.7dB at each end (Table 5.1). The reflectivity  $R$  is estimated to be 0.11 or a loss of 0.5dB at each facet. Therefore, the total loss due to the coupling efficiencies and reflectivities is 2.4dB. This means that at the best point on the spectrum on Figure 5.13, the attenuation is ~0.05dB/cm around 1.4μm. At 1550nm, the loss is ~0.15dB/cm. The values reported here are more than an order of magnitude better than the best previously reported results [78] and a two order of magnitude improvement over the best prior plasma etched waveguides [257]. The connector induced measurement uncertainty is of the same order as the total measured propagation losses and therefore prevents the derivation of an accurate loss figure, but it is clear that the losses are very low indeed.

*b) Fabry-Perot cutback and average power cutback.*

The waveguides of wafer TeO<sub>2</sub>\_12 have very low loss, therefore, the normal FP technique did not provide sufficient attenuation for an accurate measurement as discussed above. The clad waveguide chip was cleaved into a 7.5cm long piece and a 3mm long piece. Because of its high quality, the maximum length was being preserved for future experiments. The cutback estimates were made using only these two lengths. The 4μm nominal width waveguides were used to study propagation loss. Figure 5.14a and b proves the difficulties of applying the FP cutback to the loss measurement. In these graphs, the x axis is the length while the y axis is valued as  $y = -4.43 \ln[(\sqrt{r} - 1)/(\sqrt{r} + 1)]$ , and  $r = P_{\max}/P_{\min}$  is the fringe modulation. Clearly, the graphs a) and b) on Figure 5.14 are unphysical as the attenuation in a passive waveguide can not have a negative value. On the other hand, the conventional cutback method gives a loss of 0.25dB/cm for the TE and 0.24dB/cm for the TM at 1550nm compared to the 0.15dB/cm estimate from the transmission loss. The reasons for the difference in loss cannot easily be quantified without destroying the existing chip, and this was not desirable as it was required for further experimentation.

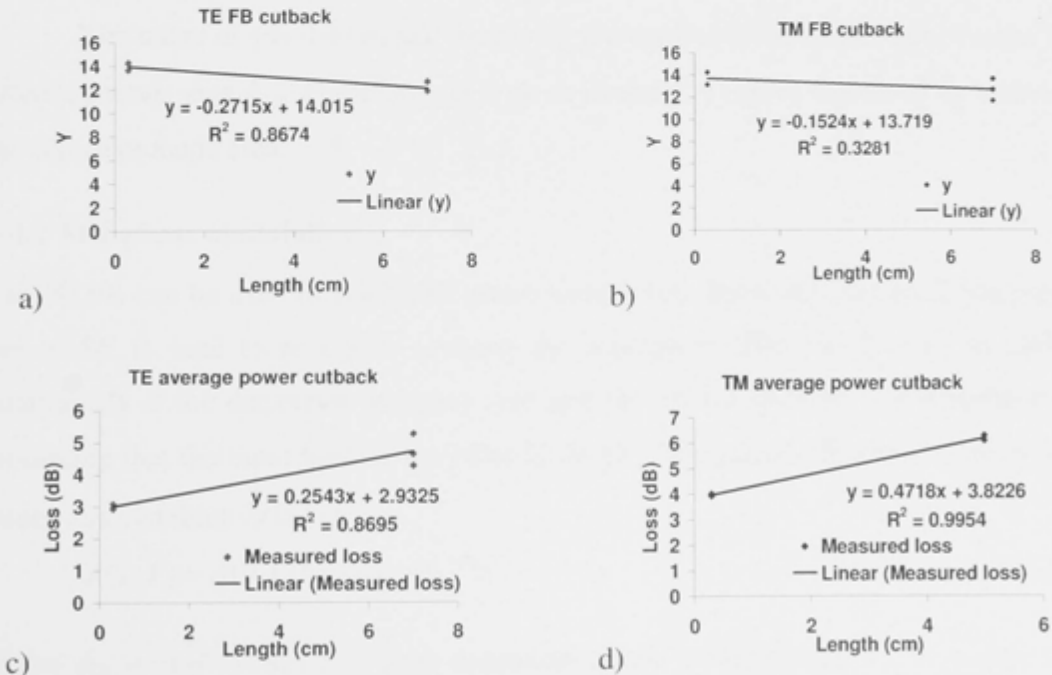


Figure 5.14: a) and b) are the TE and TM FP cut back and c) and d) are the TE and TM average power cut back for 4μm waveguide from wafer coded TeO<sub>2</sub>\_12

## 5.4 Self phase modulation

### 5.4.1 Principle: nonlinear Schrodinger equation

The study of nonlinear effects in planar optical waveguides usually involves short pulses with pulse widths often substantially below  $\sim 10$ ps. At such levels, both dispersive and nonlinear effects influence the pulse shape and spectrum. Pulse propagation inside the waveguide is governed by the Nonlinear Schrodinger Equation (NLSE) [137]:

$$i\frac{\partial A}{\partial z} + i\frac{\alpha}{2}A - \frac{\beta_2}{2}\frac{\partial^2 A}{\partial T^2} + i\frac{\beta_3}{6}\frac{\partial^3 A}{\partial T^3} + \gamma|A|^2 A = 0 \quad (5.26)$$

where  $A$  is the slowly varying amplitude of the pulse envelope,  $\alpha$  is the linear attenuation coefficient of the material,  $\beta_2$  is the group velocity dispersion (GVD) parameter,  $\beta_3$  is the third order dispersion (TOD) parameter,  $T$  is time measured in the moving frame at group velocity  $v_g$ ,  $T = t - z/v_g = t - \beta_1 z$  and  $\gamma$  is the nonlinear parameter as defined by:

$$\gamma = \frac{n_2 \omega_0}{c A_{eff}} \quad (5.27)$$

The value of  $\gamma$  is determined mainly by the nonlinear refractive index  $n_2$  and the effective mode area  $A_{eff}$ . Therefore, for a given material,  $\gamma$  can be increased by reducing the effective mode area.

### 5.4.2 Self-phase modulation

The NLSE can be used to study self-phase modulation. By setting up an initial pulse, the NLSE is used to propagate it along the waveguide. The NLSE may be solved analytically if the dispersion is set to zero and the effects of SPM can be estimated. Assuming that the input field of the pulse is  $A(0, T)$ , the general solution of the NSLE under this condition is [137]:

$$A(L, T) = A(0, T) \exp[i\phi_{NL}(L, T)] \quad (5.28)$$

where  $\phi_{NL} = -(\frac{L_{eff}}{L_{NL}})|A(0, T)|^2$ , the nonlinear length is defined as  $L_{NL} = \frac{1}{\gamma P_0}$  and the

effective length is  $L_{eff} = \frac{1 - \exp(-\alpha L)}{\alpha}$ ,  $L$  is the actual device length.

The maximum temporal phase shift of a signal pulse propagating through the waveguide due to SPM is [137]:

$$\phi_{\max} = \frac{n_2 \omega_0 L_{\text{eff}} P_0}{c A_{\text{eff}}} = \gamma P L_{\text{eff}} \quad (5.29)$$

It can be understood that a temporally varying phase implies an instantaneous optical frequency difference across the pulse from its central value  $\omega_0$ . This is given by [137]:

$$\delta\omega(T) = -\frac{\partial\phi_{\text{NL}}}{\partial T} = -\left(\frac{L_{\text{eff}}}{L_{\text{NL}}}\right) \frac{\partial}{\partial T} |A(0, T)|^2 \quad (5.30)$$

The time dependence of  $\Delta\omega$  is referred to as frequency chirping. The chirp induced by SPM increases in magnitude with the propagating distance. New frequency components are generated continuously as the pulse propagates down the waveguide. This leads to a spectral broadening effect.

In general, the spectrum depends not only on the pulse shape but also on the initial phase of the spectrum. The actual shape of the pulse spectrum  $S(\omega)$  is obtained by taking the Fourier transform of Equation (5.28):

$$A(\omega) = \left| \int_{-\infty}^{\infty} A(0, T) \exp[i\phi_{\text{NL}}(L, T) + i(\omega - \omega_0)T] dT \right|^2 \quad (5.31)$$

The Figure 5.15 shows examples of an unchirped Gaussian pulse at the input and the broadened output pulse at various values of phase shift due to SPM. In general, for nonlinear phase shifts exceeding  $\pi$  the output spectrum is split into multiple peaks. This approximation is only accurate for the simple case with no dispersion. When the dispersion is included, this simple analysis is invalid. Therefore, numerical methods are usually utilised.

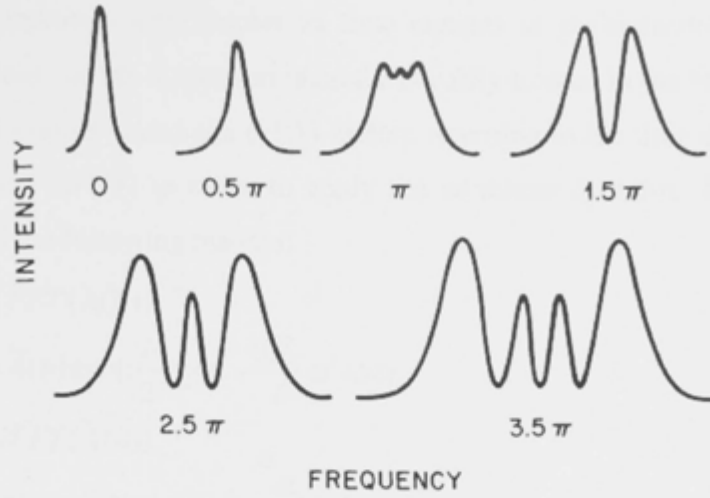


Figure 5.15: Example of SPM broadened spectra of an unchirped Gaussian pulse in nonlinear medium at various maximum nonlinear phase shift [137].

#### 5.4.3 Numerical method: split-step Fourier propagation

Except in certain special cases eg. solitons, the complete NLSE does not have analytic solutions and numerical methods are used to propagate an initial pulse. A common technique used is the split-step Fourier (SSF) method [137, 363]. To understand the method, we can write the propagation equation for the pulse envelope,  $A(z, T)$ , in term of operators as:

$$\frac{\partial A}{\partial z} = (\hat{N} + \hat{D})A \quad (5.32)$$

where  $\hat{N}$  is the nonlinear operator, and  $\hat{D}$  is dispersion operator:

$$\hat{N} = i\gamma |A|^2 - \frac{\alpha}{2} \quad (5.33)$$

$$\hat{D} = -\frac{i\beta_2}{2} \frac{\partial^2}{\partial T^2} + \frac{\beta_3}{6} \frac{\partial^3}{\partial T^3} \quad (5.34)$$

As written  $\hat{N}$  includes only the SPM nonlinear term and a loss term, but higher order nonlinear terms can be included if necessary to represent other effects. By assuming that nonlinearity and dispersion act approximately independently over a small propagation distance  $\Delta z$ , the split-step Fourier method applies the two operators sequentially:

$$A(z + \Delta z, T) = \exp(\Delta z \hat{N}) \exp(\Delta z \hat{D}) A(z, T) \quad (5.35)$$



The differential with respect to time equates to multiplication by  $i\omega$  in the frequency domain, so the dispersion operator is easily treated in the frequency domain by using a fast Fourier transform (FFT), before returning to the time domain using the inverse transform (IFFT) in order to apply the nonlinear operator. The procedure is implemented in the following manner:

$$\begin{aligned}
 \tilde{A}(v) &= FFT\{A(T)\} \\
 \tilde{A}(v) &= \tilde{A}(v) \exp\left[\left(\frac{i}{2}\beta_2\omega^2 - \frac{i\beta_3}{6}\omega^3\right)\Delta z\right] \\
 A(t) &= IFFT\{\tilde{A}(v)\} \\
 A(t) &= A(t) \exp\left[(i\gamma|A(t)|^2 - \frac{\alpha}{2})\Delta z\right] \\
 \text{Repeat until } \sum \Delta z &= L
 \end{aligned} \tag{5.36}$$

This method is accurate to second order in step size and unconditionally stable [363]. Therefore, the accuracy of the simulation only depends on the step length. It is necessary to repeat the calculation by reducing the step size to ensure the accuracy of numerical solution. The time window needs to be wide enough, typically about 10-20 times the pulse width, to ensure that the pulse energy remains confined within the window.

#### 5.4.4 Experiment and results

To characterize the nonlinear properties of the waveguides we observed the nonlinear spectral broadening of pulses propagating through low loss 3 $\mu$ m wide waveguides of chip TeO<sub>2</sub>-12. The GVD was calculated to be 30ps/km.nm for the TM0 mode based on the measured film refractive index dispersion and the effective mode area was 3.48 $\mu$ m<sup>2</sup>. Pulses of ~1ps duration at a 10 MHz repetition rate were generated using a passively mode-locked fibre laser and launched into a fibre tapered lens pigtail 1m long containing a coiled loop polarisation controller as in Figure 5.16. The input power to the waveguide was varied by backing the launch fibre away from optimum focus, and the polarisation controller was used to set the input to the desired polarisation mode in conjunction with an imaging system with a bulk polariser inserted in the parallel beam path part of the microscope.

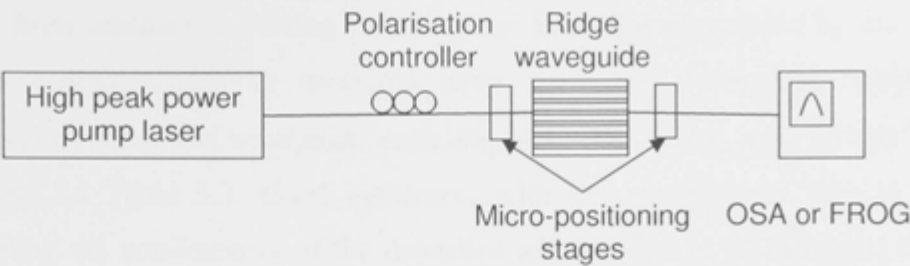


Figure 5.16: SPM setup using an high peak power pump laser and an OSA and a FROG to characterized the input and output pulse.

The pulse exiting the launch fibre tapered lens was characterized by Frequency Resolved Optical Gating-FROG (Southern Photonics model HR150) with the waveguide chip removed and the receiving lens backed away to reduce the collected power ~20dB thereby avoiding nonlinear effects beyond the tip of the launch fibre. This showed that the input pulse had been compressed to ~660fs in the launch pigtail. For an average power of 1.8mW of laser output, the power at the beginning of the waveguide corresponds to 0.9mW or a peak power of 110W. There is a total of 3dB (1.5dB due to fibre lens and connectors and 1.5dB due coupling and facet reflectivities) loss from the laser to the mode of the waveguide.

Table 5.3: Waveguide parameters for SPM simulation

Parameters	Value
Waveguide length (L)	0.07m
Input peak power ( $P_0$ )	110W
Mode area ( $A_{eff}$ )	$3.5 \times 10^{-12} m^2$
Propagation loss ( $\alpha$ )	0.2dB/cm
Nonlinear refractive index ( $n_2$ )	$65 \times 10^{-20} m^2 W^{-1}$
Nonlinear parameter ( $\gamma$ )	$0.6 W^{-1} m^{-1}$
GVD parameter ( $\beta_2$ )	$2 \times 10^{-26} s^2 m^{-1}$
TOD parameter ( $\beta_3$ )	$5 \times 10^{-40} s^3 m^{-1}$

Figure 5.17 shows the experimentally observed self phase modulation (SPM) spectral broadening of the pulses resulting in 3 spectral lobes. No nonlinear absorption (i.e. two photon absorption) was observed. Agreement with the measured spectrum from the recovered FROG spectrum was good. Also plotted in Figure 5.18 are the

results from simulations solving the nonlinear Schrödinger equation by the split-step Fourier method using the measured input pulse and parameters based on the experimental setup and waveguide modelling described above, with  $65 \times 10^{-20} \text{ m}^2 \text{ W}^{-1}$  as shown in Table 5.3. Good agreement with the experimental data is obtained confirming the non-linearity of the deposited tellurite film at an estimated 25x silica [137] and that the  $\text{TeO}_2$  displays a very fast nonlinearity.

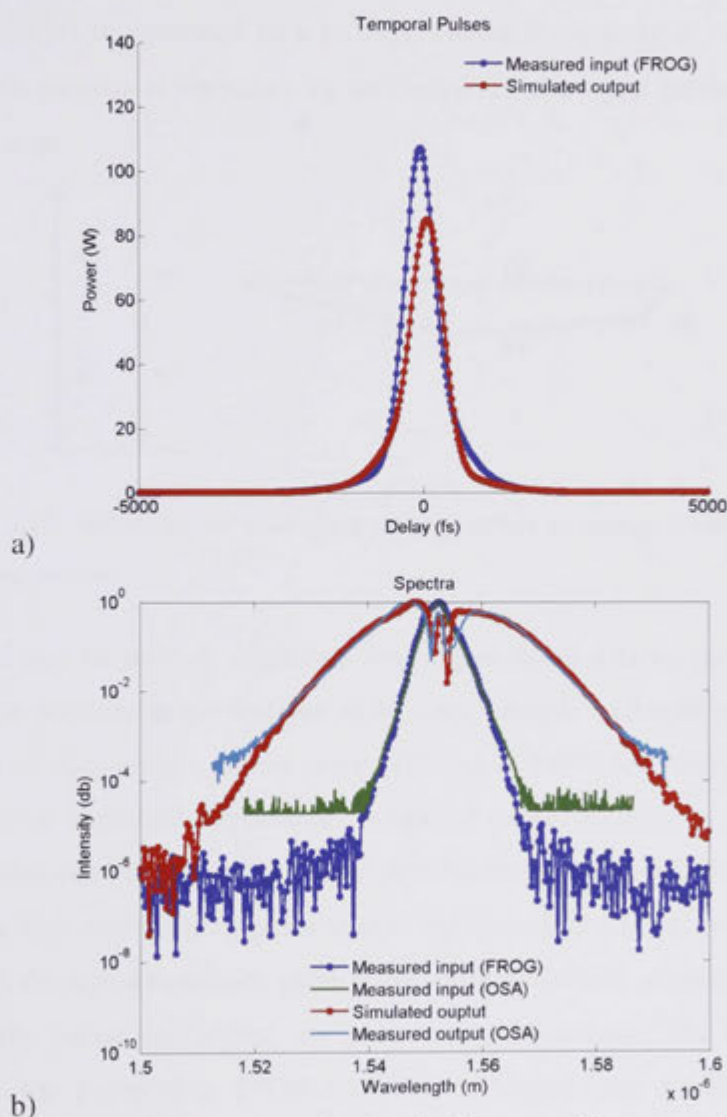


Figure 5.17. Spectral broadening of pulses inside waveguide compared with results from Split Step Fourier modeling of waveguide with measured input pulse with  $n_2$  varied to obtain best fit a) temporal pulses and b) spectra

### 5.5 Four-wave mixing: ultra-fast wavelength conversion

Four-wave mixing (FWM) is a nonlinear phase matching process resulting from the third order susceptibility. As the name indicates, the process may involve four different photons. This interaction would involve four coupled partial differential equations [137]. However, in practice, the FWM phenomena are commonly used as a wavelength conversion process with only two input sources: one as pump and one as signal. A third wavelength (idler) is generated in a process similar to parametric conversion (Figure 5.18). The two photons at frequency  $\omega_p$  are converted to a signal photon at frequency  $\omega_s$  and an idler at  $\omega_i$ .

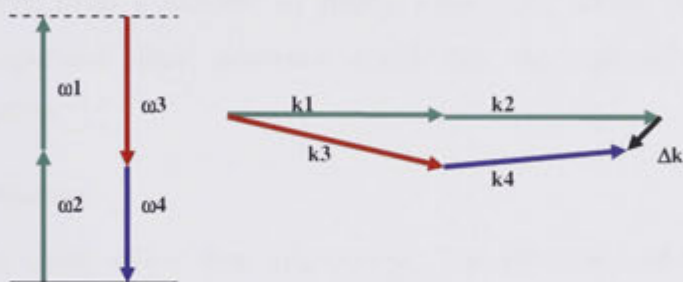


Figure 5.18: Schematic of four wave mixing effect a) energy transfer b) phase matching process

FWM can be used to amplify a low signal using a large pump at a different wavelength in parametric applications or as a wavelength converter when the signal is converted to an idler using a strong pump. The use of FWM for wavelength conversion has a number of important applications in optical communication systems. It has been used in ultrafast demultiplexing in an optical time-division-multiplexed system (OTDM) [53, 54]. If a high power pump pulse train at the base data rate is injected together and in phase with the signal multiplex pulse train, the idler wave is generated through FWM only when the pump and signal are present simultaneously. The idler is therefore generated at the pump rate. FWM transfers the signal data to the idler at a new wavelength with perfect fidelity. Recently, with the development of highly nonlinear waveguides such as in chalcogenide [53], error-free OTDM at 640GB/s has been demonstrated [54].

Another interesting feature of the idler wave is that it is the complex conjugate of the signal field [137]. Therefore, FWM process is also referred to as phase

conjugation. It is an important technique in dispersion and optical nonlinearity compensation in optical communication systems [364]. It can be used in a number of other areas such measurement of the phase of optical signal without homodyne or heterodyne detection [365], all-optical storage of picosecond pulse packets [366], suppressing frequency shifts of solitons [367] and reducing the timing jitters by amplifiers and soliton collisions [368].

FWM can also be used to determine the dispersion and the nonlinearity of waveguide structure or fibre [369]. As the gain spectra of the FWM conversion strongly depend on the dispersion and nonlinearity, the experimental data can be used to fit a calculated curve from a number of fitting parameters. Those parameters, such as dispersion, dispersion slope, nonlinear coefficient, are captured in a single FWM conversion spectra.

### 5.5.1 Basic theory

Energy conservation infers that  $2\omega_p = \omega_s + \omega_i$ . The efficiency of the FWM process depends strongly on how well the phase matching condition is satisfied [137] ie:

$$\Delta k = 2k_p - k_s - k_i = (2n_p\omega_p - n_s\omega_s - n_i\omega_i) = 0 \quad (5.37)$$

where  $\Delta k$  is the phase mismatch due to linear dispersion and  $n_p$ ,  $n_s$  and  $n_i$  are the effective indices of the waveguide modes at pump, signal and idler wavelength. FWM efficiency depends critically on the phase mismatch between the pump, signal and idler waves.

A complete description of parametric amplification often requires numerical solution of coupled partial differential equations. However, considerable understanding of the physics is gained with approximations if the pump waves are assumed to be intense compared to the signal or idler waves and remain undepleted during the parametric interaction. Furthermore, the overlaps between the waves are assumed to be complete because they are very close in wavelength. The signal and idler at the output at  $z=L$  is under these conditions given by [137, 370, 371]:

$$\begin{aligned} P_s(L) &= P_s(0)[1 + (1 + \kappa^2/(4g^2))\sinh^2(gL)] \\ P_i(L) &= P_s(0)(1 + \kappa^2/(4g^2))\sinh^2(gL) \end{aligned} \quad (5.38)$$

where the parametric gain  $g$  is given by:

$$g = \sqrt{(\gamma P_p)^2 - (\kappa/2)^2} \quad (5.39)$$

$$\kappa = \Delta k + 2\gamma P_p$$

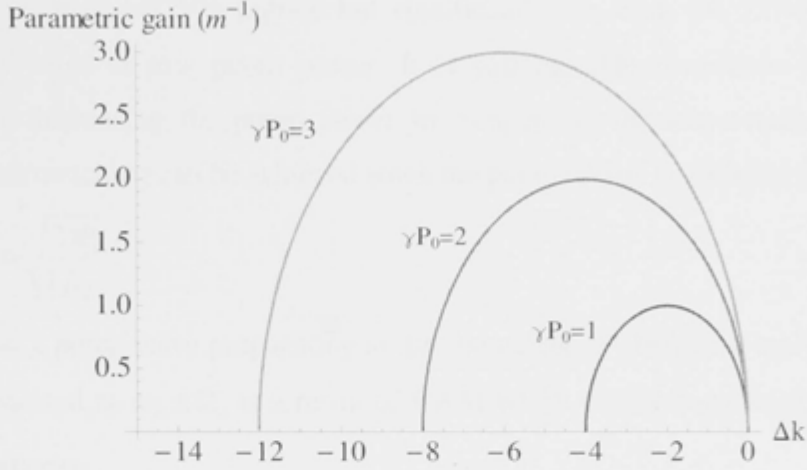


Figure 5.19: Parametric gain at various values of  $\gamma P_p$  against the wave-vector phase mismatch value

Figure 5.19 shows the dependence of  $g$  with  $\Delta k$  for various values of  $\gamma P_p$  for the parametric gain. From gain expression 5.39, the maximum gain  $g = \gamma P_p$  occurs at  $\kappa=0$  or at  $\Delta k = -2\gamma P_p$ . The range in which the gain exists is given by  $0 > \Delta k > -4\gamma P_p$ . The shift of the gain peak from  $\Delta k = 0$  is due to the contribution of self-phase modulation and cross-phase modulation to the phase mismatch.

In order to maximize the FWM gain  $g$ , the phase matching condition must be satisfied. There are a number of methods to make  $\kappa=0$ . Because  $\kappa = \Delta k + 2\gamma P_p$  for  $\kappa$  to be zero,  $\Delta k$  must be negative. Because  $\Delta k = (2n_p\omega_p - n_s\omega_s - n_i\omega_i)$  and  $\beta_j = n_j\omega_j/c$  ( $j=p, s$  or  $i$ ), the difference in wavevector  $\Delta k$  can be approximated to [53, 372]:

$$\Delta k \approx \beta_2 \Omega_s^2 \quad (5.40)$$

where  $\Omega_s$  is the frequency shift,  $\omega_p - \omega_s = \omega_i - \omega_p$ ,  $\beta_2$  is the GVD coefficient at the pump frequency. This equation is valid if the pump wavelength is not too close to the zero dispersion wavelength  $\lambda_D$  of the waveguide. In waveguide structures, it is possible to design waveguides so that the pump wavelength is in the anomalous region ( $\beta_2 < 0$ ) close to the ZDWL in order to have a perfect phase matching condition.



However, if perfect phase matching is not satisfied, as long as  $0 > \Delta k > -4\mathcal{P}_p$ , there is still parametric gain as shown in Figure 5.19. Also, when the pump wavelength lies in the anomalous-GVD regime but significantly far from the ZDWL  $\lambda_D$ ,  $\Delta k$  is significantly large at low pump power. It is still possible to achieve better phase matching by increasing the pump power to compensate the wave-vector mismatch. Perfect phase matching can be achieved when the pump power  $P_0$  satisfies the equation:

$$\Omega_s = \sqrt{\frac{2\mathcal{P}_0}{|\beta_2|}} \quad (5.41)$$

Thus, a pump wave propagating in the anomalous-GVD regime can still develop sidebands located at  $\omega_p \pm \Omega_s$  as a result of FWM which is phase-matched by the SPM nonlinear process.

#### a) Parametric amplifier

The parametric amplification is driven by the gain factor derived from Equation (5.38). The amplification gain factor can be written as [137, 370, 371]:

$$G_p = P_s(L) / P_s(0) = (1 + (\mathcal{P}_0 / g)^2) \sinh^2(gL) \quad (5.42)$$

If the phase mismatch is relatively large, then in the limit of  $\kappa \gg \mathcal{P}_0$ , the gain factor becomes:

$$G_p = (1 + (\mathcal{P}_0 L / g)^2) \sin^2(\kappa L / 2) / (\kappa L / 2)^2 \quad (5.43)$$

The parametric gain is relatively small, and increases with pump power as  $P_0^2$ . However, if the phase matching is perfect  $\kappa = 0$  and  $gL \gg 1$ , the amplification increases exponentially with  $P_0$  as:

$$G_p \approx \frac{1}{4} \exp(2\mathcal{P}_0 L) \quad (5.44)$$

#### b) Wavelength conversion

Parametric amplifiers can be useful for signal amplification but in addition, these amplifiers also generate an idler wave at frequency  $\omega_i = 2\omega_p - \omega_s$ , where  $\omega_p$  and  $\omega_s$  are the pump and signal frequencies. Thus they can also be used for wavelength conversion with or without phase conjugation depending on the pumping configuration [137].



Equation (5.38) measures the conversion efficiency in the following alternative form [53, 137, 372]:

$$\eta_c = P_i(L) / P_s(0) = (\gamma P_p L)^2 [\sin(gL) / gL]^2 \quad (5.45)$$

where  $g = \sqrt{\frac{1}{4} \Delta\beta(\Delta\beta + 4\gamma P_p)}$  with  $\Delta\beta = \beta_2 / \Omega_s^2 = \frac{2\pi |D| \Delta\lambda^2}{\lambda_p^2}$

All of the gains above are approximations for the case of a lossless waveguide, when the attenuation loss is taken into account, the gains should be reduced due to loss of pump power at the end of the propagation length. The conversion efficiency and gains become [53, 372]:

$$\eta_c = P_i(L) / P_s(0) = (\gamma P_p L)^2 \exp(-3\alpha L) [\sin(gL) / gL]^2 \quad (5.46)$$

where  $g = \sqrt{\frac{1}{4} \Delta\beta(\Delta\beta + 4\gamma P_p e^{-\alpha L})}$  with  $\Delta\beta = \beta_2 / \Omega_s^2 = \frac{2\pi |D| \Delta\lambda^2}{\lambda_p^2}$

Figure 5.20 plots conversion gain at 1540nm pumped at 1550nm for a typical case of a TeO<sub>2</sub> waveguide with  $D=-8\text{ps/km/nm}$ ,  $P=50\text{W}$ ,  $\alpha=0.2\text{dB/cm}$ ,  $\gamma=0.6\text{W}^{-1}\text{m}^{-1}$ , figures that represent the performance of the low loss waveguides demonstrated earlier. The gain increases rapidly with length at the beginning of the waveguide then reaches a saturation level. It clearly indicates that, the maximum available conversion gain of 2dB can be obtained with a waveguide length of about 8cm.

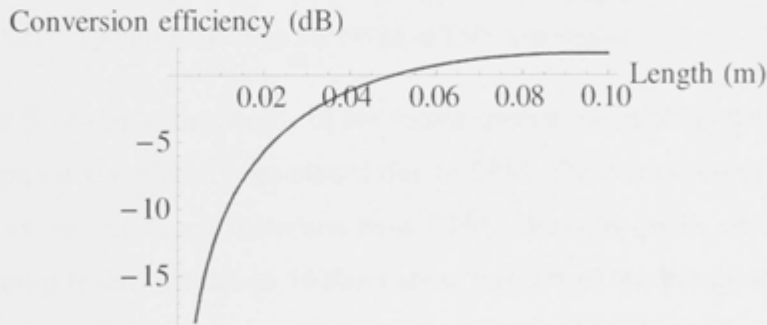


Figure 5.20: Calculation of conversion gain pumped at 1550nm, seed at 1540nm vs length with  $D=-8\text{ps/km/nm}$ ,  $P=50\text{W}$ ,  $\alpha=0.2\text{dB/cm}$ ,  $\gamma=0.6\text{W}^{-1}\text{m}^{-1}$ .

### 5.5.2 Experimental results

The experimental set up to measure FWM in TeO<sub>2</sub> waveguide is shown in Figure 5.21. Here, a 3µm nominal width waveguide of the TeO<sub>2</sub>\_12 wafer was used due to its low loss and because its TM<sub>0</sub> ZDWL was simulated to be at 1575nm which was close to 1550nm. The GVD at 1553nm is  $D=-8\text{ps/km/nm}$ . The waveguide length was 7.7cm with loss of  $\sim 0.2\text{dB/cm}$ . The dispersion slope was  $dD/d\lambda = 0.34\text{ps/km/nm/nm}$ . A high peak power pump (Pritel Er doped mode-locked fibre laser) was set up to produce: 1ps pulse width, 10MHz repetition rate, average power of 1mW, centre wavelength at 1553nm. A 10/90 combiner was used to couple the high peak pump and tunable laser (Photonics Tunics Purity tunable external cavity laser) set at 1mW. The tunable laser has an ASE suppression filter to attain very high side mode suppression ratios  $>70\text{dB}$ . Two polarisation controllers were used to independently adjust the polarisation of pump and signal to achieve TM for both. The spectra at output of the waveguide were captured by an OSA and results analysed. The pump laser was kept fixed while the wavelength of the tunable laser was tuned in range from 1490nm to 1530nm.

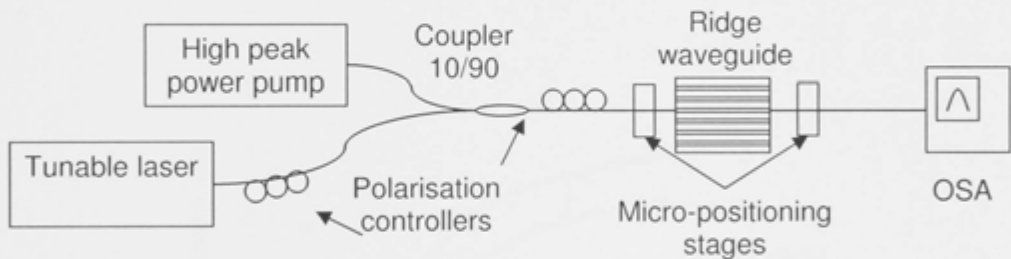


Figure 5.21: Experimental set up for FWM in TeO<sub>2</sub> waveguide

Figure 5.22 shows the results of the output spectra recorded by the OSA. Clearly, the 1550nm pump was slightly broadened due to SPM. The pump power was kept at a low level to avoid significant distortion from SPM. The idler peaks on the right hand side of the pump from 1580nm to 1610nm show transfer of the pump modulation and some spectral dependence. Figure 5.23 shows the measured FWM conversion efficiency defined as the integral of the idler power divided by the signal power taking into account the pump duty cycle of 1ps with the repetition rate 10MHz. So the CW signal is only  $10^{-5}$  of the total signal. It is clear from the FWM efficiency curve that there is good conversion over a band of at least 30nm. Figure 5.23 also plots the calculated FWM efficiency as a function of signal wavelength with  $D=-8\text{ps/km/nm}$ ,  $dD/d\lambda = 0.34$

ps/km/nm/nm,  $P=50\text{W}$ ,  $\alpha=0.2\text{dB/cm}$  and  $\gamma=0.6\text{W}^{-1}\text{m}^{-1}$ . The difference between the measured and calculated conversion gains is within 5dB. There are a number of possible causes for this discrepancy such as the phase matching condition, peak pulse power deterioration due to SPM and incorrect values of powers, dispersions and the nonlinear coefficient. Also, there is variation of the waveguide dimension along the length of the waveguide due to deposition and etching conditions. This leads to variable dispersion. Furthermore, the pump is pulsed; the model works best for CW case.

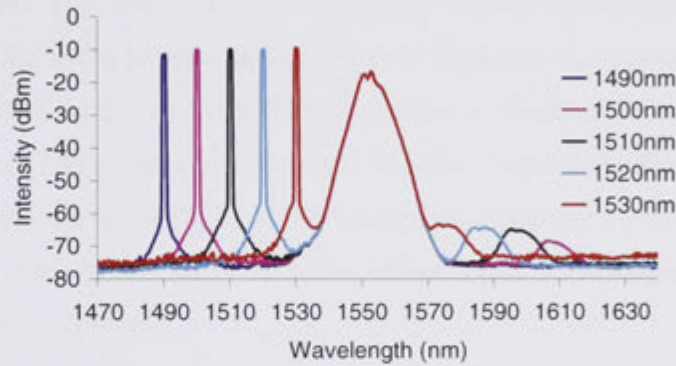


Figure 5.22: The optical spectra for various CW probe signal wavelengths

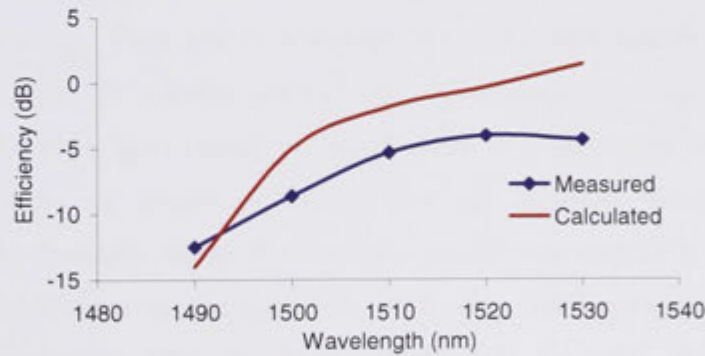


Figure 5.23: Measured and calculated FWM efficiency as a function of signal wavelength.

The amplitude of FWM efficiency reported here is comparable with the value reported by Galili *et al.*, 2008 [54] in the  $\text{As}_2\text{S}_3$  waveguide used in 640Gbit/s demultiplexing despite the fact that the nonlinear parameter in the  $\text{As}_2\text{S}_3$  case was an order of magnitude higher than the waveguide used here. The lower nonlinearity is compensated by higher peak power used in the pump ( $\sim 50\text{W}$  here compared to  $\sim 17\text{W}$ ).

However, the gain spectrum width is much higher in this situation due to the very low dispersion of the TeO<sub>2</sub> waveguide used.

Recent work on FWM in microstructured fibres suggests that it is possible to increase the gain further by using the tapering method [187]. As demonstrated in fibre by tapering the fibre from 4.2  $\mu\text{m}$  diameter to 1.2  $\mu\text{m}$  along the propagation direction, there is a continuous change of the zero-dispersion wavelength that enables the phase matching condition of FWM or the generation of dispersive waves for a wide range of wavelength. The nonlinear behaviour of the tellurite waveguides modelled here is very similar as the width is reduced from 4  $\mu\text{m}$  to 1  $\mu\text{m}$  but the dispersion of the TM<sub>0</sub> mode make a gradual transit of the ZDWL therefore, it should behave in very similar manner as in tapered fibre and enable the same benefits. Tapering in waveguides can be achieved by varying the dimensions of the waveguide gradually along the waveguide. The waveguide width can be varied via mask design while the thickness can be varied via thin film deposition process.

## 5.6 Conclusion

The results in this chapter demonstrate a significant advance in tellurite planar waveguide technology. Very low loss waveguides were fabricated from reactive RF sputtering TeO<sub>2</sub> films by reactive ion etching with CH<sub>4</sub>/H<sub>2</sub>/Ar plasma. The obtained TeO<sub>2</sub> waveguides have been optically characterised. A propagation loss of less than 0.1 dB/cm, an order of magnitude better than any reported values for tellurite waveguides in the literature, has been achieved in small mode area TeO<sub>2</sub> rib waveguides. The nonlinear coefficient of the sputtered TeO<sub>2</sub> was characterised by a self-phase modulation experiment. The nonlinear coefficient  $n_2$  was measured to be  $65 \times 10^{-20} \text{ m}^2 \text{ W}^{-1}$ , 30 times that of silica. Four-wave mixing experiments were also conducted on the low loss and low dispersion waveguides. Significant signal conversion was achieved with large bandwidth. This chapter confirms the excellent potential of tellurite glasses and the capability of plasma etching approach to waveguide fabrication in these glasses.

## **Chapter 6:**

### ***Erbium doped Tellurium oxide films***

This chapter will investigate Erbium doped co-sputtered Tellurium Oxide films. The films are fabricated by reactive radio-frequency magnetron sputtering. Erbium is incorporated directly into the films by co-sputtering of an Erbium metal target on a separate gun. Fabrication, characterisation processes, and properties of Erbium doped thin films are described in detail. The main goal is the fabrication and measurement of films with long excited state lifetimes. The lifetime of 1.5 $\mu$ m radiation was found to depend on the Erbium concentration, Oxygen content of the film and the OH contamination.

#### ***6.1 Properties of rare earth doped glasses***

##### **6.1.1 Rare earth ions in crystalline solid or glass hosts**

The rare earths, also referred to as the Lanthanides, consist of the series of elements in the sixth row of the periodic table stretching from Lanthanum to Ytterbium. They have a partially filled 4f shell which is shielded from external fields by 5s<sup>2</sup> and 5p<sup>6</sup> electrons, therefore, their energy levels are relatively insensitive to the host environment. They exist as 3<sup>+</sup> or sometimes 2<sup>+</sup> valency ions in crystalline or amorphous hosts. As a result of shielding of the 4f electrons, the rare earth energy levels are influenced much more by spin-orbit interactions than by the applied crystal field. The intra-4f transitions are parity forbidden and are made partially allowed by crystal field interactions. Luminescence lifetimes are often long (in the millisecond range) and narrow linewidths are possible in crystal hosts. Figure 6.1 shows the effect of spin-orbit and crystal field interactions on the energy levels of Erbium ions in a solid host [188].

The standard notation for the quantum levels of an element is <sup>2S+1</sup>L<sub>J</sub>, where L is the overall angular momentum number, S is the overall spin and J is the total angular moment. For an isolated atom, the states with the same total angular momentum have the same energy. However, this degeneracy is no longer valid when ions are close to other ions or are placed in glass or crystalline hosts due to the Stark splitting effect

resulting from the electric field of the local environment. Although shielding of the 4f shells means that the rare earth ion energy levels are largely independent of host, Stark splitting broadens the levels as the result of the applied crystal field. The energy level is divided into  $J+1/2$  sublevels of slightly different energy. However, these levels may only be resolved in low temperature measurement of the emission spectra of crystalline hosts; at room temperature the Stark levels broaden and overlap to produce an inhomogeneously broadened emission band. For Erbium, the ground state is split into 8 levels and the first excited state is split into 7 levels.

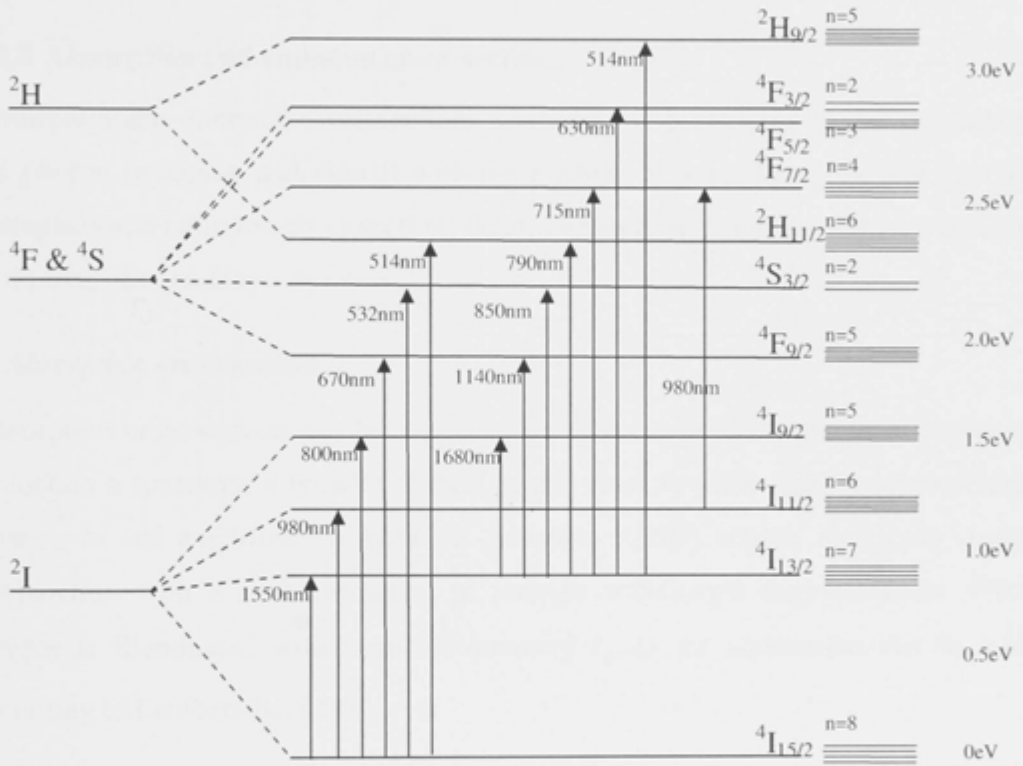


Figure 6.1: Energy levels of Erbium quantum energy with effect of spin-orbit and crystal splitting and excitation wavelengths from  $4I_{15/2}$ ,  $4I_{13/2}$  and  $4I_{11/2}$  to various levels [188].

In the case of Erbium in Silicon dioxide for example, the  $4I_{13/2}$  level is a metastable state. The radiative lifetime from this level to the ground state is often very long (potentially tens of ms) compared to those of the higher states ( $\mu$ s). Therefore, there are a number of possible pumping schemes for Erbium. Typically, a 980nm pump is usual in a three level system. The ion in its ground state is excited to the higher energy  $4I_{11/2}$ . Since the lifetime of this level is extremely short due to interactions with

phonons in the silica host, the Er ion rapidly relaxes non-radiatively to the metastable state  $^4I_{13/2}$ . High population inversion may be possible for this scheme limited only by co-operative upconversion, cross-relaxation energy transfer and excited state absorption. 1480nm pumping is treated as a quasi two level system. The ions in the ground state can be directly excited to the first excited manifold ( $^4I_{13/2}$ ). The disadvantage of this quasi pumping scheme is that the pump photons also induce stimulated emission instead of being completely absorbed. Therefore, there is a limit on the population inversions can be achieved. It is also possible to pump with 800nm, 670nm and 532nm.

### 6.1.2 Absorption and emission cross-sections

Absorption and emission cross-sections represent the probability of the interaction of the photon (pumping and signal) with the medium it is travelling in. The spectra of absorption and emission cross-sections determine suitable pump and signal wavelengths in the amplifier and laser systems.

#### a) Absorption cross-section

Absorption cross-section can be measured by direct light transmission measurements. To obtain a spectrum, a broadband light source such as white light, a supercontinuum source, or an amplified spontaneous emission (ASE) source is usually used in conjunction with a monochromator to provide wavelength discrimination. When a sample is illuminated with beam of intensity  $I_0(\lambda)$  the attenuation can be written according to Lambert-Beer law:

$$I(L, \lambda) = I_0(\lambda) \exp(\alpha(\lambda)L) \quad (6.1)$$

where  $\alpha(\lambda)$  is the absorption coefficient and  $L$  is the length (or thickness) of the sample along the propagation direction. The absorption cross-section  $\sigma_a(\lambda)$  is then defined as the absorption coefficient. The relation between  $\sigma_a(\lambda)$  and  $\alpha(\lambda)$  can be normalized by the doped ion concentration  $N$  as:

$$\sigma_a(\lambda) = \frac{\alpha(\lambda)}{N} = \frac{1}{NL} \ln \frac{I_0(\lambda)}{I(L, \lambda)} \quad (6.2)$$



**b) Emission cross-section**

The emission cross-section measurement is usually more difficult than the absorption. In order to detect the emission a pumping scheme is required and a detection set up which usually involves a monochrometer and a sensitive detector. During the measurement, the ions are excited into higher energy level and spontaneously emit a photon at a certain wavelength. For Erbium, the main emission of interest is in the range from 1400nm to 1650nm. Once an un-normalized emission spectrum is obtained, appropriate scaling must be performed to determine the value of the peak. If the metastable state radiative lifetime is known, the following Ladenburg-Fuchtbauer relationship can be used [190, 373]:

$$\frac{1}{\tau} = \frac{8\pi n^2}{c^2} \int \nu^2 \sigma_e(\nu) d\nu \quad (6.3)$$

where  $\tau$  is the radiative lifetime,  $n$  is refractive index of the sample,  $c$  is the speed of light in vacuum. The integration is over the emission spectrum of one level. The method has been known to work very well for Erbium doped glasses [374].

An alternative method is to use the dependence of absorption and emission cross-section spectra as they are ultimately linked to each other. One such fundamental relationship is the Einstein relation [190, 374]:

$$g_1 \int \nu^2 \sigma_a(\nu) d\nu = g_2 \nu^2 \int \sigma_e(\nu) d\nu \quad (6.4)$$

where  $g_i$  is the degeneracy of level  $i$ ,  $\nu$  is the photon frequency  $\sigma_a$  and  $\sigma_e$  are absorption and emission cross-section, respectively. The Einstein relation is only valid if either all components of the multiples involved are equally populated or all transitions have the same oscillator strengths. In Er doped glasses neither of the two conditions is fully qualified. This is because the manifold width of the ground state and metastable states of Er doped glass are typically a few meV (300-400cm<sup>-1</sup>) so at room temperature the first condition is not satisfied. Moreover, at low temperature, absorption and emission measurements indicate that the transition strength is quite sensitive to the Stark level involved [374]. Therefore, an alternative method known as McCumber theory is used.

### c) McCumber theory

McCumber, 1964 [373] proposed a theory to describe phonon-terminated masers. The relationship between absorption and emission cross-sections is proposed as following:

$$\sigma_e(\nu) = \sigma_a(\nu) \exp\left(\frac{\mathcal{E} - h\nu}{kT}\right) \quad (6.5)$$

where  $\sigma_e$  is the stimulated emission cross-section,  $\nu$  is the photon frequency,  $h$  is Plank's constant,  $k$  is the Boltzmann constant, and  $\mathcal{E}$  is the effective energy required to excite one  $\text{Er}^{3+}$  ion from the  $^4\text{I}_{15/2}$  to  $^4\text{I}_{13/2}$  state (ie ground to metastable state) at temperature  $T$ . This formula was first used for the study of transition metal ions but later applied to rare earth ions by Miniscalco, 1991 [374]. It was found that it generally links the absorption and emission spectrum very well once the correct energy  $\mathcal{E}$  is used. Miniscalco, 1991 [374] suggested a simple method for  $\mathcal{E}$  approximation by using the room temperature absorption and emission spectrum half-width. Under low optical excitation, it can be written that:

$$\frac{N_1}{N_2} = \exp\left(\frac{\mathcal{E}}{kT}\right) \quad (6.6)$$

where  $N_1$  and  $N_2$  are the population of ground level and excited level at temperature  $T$ . However, this ratio can also be expressed as [374]:

$$\frac{N_1}{N_2} = \frac{1 + \sum_{j=2}^{g^{1/2}} \exp\left(-\frac{E_{1j}}{kT}\right)}{\exp\left(-\frac{E_0}{kT}\right) \left[1 + \sum_{j=2}^{g^{2/2}} \exp\left(-\frac{E_{2j}}{kT}\right)\right]} \quad (6.7)$$

where  $E_{ij}$  is the energy difference of the Stark level  $j$  and the lowest component of level  $i$ . It is also appropriate to assume that the Stark level spacings for a given manifold are equally distributed. This reduces the number of unknowns from 14 to 3:  $E_0$  and the manifold spacing  $\Delta E_1$  and  $\Delta E_2$ . The final formula can then be simplified as follows:

$$\frac{N_1}{N_2} = \frac{A}{B} \exp(-E_0/kT) \quad (6.8)$$

where  $A = 1 + \sum_{n=1}^7 \exp(-n\Delta E_1/kT)$  and  $B = 1 + \sum_{n=1}^6 \exp(-n\Delta E_2/kt)$

A and B can be evaluated as:

$$A = \frac{1 - \exp(-8\Delta E_1 / kT)}{1 - \exp(-\Delta E_1 / kT)} \quad (6.9)$$

$$B = \frac{1 - \exp(-7\Delta E_2 / kT)}{1 - \exp(-\Delta E_2 / kT)} \quad (6.10)$$

Therefore:

$$\exp\left(\frac{\mathcal{E}}{kT}\right) = \exp\left(\frac{E_0}{kT}\right) \left(\frac{1 - \exp(-\Delta E_2 / kT)}{1 - \exp(-\Delta E_1 / kT)}\right) \left(\frac{1 - \exp(-8\Delta E_1 / kT)}{1 - \exp(-7\Delta E_2 / kT)}\right) \quad (6.11)$$

A good approximation of  $E_0$ ,  $\Delta E_1$  and  $\Delta E_2$  can be made from the shape of the absorption and emission spectra. The highest absorption and emission peaks are usually due to the transition between the lowest components of each manifold, or  $E_0$ . The bandwidth of the ground state is approximately  $7\Delta E_1$  and given by low-energy half-width of the room temperature emission spectrum. Similarly, the bandwidth of the excited state is  $6\Delta E_2$  and given by the high-energy half-width of the absorption spectrum. For tellurite,  $E_0$  is approximately  $6547\text{cm}^{-1}$  [147].

In comparing the bandwidth between various rare earth doped glasses, the effective bandwidth is more meaningful than the full-width at half-maximum (FWHM) due to the asymmetric nature of the emission spectrum. The definition of the effective bandwidth is:

$$\Delta\lambda = \int \frac{I(\lambda)d\lambda}{I(\lambda_p)} \quad (6.12)$$

where  $I(\lambda)$  is the emission intensity at the wavelength  $\lambda$ , and  $I(\lambda_p)$  is the intensity at the peak wavelength  $\lambda_p$ . For Er doped tellurite, the effective bandwidths generally increase with Er concentration in the range from 60-70nm, which is around 50% more than that of silicates [147, 244].

### 6.1.3 Judd-Ofelt theory

In order to determine the transition probabilities or oscillator strength of any particular transitions between energy levels in rare earth ions, Judd-Ofelt theory [375, 376] is used. The theory states that the oscillator strength for the transition between two states  $^{2S+1}L_J$  and  $^{2S+1}L_{J'}$  is given by [377, 378]:

$$f = \frac{2m\omega_0}{3\hbar e^2(2J+1)} \times |\mu|^2 \quad (6.13)$$

where  $\omega_0$  is an average frequency corresponding to  $J \rightarrow J'$  transition,  $m$  is electron mass,  $\hbar$  is Plank's constant and  $|\mu|^2$  is the matrix element of the electric dipole moment, which can be approximated by parameterized in form of a reduced matrix elements [377]:

$$|\mu|^2 = e^2 \sum_{t=2,4,6} \Omega_t \times |\langle \alpha J \| U^{(t)} \| \alpha' J' \rangle|^2 \quad (6.14)$$

$\Omega_{2,4,6}$  are Judd-Ofelt intensity parameters whose values have been extensively measured are generally readily available for most hosts, and  $|\langle \alpha J \| U^{(t)} \| \alpha' J' \rangle|^2$  is the reduced electric dipole matrix elements which can be calculated and are generally host-independent. These numbers for many rare earths have been tabulated by Carnall *et al.*, 1968 [379-383]. This means that the oscillator strength for any absorption or emission transition can be determined if the  $\Omega_{2,4,6}$  are known.

The Judd-Ofelt intensity parameters can be obtained for a material system by analysing the room temperature absorption spectrum of rare earth ion doped materials provided that the concentration of these ions and the refractive index of the material are known. The main advantage of the Judd-Ofelt formalism is that when  $\Omega_{2,4,6}$  parameters are known, the oscillator strength can be calculated for any given transition between any pair of  $J$  states. For instance, the transition strength of the electric dipole component of Er in glassy materials from  $^4I_{13/2} \rightarrow ^4I_{15/2}$  is [384, 385]:

$$S^{ed}[^4I_{13/2}; ^4I_{15/2}] = 0.019\Omega_2 + 0.118\Omega_4 + 1.462\Omega_6 \quad (6.15)$$

And the magnetic dipole interaction for transition  $^4I_{13/2} \rightarrow ^4I_{15/2}$  is given by:

$$S^{md}[(S', L')J'; (S, L)J] = \frac{1}{(2mc)^2} |\langle (S', L')J' \| L + 2J \| (S, L)J \rangle|^2 \quad (6.16)$$

In the absence of a strong magnetic field, the magnetic dipole interaction is approximately independent of the host. The spontaneous emission probability,  $A_{J,J'}$ , is calculated by taking into account both electric and magnetic dipole interactions:

$$A[(S', L')J'; (S, L)J] = \frac{64\pi^4 e^2}{3h(2J'+1)\lambda^3} (\chi_{ed} S^{ed} + \chi_{md} S^{md}) \quad (6.17)$$

The  $\chi$  terms correct the effective field at the localized centre of the medium of isotropic index  $n$  and are given by  $\chi_{ed} = n(n^2 + 2)^2/9$  and  $\chi_{md} = n^3$ . Webber, 1967 [384] has calculated the magnetic dipole spontaneous probability for  $^4I_{13/2} \rightarrow ^4I_{15/2}$  of Er in  $\text{LaF}_3$ , which has index of 1.5, to be  $37.6 \text{ s}^{-1}$ . For materials such as Tellurium oxide with index of  $\sim 2$ , the value would be  $\sim 90 \text{ s}^{-1}$ . Meanwhile, the typical values of  $\Omega_{2,4,6}$  for Tellurite glasses are:  $\Omega_2 = 5.93 \times 10^{-20} \text{ cm}^2$ ,  $\Omega_4 = 1.50 \times 10^{-20} \text{ cm}^2$ , and  $\Omega_6 = 1.07 \times 10^{-20} \text{ cm}^2$  [147, 386]. The electric dipole spontaneous probability for  $^4I_{13/2} \rightarrow ^4I_{15/2}$  approximately equals  $180 \text{ s}^{-1}$  leading to the total spontaneous emission probability of  $270 \text{ s}^{-1}$  or theoretical lifetime of 3.7ms. This number is lower than that of Er doped silica (as high as 12ms) or phosphosilicate glasses (up to  $\sim 20 \text{ ms}$ ), however, it is still an excellent value for a laser or amplifier system and is compensated by the correspondingly high emission cross section also resulting from the high refractive index.

#### 6.1.4 Solubility in solid hosts

Rare earth ions tend to form precipitates in most solid hosts beyond a critical concentration. This can be in the form of clusters of rare earth ions or can be compounds or alloys formed within the host matrix. Such processes serve to quench luminescence either by increasing ion-ion interactions between rare earth ions or groups of ions or forming compounds that are not optically active. This places a clear technological limitation on short Erbium doped silica fibre amplifiers. Therefore, typical silica based fibre amplifiers contain several meters of lightly-doped fibre in order to obtain substantial gain. Quenching concentrations for silicate glass and phosphate glass are in range from  $4\text{--}9 \times 10^{20} \text{ ions/cm}^3$  [188]. However, tellurite is known to have very high rare earth solubility. Brovelli *et al.*, 2007 [195] reported Er concentration in tellurite at 5 mol.% without any evidence of clustering. This is due to the fact that Tellurium atoms are significantly larger than Silicon or Phosphorus leading to further separation of Er ions in the matrix. Also, the bond frame work of Tellurium has some degree of flexibility in order to create more sites for rare earth ions. Grew, *et al.* 2006 [386] made Er doped sodium zinc tellurite samples with various Er

concentrations. There were crystals in the 12.5% Er by mass but not in any other samples with lower concentrations.

### 6.1.5 Phonon interaction

Multiphonon transitions can under some circumstances rapidly depopulate the upper excited state and therefore quickly quench luminescence. Multiphonon effects occur when a small number of phonons are required to bridge the energy gap between the levels. As a guide, if the phonon cut-off energy of the host is greater than 25% of the energy gap, rare earth luminescence will be completely quenched [188]. For phonon energy between 10% and 25% of the gap, the quenching will result in a temperature-dependent lifetime, while for phonon cut off energy smaller than 10%, the multiphonon relaxation will be negligible. In the case of Erbium, the gap is  $6500\text{cm}^{-1}$  for the  $^4\text{I}_{13/2}$  to  $^4\text{I}_{15/2}$  transition. The phonon cut-off energy is  $1100\text{cm}^{-1}$  for silica, therefore, it is only weakly quenched at room temperature. Low phonon hosts such as fluoride and tellurite glasses can reduce the contribution of multiphonon relaxation and allow transitions that are otherwise unavailable in silica based materials.[188, 190, 378].

In a given multiplet, when there is no or low population inversion due to external excitation such as optical pumping and at room temperature, the higher-lying states tend to relax very fast to the lowest state within the multiplet again via phonon interaction. The lifetime of the lowest lying state is strongly governed by the transition rate to the next lower multiplet.

The lifetime,  $\tau$ , of a level is the inverse of the probability per unit time of the exit of an ion from that excited level. The decay of the population in a given level drops exponentially with a time constant equal to the lifetime. There are a number of pathways for the population decays. The total probability is equal to sum of the individual probabilities for each pathway. Each pathway can have a separated lifetime. Usually they can be classified as radiative lifetime  $\tau_r$  or nonradiative lifetime  $\tau_{nr}$ . The total lifetime can then be written as:

$$\frac{1}{\tau} = \frac{1}{\tau_r} + \frac{1}{\tau_{nr}} \quad (6.18)$$

Radiative lifetime comes from the fluorescence from the excited level to all the levels below it. It can be determined directly from Judd-Ofelt analysis. Radiative lifetimes tend to be long, on order of microseconds to milliseconds.

Nonradiative lifetime depends mainly on the glass or crystal host, dopant interactions with other dopants or contaminants (discussed below in Section 6.1.6), and the interaction between phonons and the ions. The phonon component of the nonradiative transition probability drops exponentially with the number of phonons  $n$  required to bridge the energy gap to the next lowest level. The most commonly used formulism for the relationship between the multiphonon relaxation rate  $\tau_{mp}$  and the energy gap  $\Delta E$ , phonon energy  $\hbar\omega$  at temperature  $T$  is [190]:

$$\left( \frac{1}{\tau_{mp}} \right)_{n,T} = B \exp(-\alpha\Delta E) \left[ 1 - \exp\left(\frac{\hbar\omega}{kT}\right) \right]^{-n} \quad (6.19)$$

where  $n \approx \Delta E / \hbar\omega_m$  is the number of phonons needed to bridge the gap,  $\Delta E$  is the energy gap, and  $\hbar\omega_m$  is the maximum phonon energy of the phonons that can couple to the ion. The known measured constants  $B$  and  $\alpha$  are tabulated in Table 6.1. The nonradiative transition rates for  $\text{Er}^{3+}$  in several glass hosts are plotted in Figure 6.2. For Er transition from  $^4\text{I}_{13/2} \rightarrow ^4\text{I}_{15/2}$ , the energy gap is around  $6500\text{cm}^{-1}$ . The multiphonon relaxation rate is low compared to the radiative rate. Even with silica where the phonon cut off energy is  $1100\text{cm}^{-1}$  the Er luminescence at  $1530\text{nm}$  is only weakly quenched at room temperature. Selection of lower phonon hosts such as fluoride or tellurite glasses can reduce the contribution of multiphonon relaxation and allow radiative transitions that would otherwise be quenched (for example, the  $2.7\mu\text{m}$   $^4\text{I}_{11/2} \rightarrow ^4\text{I}_{15/2}$  transition in Er) [188]. The nonradiative transition rate of  $\text{Er}^{3+}$  in tellurite is one of the lowest, just behind ZBLAN glasses. This allows the strong competition of tellurite with ZBLAN as an alternative low phonon energy host for number of important laser lines such as the  $1.3\mu\text{m}$  transition in  $\text{Pr}^{3+}$ .



Table 6.1: Multiphonon transition parameters for some glasses [190, 197].

Host	$B \text{ (s}^{-1}\text{)}$	$\alpha \text{ (cm)}$	$\hbar\omega_m \text{ (cm}^{-1}\text{)}$
Tellurite	$6.3 \times 10^{10}$	$4.7 \times 10^{-3}$	700
Phosphate	$5.4 \times 10^{12}$	$4.7 \times 10^{-3}$	1200
Silicate	$1.4 \times 10^{12}$	$4.7 \times 10^{-3}$	1000
Germanate	$3.4 \times 10^{10}$	$4.9 \times 10^{-3}$	900
ZBLAN	$1.6 \times 10^{10}$	$5.2 \times 10^{10}$	500

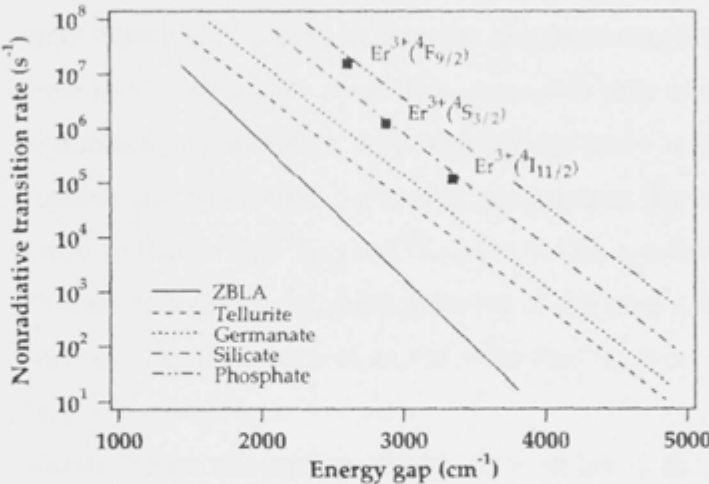


Figure 6.2: Nonradiative lifetime in different materials [190]

6.1.6 Dopant interaction mechanisms

Ion-ion interaction involves various, usually gain limiting, processes which take place in highly doped materials and results in non-radiate decay, luminescence quenching and dissipation of energy. There are quite a number of possible interactions in rare earth doped materials of which the most important include: co-operative upconversion, energy migration, cross-relaxation, excited state absorption (ESA), and OH quenching. Figure 6.3 shows schematic diagrams of several of these processes [188, 190]:

- a) **Co-operative upconversion.** Ions in the metastable state can couple in such a way that the decay of ion 1 promotes a nearby ion 2 into a higher level. Thus ion 1 loses its energy non-radiatively. Once in the higher state, ion 2 radiates to lowest level to emit light or may then

decay rapidly non-radiatively and return to the metastable state and subsequently emits light. This process results in loss of excitation to heat. In Erbium, the process is  $2^4I_{13/2} \Rightarrow ^4I_{9/2} + ^4I_{15/2}$ .

- b) **Energy migration.** An ion in the metastable state can interact with a nearby ground state ion, exciting it to the metastable state. Although radiative decay might occur from the second ion, the probability of non-radiative decay is increased with each successive transfer, making it a lossy process for the overall efficiency. In Erbium, the process is  $^4I_{13/2} \Rightarrow ^4I_{13/2}$ .
- c) **Cross relaxation.** This process involves an ion in a highly excited state transferring energy to a nearby ion promoting it from the ground state to the metastable state. This process is only in effect if there is significant population at very high energy level as a result of other interactions. In Erbium, the energy gap between  $^4I_{9/2}$  and  $^4I_{13/2}$  levels is close to that of the  $^4I_{13/2}$  and  $^4I_{15/2}$  levels. As a consequence, at high Erbium concentrations, the population of the metastable state may be increased by the decay of an ion from the  $^4I_{9/2}$  level. The process is:  $^4I_{9/2} + ^4I_{15/2} \Rightarrow 2^4I_{13/2}$ .
- d) **Excited state absorption (ESA).** Here an ion in the metastable state is further excited into an upper state by the absorption of another pump photon. Clearly this requires an available energy level which is roughly the pump energy above the metastable state to occur. The upper state excited ion can return to the metastable state by multiphonon relaxation or radiative decay or bypass the metastable state entirely by high energy emission. However, the process results in two absorbed photons of which at least one photon is lost to either heat or emission at different wavelength. Excited state absorption therefore constitutes a loss mechanism and impacts pumping efficiency. Figure 6.3 d) illustrates ESA for  $\text{Er}^{3+}$  ion.
- e) **Pair-induced quenching (PIQ).** Pair induced quenching is similar to the cooperative upconversion process in that the interaction occurs when two ions are closely coupled together that they cannot be both

simultaneously excited to level  $^4I_{13/2}$ . The energy transfer rate between the two ions is on time scale that is significantly faster than that of the pumping rate so that the pump is unable to keep both ions excited. In this pair model, the ions are no longer considered independent. When one of the ions of the pair is in the  $^4I_{13/2}$ , it then assumes that the other ion must be on the ground state. The overall ion population can be considered as two sets of ions one is isolated single atoms and one with paired-ions. The rate of pair-induced quenching process depends on the number of ions already in the excited state and the pump intensity, which excites the second ions. The dependence is similar to ESA.

- f) **OH quenching.** Another deleterious process involves energy transfer from ions in the metastable state to the OH complex which has a bond resonance in the 1550nm region, which serves a quenching centre and is extremely effective at quenching excited rare earth ions. At high OH concentrations, this can occur through direct transfer from the excited ions, at lower OH- concentration, a more likely process is fast energy transfer between interacting donor ions until the excitation reaches one near an OH- centre.

All of the transitions in Figure 6.3 can occur resonantly and/or with phonon assistance. At resonant conditions, the energy is transferred between different ions without the involvement of a phonon from the host, whilst in phonon assisted processes, the total energy of the involved ions either increases or decreases due to the absorption or emission of one or more phonons. The host can provide phonons with energy up to a cut off phonon energy as in Table 6.1. For instance, in tellurite, the maximum phonon energy is around  $700\text{cm}^{-1}$ . Therefore, when the total energy of the two ions before and after the nonlinear transition is less than this maximum phonon energy, the transition probability is reasonably high due to the ready availability of suitable phonons in the host.

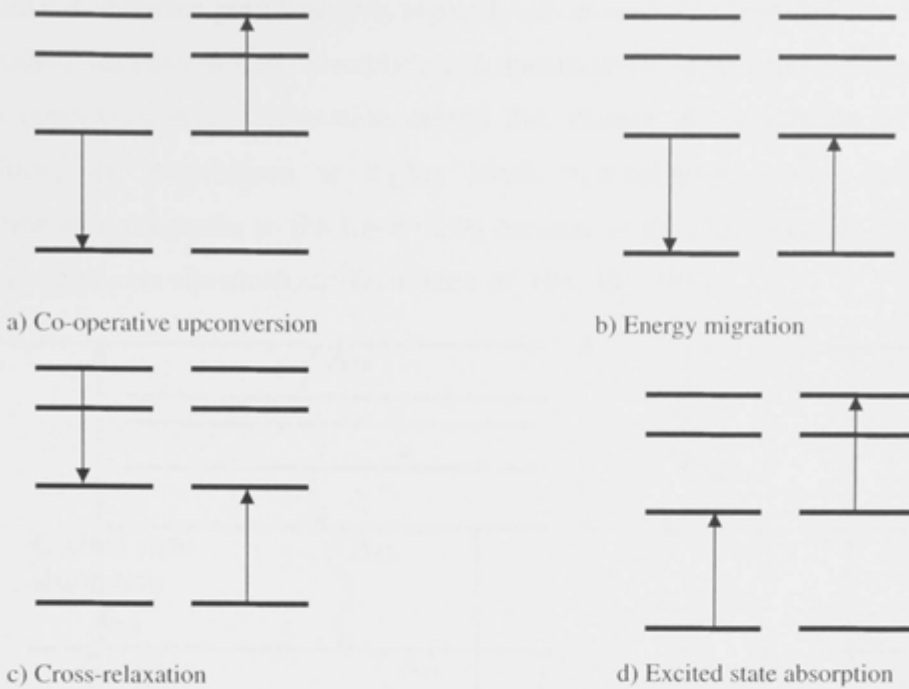


Figure 6.3 Ion-ion interactions in Er doped glasses and excited state absorption [188, 190].

## 6.2 Rate equations for photoluminescence study

For lifetime and fluorescence studies, Erbium doped samples are pumped with a 980nm source as shown in Figure 6.4. The fluorescence signal at  $1.5\mu\text{m}$  is generally very weak and unguided and therefore, its contribution to the stimulated emission process can be neglected. The pump power is usually modulated on for a sufficient duration to produce a population inversion. Then it is turned off and the decay signals are monitored. There are a number of approximations that can be made to simplify the treatment of the system.

With a 980nm pump, the system is basically a 3 level scheme in the ideal situation where there is no effect of ion-ion interactions or excited state absorption. The ions at ground state are excited by the pump to level 3. They quickly make a non-radiative transition to the metastable state at level 2. The population inversion is built up between the metastable level 2 and ground state 1. The next transition from 2 to 1 would be a photon emission via stimulated or spontaneous process. However, when taking into account all ion-ion interactions and excited state absorption as shown on

Figure 6.4, there are populations at higher levels as well. The population at level 5 ( $^4F_{7/2}$ ) is excited via excited state absorption and upconversion from level 3 ( $^4I_{11/2}$ ). There are also upconversion and relaxation effects that change the population of level 4. In addition, the populations at higher levels non-radiatively decay via single or multiphonon processes to the lower level because of the close spacing between them. The coupled rate equations can be written as [194, 387, 388]:

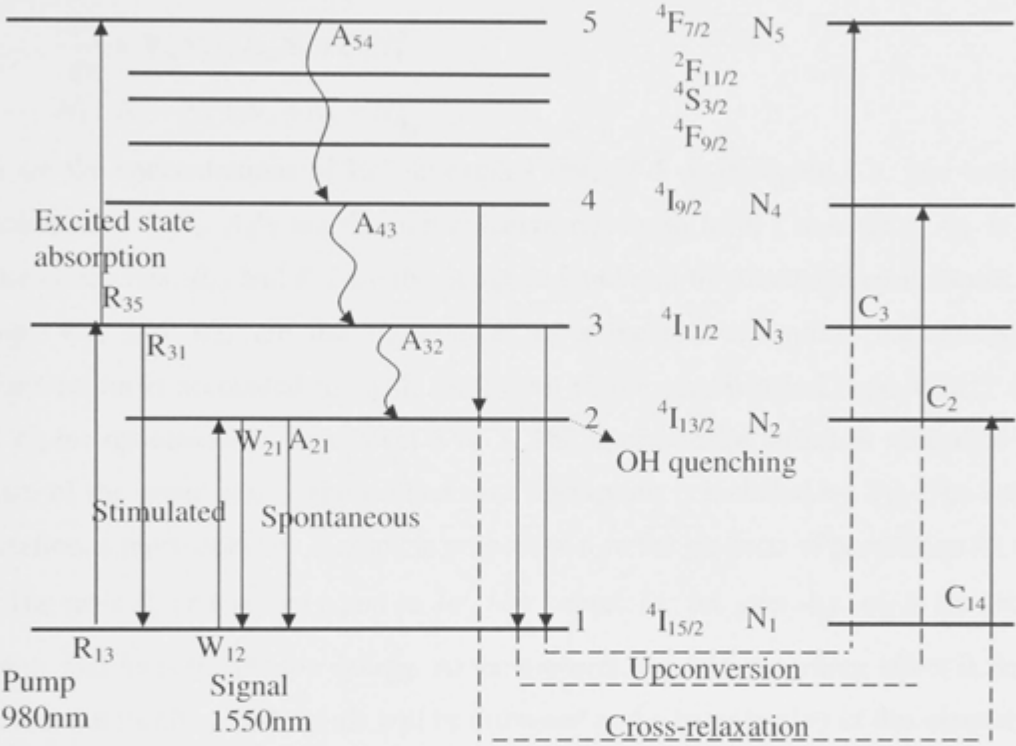


Figure 6.4: Schematic diagram of main transitions of Er in glasses pumping at 980nm. The curves arrows indicate non-radiative transitions and solid arrows indicate the radiative transitions.

$$\begin{aligned}
\frac{dN_1}{dt} &= -R_{13}N_1 + R_{31}N_3 - W_{12}N_1 + W_{21}N_2 + A_{21}N_2 + C_2N_2^2 + C_3N_3^2 - C_{14}N_1N_4 \\
\frac{dN_2}{dt} &= -A_{21}N_2 + A_{32}N_3 + W_{12}N_1 - W_{21}N_2 - 2C_2N_2^2 + 2C_{14}N_1N_4 \\
\frac{dN_3}{dt} &= R_{13}N_1 - R_{31}N_3 - A_{32}N_3 + A_{43}N_4 - 2C_3N_3^2 - R_{35}N_3 \\
\frac{dN_4}{dt} &= -A_{43}N_4 + A_{54}N_5 + C_2N_2^2 - C_{14}N_1N_4 \\
\frac{dN_5}{dt} &= R_{35}N_3 - A_{54}N_5 + C_3N_3^2 \\
N_1 + N_2 + N_3 + N_4 + N_5 &= N_0
\end{aligned} \tag{6.26}$$

$N_{1-5}$  are the concentrations of  $\text{Er}^{3+}$  in excited states 1-5 as in Figure 6.4. The total Er concentration is  $N_0$ .  $A_{ij}$ 's are the non-radiative rate from level  $i$  to level  $j$ .  $A_{21}$  is the fluorescence rate.  $R_{13}$  and  $R_{31}$  are the pump rate and rate of stimulated emission of the pump.  $W_{12}$  and  $W_{21}$  are the signal rates of stimulated absorption and emission. Upconversion is accounted for with coefficient  $C_2$  for upconversion from level 2 to 4 and  $C_3$  for upconversion from level 3 to 5. The upconversion effect is related to the square of the populations. The excited state absorption is included by  $R_{35}$ . The cross-relaxation is represented by  $C_{14}$  and is proportional to the products of population  $N_1$  and  $N_4$ . The rates  $R_{ij}$  and  $W_{ij}$  are equal to  $I\sigma_{ij}/h\nu$  where  $I$  is the intensity,  $\sigma_{ij}$  is the cross-section, and  $h\nu$  is the photon energy. At the moment, the OH-quenching effect is being ignored, but its effect on lifetime will be discussed in the latter section of this chapter.

In addition to the transitions shown on Figure 6.4, there are also other radiative branches such as  $5 \rightarrow 1$ ,  $4 \rightarrow 1$ . These transitions are responsible for the visible light such as the green when the Er doped devices are pumped at high intensity. However, populations at level 4 and 5 are small due to very fast nonradiative decay rate to lower levels near by leading to insignificant contributions. They are ignored in the rate equations.

These coupled differential Equations (6.26) represent a relatively complex system. It is usually time consuming to calculate even numerically. During the photoluminescence lifetime measurement, the pump is modulated. There are certain approximations that can be used to reduce the complexity of the system. When the pump is off, all of the pump-stimulated terms are zero or  $R_{13}=R_{31}=R_{35}=0$ . Furthermore, because the signal is not confined the signal intensity is very low meaning the  $W_{ij}$ 's can

be considered equal to zero. The pump level population  $N_3$  can be deemed negligible since the pump is off. Also, it can be assumed that the non-radiative decay transitions from between level 3 to 5 are dominate over the optical transitions. Therefore, once the pump is turned off, the above rate Equations (6.20) then simplify to become:

$$\begin{aligned}
 \frac{dN_1}{dt} &= A_{21}N_2 + C_2N_2^2 + C_3N_3^2 - C_{14}N_1N_4 \\
 \frac{dN_2}{dt} &= -A_{21}N_2 + A_{32}N_3 - 2C_2N_2^2 + 2C_{14}N_1N_4 \\
 \frac{dN_3}{dt} &= -A_{32}N_3 + A_{43}N_4 - 2C_3N_3^2 \\
 \frac{dN_4}{dt} &= -A_{43}N_4 + A_{54}N_5 + C_2N_2^2 - C_{14}N_1N_4 \\
 \frac{dN_5}{dt} &= -A_{54}N_5 + C_3N_3^2 \\
 N_1 + N_2 + N_3 + N_4 + N_5 &= N_0
 \end{aligned} \tag{6.21}$$

A further assumption can be made for the system. The population  $N_4$  and  $N_3$  are significantly less than the metastable level population  $N_2$ . The two terms  $A_{32}N_3$  and  $2C_{14}N_1N_4$  in the first line of Equation 6.21 are therefore small compared to the other terms. Therefore  $N_2$  is decoupled from the rest of the population levels or:

$$\frac{dN_2}{dt} = -A_{21}N_2 - 2C_2N_2^2 \tag{6.22}$$

This simple differential equation can be solved to have the following analytical solution [192, 388]:

$$N_2(t) = \frac{N_2(0)}{[1 + N_2(0)C_2\tau_2]\exp(t/\tau_2) - N_2(0)C_2\tau_2} \tag{6.23}$$

where  $N_2(0)$  is the Er ion population in level 2 at the moment the pump is turned off, and  $\tau_2 = 1/A_{21}$  is the radiative lifetime of level 2. The decay PL signal only depends on the lifetime  $\tau_2$ , the initial population  $N_2(0)$  and the upconversion coefficient  $C_2$ . In the absence of upconversion  $C_2=0$ , the decay is single exponential. The decay signal forms a straight line in a logarithmic scale graph with the slope depending on the lifetime of metastable level. In the upconversion regime, the signal decay is non-exponential at the beginning of the curve but become an exponential as the signal gets weaker. The intrinsic lifetime  $\tau_2$  can be measured by the slope of the semi-logarithmic scale graph



of the decay signal at the low signal end. The analysis so far relies on the assumption that the rate  $A_{21}$  is purely due to radiative transition. However, in reality, there is also energy transfer rate between Er ions and OH contaminant. The next section further analyses the effect of OH quenching on the measured lifetime.

### 6.3 Effect of OH quenching centre concentration on lifetime

The measured lifetime  $\tau_m$  of the  $1.5\mu\text{m}$  transition of Er doped sample is influenced by not only the intrinsic (radiative,  $\tau_2$ ), the multiphonon assisted transition  $\tau_{mp}$  lifetime but also the quenching effect due to the presence of OH impurity represented by  $\tau_{OH}$ . The OH quenching dependent PL lifetime can be simply expressed as:

$$\frac{1}{\tau_m} = \frac{1}{\tau_2} + \frac{1}{\tau_{mp}} + \frac{1}{\tau_{OH}} \quad (6.24)$$

The bandgap between  $^4I_{13/2} \rightarrow ^4I_{15/2}$  is  $6500\text{cm}^{-1}$ , the multiphonon transition rate is very negligible for tellurite glasses as seen on Figure 6.2. Therefore, only the intrinsic lifetime  $\tau_2$  and OH quenching rate  $\tau_{OH}$  affect the measured lifetime  $\tau_m$ .

Further insight can be revealed if the following assumptions are proposed [389]: a) the OH quenching centres are only coupled to a fraction of the Erbium ions, b) the fraction of Er ions coupled to OH groups is dependent on the OH concentration and c) non-radiative quenching occurs after the excitation energy is transferred to Er ions and then coupled to OH group via energy migration. Taking into account these assumptions, the concentration of Er ions coupled to OH  $N_{Er-OH}$  can be written as [147, 221, 389]

$$\frac{1}{\tau_{OH}} = \frac{1}{\tau_m} - A_{21} = 8\pi C_{Er-Er} N_{Er} N_{Er-OH} \quad (6.25)$$

where  $C_{Er-Er}$  is the migration rate which has been measured in tellurite hosts to be  $46 \times 10^{-40} \text{cm}^6 \text{s}^{-1}$  [147, 221]. By plotting the value of  $1/\tau_m$  against the Er concentration  $N_{Er}$ , the value of  $N_{Er-OH}$  can be calculated from the slope and the intrinsic radiative lifetime can also be measured from the intercept.

## **6.4 *Fabrication of Er doped Tellurium oxide by sputtering***

### **6.4.1 Film deposition**

Erbium doped thin films were obtained by co-sputtering of Er and Te targets in an Ar/O<sub>2</sub> atmosphere. The Te target is a pure sintered powder Tellurium metal at 99.95% purity in a copper cup to help with heat dispersion. The Er target is solid metal piece with 99.99% purity. The gas mix was ultra high purity O<sub>2</sub> and Ar. The flow of Ar was 9.5sccm and of O<sub>2</sub> was 5.5sccm. The pressure of the chamber was maintained at 5mTorr during the deposition process. The Te gun was supplied with a power of 150W (25% of the 600W maximum power of the gun), all as per the fabrication of stoichiometric TeO<sub>2</sub> films. The power to the Er guns was varied depending on the required concentration of Er. Generally, the Er gun powers are in the range 5% to 15% (30W to 90W). These produced films with Er/Te ratios in the range from 0.1% to 3%.

Generally, the wafer used during this entire project is 4" Silicon wafer with 2μm thermal oxide layer, which will act as a lower cladding for the fabricated devices. Small pieces of bare Si substrate (cut in 100 plane) were also used for characterization such as refractive measurement, composition analysis etc. A small piece of glass slide was also used as a substrate for photospectral measurements and lifetime.

### **6.4.2 Laser ablation ICP mass spectrometer**

The compositions of the obtained films were measured using an ICP mass spectrometer and excimer laser ablation attachment at the Research School of Earth Science, the Australian National University. A COMPex 110 Excimer laser using ArF (193 nm wavelength) was connected to an Agilent 7500s ICP-MS through an in-house-developed ablation chamber. Helium filled the main part of the chamber and carried the sample from the ablation site. That aerosol was mixed with Argon in a cone-shaped space above the ablation site, and was mixed down stream with Hydrogen and delivered to the torch of the ICP. The laser pulse energy was approximately 50mJ at 5Hz repetition rate. The aperture was chosen to produce a 40μm diameter pit. The beam was fixed and the sample was moved at rate of 10μm/second. Gas flows were 1.1l/min Argon, 0.34l/min Helium and 0.1l/min Hydrogen. Sample ablations were typically 30 seconds of background followed by up to 3 minutes of "laser-on" signal. Concentration

data were produced using the method of Longerich *et al.*, 1996 [390] using an Excel workbook. A certified standard, coded 610 from NIST, was used to calibrate the measurements.

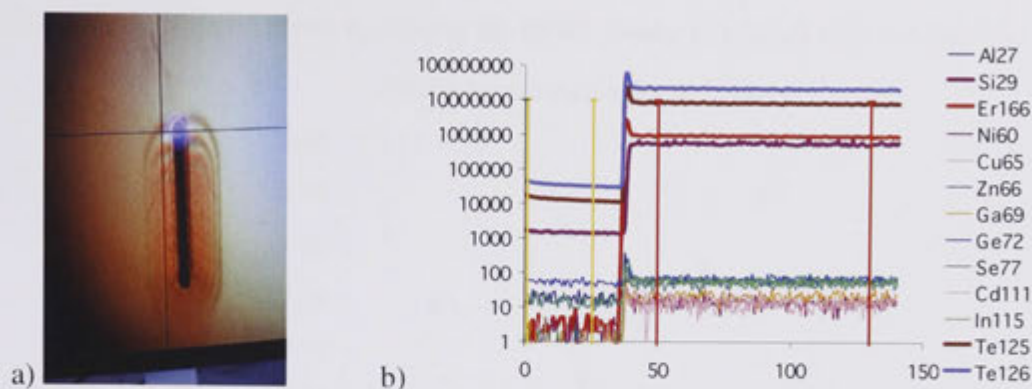


Figure 6.5: Excimer laser ablation ICP mass spectrometer a) a image of ablated site and b) a typical mass spectrometer spectrum using exciter laser ablation (x axis is time and y axis is number of count, the four vertical bars are for selection of the background and data for calculation of the composition).

A typical spectrum obtained is showed on Figure 6.5. At the time the laser is switched on, there is a spike due to the sudden flux of the materials from the ablation chamber to the ICP. After a few seconds, the spectrum stabilises and the count levels become flat. The flatness of the spectrum indicates that the elements are uniform and the system is in a good operation condition. The fluctuation is highest in Silicon due to the fact that the films are deposited on the Silicon substrates. The laser drills to the Silicon slightly unevenly. This indicates that the laser pulses only drilled to the Silicon substrate after a number of shots.

Also, the background level for Tellurium is relatively high for both measured isotopes at round  $10^3$  or  $10^4$ . This indicates that Tellurium has relatively long lifetime in the system. The materials could stick to various elements of the system such as the ablating cells, the tubes, and the torch. Despite that, the background count is around  $10^4$  lower than the signal when ablation is on. Therefore, the effect of the background is negligible. Other contaminants including Ni, Cu, Zn, Ga, Ge, Cd and In are at very low concentrations at only 100 counts compared to Er at a million counts. These contaminants are either from the original targets or from the sputtering chamber.

The extracted data of Er/Te ratio against the RF Er gun power are plotted in Figure 6.6. It is clear that the Er concentration can be accurately controlled by simply

setting the Er gun RF power. The plasma threshold for the Er target was around 30W. After that, the increase tended to be exponential. To achieve sufficient optical gain, the Er concentration should be at order of  $2 \times 10^{20}$  ions/cm<sup>3</sup> or around 1% Er/Te. This criterion is readily obtained by setting the Er RF power to around 10% (of 600W).

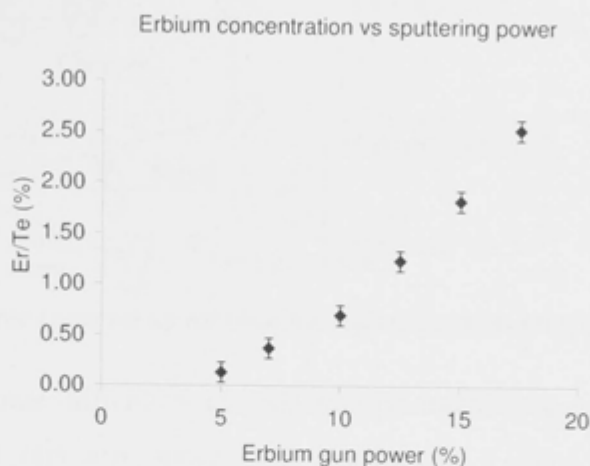


Figure 6.6: Dependence of Er/Te in co-sputtered film.

## 6.5 Characterisation of Er doped Tellurium oxide films

### 6.5.1 Photoluminescence using free space set up

The experimental setup as shown on Figure 6.7 was used to characterize the photoluminescence spectrum, using a CW Argon ion laser (Spectra Physics Stablite 2017) emitting 488nm wavelength as a pump. The laser beam was modulated by a mechanical chopper with a disc having two cut outs providing a duty cycle of 50%. The power of the laser was set to 100mW at the sample. The beam was focused onto the film surface using a 200mm lens to produce a spot of ~200microns waist diameter and the fluorescent emission was collected and collimated by lenses with a diameter of 75mm and focal lengths of 200mm. A long pass filter was placed in front of the monochromator entrance to filter the pump. The dual grating monochromator was set with 2mm front and back slits. The gratings had 900groove/mm rulings. The signal was picked up by a Liquid Nitrogen cooled Ge detector. The signal was then amplified by an SRS lock-in amplifier before being sent to the computer for acquisition and analysis. Since the interesting emission is around 1550nm, the monochromator was set to scan from 1450nm to 1650nm with 7s integration time and at a bandwidth of 2nm.

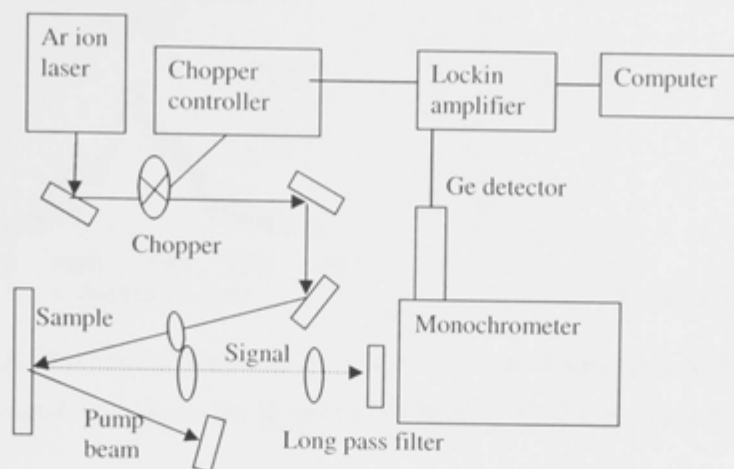


Figure 6.7: A free-space set up for photoluminescence measurement

There are some difficulties in collecting photoluminescence spectra from thin films. First, due to very low optical path length, only 1-2 $\mu\text{m}$ , the amount of light absorbed is very low. Furthermore, due to Fabry-Perot effects in the film, the pump wavelength might fall on the reflection maximum (which can be close to 100% for a multilayer film stack) reducing the available pump power very considerably; the luminescence signal might also be at a resonance at the same time leading to very low signal levels out of the film. This can result in a low signal to noise ratio of the photoluminescence spectrum in some instances as some traces in Figure 6.8 a) show. It is not the case that the highest Er concentration produces the cleanest signal as might be expected purely on the basis of the emission power. The peak emission in all cases was at 1533nm. The effective emission bandwidth was calculated by Equation 6.12 and is plotted on Figure 6.8 b). The bandwidth is about 60nm, with only slight variation of the width over the concentration range studied. The values obtained from these films are comparable with reported values in the literature [147, 221, 244]. Unlike the spectra reported by Jaba *et al.*, 2009 [147] and Dai *et al.*, 2006 [221], there is no significant sign of spectral broadening due to Er concentration increase. This is because those authors measured lifetime in bulk samples where the re-absorption of the 1.53 $\mu\text{m}$  signal leads to a lowering of the peak and so an effective bandwidth increases while the films measured here are so thin, there is no re-absorption effect.



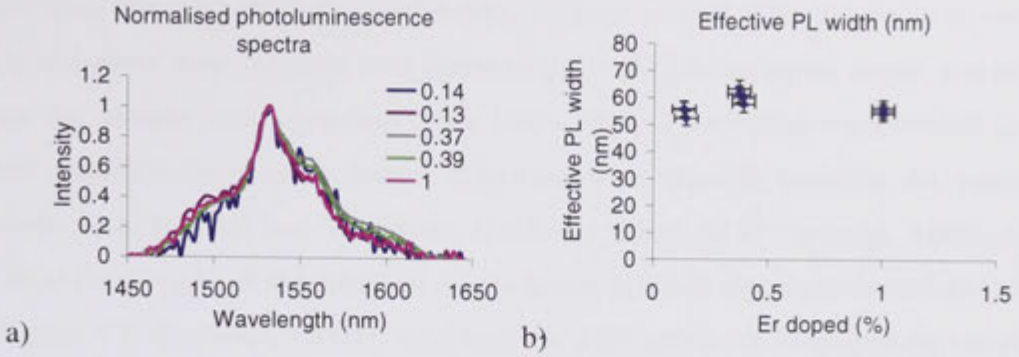


Figure 6.8: Photoluminescence of Er doped Tellurium Oxide films a) Normalised emission spectra at various Er/Te and b) Effective width of the emissions.

The Ladenburg-Fuchtbauer analysis (Eq. 6.3)  $1/\tau = (8\pi^2/c^2) \int \nu^2 \sigma_e(\nu) d\nu$  applied to the spectra gives the radiative lifetime of transition  $^4I_{13/2} \rightarrow ^4I_{15/2}$  in Er doped  $\text{TeO}_2$  films at 2.4ms. This number is smaller than those quoted in the literature using Judd-Ofelt analysis for bulk multicomponent tellurite glasses of 3.7ms to 4ms [144, 147, 188, 386, 391-395]. Since there has been no Erbium doped Tellurium oxide work reported in the literature before this work, the comparison is questionable, although the predicated lifetime is not much less than that for the multicomponent glasses.

### 6.5.2 Lifetime measurement using all fibre setup

To avoid the Fabry-Perot effects and maximize the collection efficiency of the photoluminescence signal an all-fibre set up as shown in Figure 6.9 was used. A grating stabilized 975nm pump was modulated by a pulse train from a function generator, with typically 5ms pulses and ~50Hz repetition rate. A broadband 980nm/1550nm WDM was used to couple the pump light to a tapered fibre lens. The lens focused the pump to a spot size of  $2.5\mu\text{m}$  ( $1/e^2$ ) diameter at  $14\mu\text{m}$  distance from the tip. The beam illuminated the sample from the edge of the film, top down to the film or via the end facet of a waveguide. The same lens acted as a collector for the PL signal. The PL signal travelled backward to the WDM where it was coupled through to the 1550nm output port. A second identical WDM is used to further suppress the pump signal. An InGaAs detector (Fermionics) was used to measure the  $1.5\mu\text{m}$  PL signal. The electrical signal was amplified using a low noise pre-amplifier (Signal Recovery Inc. transimpedance amplifier). The amplified electrical signal was then displayed on a digital oscilloscope or fed to a data acquisition device attached to a PC. The system had

an intrinsic rise time of  $\sim 8\mu\text{s}$ , could rapidly average several thousand traces to reduce noise and allow measurements over potentially 4-5 decades of signal decay, and could pump the sample with intensities from levels approaching those experienced in an actual amplifier down to its lowest detection limit, thereby, enabling the intensity dependence of lifetime and the various non-linear effects to be captured. Additionally the short focal length of the detection means the probed path was very short as the insert in Figure 6.9 illustrates, thereby enabling the elimination of absorption/re-emission issues previously observed [221, 386].

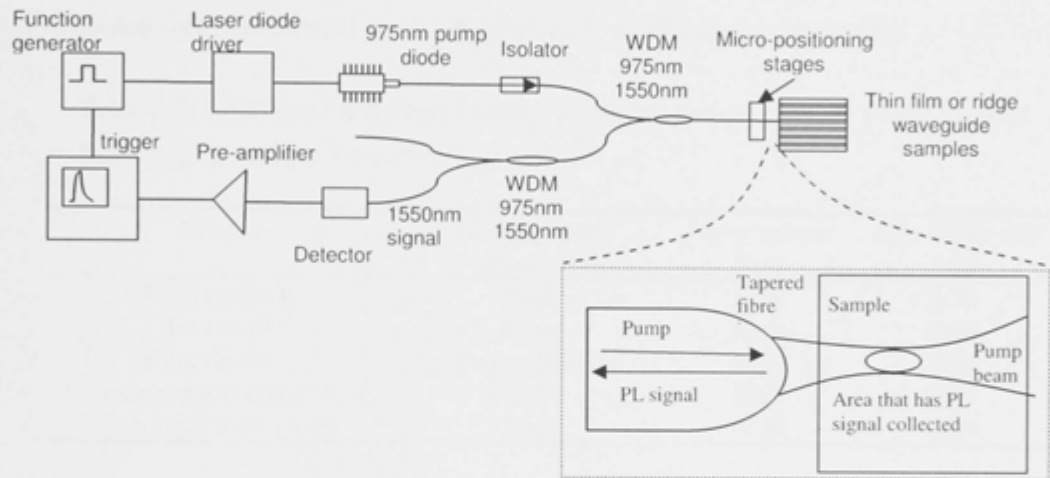


Figure 6.9: All fiber setup for photoluminescence measurement of film and waveguides

Further advantages of this method include the fact that the fibre lens only collects PL signal from the volume where the pump is most intense. The depth of focus is only a few micrometer long, therefore this helps to avoid the effect of signal reabsorption enhancement of lifetime seen in heavily doped bulk samples [147, 221, 386]. Furthermore, the directly modulated pump has a fall time of less than  $10\mu\text{s}$ . This is significantly better than the normal modulation method using a mechanical chopper which produces modulated pumps with fall times of a few hundred micro seconds. This means films with short lifetimes can be measured which is helpful in determining concentration dependent effects. In addition, this setup can be used under normal room lighting as the tapered fibre lens only collects light from an extremely small volume inside the sample.



### 6.5.3 Lifetime and measurement configuration

A measurement technique dependence for the high power lifetime was seen. The role of the waveguide structure has been previously identified [396] through its modification of the emission modes and so the high power lifetime was measured in three geometries; at the unstructured film edge, perpendicular to the film, and at the facet of two different waveguide lengths (4mm and 5cm). The results for the  $1/e$  lifetime are presented in Table 6.2. The first three film lifetime measurements on the Table 6.2 were performed on film deposited on glass slide, whereas the measurements of lifetime of Er doped waveguides were performed on those fabricated on thermal oxide wafer.

Table 6.2: Lifetimes for different measurement geometries (sample coded 45 with Er concentration of 1.3% or  $2.9 \times 10^{20} \text{ cm}^{-3}$ )

<i>Sample</i>	<i>Measurement geometry</i>	<i>Pump power level</i>	<i>Lifetime at <math>1/e</math> (ms)</i>
Film on SiO <sub>2</sub>	Edge	Low	0.56
Film on SiO <sub>2</sub>	Edge	High	0.44
Film on SiO <sub>2</sub>	Perpendicular	High	0.38
4mm long waveguide	End	High	0.31
5cm long waveguide	End	High	0.19

The waveguide geometries considerably shorten the observed lifetime. The longer waveguide produces lower lifetime than the shorter waveguide. We believe this is due to the depletion of the excited Er ions in the measurement region by stimulated emission with photons generated elsewhere in the waveguide. Clearly the rate of stimulated depopulation depends on the number of incident photons which is a function of both the length of the waveguide and the pump power. Consequently a longer waveguide generates more photons outside the measurement region which propagate to the measurement region and depopulate the excited Er ions faster thereby reducing the observed lifetime further. Measuring perpendicular to the film surface also has a shorter lifetime than measuring through the film edge. Here, although no photons are generated outside the measurement region to depopulate the excited Er ions by stimulated emission as in the waveguide case, the measurement region is in fact contained inside a Fabry-Perot cavity comprising the film (high index) and air/the silica substrate (both low index). Thus some photons initially generated by spontaneous emission in the film are reflected at the surfaces and produce repeated stimulated emission events as they

“bounce” inside the film thereby again reducing the number of excited ions by a non-spontaneous decay process thereby shortening the observed lifetime. In contrast to the two prior cases, measuring through the film edge results in the pump diffracting away quickly in the plane of the film as it is unguided there, so little spontaneous emission occurs outside the measurement zone and any that is generated is not guided back into the measurement zone. Thus the number of stimulated emission results is considerably reduced and the measured results are expected to be far more representative of the true spontaneous decay rate of the film than the other measurement modalities. However the results of Table 6.2 pose the question of whether this measurement modality remains completely unaffected by backward propagating spontaneous emission. The definitive measurement to clarify this would be to deposit the Er doped Tellurite film on an index matched substrate with top side anti-reflection coating and then measure perpendicular to the film. In this case there is by definition no spontaneous emission outside the measurement region, and no reflections of spontaneous photons generated inside the measurement region back into it for stimulated emission to occur. Therefore, it would be expected that this geometry would measure only the spontaneous decay rate. Unfortunately, no suitable substrates were available to try this.

#### **6.5.4 Decay and upconversion**

In the first set of experiments, a sample with Er/Te ratio of 1.5% was measured at various pump pulse durations from 2ms to 30ms. Most of the obtained decay curves are non-exponential as shown on Figure 6.10. They consisted of a rapid decay initial part following by exponential lines in the semilog scale graph. The decay curves were almost identical with the pump period ranging from 2ms to 30ms. There is only slight deviation after 3ms or after the signal has dropped to 0.01 below the initial signal. The deviation is mainly on the 2ms pulse. This is because the signal at this particular pump duration was very low even at the delay 0ms, by the time it gets to 3ms, the signal becomes very weak leading to large detection error.

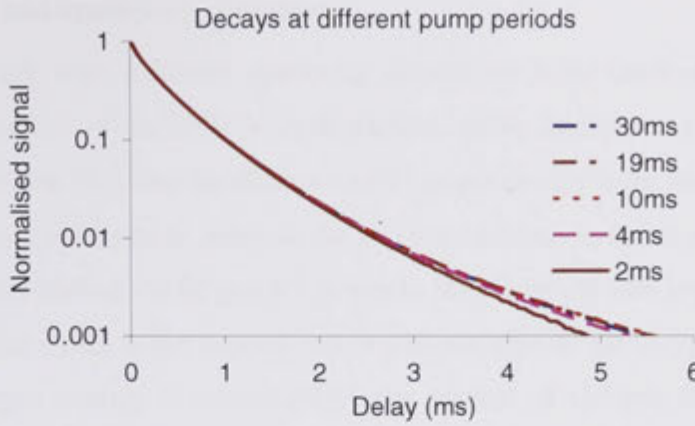


Figure 6.10: Typical decay curves for a sample with various pumping on periods.

The fitting is using upconversion expressions as in Equation (6.23) in form of:

$$I(t) = \frac{1}{[1 + K] \exp(t/\tau_m) - K} \quad (6.26)$$

where  $K = N_2(0)C_2\tau_m$  represents the upconversion effect,  $\tau_m$  is the lifetime of the metastable state,  $I(t)$  is the normalised signal. The fitting of the data on Figure 6.10 results in Figure 6.11 with a) lifetime  $\tau_m$  and b) upconversion coefficient  $K$ . The upconversion fitting process produces not only good fitting but also reflects the physical evidence. The lifetime after a long decay is roughly constant. The saturation parameter  $K$  is lower at first because the population  $N_2(0)$  has not been fully saturated. As the pump duration increases, the population  $N_2$  is in steady state and independent of the length of pumping pulse. At a very short pumping duration, the upconversion is less profound because the initial population is well below saturation.

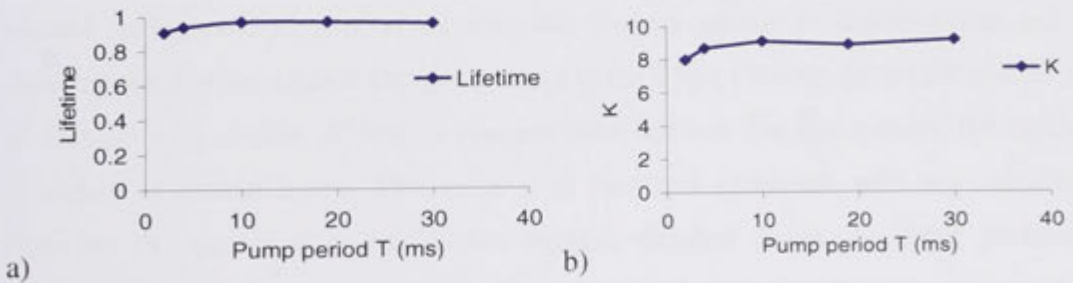


Figure 6.11: Lifetime a) and upconversion effect b) against pumping duration

### 6.5.5 Lifetime and sputtering condition

A series of films with different sputtering conditions were fabricated to determine whether the lifetimes of the films were dependent on the fabrication parameters. In the first experiment, the chamber conditions and Te target setting were fixed while varying the RF power of the Er gun to increase the Er concentration in the deposited films. The dependence of Er content on Er gun RF power in the deposited film is plotted on Figure 6.6. The next set of data is the dependence of lifetime against the Oxygen content in the film. The Oxygen content is controlled by the amount of Oxygen flow. The starting point for the Oxygen flow was the condition that obtained stoichiometric  $\text{TeO}_2$ . Increased Oxygen flow results in higher Oxygen incorporation into the films.

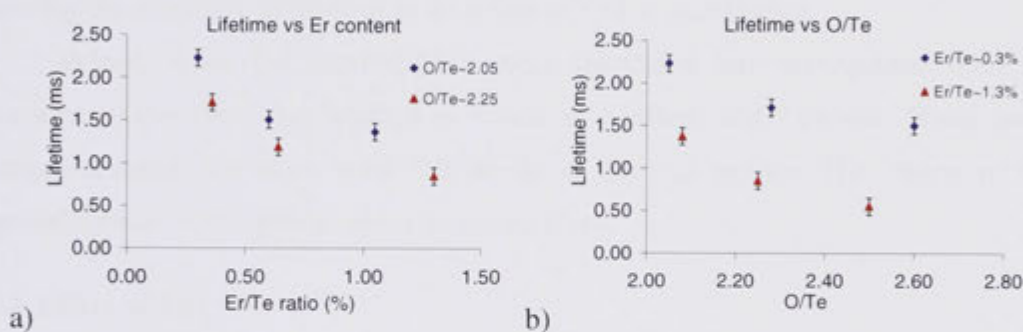


Figure 6.12: Lifetime of sputtered film with varying sputtering condition a) lifetime vs Er/Te when the Oxygen flow is kept at 5.6 (O/Te~2.05) and 6.6 (O/Te~2.25) and b) lifetime vs O/Te when the Er target is set at 7.5% (Er/Te~0.3%) and 12.5% (Er/Te~1.3%)

The lifetime was measured by fitting an exponential function to the tail of the decay curve. This is when the upconversion effect has become negligible. The data are plotted on Figure 6.12 with a) showing the lifetime against Er concentration and b) showing the lifetime against Oxygen content in the films. Clearly, the trends of both set of data are very similar. At low Er concentration and low Oxygen content, the lifetime is highest at around 2.4ms. This value is in excellent agreement with one calculated from the PL spectra using McCumber analysis detailed above. As either parameter increases, the lifetime was reduced. This trend indicates that there is a quenching mechanism that depends on the concentration of Er and the amount of Oxygen in the films.

The measured lifetime is the effective decay rate from level  $^4I_{13/2}$  to  $^4I_{13/2}$ . Upconversion has been eliminated in obtaining the lifetime represented in Figure 6.12. There are several possible lifetime quenching mechanisms including cross relaxation, energy migration, pair-induced quenching (PIQ) or OH contamination as discussed in Section 6.1.6. Cross relaxation involves the population of higher level. However, when the pump is turned off, the effect is very small. Energy migration only conserves the excited ion population as the energy is directly transferred from one ion to the other. PIQ only can be a factor at very high level pumping when the excited ion concentration is significant. It is not the case here where the lifetime is measured from the fit to the decay curve after a significant delay after the pump is turned off. Therefore, a possible cause for the reduction in lifetime is the effect of OH contamination.

Indeed, when the passive films were fabricated into waveguides, there are occasions where there are absorption bands at 1480nm and 1280nm. These bands clearly indicated that there were OH bonds in the waveguides. The effects of OH required further investigation in the Er doped films.

#### 6.5.6 Effect of OH

It is well understood that water contamination in Er doped glasses can strongly quench the lifetime of the 1.5 $\mu$ m emission [144, 146, 147, 219, 221, 397]. This is because the Er ions can be in direct interaction with the OH bond. When the Er ions are excited, the energy can be resonantly transferred to the OH unit as OH has an overtone vibration in the 1.5 $\mu$ m region, and so the energy is lost via the vibrational mode of the OH units. The OH groups are coupled with the cation in the glass network, especially with the network forming cations (in this case, Te<sup>4+</sup>).

The detailed spectroscopic properties of OH in silica have been investigated [398, 399]. In silica, the main OH fundamental vibration is at around 2.7 $\mu$ m, while the first overtone is around 1.4 $\mu$ m, and the third overtone (OH vibration and SiO<sub>4</sub> vibration) is at around 1.25 $\mu$ m [398, 399]. The ratio of the fundamental and the first overtone absorption in Silica is around 160 times. The ratio of the first overtone to the second overtone is 23 times [398].

Detailed studies of OH absorption in tellurite are limited [144-148]. The absorption peaks for tellurite are shifted to longer wavelengths due to the larger mass of



Tellurium compared to Silicon, with a fundamental at  $3.3\mu\text{m}$ , and first overtone at  $1.48\mu\text{m}$  [148]. The strength of the absorption at  $3.3\mu\text{m}$  is around 667 times stronger than that of  $1.48\mu\text{m}$  peak. Until now, there has been no reported direct measurement of the second overtone at  $1.3\mu\text{m}$  in Tellurite glass. We now are in the position to study this because of the availability of long low loss waveguides.

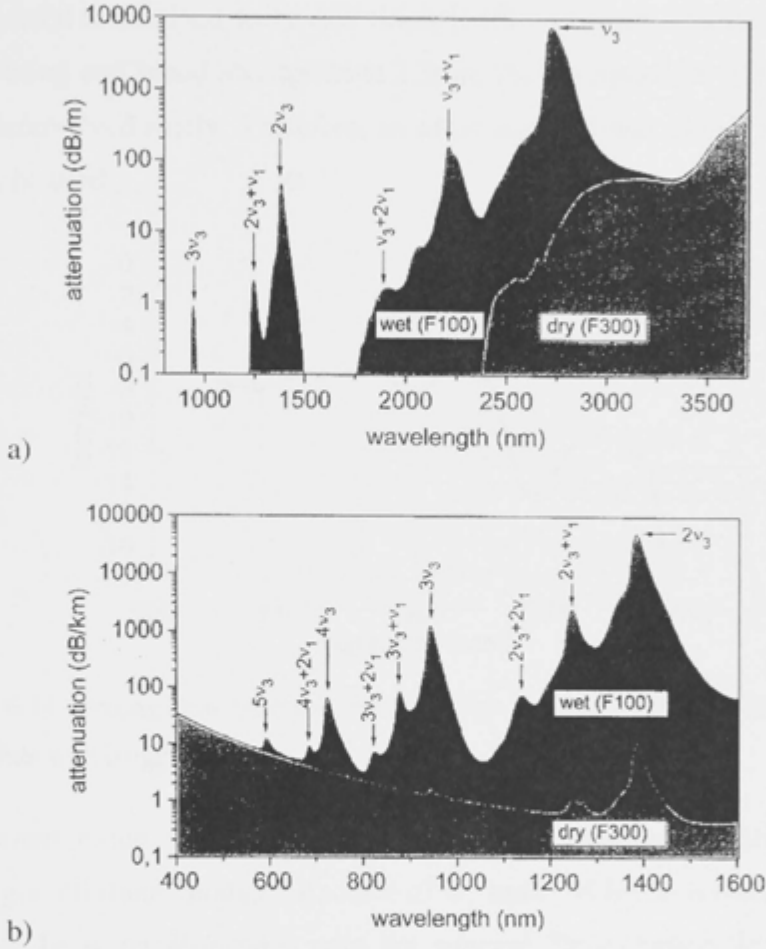


Figure 6.13: Absorption spectrum of OH in silica glass [398].

#### a) OH concentration estimation

The content of the OH groups can be estimated from the measured absorption coefficients at  $\sim 3\mu\text{m}$  by the formula [144, 147].

$$N_{OH} = \frac{N_A}{\epsilon} \alpha_{OH} \quad (6.27)$$

where  $N_A$  is the Avogadro number,  $\epsilon$  is the molar absorptivity of the free OH groups in

the glass,  $\alpha$  is the peak loss per unit length. The absorptivity adopted was the silicate value of  $49.1 \times 10^3 \text{ cm}^2/\text{mol}$  because there is no report on this parameter in tellurite glasses [144, 147, 400]. Since, there was no practical method available to measure the absorption at  $3\mu\text{m}$  directly in Tellurium oxide thin films or waveguides, the value of the absorption at  $3\mu\text{m}$  is estimated by the measurement of the first overtone at  $1.5\mu\text{m}$  and the ratio has been determined to be 667 times [148]. However, because the Er doped sample has strong and broad absorption at  $1.5\mu\text{m}$ , the absorption at  $1.5\mu\text{m}$  due to OH cannot be deconvolved easily. Therefore, an alternative method to estimate the loss at  $1.5\mu\text{m}$  has to be used.

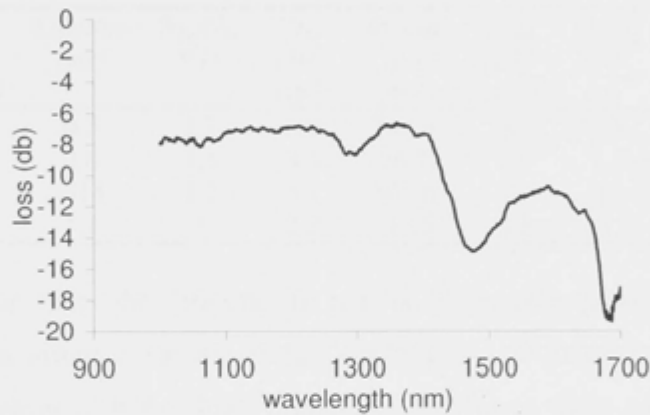


Figure 6.14: Propagation loss spectrum of high OH content Tellurium Oxide waveguide with length of 7cm.

Tellurium oxide waveguides which had large amounts of OH bonds were available by good fortune, though the source of the high OH levels is uncertain (thought most likely to be water absorption onto the sintered Te sputtering target). The loss spectrum was measured in the range from 900nm to 1700nm in the set up as discussed in Chapter 5. The Figure 6.14 is a loss spectrum of  $\text{TeO}_2$  waveguide coded 11. The spectrum shows clearly two dips due to OH absorption. The dip at  $1.48\mu\text{m}$  is due to the first overtone and the dip at  $1.3\mu\text{m}$  is due to the second overtone. The dip at  $1.7\mu\text{m}$  is due to the absorption of the IPG cladding. Clearly, the absorption loss at  $1.3\mu\text{m}$  is around 4.5 times less than that at  $1.5\mu\text{m}$ . This ratio is significantly less than that of OH in Silica as in Figure 6.13 where it is  $\sim 20$  times. In summary, the ratio of first to second overtone is 4.5, the ratio of fundamental vibration to the first overtone is 667 thus the



loss at the fundamental vibration can be calculated from the second overtone using factor of  $4.5 \times 667 = 3002$ .

Table 6.3 give the results of the measurement for some Er doped waveguides. A very large amount of OH groups, with concentration higher than the Er doping level, are presented in the first 3 films. Because this method only works if there is a measurable absorption at  $1.3\mu\text{m}$ , the samples that give absorption of less than 0.1dB at  $1.3\mu\text{m}$  over the whole waveguide length are not absorbing enough to give a reasonable degree of confidence in this analysis.

Table 6.3: Estimation of OH content in Er doped Tellurium oxide films

Sample ID	Loss at 1300 (dB/cm)	Lifetime (ms)	$N_{Er}/N_{Te}$ (%)	$N_{Er}$ ( $10^{20} \text{ cm}^{-3}$ )	loss at $3\mu\text{m}$ ( $\text{cm}^{-1}$ )	$N_{OH}$ ( $10^{20} \text{ cm}^{-3}$ )	$N_{Er-OH}$ ( $10^{19} \text{ cm}^{-3}$ )	OH coupled to Er (%)	Er coupled to OH (%)
44	0.36	0.3	2.7	6.0	241.8	30	3.8	1	6
45	0.14	0.8	1.5	3.3	96.7	12	1.9	2	6
46	0.45	0.14	1.3	2.9	307.8	39	18	5	62
64	~0.02	1.3	1	2.2	~13.5	~1.3	~1.3	8	6

It is clear that, the lifetime is not only directly proportional to the Er concentration. For instance, sample 46 has a relatively low Er concentration compared to #44 but the lifetime of #46 is highly quenched to 0.14ms while #44 has a lifetime of 0.3ms. However, the lifetime seems directly related to the OH concentration as the lower the OH concentration the higher the lifetime. Figure 6.15 plots the lifetime against the 1300nm loss, data taken from Table 6.3. The trend is clearly that as more OH is incorporated into the films the lifetime is quenched more quickly.

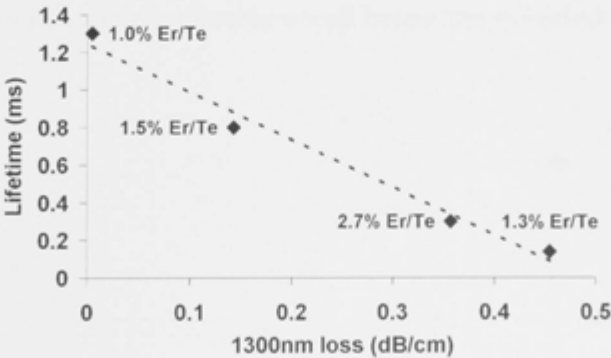


Figure 6.15. Measured lifetime against 1290nm absorption loss in waveguide with ~1-3% Er/Te

According to Equations (6.25), the inverse of the measured lifetime is proportional to the product of Er concentration and the Er-OH coupled pair concentration. However, not all Er ions are coupled to quenching centres due to the random distribution of both Er and OH groups. It is possible to evaluate the Er-OH coupling pair concentration as in the following method.

#### ***b) OH quenching centre concentration***

A series of Er doped films with exactly the same sputtering condition except the Er concentration was made. These films were assumed to have similar amount of OH. This assumption is sensible due to the fact that the first run when the chamber is open was a preconditioning run and the sample is not included in the characterisation. The following samples in this series were fabricated in consecutive runs with the chamber and targets in the same conditions. Figure 6.16 plots the dependence of  $1/\tau_m$  against Er concentration. The slope of this graph gives the value of  $N_{Er-OH}$  of  $1.5 \times 10^{19} \text{ cm}^{-3}$ , and the radiative decay lifetime of  $(2.8 \pm 0.4) \text{ ms}$ , which is consistent with the value obtained from the Ladenburg-Fuchtbauer calculation in Section 6.5.1

Once the intrinsic lifetime is known, the concentration of Er-OH coupled pairs for the samples in Table 6.2 are calculated from Equation 6.25. The values are tabulated in the 3<sup>rd</sup> column from the right on the Table 6.3. Also, the last two columns are the percentage of Er coupled to OH and percentage of OH coupled to Er, respectively. Most numbers are below 10% except sample 46. The sample 46 has more than 60% of Er concentration coupled to OH groups resulted in measured lifetime of only 0.14ms. This makes the lifetime of this sample quenched well below the expected value.

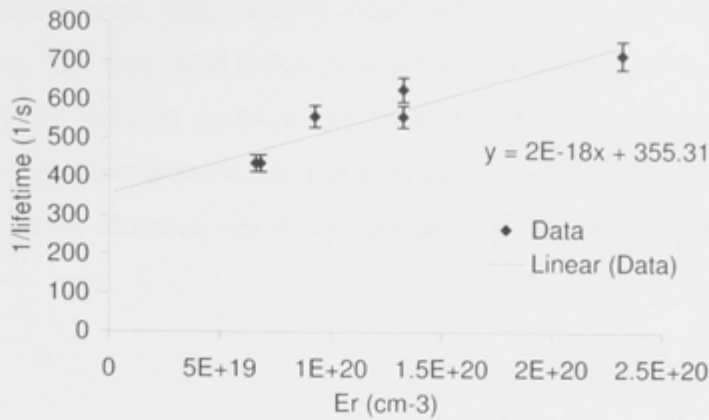


Figure 6.16: The dependence of total rate of decay against Er concentration

The high concentration of Er-OH inside the film can come from three main possible sources. The first possible source is from the vacuum in the sputtering chamber and water desorbed from the system surfaces. The second option is from the Tellurium sintered powder target and the remaining option is from the Er target. The base pressure for the sputtering chamber is  $2 \times 10^{-7}$  Torr. The chamber is usually pumped down overnight after a target change. Unfortunately, the residual gas analyser (RGA) was inoperable for an extended period, therefore, the remnant water in the chamber could not be measured. The Tellurium target was a sintered powder construction and therefore had a large surface area which could absorb a fair amount of OH when it was left in the air for extended durations. Similarly the Er target could also carry water on it though it had far smaller surface area as it was a solid metal target. Further work is required to clearly identify the source that leads to most OH contamination and the measures necessary to prevent it.

6.6 Conclusion

High quality Er doped TeO<sub>2</sub> thin films have been achieved by reactive RF magnetron co-sputtering. The obtained films have been characterised extensively. Concentration of Er can be precisely controlled via changing the Er gun power in range from 0.1% Er/Te to more than 3% Er/Te. The photoluminescence spectra were measured with both free space and fiberised set ups. A highly sensitive fiberised set up was used to measure the lifetime of the 1.5µm emission in thin films and waveguides. These films are highly suitable for compact Er doped waveguide amplifier with broad 1.5µm

photoluminescence spectra with effective bandwidth of more than 60nm and intrinsic lifetime of 2.8ms. The measured lifetimes depend on a number of factors such as Er concentrations, O/Te ratios in the films and critically OH contamination concentration. Therefore, avoiding OH contamination is a very crucial task in producing high lifetime Er doped TeO<sub>2</sub> films. However films suitable for experimental amplifiers have been obtained.

## **Chapter 7:**

# ***Erbium doped Tellurium oxide waveguide amplifiers***

This chapter investigates Tellurium dioxide Erbium doped waveguide amplifiers fabricated using reactive radio-frequency magnetron co-sputtering of Erbium and Tellurium, lithography and inductively coupled plasma (ICP) etching. The obtained waveguides were bi-directionally pumped at 1480nm to obtain signal gain from 1520 to 1630nm. An amplifier with a peak gain of 13dB in a 5cm length was achieved. Simulation of the amplifier performance shows very good agreement with the experimental data. The results show that rare earth doped tellurite waveguides have great potential for use in integrated nonlinear optics as loss compensators, CW lasers, short pulse amplifiers, or mode locked lasers.

### ***7.1 Development of Er doped planar waveguide amplifier***

The advent of Er doped fibre amplifiers (EDFAs) in the 1980s led to a revolution in optical fibre networks propelling optical communications to the status of one of today's key technologies [378]. The EDFAs removed the need for repeaters making very long distance communication possible and enabling wavelength division multiplexing and all optical networks. With the ever increasing penetration of optical fibre even into the local loop, increased transmission speeds, and the need for reduced footprints and lower power consumption, the need for highly multifunctional integrated optical devices is rapidly increasing.

A number of interesting nonlinear materials have been successfully fabricated into single mode waveguides and nanowires such as Silicon on Insulator (SOI) [13, 15-17, 401], and chalcogenide [56, 402, 403]. For instance, SOI waveguides have been intensively studied as optical interconnect technology. Because of its high index contrast, single mode wires at 1.3-1.5 $\mu\text{m}$  need to have dimensions of  $\sim 300\text{nm} \times 300\text{nm}$ . The critical bending radius can be as low as 5 $\mu\text{m}$ . The nonlinear coefficient for this type of

wire is of order of  $300\text{W}^{-1}\text{m}^{-1}$ , 300000 times larger than standard silica fiber. However, the devices still suffer from significant propagation loss. The typical reported propagation loss for SOI technology is 1.5dB/cm [16]. Loss is perhaps the most taxing limitation on multifunctional compact integration. If the loss can be compensated by incorporating an amplifier system such as Er doped waveguide amplifiers (EDWAs), signal can continue to propagate and optical processing can occur over a very long distance on the chip.

EDWAs have excellent potential to provide high gain from a very short device which is advantageous for short pulse amplification, low cost amplifiers, as gain sections for integrated on chip mode locked or CW lasers, and the provision of on chip gain to compensate loss in complex integrated optics devices. They are, therefore, key components in integrated optics. EDWAs have previously been realized by differing techniques in various materials [244], most successfully until now in  $\text{Al}_2\text{O}_3$  [404] or multicomponent phosphate glass [405]. Devices are now commercially available, on chip gains as high as 5.3 dB/cm [251] have been attained along a 3.1cm long waveguide with  $\sim 5\text{nm}$  FWHM gain bandwidth. In one case, 4.1dB in a 0.3cm long (13.7dB/cm) very highly doped device was reported with a  $\sim 35\text{nm}$  FWHM bandwidth [406] though whether this can be scaled to technologically useful gains ( $>15\text{dB}$ ) remains unclear as a longer device reported by the same authors exhibited lower gain per unit length. However there has seemingly been no progress in simultaneously achieving high gains and attaining wider bandwidth operation as is considered desirable for future transmission systems and has been demonstrated for fibre amplifiers [117]. The reasons are many and complex and are related mostly to the intrinsic glass host environment and effects involving the high Erbium concentrations required leading to clustering, concentration quenching, co-operative upconversion, excited state absorption, or other such effects.

Berneschi *et al.*, 2007 [244] summarized some of the recent advances in EDWAs in various materials and technologies. The reproduced data with additional relevant references are shown in Table 7.1. The columns are organized in chronological order from left to right. Comparison between these various devices is not straightforward because each paper has given results under different definitions. For instance, some refer to gain as only signal enhancement (increase of transmitted signal

after turning on the pumping) or internal gain (signal enhancement minus absorption at low input signal levels with no pumping) rather than to the true net gain. Some papers use the value of pump power actually injected into the waveguide while others use the power available at the end of the input fibre. Despite these definition issues, some clear trends can be deduced from the reported results in the literature. It is noted that RF-magnetron based sputtering techniques and ion exchange in particular seem to give the best results in terms of gain per unit length in comparison with direct writing techniques. There are a number of explanations for this. Firstly, waveguides obtained using lithographic methods usually have high index contrast leading to better confinement for both signal and pump modes. Secondly, the high quality and homogeneity of multi-component glassy thin films deposited from the bulk starting glass in typical sputtering methods reduces the possibility of rare earth ion-ion interactions and improves the lifetime.



Table 7.1: Summary of EDWA reported in literatures [244, 407, 408].

Reference	Nykolak [409]	Ghosh [410]	Yan [405]	Van De Hoven [411]	Camy [412]	Li [413]	Wong [414]	Patel [406]	Della Valle[415]	Della Valle [251]	Bradley [416]
Year	1993	1996	1996	1996	1996	1997	2002	2004	2005	2006	2009
Core composition	Soda lime	Soda lime	Phosphate	Al <sub>2</sub> O <sub>3</sub>	Borosilicate	Soda-lime	Phosphate	Phosphate	Phosphate	Phosphate	Al <sub>2</sub> O <sub>3</sub>
Er/Yb concentration	14600ppm	0.7x10 <sup>20</sup> cm <sup>-3</sup> Er	5.3x10 <sup>20</sup> cm <sup>-3</sup> Er	2.7x10 <sup>20</sup> cm <sup>-3</sup> Er	3 et% Er <sub>2</sub> O <sub>3</sub> 3%wtYb <sub>2</sub> O <sub>3</sub>	3.3 wt% Er <sub>2</sub> O <sub>3</sub>	2 wt% Er 2 wt% Yb	8 wt.% Er 12 wt% b	2%wt Er <sub>2</sub> O <sub>3</sub> 4%wt Yb <sub>2</sub> O <sub>3</sub>	2.3 wt% Er 3.6 wt%Yb <sub>2</sub> O <sub>3</sub>	1.17x10 <sup>20</sup> cm <sup>-3</sup>
Technology	Sputtering	Sputtering	Sputtering	Sputtering	Ion exch.	Sputtering	Ion exch.	Ion exch.	Fem. writing	Ion exch.	Sputtering
Length (cm)	4.5	6	1	4	3.9	1.7	~2	0.3	3.7	3.1	5.4
Gain (dB)	15 net	4.5 net	4.1 net	2.3 int.1	9 net	7.2 net	-	4.1 net	9.2 internal	16.7	9.2 int.
Gain/length (dB/cm)	3.3 net	0.75 net	4.1 net	0.6 internal	2.3 net	4.2 net	3.3 net	13.7 net	2.5 internal	5.3 internal	1.7 internal
Pump (mW)	280	80	21 inside	9 inside	130	40 inc.	120 inc.	150 inside	450 inc.	460 inc.	95 inc.
Threshold (mW)	50	8	20	4	40	-	51	-	200	160	~7
Pump wavelength (nm)	980	975/980	980	1480	978	980	980	980	975	975	977
Geometry	Ridge	Ridge	Ridge	Ridge	Diffused	Ridge	Diffused	Diffused	Channel	Diffused	Ridge
Dimension (μm)	1.5 x 5	1.4x9	1.5x4	0.6x2	6.5x5	1.5x8	6x6	4x4	-	5x5	-
Loss (dB/cm)	-	0.1	0.9	0.34	-	0.4	0.8	0.5	0.4	0.4	-

## 7.2 Development of Er doped tellurite devices

Tellurite glasses are well known as excellent rare earth hosts for optical amplification [88]. Tellurites offer a number of advantages as emission hosts for EDWAs over other materials because of their high refractive index (larger emission cross section and more compact devices), large emission bandwidth, low ion to ion cross relaxation, relative independence of the 1.5 $\mu\text{m}$  Er lifetime on concentration, and high Erbium solubility as has been demonstrated in tellurite glass and fibre amplifiers [74, 117, 191, 221]. Whilst there has until now been no demonstration of tellurite based EDWAs with net fibre to fibre gain, it is clear that tellurite based devices have the potential to deliver higher ultimate gain per unit length and bandwidth than previous demonstrations in other materials [74]. The low phonon energy of around 600-800 $\text{cm}^{-1}$  in tellurite also enables the potential use of transitions not possible in other materials commonly used in EDWAs, (for example with  $\text{Pr}^{3+}$  gain at 1.3 $\mu\text{m}$ ).

### 7.2.1 Er doped tellurite fibre amplifier.

The high gain Er doped tellurite fibre amplifier (EDTFA) was first demonstrated by NTT labs in 1997 [199]. An 85cm long Er doped tellurite fibre was pumped with 130mW of 975nm and resulted in a small signal gain of 16dB. The slope efficiency was 0.29dB/mW. The same group also reported high performance EDTFAs with a length of only 50cm but gain of up to 40dB when pumped at 200mW with a 1480nm source. Upon further investigation, the authors found that the gain per unit length for Er doped tellurite fibre was five times larger than that for Er doped silica fibre with almost the same fibre parameters. With the help of a fibre-grating-type gain equalizer, it was possible to achieve a gain of more than 25dB and noise figure of less than 6dB over a wide wavelength range from 1533 to 1603nm, 70nm gain bandwidth [117, 224]. Higher gain (over 25dB) and lower noise (less 5dB) EDTFAs have been obtained with pumping at both 980nm [225] and 1480nm [226]. With the availability of high gain and broadband EDTFAs, demonstration of 1.5Tbits/s (75 x 20Gbits/s) dense wavelength division multiplexed (DWDM) transmission over 200km was achieved [228]. These achievements have proven that Er doped tellurite devices have potential to provide high gain and broad bandwidth for high transmission capacity applications.

### 7.2.2 Er doped tellurite waveguide amplifiers

The potential performance of tellurite based waveguide amplifiers has been modelled by several authors such as Chryssou *et al.*, 2000 [227] who analysed the performance of EDWAs fabricated in tellurite, aluminium oxide and silica waveguides with high Er concentrations. The effects of uniform and pair-induced up-conversion on amplification were examined by Runge-Kutta and full-vectorial finite element analysis. The authors showed that the tellurite glass host materials had many advantages for the fabrication of high-gain integrated optical amplifiers. EDTWAs exhibited higher signal gain and broader bandwidth than EDSWAs. Coupled to its higher cross-section coefficients, then gain flattened amplifiers could easily be achieved. For an optimized length of 8cm, a tellurite waveguide of  $2 \times 2 \mu\text{m}^2$  with dopant concentration of  $1.7 \times 10^{20} \text{ ions/cm}^3$  would produce 1530nm small signal gain of 15dB with 300mW pump at 980nm. In other similar studies [417, 418] the theoretical performances of various glasses including silicate, phosphate, tellurite and borate glasses in broadband systems were investigated. Tellurite was found to outperform phosphate, borate, and silicate glasses in term of peak gains, spectral bandwidth, and transmission capacity.

Despite the development of high gain fibre amplifiers and the potential for high gain EDTWAs, there were no reports of active planar EDTWAs at the outset of the project due to a number of fabrication challenges such as obtaining low loss thin films, waveguides and etching technology. The only demonstration of an EDTWA prior to our published results was a device fabricated in 2008 by femtosecond laser irradiation [248]. The device produced very limited amounts of internal gain (1.2dB over 2.5cm) due mainly to the high propagation losses in the waveguide of 1.3dB/cm at the signal wavelength, this representing the state of the art in tellurite waveguides at the time of this work. This high loss is the main reason for the lack of progress on EDTWAs, and this constraint itself has only recently been released with the demonstration of high quality waveguides reported earlier in this thesis [419]. There have been other attempts to fabricate EDTWAs using different techniques such as ion-exchange, direct writing using UV, femtosecond laser and ion irradiation, and these are now briefly summarised.

**a) Ion-exchange**

As seen in Table 7.1 ion exchange technology can produce high gain EDWAs [251, 412] and waveguide lasers [252], and was therefore investigated in tellurite glasses. Ding *et al.*, 2001 [83] demonstrated Er doped Tungsten tellurite ( $15\text{NaO}-25\text{WO}_3-60\text{TeO}_2-1\text{Er}_2\text{O}_3$ ) slab waveguides using Ag-Na ion-exchange. The ion-exchange was performed by immersion of the glass samples into a molten salt bath of  $2\text{AgNO}_3-49\text{NaNO}_3-49\text{KNO}_3$  (wt%) at temperature in range from  $290^\circ\text{C}$  to  $360^\circ\text{C}$ . The index change achieved at  $1550\text{nm}$  was 0.115. However, the author also reported serious surface corrosion after the long exchange process (34h). Nunzi Conti *et al.*, 2003 [253] used ion exchange to fabricate multimode and single mode slab waveguides in tellurite glasses. Tungsten tellurite ( $\text{WO}_3$ ,  $\text{Na}_2\text{O}_3$  and  $\text{TeO}_2$ ) and zinc tellurite glasses ( $\text{ZnO}$ ,  $\text{Na}_2\text{O}$  and  $\text{TeO}_2$ ) were doped with Er concentration ranging from 0 to 2 mol%. The ion exchange process was performed close to the glass transition in a eutectic solution of  $\text{AgNO}_3$ ,  $\text{KNO}_3$  and  $\text{NaNO}_3$  at  $280^\circ\text{C}$  to  $330^\circ\text{C}$ . The index change for these samples was order of 0.13 and diffusion depths of  $2\mu\text{m}$  were measured. The diffusion constant for  $\text{Ag}^+ \rightleftharpoons \text{Na}^+$  was relatively low leading to exchange times of up to 6h. The authors reported light guiding in the planar structure but fell short of producing active devices. In a more recent ion-exchange experiment by Sakida *et al.*, 2006 [255] on Er doped tungsten tellurite ( $\text{WO}_3$ ,  $\text{Na}_2\text{O}_3$  and  $\text{TeO}_2$ ) the propagation losses on a  $3\mu\text{m}$  thick slab waveguide was measured for the first time to be in range of 2.2 to 6.2 dB/cm. These losses are still too high for any waveguide applications. Furthermore, the index changes obtained was only order of 0.13 leading to a large mode area in the fabricated waveguides. Ion exchange on Er doped tellurite has therefore not been proven to be a good route for waveguide fabrication.

**b) UV and femtosecond direct writing**

Tellurite glasses are known to have some photosensitive effect with UV or femtosecond light [78, 81, 245, 246]. Therefore, it is possible to fabricate an Er doped waveguide by direct writing with laser beams. Nandi and Jose, 2006 [392] reported waveguide writing in an Er doped alumino-phosphate tellurite glass using 45 fs-pulses at  $806\text{nm}$  and  $1\text{kHz}$  repetition rate. The addition of phosphate seems to favour waveguide formation. The waveguide loss was estimated to be less than  $2\text{dB/cm}$ . During 2010, tellurite based Er

doped active waveguides fabricated by femtosecond laser pulses have been made to produce limited amounts of gain [248, 420]. However, the propagation losses remain high (0.9dB/cm), core-cladding index differences are low, mode areas are large, and gain is limited to only 1-2dB over the length of the device.

### *c) Ion Implant*

Ion implant, particularly using Nitrogen, is another method of making waveguides in many materials, e.g. silica, lithium niobate [421-423].  $N^+$  ions have been implanted into the surface of bulk Er doped glass samples to form guiding structures [249, 250, 424]. A 24 $\mu$ m gap created by two 75 $\mu$ m thick silicon covers was used to gate the  $N^+$  ions. The  $N^+$  ions had energy of 1.5MeV penetrate 1.5 $\mu$ m into the WNT glass. The introduction of  $N^+$  into the sample induced negative density changes at the ion stopping range. Light guiding was possible due to the lowering the of index in the stopping layer buried ~1.5  $\mu$ m below the surface. The optical properties such as propagation loss of these waveguides remain to be seen but there has been little effort to reduce the losses below 1 or 2dB/cm[423].

### *d) Summary*

In short, despite notable successes in EDTFAs, EDTWAs with technologically useful gain have not been achieved until now despite intensive experimentation via several different routes. This chapter reports tellurite EDWAs that exhibit high internal gain and net fibre to fibre gain fabricated using reactive RF magnetron co-sputtered Er doped  $TeO_2$  films. Ridge waveguides were fabricated from a layer of pure  $TeO_2$  deposited on top of the Er doped film using standard lithography and reactive ion etching (RIE) with a Hydrogen/Methane/Argon gas mix [419].

## **7.3 EDTWA fabrication with co-sputtering and ICP etching**

### **7.3.1 Thin film deposition**

Erbium doped Tellurium dioxide films were deposited by co-sputtering 3" diameter Te and Er targets in an Oxygen/Argon gas mix as discussed in Chapter 6. The Te target was run at 148W, the chamber pressure was 5mTorr, and the total flow of Ar and  $O_2$  was kept at 15sccm. Varying the  $O_2$ /Ar mix allows tuning of the Oxygen content in the

films, higher O<sub>2</sub> flow leading to higher Oxygen content in the deposited films but also a slower deposition rate. Typical conditions were 6sccm O<sub>2</sub>, 9sccm Ar. The Erbium concentration was controlled via the Er gun power, and was measured post deposition by a laser ablation ICP mass spectrometer. Films with an Er/Te ratio of up to 3% were fabricated by this method. Typically, a 1% Er/Te ratio film was achieved with 72W of RF power on the Er gun.

### 7.3.2 Etching of Er doped TeO<sub>2</sub> waveguide

As mentioned in the previous chapter, one of the major challenges in the development of low loss tellurite waveguides has been etching technology. Plasma etching is more favoured than other etching techniques because it can provide high quality etched surfaces with high anisotropy, and accurate in situ etch rate monitoring [305]. Previous work on plasma etching of Tellurium oxide waveguide employed physical etching using an Argon plasma resulting in propagation losses of 6dB/cm [257]. As reported in Chapter 5 and in our recent paper [419], etching with a Hydrogen/Methane/Argon gas mix produced high quality stoichiometric Tellurium oxide waveguides with propagation losses less than 0.1dB/cm. This fabrication route then seemed to be a natural candidate for EDTWAs.

Figure 7.1 a) shows a typical profile of an etched Tellurium oxide waveguide. The obtained structures have smooth etched surfaces and vertical side walls. However, when the Er doped thin films were etched using the Hydrogen/Methane/Argon gas mixture, the surfaces became very rough with columnar and grassing effects as seen on Figure 7.1 b). This result was due to re-deposition of low volatility of Erbium and Erbium compounds such as Erbium tellurite, Erbium dihydride [425, 426]. Whilst ultimately these compounds can be made volatile by heating up the substrate to high temperature[425, 426], this required substantive modifications to the etch machine and could not easily be undertaken within the scope of this project. Thus an alternative method to fabricate a waveguide was sought which would not involve etching the Er doped material.

A design with two layers, Er doped underneath and pure Tellurium oxide on top, provides a solution to overcome the need to etch the Er doped films directly. However, the etching depth has to be precise in order to avoid over etching into the Er doped layer.

Since the RIE system used in Chapter 4 to achieve low loss passive waveguides was not equipped with an etch rate monitor it could not be used to fabricate this Er doped structure.

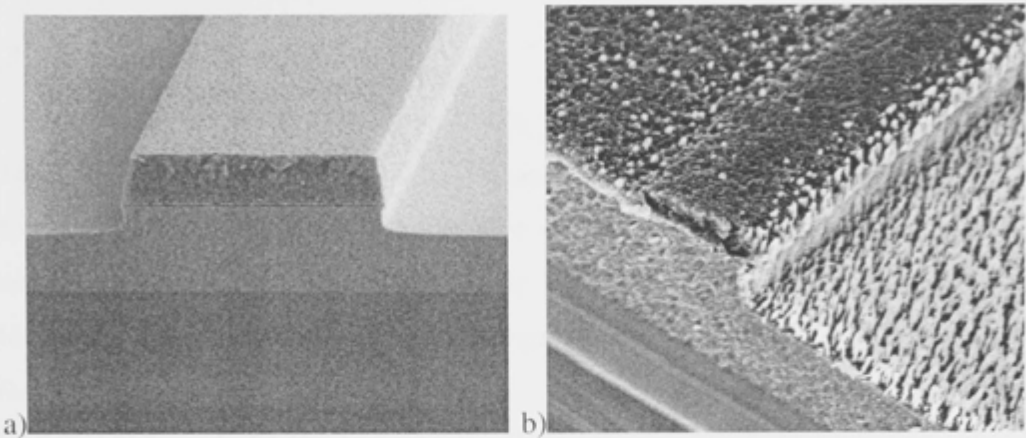


Figure 7.1: Etching of a)TeO<sub>2</sub> only waveguide and b)Er doped waveguide (image size ~5μx5μm)

Table 7.2: ICP etching parameter setting

<i>Parameter</i>	<i>Value</i>
Pressure (mTorr)	10
CH <sub>4</sub> flow (sccm)	10
H <sub>2</sub> flow (sccm)	30
Ar flow (sccm)	30
FW power (W)	50
ICP power (W)	0
Etching rate (nm/min)	~50

The inductively coupled plasma (ICP) system was instead used to etch the films to fabricate the waveguide. The detailed steps for the fabrication were reported in Section 4.3. The sample was loaded into the chamber which was pumped to the base pressure of  $2 \times 10^{-6}$  Torr. The temperature of the substrate holder was kept at 20°C. The parameter settings used to etch this sample are shown on Table 7.2. The in situ etching rate monitor using an interferometric technique with a 677nm laser beam was used to measure etching rate. This enabled high accuracy monitoring of the etch rate and allowed the pure TeO<sub>2</sub> layer to be etched down to 100nm above the Er doped layer. The



remaining photoresist was stripped using an Oxygen plasma and wet etching. The obtained strip loaded waveguides have high quality etching on both vertical and horizontal etched surfaces.

### 7.3.3 Properties of Er doped waveguides

A bilayer film was fabricated with a 1.0% Er/Te ( $\sim 2.2 \times 10^{20}$  ions/cm<sup>3</sup>) 1350nm Er layer and index at 1550nm of 2.075, and a pure TeO<sub>2</sub> layer 530nm thick. The lifetime of the film measured from the edge was 1.3ms, which suggested that residual water contamination remains. A waveguide was prepared as previously described to yield a ridge waveguide with 400nm etch depth (see Figure 7.2 a)). The bare patterned wafer was then coated with a cladding. The material used was an inorganic polymer glass (IPG<sup>TM</sup>) from RPO Pty Ltd. Finally, the wafer was hand cleaved with a diamond scribe. The final chip length was 5cm with waveguide nominal widths of 1, 2, 3 and 4 $\mu$ m. The modal properties of the obtained waveguides were calculated and are tabulated in Table 7.3. The 1 and 2 $\mu$ m waveguides are single moded with only TE<sub>0</sub> and TM<sub>0</sub>. However, the TM<sub>0</sub> is very weakly guided in the 1 $\mu$ m waveguides. The 2 $\mu$ m wide waveguide confines both TE<sub>0</sub> and TM<sub>0</sub> as well. The 3 $\mu$ m and 4 $\mu$ m also support TE<sub>1</sub> and TM<sub>1</sub> modes. The coupling efficiencies from the 2.5 $\mu$ m spot diameter tapered fibre lens are relatively good for all the waveguide widths, in the range of  $\sim 1$ -1.3dB each end. Including reflective effects, this leads to an expected insertion loss minimum of 3-3.5dB. The fundamental modes are well confined in 2-4 $\mu$ m waveguides with the mode areas of 5.3-5.8 $\mu$ m<sup>2</sup> and 4.3-5.4 $\mu$ m<sup>2</sup> for TE and TM, respectively (Table 7.3).

Since the waveguide is a version of a strip-loaded structure the modes do not overlap with the Er doped area 100%. The overlap factor can be calculated by:

$$\Gamma = \frac{\int_A I(x, y) n(x, y) dx dy}{\int_A I(x, y) dx dy} \quad (7.1)$$

where  $I(x, y)$  is the intensity profile of the mode and  $n(x, y)$  is the normalized Er density. Despite the strip-loaded structure using here, the overlap factor is in order of 84-96% for all modes as shown on Table 7.3.

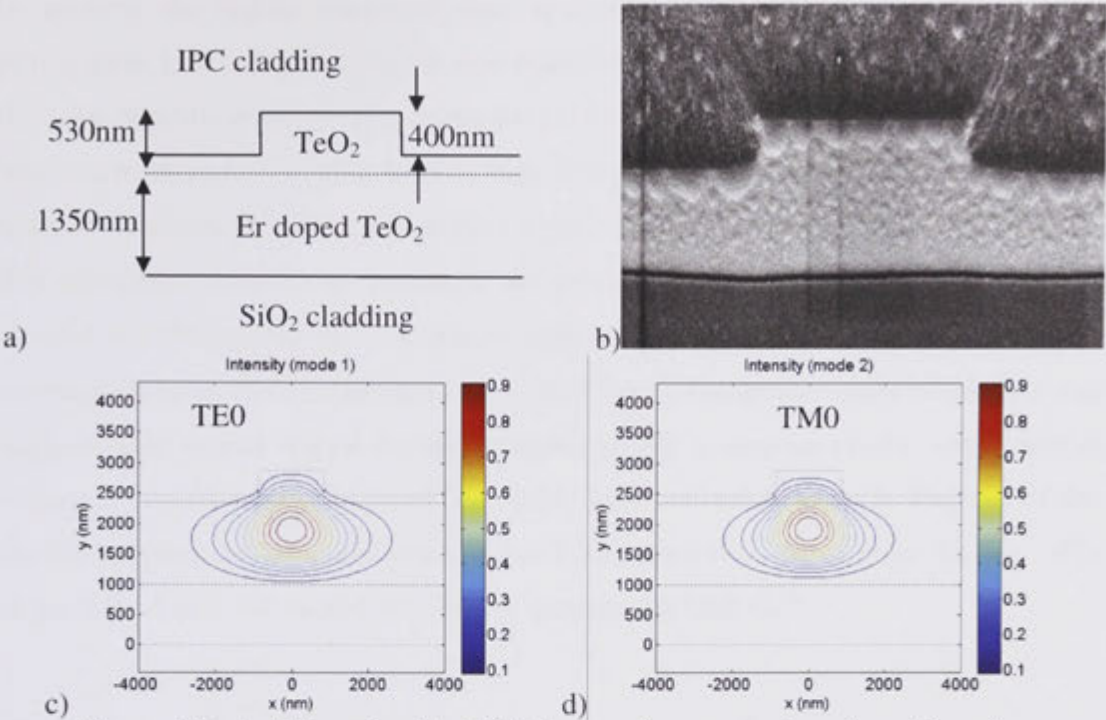


Figure 7.2: a) Schematic, b) SEM image of cross-section of an Er active waveguide; c) and d) are TE<sub>0</sub> and TM<sub>0</sub> mode profiles of the 2μm wide waveguides, respectively The spotty surface and angled interface are due to imperfect cleaving.

Table 7.3: Dimension and fundamental mode properties of Er doped waveguide (coded 64\_4).

Mask nominal width (μm)	Waveguide width (μm)	Overlap with Gaussian (dB)		Overlap with Er layer		Effective mode area (μm <sup>2</sup> )	
		TE	TM	TE	TM	TE	TM
4	3.7	1.17	1.13	0.84	0.85	5.85	5.22
3	2.7	1.04	0.94	0.86	0.87	5.28	4.58
2	1.7	1.25	1.02	0.89	0.89	5.31	4.34
1	0.8	2.06	1.65	0.95	0.96	6.43	7.60

The white light loss spectrum for the 2μm nominal width waveguide measured with the 2.5μm waist tapered fibre lens is shown in Figure 7.3. A total fibre to fibre insertion loss of 6.5dB at 1550nm, comprising 3.5dB of mode overlap and facet reflection leads to 3.0dB of background loss for 5cm (~0.6dB/cm). The background loss

is uniform the whole measured loss spectrum from 1100nm to 1650nm. This propagation loss is higher than the one reported early in pure  $\text{TeO}_2$  waveguides using the same deposition and etching technique [419]. It can be explained by the background loss due to imperfect etching in ICP, high Erbium concentration and the effect of the interface between the active and passive layers. It can also be attributed to the fact that this calculation tend to overestimate the propagation loss. The loss spectrum also showed a 1290nm loss of  $\sim 0.02\text{dB/cm}$  indicating a  $3\mu\text{m}$  OH loss of  $\sim 14\text{cm}^{-1}$ . This corresponds to an OH concentration of  $1.3 \times 10^{20}\text{cm}^{-3}$ . The measurement of lifetime also suggests that around 6% of Er have coupled to OH quenching centre, which has an estimated concentration of  $1.3 \times 10^{20}\text{cm}^{-1}$  (See Section 6.5.5, Table 6.2). Because of this Er-OH coupling the measured lifetime was 1.3ms. However, the intrinsic lifetime of Er in the  $\text{TeO}_2$  films still should be 2.8ms as measured in Chapter 6.

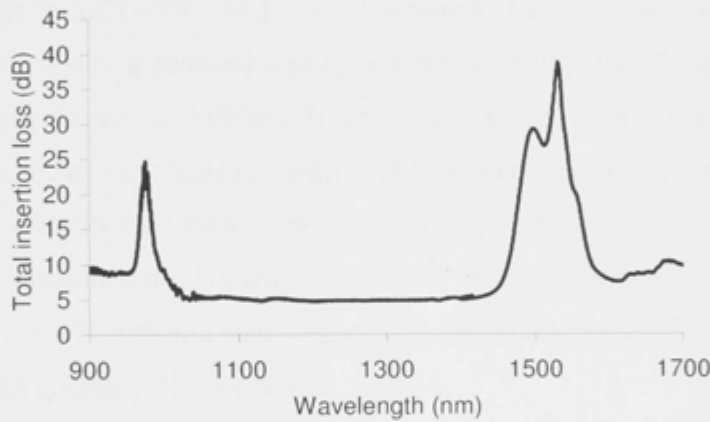


Fig.7.3: Insertion loss spectrum of  $1.5\mu\text{m}$  wide 1.0%Er/Te. The whole spectrum is combined from 2 measurements, first with white light from an Arc mercury lamp for range from 900nm 1400nm and the second with supercontinuum source for 1400nm to 1700nm range.

The absorption spectrum also allows the peak absorption cross-section to be estimated. White light loss measurement gave a maximum absorption at 1530nm for the 5cm long waveguide of 33dB (6.6dB/cm). The overlap factors for both  $\text{TE}_0$  and  $\text{TM}_0$  modes are 0.9. Therefore, the peak cross-section is calculated as  $7.7 \times 10^{-25}\text{m}^{-2}$ . The McCumber theory then allows the emission cross-section to be calculated as outlined in Section 6.5. Figure 7.4 shows the scaled measured absorption and emission cross-section for Er doped Tellurium oxide films and waveguides. The McCumber theory and

measured emission cross-section agree very well except out in the 1600nm tail region. The agreement here is compromised as the actual waveguide losses here are uncertain due to the OH contamination and the effects of top cladding absorption in the IPG film. The emission cross-section extends to beyond 1630nm. The locations of the peak of the absorption and emission curves are almost identical at 1533nm and peak value of  $7.7 \times 10^{-25} \text{m}^{-2}$ . Also on Figure 7.4, a maximum pump efficiency curve is plotted. This curve represents maximum inversion possible versus pump wavelength in the ideal scenario when pumped in the vicinity of 1480nm. Due to pump stimulated emission, the population inversion is capped by the value [378]:

$$\beta(\lambda) = \frac{\sigma_a(\lambda)}{\sigma_a(\lambda) + \sigma_e(\lambda)} \quad (7.2)$$

The pumping efficiency is decreasing as the pump wavelength increases. At 1480nm the efficiency is around 75%. At lower wavelength, the efficiency is higher but the absorption cross-section is reduced leading to lower overall pump absorption. The slope of the efficiency curve at 1480nm is relatively gentle at 3%/10nm. The capped efficiency is a major disadvantage with 1480nm pumping. Pumping at 980nm can eliminate this issue because there is no emission cross-section at 980nm compared to the absorption cross-section. However, this is an object of future experiments where improvements for 980nm pump coupling into the waveguide have to be made while still maintaining high quality 1.5 $\mu\text{m}$  operation.

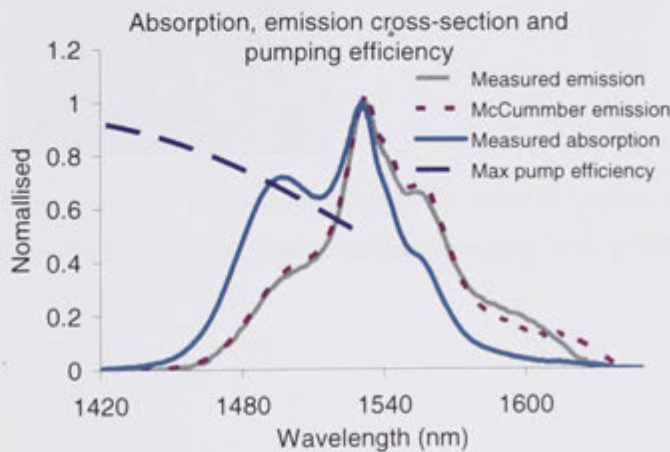


Figure 7.4: Measured absorption, emission cross-section spectra for Er doped Tellurium Oxide thin film. The y axis is normalized to  $7.7 \times 10^{-25} \text{m}^{-2}$ .



## 7.4 EDTWA characterisation

### 7.4.1 Experimental measurement of gain curves

The high reflectivity of the AR coatings on the tapered fibre lens and additional 980nm propagation losses in the waveguide made pumping at 980nm impractical so gain measurements were performed using the bi-directional pumping setup shown in Figure 7.5. The 5cm long Er doped waveguide was pumped bi-directionally by two 1475nm pumps. Each pump could deliver 250mW of broad band (10nm bandwidth) multiple longitudinal mode output measured at the fibre output after the isolator. The pump output spectra are highly dependent on the current and temperature as there was no fibre Bragg grating attached to the diode as shown in Figure 7.6. The observed increase in wavelength with drive current could lead to slight lowering of the pump efficiency, but this effect was not too drastic due to the low slope of the pump efficiency curve, as shown in Figure 7.4. Another issue with this high dependence of pump output against diode setting is in setting suitable simulation parameters.

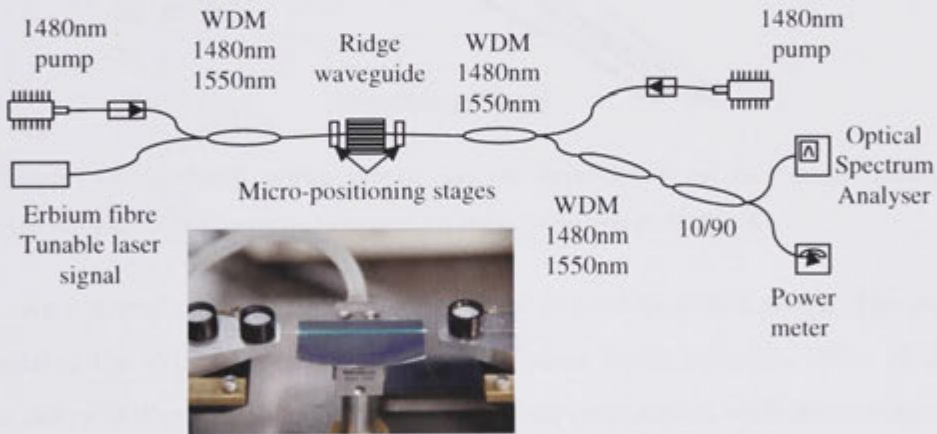


Figure 7.5: Gain measurement experimental setup, the inserted picture show the pumped waveguide which emits green due to nonlinear process such as ESA.

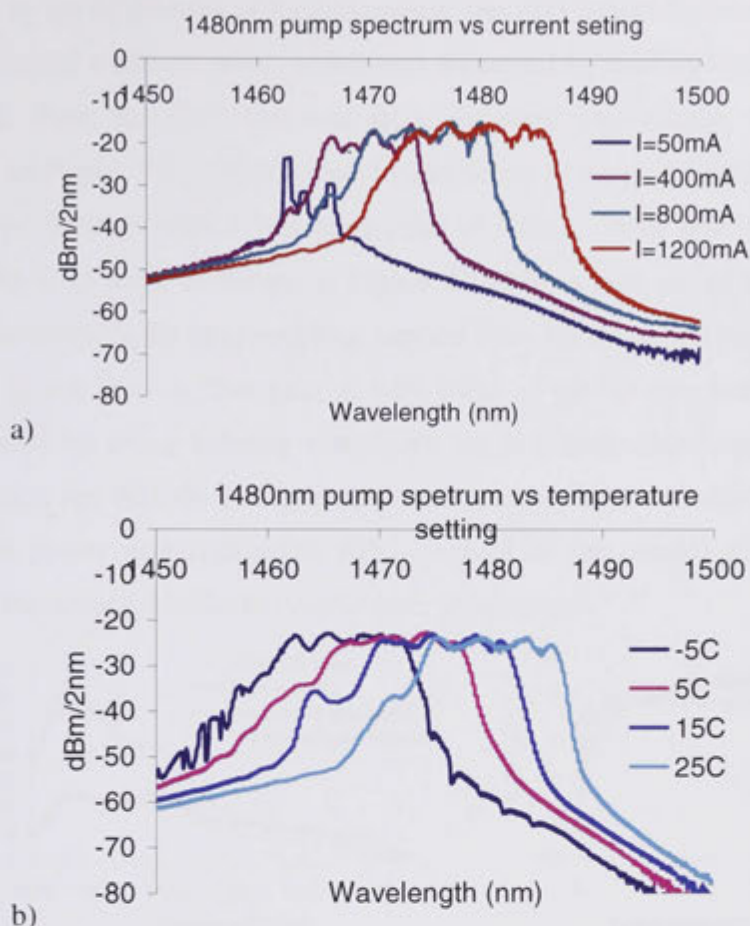


Figure 7.6: 1480nm pump output spectra dependence on a) current setting (temperature=25°C) and b) temperature setting (current at 1200mA)

An external cavity tunable CW source was used as a seed signal. The power of the signal at the WDM input was tuned to different levels between -30 to 10dBm. At powers below 0dBm, the tunable laser was used in conjunction with attenuators. Higher powers were achieved by the addition of an EDFA. The CW laser could be tuned from 1520nm to 1630nm. The pumps and signal were combined and decoupled by broadband 1420-1490nm/1520-1620nm WDMs. Pump and signal were coupled into and out of the waveguide by tapered fibre lenses made from SMF28 fibre. The lenses provided a Gaussian beam with waist diameter of  $2.5\mu\text{m}$  and working distance of  $14\mu\text{m}$ . The internal gain was measured by the signal enhancement at the output minus the absorption. The signal enhancement was measured by the signal difference between pump on and pump off. The absorption was measured at low average power with white light or supercontinuum sources to avoid bleaching.

In the first series of measurements, the gain spectrum from 1520nm to 1640nm at maximum available pump power was measured by seeding with two different types of light. First, the CW laser was set at different wavelengths. The gain spectra are shown on Figure 7.7 a). Gain existed from below 1520nm (limited by the pump WDM) to above 1630nm with a 3dB bandwidth of  $\sim 40$ nm. Peak internal gain of 14dB was obtained at 1530nm as shown on Figure 7.7 a) for a gain per unit length of 2.8dB/cm. Even factoring in the total coupling, tapered fibre lenses and propagation losses this still results in net fibre to fibre gain of 6dB. Most of the off chip losses can ultimately be eliminated by using existing techniques for low loss mode matching [427] and by integrating the WDMs. The gain spectrum accuracy was also checked by injecting low average power supercontinuum light in place of the tunable laser. As Figure 7.7a) shows the accuracy with the tunable laser is adequate.

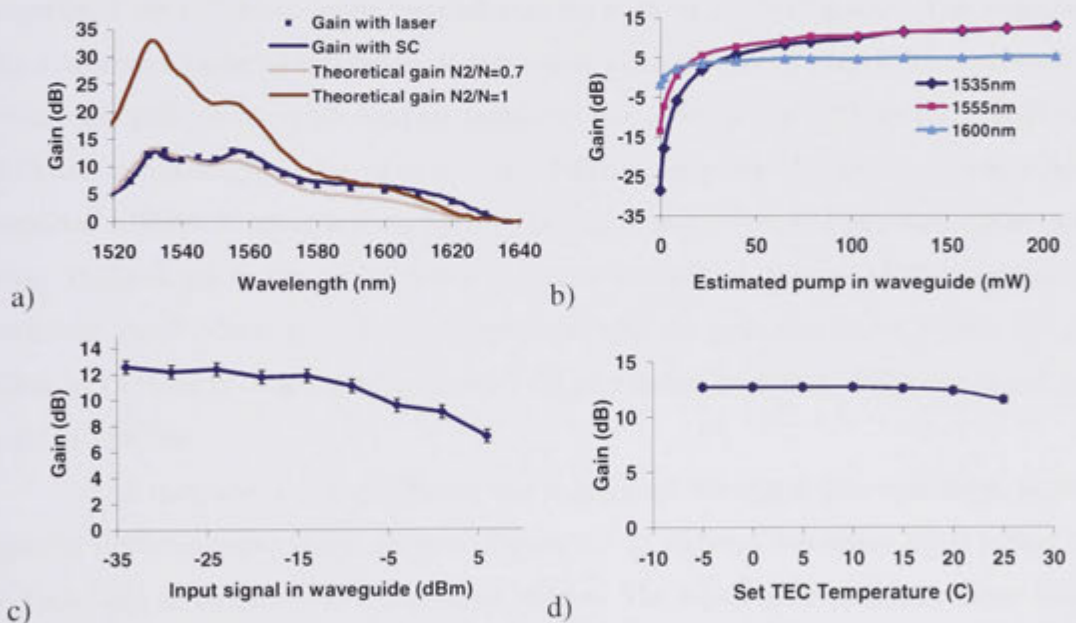


Figure 7.7: a) Measured small signal internal gain, b) pump saturation response at 1535nm 1555nm and 1600nm, c) signal gain saturation gain characteristics at 1535nm with both pumps and d) dependence gain at 1535nm on pump temperature (pump wavelength tuning).

The measured gain curves appear limited by inversion clamping at about 70% as gauged by the shape of the gain curve [117] due to the 1480nm pumping [428]. Along with the measured gain data in Figure 7.7 a) are plotted theoretical curves for the gain. These were obtained from the infinite pump approximation [406] at 100% and 70%



inversion, for the latter with the 1480nm pump effective cross-section calculated as from Becker *et al.*, 1997 [190] using the measured absorption and McCumber emission theory. This simple theoretical estimation gives good agreement with the experiment and predicts that the peak gain at 1533nm would be considerably improved to 33dB by using non-resonant 980nm pumping to achieve higher inversion. However, there is a penalty in the bandwidth as the 1530nm peak is much narrower (10nm width at 3dB down). Higher Er doping and gain flattening devices could, however, be used to extend the gain bandwidth.

In the second series of measurements, the gain saturation curve, ie. the gain at different pump powers, was measured. The pump power was tuned by setting the diode pump current to various values. The CW laser was tuned to 3 wavelengths 1535, 1555 and 1600nm. The three curves are shown on Figure 7.7 b). Here, the pump power axis represents the estimated pump coupled into the ends of the waveguides. The amplifier gain appeared close to saturation at maximum available pump power. The thresholds where the gain curves cross zero are relatively low at 9mW for 1555nm and 20mW for 1535nm compared to value of 60mW and 100mW, respectively, of the previous best reported EDWA in tellurite glass [420]. The signal at 1555nm initially had higher gain than 1535nm but as the pump power increased further the gain at 1535nm started to overtake the 1555nm gain. This is consistent with the gain spectra on Figure 7.7 a). Gain at 1535nm is strongly dependent on the population inversion whilst this is not the case at 1550nm.

The third series of experiments was to measure the signal gain saturation, ie. the gain at different input signal powers. Figure 7.7 c) shows a saturation input power of 0.4mW and an output power exceeding 10dBm. The signal gain gradually drops from 13dB at low input signal to around 8dB at 5dBm of input signal. Therefore, potentially, high power output EDWAs in TeO<sub>2</sub> are possible.

Finally, the diode pump temperature was tuned in order to see the effect of pump spectrum on the gain. It was found that the spectra of the pump did have some small effect on the gain as shown on Figure 7.7 d). The reduction in gain at 1535nm was around 1dB when the temperature setting was tuned from -5°C to 25°C. This is because there is significant shift in operating wavelength of the Fabry-Perot pump diodes depending on the diode setting. When the temperature setting was changed from

-5°C to 25°C, the centre wavelength of the pump shifted around 13nm from around 1467nm to 1480nm. This reduced the maximum pump efficiency around 5% as shown on Figure 7.4. Hence, the reduction of gain at higher temperature setting occurred.

#### 7.4.2 Modelling of Er doped Tellurium oxide waveguides

The simple theoretical calculations of gain spectra in Figure 7.7 a) are crude approximations as no pumping dynamics are taken into account. Proper modelling of Er doped waveguides involves solving the modal properties of the excited waveguide and the partial differential equations describing the populations of the different levels discussed in Chapter 6. Also, the ASE has to be taken into account. A commercial package from Optiwave System Inc. was used to fully model the performance of the Er doped waveguide. The Er/Yb doped waveguide amplifier package was used as the main element of the simulation. Since there is no Yb in this device, its concentration was simply set to zero. The model is based on the solution of the propagation equations using, directly, the solutions of the involved electromagnetic fields and the exact Er transversal distribution. The modal and propagation equations are solved using the finite-element method and the Runge-Kutta algorithm, respectively.

The 1480nm pumping schematic diagram is shown in Figure 7.8. In this case, the pump energy level belongs to the main level 2 ( $^4I_{13/2}$ ). However, due to the presence of the nonradiative transitions inside the level  $^4I_{13/2}$ , the pump level is called level 3. This is not to be confused with the level  $^4I_{11/2}$  when the system is pumped at 980nm region. The non-radiative rate  $A_{43}$  embodies the non-radiative rate between the levels  $^4I_{9/2} \rightarrow ^4I_{11/2}$  and  $^4I_{11/2} \rightarrow ^4I_{13/2}$  so that the level  $^4I_{11/2}$  is not considered in the rate equations. Hence, the upconversion effect due to  $C_3$  from level  $^4I_{13/2}$  is also ignored. This is acceptable due to the fact that there is no direct excitation to this level and there is very fast non-radiative decay from  $^4I_{11/2}$  to  $^4I_{13/2}$ . The rate equations for 1480nm pumping are therefore:

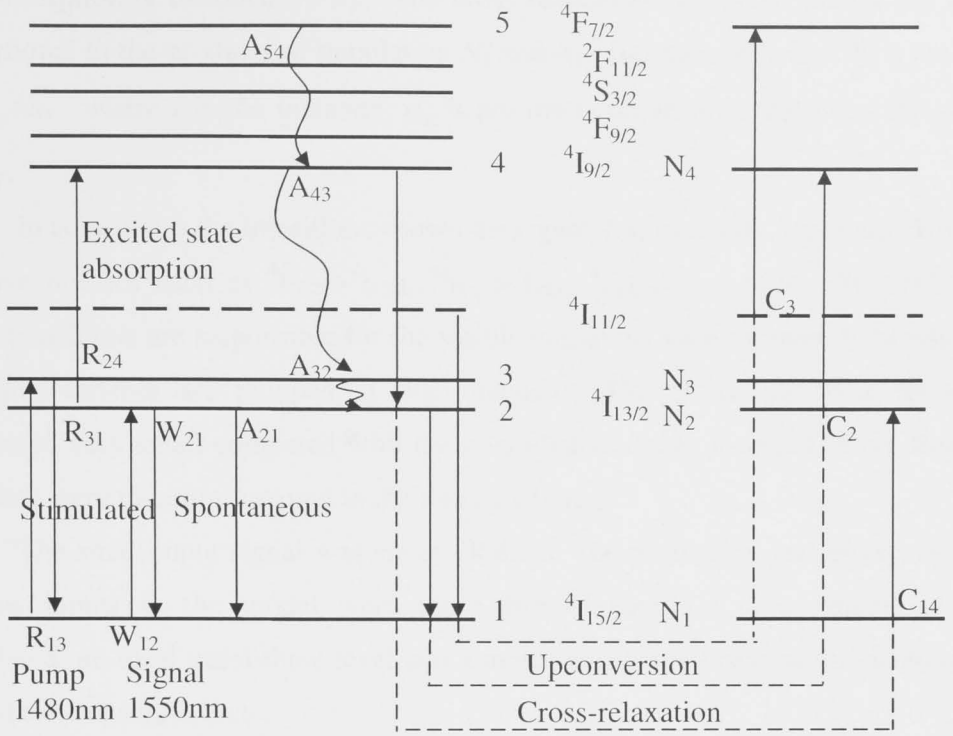


Figure 7.8: Schematic diagram of major transition of Er in glasses pumping at 1480nm with excited state absorption, cross-relaxation and up-conversions. The curved arrows indicate non-radiative transitions and solid arrows indicate the radiative transitions.

$$\begin{aligned}
 \frac{dN_1}{dt} &= -R_{13}N_1 + R_{31}N_3 + A_{21}N_2 - W_{12}N_1 + W_{21}N_2 + C_2N_2^2 - C_{14}N_1N_4 \\
 \frac{dN_2}{dt} &= -A_{21}N_2 + A_{32}N_3 + W_{12}N_1 - W_{21}N_2 - 2C_2N_2^2 + 2C_{14}N_1N_4 - R_{24}N_2 \\
 \frac{dN_3}{dt} &= R_{13}N_1 - R_{31}N_3 - A_{32}N_3 + A_{43}N_4 \\
 \frac{dN_4}{dt} &= R_{24}N_2 - A_{43}N_4 + C_2N_2^2 - C_{14}N_1N_4 \\
 N_1 + N_2 + N_3 + N_4 &= N_0
 \end{aligned} \tag{7.3}$$

$N_{1-4}$  are the concentrations of  $\text{Er}^{3+}$  in excited states 1-4 as in Figure 7.8. The total Er concentration is  $N_0$ .  $A_{ij}$ 's are the non-radioactive rate from level  $i$  to level  $j$ .  $A_{21}$  is the fluorescent rate.  $R_{13}$  and  $R_{31}$  are the pump rate and rate of stimulated emission of the pump. Upconversion is accounted for with coefficient  $C_2$  for upconversion from level 2 to 4. The upconversion effect is related to the square of the populations. The excited

state absorption is included by  $R_{24}$ . The cross-relaxation is represented by  $C_{14}$  and is proportional to the products of population  $N_1$  and  $N_4$ . The rates  $R_{ij}$ 's and  $W_{ij}$ 's are equal to  $I\sigma_{ij}/h\nu$  where  $I$  is the intensity,  $\sigma_{ij}$ 's are the cross-section, and  $h\nu$  is the photon energy.

In addition to the transitions shown on Figure 7.8, in reality, there are also other radiative braches such as  $^4F_{7/2} \rightarrow ^4I_{15/2}$ ,  $^4S_{3/2} \rightarrow ^4I_{15/2}$ ,  $^4F_{9/2} \rightarrow ^4I_{15/2}$  [194, 386, 393, 429]. These transitions are responsible for the visible emissions such as green light when the Er doped devices are pumped at high intensity. The effects of these terms are considered very small compared with the nonradiative decay included in the Equation 7.3. They were therefore ignored in the rate equations.

The small input signal was set at -30dBm. The absorption and emission cross-sections inputs to the model were those from Figure 7.4. Two situations were considered: an ideal quasi-three level and a more practical scenario with upconversion, excited state absorption etc.

Table 7.4 Parameters for gain simulations. Some parameters are based on Hu *et al.*, 2001 [194], Lopez-Barbero *et al.*, 2000 [430].

Parameters	Ideal	Model
Lifetime (ms)	2.6	2.6
Propagation loss (dB/cm)	0.6	0.6
Waveguide length (cm)	5.0	5.0
$A_{32}(s^{-1})$	$1 \times 10^9$	$1 \times 10^6$
$A_{43}(s^{-1})$	$1 \times 10^9$	$1 \times 10^6$
$A_{54}(s^{-1})$	Infinite	Infinite
$C_2(m^3/s)$	0	$2.5 \times 10^{-23}$
$C_3(m^3/s)$	0	$1 \times 10^{-24}$
$C_{14}(m^3/s)$	0	$3.5 \times 10^{-23}$
$\sigma_{24}$ -ESA cross-section ( $m^2$ )	0	$4 \times 10^{-26}$
Pair-induced (%)	0	0

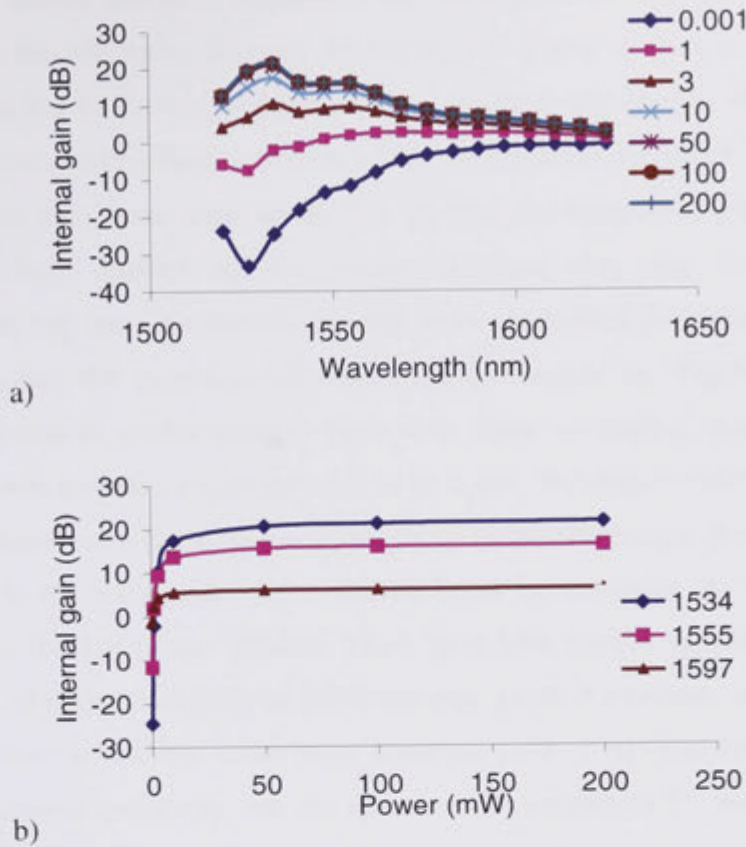


Figure 7.9 a) Gain spectra at various pump power in an ideal 2 level Er doped system pumped at 1475nm-the pump power on the legend is in mW at each end b) the gain saturation simulation at 1535, 1555 and 1597nm.

In the ideal case, the system has no nonlinear processes occurring such as up-conversion, cross-relaxation, ESA and only pumping from level 1 to level 2, and the stimulated and spontaneous emission from level 2 to level 1. There are no loss mechanisms in this idealised case. All pump power into the system returns as amplified signal, stimulated pump emission, or as ASE. The parameter settings for this case are tabulated in Table 7.4. The results of the gain spectra calculations at various pump powers and gain saturation at 1534nm, 1555nm and 1600nm are shown on Figure 7.9. A very low pump power of 0.0001mw was run to obtain the absorption spectrum of the waveguide. It agrees very well with the measured input absorption. As the pump power increases, the signal obtains gain very quickly. It takes less than 3mW to obtain positive gain at 1535nm. The maximum gain is 20dB at 1535nm. The gain appears saturated at around 50mW pump at each end.

In the second scenario, parameters are introduced for non-linear loss process represented in the schematic diagram on Figure 7.8. There are loss mechanisms that now take place due to the cross-relaxation, up-conversion and excited state absorption. As those processes take effect, a portion of the energy from the pump is converted to phonons in the transitions from levels 5 to 2. The pair-induced and OH quenching centres have been ignored for the moment because they only have significant contribution to the loss mechanism at very high population inversion. In order to accurately explain the experimental results, all parameters on Figure 7.8 must be reasonably estimated. Unfortunately, there have been no detailed measurements of radiative and non-radiative transition rates in Er doped Tellurium oxide thin films. The radiative transition rates could be calculated using Judd-Ofelt theory. Nevertheless, it is not practical in the waveguide due to the difficulty in measuring the full absorption spectrum from the UV to the infrared. There have been limited reports of simulation parameters in Er doped bulk tellurite [194] and fibre [430]. Parameters such as  $A_{32}$ ,  $A_{43}$ ,  $C_3$  and  $C_{14}$  were selectively taken from literature [194, 430]. The two critical (and relatively unknown) parameters are the upconversion coefficient  $C_2$  and pump excited state absorption cross section  $\sigma_{24}$ . Therefore, fitting to the measured gain spectra and gain saturation curves was performed by adjusting those two parameters. The ESA cross-section  $\sigma_{24}$  strongly affects the maximum saturated gain while the upconversion  $C_2$  is critical in determining how fast the gain approaches that maximum value, ie. the slope and curvature of the gain saturation curves. The simulation results are shown on Figure 7.10 a) and b). Here the all gains are internal gain. The gain saturation curves agree extremely well for most parts of the data. There is a somewhat larger discrepancy between the simulation and experimental data on the gain spectrum, reaching a maximum difference of around 3dB at 1530nm. This could simply due to the error in emission cross-section calculation as it was estimated from McCumber theory.

The effects of up-conversion, cross-relaxation and ESA are significant. In the ideal case, the pump threshold for the gain to be positive was only 1-3mW compared to 20mW when these effects were included. The signal gain was saturated at 50mW for the ideal case. Further pumping did not provide any additional gain. The full model case and the experiment were not saturated despite being pumped at more than 200mW. The



peak 1530nm gain also experiences a reduction from 20dB to 16dB, once the non-linear effects are added.

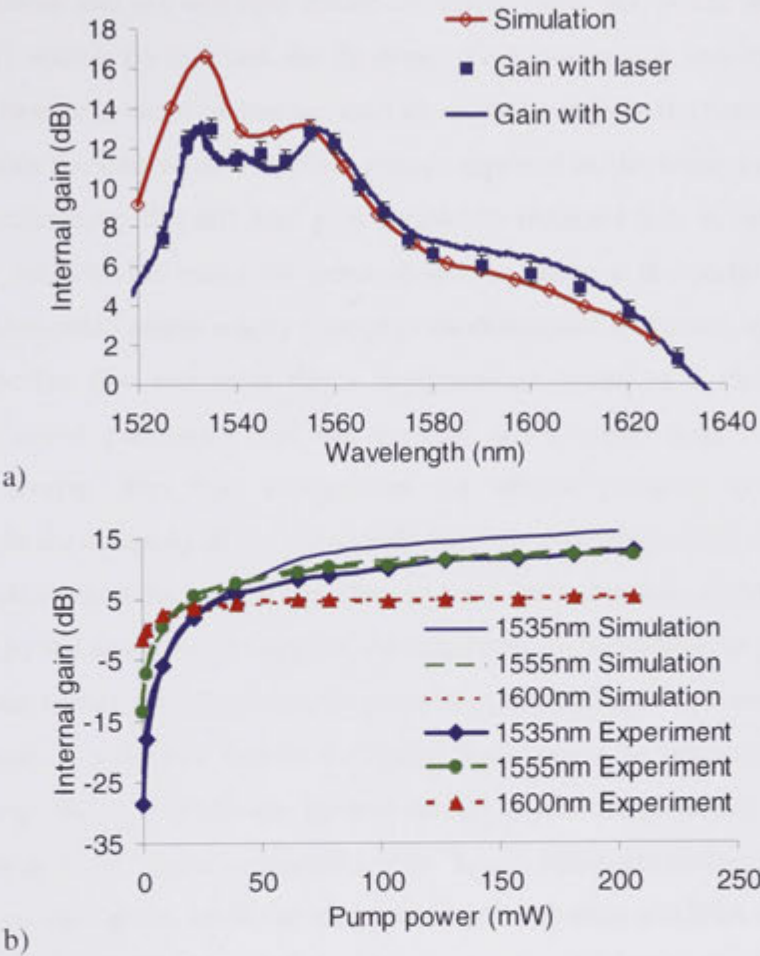


Figure 7.10: a) Gain spectra simulation with experiment data, b) gain saturation at 1535, 1555 and 1600nm.

### 7.4.3 Discussion

The gain results achieved in these waveguides are far better than any other EDTWAs reported in the literature. The only other reported gain in a tellurite waveguide was in a femtosecond laser written device in multicomponent glass with internal gains at best reaching ~1dB/cm [248, 420]. The best of these results were achieved in complex multicomponent tellurite glass waveguide made from only 50% TeO<sub>2</sub> (Na<sub>3</sub>P<sub>3</sub>O<sub>9</sub>, ZnO, ZnF<sub>2</sub> comprising the remainder) doped with 1wt% Er<sub>2</sub>O<sub>3</sub>, 1wt% CeO<sub>2</sub> and 2wt% Yb<sub>2</sub>O<sub>3</sub> with a refractive index of 1.66. The measured lifetime in the glass was 9.7ms, reflecting the large phosphate component in the glass. The index difference between core and



cladding in this device was only  $2.5 \times 10^{-3}$  and the device had a mode field area of  $\sim 70 \mu\text{m}^2$ . This device thus utilised a highly optimised glass host and the best pumping geometry available and yet was still unable to realise gains that would be regarded as technologically useful. By contrast, the Er doped  $\text{TeO}_2$  waveguide amplifiers obtained in this work, despite a range of known limitations that can be addressed, are in direct competition with the best results in other glasses reported in the literature as listed on Table 7.1. Furthermore, the full 3dB gain bandwidth obtained here is order of 40nm. There is also considerable room for improvement to increase the performance of Er doped  $\text{TeO}_2$  waveguide amplifiers by a range of modifications discussed below.

Perhaps the first and most direct improvement would be a move to 980nm pumping. As noted previously this can provide much higher gain due to higher maximum inversion. The first requirement for 980nm pumping scheme is the improvement in the coupling of the pump light into the waveguide. This can simply be achieved by AR coating the tapered fibre lens to have low reflection at 980nm. This can be performed by the commercial supplier. Alternatively, an integration of pump WDMs into the chip can be designed such that the pump is injected into a separate port.

However, it is known that in  $\text{TeO}_2$  that there might be potential issues with 980nm pumping. Because of the low phonon energy in tellurite glass, the non-radiative decay from pump level  $^4\text{I}_{11/3}$  to metastable level  $^4\text{I}_{13/3}$  is relatively slower than in silica. This leads population build up in the pump level and enhances the ESA of the 980nm pump [194, 386]. High ESA means the pump energy is partly lost to phonons when the excited ions decay down to the lower states. There have been a number of suggestions on means to alleviate the aforementioned issues with 980nm pumping including doping with Eu and/or Ce to reduce the upper level populations [200, 202, 203, 431-436]. There is visible green emission in the inserted picture on Figure 7.5. This clearly indicates that there is a substantial amount of radiation from level 5 to 1. The excitation of level 5 is due to the second-order upconversion. The ions are first excited to the  $^4\text{I}_{11/2}$  level through first order upconversion and excited state absorption. Then the second order upconversion causes some ions to excite into the  $^2\text{F}_{7/2}$  and  $^4\text{S}_{3/2}$  that emit in green. There are a number of schemes that can be used to reduce the upconversion process. The transitions  $^7\text{F}_0$ - $^7\text{F}_4$  of Eu and  $^2\text{F}_{7/2}$  to  $^2\text{F}_{5/2}$  of Ce are resonant with the  $^4\text{I}_{11/2}$ - $^4\text{I}_{13/2}$  transition of Er. Therefore, the energy transfer from Er/Ce to Eu can help reduce the

population of the  $^4I_{11/2}$  level in Er. This is particularly important for 980nm pumped systems as the  $^4I_{11/2}$  population is much higher than when pumped at 1480nm. Ce has been found to a better candidate for co-doping with Er in tellurite glass fibre [203]. In another report, the lifetime of the  $^4I_{11/2}$  level reduced from 70 $\mu$ s to 40 $\mu$ s without effecting the  $^4I_{13/2}$  in one tellurite glass ( $\text{TeO}_2\text{-WO}_3\text{-Na}_2\text{O}$ )[434]. A Ce/Er co-doped tellurite EDFA was also shown to provide much higher gain than both Er- only doped and Er/Eu doped ones. This is because Ce/Er co-doped tellurite glass maintains higher metastable lifetimes while reducing upconversion and ESA effects. Shen *et al.*, 2003 [200] reported gain increases from 16dB to 31dB in a 12cm long Er/Ce doped tellurite fibre amplifier.

Ytterbium can also be added to the mix as a sensitizer to increase the pump absorption at 980nm if required. The transition from  $^2F_{5/2}$  to  $^2F_{7/2}$  in Yb is in resonance with  $^4I_{11/2}$  to  $^4I_{15/2}$ , therefore the excited Yb ion transfers energy to Er ions during an efficient cross-relaxation process. Because the absorption at 980nm of Er doped waveguides is lower than at 1480nm, then typically high levels of Er doping are required to achieve sufficient absorption of a 980nm pump. In materials such as silicate or phosphate glasses the maximum Er concentrations allowed are much lower than in tellurite leading to weak pump absorption at 980nm for short length devices such as waveguide amplifiers. Therefore, most other Er doped materials pumped at 980nm reported in the literature required additional pump absorption due to lower Er concentrations than this work.

Higher gains can certainly be achieved by using higher Er concentrations. As shown in Chapter 6, Er concentrations of 3% Er/Te have been demonstrated in this work by reactive sputtering with no deleterious effects on waveguide performance. Peak gain per unit length scales directly with Er concentration in the ideal case so significant enhancements are feasible based on the work presented here.

Furthermore, there is still clearly an issue with the water contamination. Even though some samples have only 5-6% of Er coupled to OH quenching centres, the lifetime quenching is still very significant as seen on Table 6.2. Therefore, steps to reduce water contamination such as better target preparation and sputtering chamber preparation clearly need to be taken.

Additional simulation of the waveguide pumped at 980nm and parameters as shown on third column of Table 7.4 was performed. The set up is the same as the 1480nm pump but where the absorption spectra of 980nm was taken from Ref. [194]. The background loss of the pump was assumed to be same at the signal at 1550nm at 0.6dB/cm. The internal gain spectra at different total pump powers and the gain characteristics of signals at different wavelengths (1535nm, 1555nm and 1600nm) against different total pump powers are shown on Figure 7.11. The maximum gain can be as high as 27dB over 5cm length. Even with only slight improvements to the current design, an amplifier with gain per unit length of 5.4dB/cm is possible.

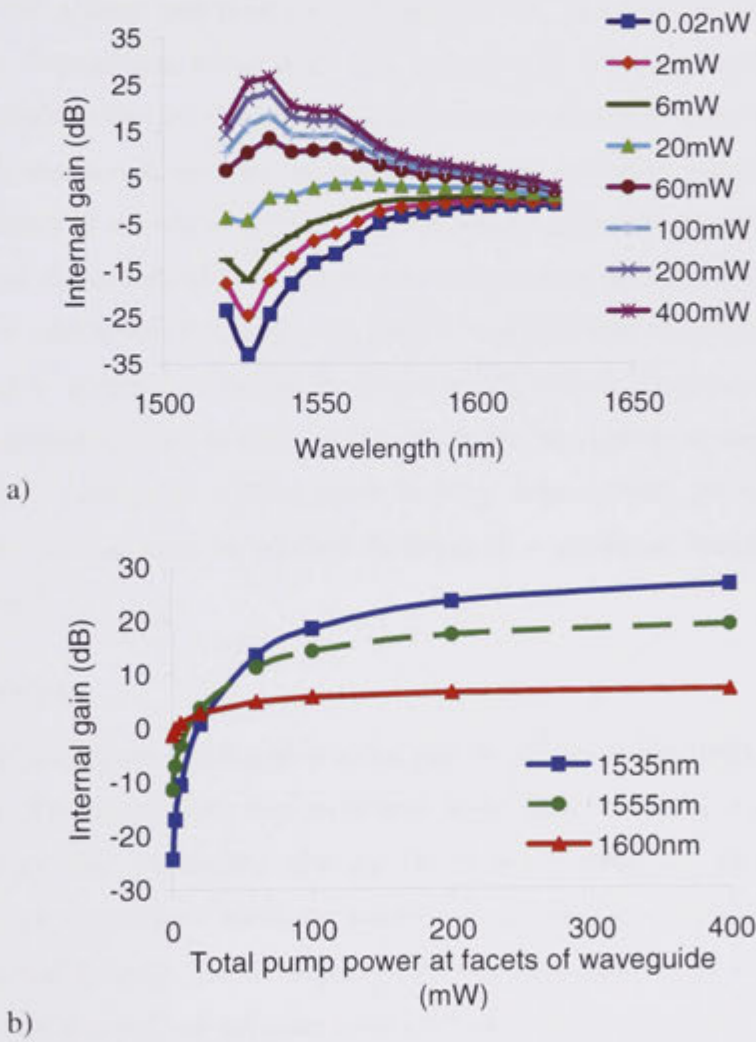


Figure 7.11: a) Gain spectra simulation with 980nm pump, b) gain saturation at 1535, 1555 and 1600nm pumped at 980nm.

Although considerable scope for improvement exists, a waveguide with 13dB gain itself has applications to a number of interesting active devices, for instance integrated on chip CW, Q-switched, or mode locked lasers. There have been a number of reports on the realisation of waveguide lasers [252, 437-441]. The CW laser can be configured with a linear cavity with fibre Bragg gratings [252, 438, 441], or a ring cavity with couplers [439]. Mode locked operation of an Er doped waveguide laser has been achieved [440, 441] though not yet in a fully planar integrated form. The authors reported passive mode locking of an Er-Yb doped phosphate glass femtosecond written waveguide amplifier using carbon nanotubes as saturable absorber. The waveguide is incorporated into a fibre ring laser cavity configuration. The FWHM band width and pulse duration obtained was 1.6nm and 1.6ps, respectively. The time bandwidth product of 0.329 is transform-limited. Carbon nanotube saturable absorbers have limitations due to the inherent insertion losses and multiphoton induced oxidation, which degrades the long term stability of the absorber [442]. An alternative saturable absorber is graphene which has been demonstrated as an excellent mode-locking material [443-449]. Pulse width of below ~400fs has been achieved. Only a very thin layer of graphene (only few atomic layers) is required to make the laser mode locked. Therefore, it might be possible that graphene layer attached to the end of the waveguide or the side walls of the waveguide is enough to achieve mode locking. Alternatively given that TeO<sub>2</sub> is quite nonlinear itself, it may be possible to integrate a nonlinear switch as the mode locking element.

## 7.5 Conclusion

Er doped TeO<sub>2</sub> waveguides with high internal gain have been successfully fabricated for the first time. The waveguide was fabricated from films made by reactive RF co-sputtering of Er and Te targets into an O<sub>2</sub>/Ar filled chamber. The strip loaded waveguides were etched by CH<sub>4</sub>/H<sub>2</sub>/Ar plasma to overcome the difficulties in etching Er doped material directly. The Er doped TeO<sub>2</sub> waveguide amplifiers were pumped at 1480nm to obtain internal and net gains over 1520nm to beyond 1600nm. The peak gain of 14dB over 5cm length and 3dB bandwidth of 40nm have been achieved when bidirectionally pumped with a total of 250mW at 1475nm. The simulation of the performance of the amplifier shows very good agreement with the experimental data

and the potential for much higher gain can be achieved by pumping at 980nm for higher pump efficiency.

## **Chapter 8:**

# **Conclusions and recommendations**

### **8.1 Conclusions**

This work focused on the fundamentals of fabrication and characterisation of planar waveguides using Tellurium oxide. There have been a number of important achievements that advance the field. The thin films were fabricated using reactive RF magnetron sputtering. Low loss stoichiometric films were obtained at a loss level that no one else has achieved before by any technique in the tellurite materials platform. The fabrication of waveguides using  $\text{CH}_4/\text{H}_2/\text{Ar}$  plasma mixture is the first successful demonstration of plasma etching in tellurite glasses and has been proven to be very versatile. The etching recipes are applicable not only to tellurite but also to chalcogenide. Losses of below 0.1dB/cm have been achieved in  $\text{TeO}_2$  waveguides, again for the first time. The linear and nonlinear properties of Tellurium oxide have been confirmed. More importantly, the Erbium doped films have been fabricated into high gain EDWAs for the first time clearing a way for all in one material integrated photonics.

This work has extensively investigated the fabrication method for high quality Tellurium oxide thin film. Reactive RF sputtering technique was used with a pure Tellurium target. The Tellurium oxide films were formed in an Argon and Oxygen plasma chamber. With the DOE method, the optimum condition for film growth was obtained with 0.1dB/cm or lower propagation losses for stoichiometric compositions. It was found that the films are robust to annealing even at up to 300°C. Reactive RF sputtering is a very appropriate technique for Tellurium oxide film fabrication.

Plasma etching of Tellurium oxide thin films that involved RIE and ICP machines was studied in detail. A high quality RIE etching process using Hydrogen, Methane and Argon has been demonstrated. The quality of etching in the two systems is slightly different. The RIE machine gives better propagation loss. Very low propagation loss (below 0.1dB/cm) has been achieved in rib Tellurium oxide waveguides. The outcome of this study is a recipe for etching high optical quality

tellurite waveguides. The etch recipe has also been demonstrated to be highly suitable for chalcogenide glass thin films.

The nonlinearity of low loss Tellurium oxide has been measured and utilised in nonlinear processes of SPM and FWM. The nonlinear coefficient of the sputtered  $\text{TeO}_2$  was characterised by an SPM experiment and the nonlinear coefficient  $n_2$  was measured to be  $65 \times 10^{-20} \text{ m}^2 \text{ W}^{-1}$ , around 25 times that of silica. Significant signal conversion was achieved with large bandwidth in the FWM experiment pumped at 1550nm in a slightly normal dispersion waveguides.

Erbium doped tellurium oxide thin films have been fabricated and characterised extensively. Reactive co-sputtering deposition allowed good Erbium concentration control to obtain films with 0.1% Er/Te to more than 3% Er/Te. Low loss waveguides were obtained even at 3% concentration indicating no clustering problems. A highly sensitive fiberised set up was used to measure lifetime of the  $1.5 \mu\text{m}$  emission in thin films and waveguides. The  $1.5 \mu\text{m}$  photoluminescence properties of the films were excellent with effective bandwidth of more than 60nm and intrinsic lifetime of order of 3ms. The OH contamination plays a critical role in the lifetime of the  $1.5 \mu\text{m}$  transition.

For the first time, an Er doped Tellurium oxide waveguide amplifier with high internal gain has been successfully obtained. The 1480nm pumped amplifier achieved internal gain from below 1520nm to beyond 1600nm. The peak gain of 2.8dB/cm and 40nm gain bandwidth have been accomplished.

## 8.2 *Recommendations for future work*

All of the films and waveguides fabricated in this project were based on pure Tellurium oxide. Multicomponent tellurite glasses can have tailored optical properties such as higher nonlinearity, higher refractive indices, better chemical, thermal and mechanical stability. For instance, Tungsten tellurite glass ( $\text{WO}_3\text{-TeO}_2$ ) has been proven to exhibit some better characteristics than pure  $\text{TeO}_2$  [253, 255, 450, 451]. Multicomponent thin films can be achieved via two routes: one with co-sputtering different elemental targets and one with sputtering multicomponent glass. The first method gives the flexibility in tuning the composition on demand however, achieving the stoichiometry (ie. correct amount of oxygen) can be more difficult than sputtering only a Tellurium target. Furthermore, there is limited number of targets that can be used in each system due to



equipment limitations. In addition, there are materials such as Sodium that are not possible to have single solid target. The second method can overcome some of the shortcoming of co-sputtering just mentioned. However, the control of film composition can be restrictive as the composition transfer from target to film is not tunable. However it is clear that there could be substantial benefits in exploring more complex glass chemistries.

The etching process could be improved to take the full advantage of the ICP plasma etching system. As discussed detail in Chapter 4, etching using the ICP has met some roughness issues which required special treatment of the photoresist to remove “bat ear” growth. The origin of this effect needs to be tracked down and better etching conditions be identified to eliminate it but still obtain high quality waveguides.

Due to the high nonlinear coefficient of Tellurium oxide waveguides, supercontinuum generation might be possible with a very short length of waveguide. In order to achieve that, the zero dispersion wavelength of the waveguide needs to be around the pump wavelength. Theoretically, dispersion engineering is required to achieve this. However, there are usually errors in fabrication that produce waveguides with dimensions differing from the intended values. Tapered waveguides can be used to have some zero dispersion length on the waveguide. Since there have been reports of supercontinuum in short (few centimetres) tapered tellurite fibres [139, 180, 182, 187], the equivalent version of the waveguide should be possible. An advantage of the waveguide version is that the modal area can be much smaller than in fibres therefore, it is easier to achieve supercontinuum with even shorter device length and lower peak power of the pump.

The properties of the active waveguides can be significantly improved in a number of directions. First, the lifetime of the films can be increased by reducing quenching due to OH contamination. With the reduction in OH concentration, higher Erbium concentration can be incorporated into the films leading to higher gain per unit length of the device. This can be achieved with better handling of the start targets and fabrication process. The increase in lifetime will increase the quantum efficiency of amplifier. This will lead to the lower threshold pump power as well as lower the pump power required to saturate the amplifier.

Furthermore, changing the pump wavelength from 1480nm to 980nm can significantly increase the maximum amplifier gain. The pumping scheme at 980nm can potentially lead to much higher population inversion level, close to 100%. However, this change requires a number of improvements not only in the pump coupling efficiency but also in the upconversion and excited state absorption of the 980nm pump. In the current pumping configuration, the pump power and signal are combined via WDM made from SMF28 fibres and tapered fibre lenses. The fibre lenses are AR coated at 1550nm but not at 980nm. Therefore, the pump delivery is not efficient enough. A simple step to improve the current set up is with AR coating to cover both wavelengths. Still, as the connecting fibres and waveguides become multimode at 980nm, the coupling between them is not very efficient. A design with integrated pump couplers at both ends of the waveguides can solve this problem.

As discussed in Chapter 6 and 7 for 980nm pump, the upconversion and ESA should be improved in tellurites by co-doping Erbium with Europium and/or Cerium. For the sputtering deposition, co-sputtering can be used in a multi-target configuration or with single target with a suitable mixture of correct elements.

In conclusion, tellurium oxide has been shown to have great potential as an all in-one platform for integrated optics with a range of excellent properties obtained in planar waveguides.

# Bibliography

1. G. Lifante, *Integrated photonics: fundamentals* (John Wiley & Sons Ltd., Chippenham, UK, 2003).
2. G. Chen, H. Chen, M. Haurylau, N. A. Nelson, D. H. Albonesi, P. M. Fauchet, and E. G. Friedman, "Predictions of CMOS compatible on-chip optical interconnect," *Integration, the VLSI Journal* **40**, 434-446 (2007).
3. M. Haurylau, G. Chen, H. Chen, J. Zhang, N. A. Nelson, D. H. Albonesi, E. G. Friedman, and P. M. Fauchet, "On-chip optical interconnect roadmap: Challenges and critical directions," *IEEE J. Sel. Top. Quantum Electron.* **12**, 1699-1704 (2006).
4. R. W. Waynant and M. N. Ediger, eds., *Electro-optics handbook*, 2nd ed. (McGraw-Hill, 2000).
5. Y. Vlasov and S. McNab, "Losses in single-mode silicon-on-insulator strip waveguides and bends," *Opt. Express* **12**, 1622-1631 (2004).
6. L. Eldada, "Advances in telecom and datacom optical components," *Opt. Eng.* **40**, 1165-1178 (2001).
7. M. Kawachi, "Silica waveguides on silicon and their application to integrated-optic components," *Opt. Quantum Electron.* **22**, 391-416 (1990).
8. A. Kaneko, T. Goh, H. Yamada, T. Tanaka, and I. Ogawa, "Design and applications of silica-based planar lightwave circuits," *IEEE J. Sel. Top. Quantum Electron.* **5**, 1227-1236 (1999).
9. A. Himeno, K. Kato, and T. Miya, "Silica-based planar lightwave circuits," *IEEE J. Sel. Top. Quantum Electron.* **4**, 913-924 (1998).
10. M. Abe, "Silica-based waveguide devices for photonic networks," *J. Ceram. Soc. Jpn.* **116**, 1063-1070 (2008).
11. C. R. Doerr and K. Okamoto, "Advances in silica planar lightwave circuits," *J. Lightwave Technol.* **24**, 4763-4789 (2006).
12. W. J. Miniscalco, "Erbium-doped glasses for fiber amplifiers at 1500 nm," *J. Lightwave Technol.* **9**, 234-250 (1991).
13. F. Li, M. Pelusi, D. X. Xu, A. Densmore, R. Ma, S. Janz, and D. J. Moss, "Error-free all-optical demultiplexing at 160Gb/s via FWM in a silicon nanowire," *Opt. Express* **18**, 3905-3910 (2010).
14. D. K. Sparacin, S. J. Spector, and L. C. Kimerling, "Silicon Waveguide Sidewall Smoothing by Wet Chemical Oxidation," *J. Lightwave Technol.* **23**, 2455 (2005).
15. H. Yamada, M. Shirane, T. Chu, H. Yokoyama, S. Ishida, and Y. Arakawa, "Nonlinear-optic silicon-nanowire waveguides," *Jpn. J. Appl. Phys., Part 1* **44**, 6541-6545 (2005).
16. R. Salem, M. A. Foster, A. C. Turner, D. F. Geraghty, M. Lipson, and A. L. Gaeta, "Signal regeneration using low-power four-wave mixing on silicon chip," *Nat. Photonics* **2**, 35-38 (2008).
17. H. Ji, M. Galili, H. Hu, M. Pu, L. K. Oxenlowe, K. Yvind, J. M. Hvam, and P. Jeppesen, "1.28-Tb/s demultiplexing of an OTDM DPSK data signal using a silicon waveguide," *IEEE Photonics Technol. Lett.* **22**, 1762-1764 (2010).
18. Intel, retrieved 30 June, 2011, [http://www.intel.com/pressroom/archive/releases/2010/20100727comp\\_sm.htm#story](http://www.intel.com/pressroom/archive/releases/2010/20100727comp_sm.htm#story).
19. D. Liang and J. E. Bowers, "Recent progress in lasers on silicon," *Nat. Photonics* **4**, 511-517 (2010).
20. J. Bowers, D. Liang, A. Fang, H. Park, R. Jones, and M. Paniccia, "Hybrid silicon lasers: The final frontier to integrated computing," *Optics and Photonics News* **21**, 28-33 (2010).
21. L. Chen and M. Lipson, "Ultra-low capacitance and high speed germanium photodetectors on silicon," *Opt. Express* **17**, 7901-7906 (2009).

22. L. Vivien, J. Osmond, J. M. Fedeli, D. Marris-Morini, P. Crozat, J. F. Damlencourt, E. Cassan, Y. Lecunff, and S. Laval, "42 GHz p.i.n germanium photodetector integrated in a silicon-on-insulator waveguide," *Opt. Express* **17**, 6252-6257 (2009).
23. Luxtera, retrieved 30 June, 2011, <http://www.luxtera.com/blazar-lux5010a.html>.
24. T. Alasaarela, D. Korn, L. Alloatti, A. Saynatjoki, A. Tervonen, R. Palmer, J. Leuthold, W. Freude, and S. Honkanen, "Reduced propagation loss in silicon strip and slot waveguides coated by atomic layer deposition," *Opt. Express* **19**, 11529-11538 (2011).
25. W. Bogaerts and S. K. Selvaraja, "Compact single-mode silicon hybrid rib/strip waveguide with adiabatic bends," *IEEE Photonics Journal* **3**, 422-432 (2011).
26. A. Spott, T. Baehr-Jones, R. Ding, Y. Liu, R. Bojko, T. O'Malley, A. Pomerene, C. Hill, W. Reinhardt, and M. Hochberg, "Photolithographically fabricated low-loss asymmetric silicon slot waveguides," *Opt. Express* **19**, 10950-10958 (2011).
27. L. Eldada and L. W. Shacklette, "Advances in polymer integrated optics," *IEEE J. Sel. Top. Quantum Electron.* **6**, 54-68 (2000).
28. H. Ma, A. K. Y. Jen, and L. R. Dalton, "Polymer-based optical waveguides: Materials, processing, and devices," *Adv. Mater.* **14**, 1339-1365 (2002).
29. J. Voros, J. J. Ramsden, G. Csacs, I. Szendro, S. M. De Paul, M. Textor, and N. D. Spencer, "Optical grating coupler biosensors," *Biomaterials* **23**, 3699-3710 (2002).
30. K. B. Mogensen, J. El-Ali, A. Wolff, and J. P. Kutter, "Integration of polymer waveguides for optical detection in microfabricated chemical analysis systems," *Appl. Opt.* **42**, 4072-4079 (2003).
31. S. M. Garner, S. S. Lee, V. Chuyanov, A. Chen, A. Yacoubian, W. H. Steier, and L. R. Dalton, "Three-dimensional integrated optics using polymers," *IEEE J. Quantum Electron.* **35**, 1146-1155 (1999).
32. C. Y. Chao and L. J. Guo, "Polymer microring resonators fabricated by nanoimprint technique," *J. Vac. Sci. Technol., B* **20**, 2862-2866 (2002).
33. Gemfire, retrieved 30 June, 2011, <http://www.gemfire.com>.
34. Gigoptix, retrieved 30 June, 2011, <http://www.gigoptix.com/>.
35. L. Arizmendi, "Photonic applications of lithium niobate crystals," *Phys. Status Solidi A* **201**, 253-283 (2004).
36. S. Kilburger, E. Millon, P. Di Bin, A. Boulle, R. Guinebreiare, and C. Di Bin, "Properties of LiNbO<sub>3</sub> based heterostructures grown by pulsed-laser deposition for optical waveguiding application," *Thin Solid Films* **518**, 4654-4657 (2010).
37. G. W. Burr, S. Diziain, and M. P. Bernal, "Theoretical study of lithium niobate slab waveguides for integrated optics applications," *Opt. Mater.* **31**, 1492-1497 (2009).
38. V. Bornand, B. Gautier, and P. Papet, "Growth and nanoscale ferroelectric investigation of radiofrequency- sputtered LiNbO<sub>3</sub> thin films," *Mater. Chem. Phys.* **86**, 340-346 (2004).
39. E. L. Wooten, K. M. Kissa, A. Yi-Yan, E. J. Murphy, D. A. Lafaw, P. F. Hallemeier, D. Maack, D. V. Attanasio, D. J. Fritz, G. J. McBrien, and D. E. Bossi, "Review of lithium niobate modulators for fiber-optic communications systems," *IEEE J. Sel. Top. Quantum Electron.* **6**, 69-82 (2000).
40. R. A. Ganeev, I. A. Kulagin, A. I. Rysanyansky, R. I. Tugushev, and T. Usmanov, "Characterization of nonlinear optical parameters of KDP, LiNbO<sub>3</sub> and BBO crystals," *Opt. Commun.* **229**, 403-412 (2004).
41. S. Roland, S. Robert, and I. S. George, "Measurement of Third-Order Nonlinear Susceptibility Tensor Elements in Lithium Niobate," in *Frontiers in Optics*, (Optical Society of America, 2005), JWA74.
42. R. Osellame, M. Lobino, N. Chiodo, M. Marangoni, G. Cerullo, R. Ramponi, H. T. Bookey, R. R. Thomson, N. D. Psaila, and A. K. Kar, "Femtosecond laser writing of waveguides in periodically poled lithium niobate preserving the nonlinear coefficient," *Appl. Phys. Lett.* **90**, 241107-241103 (2007).

43. T. L. Koch, U. Koren, G. Eisenstein, M. G. Young, M. Oron, C. R. Giles, and B. I. Miller, "Tapered waveguide InGaAs/InGaAsP multiple-quantum-well lasers," *IEEE Photonics Technol. Lett.* **2**, 88-90 (1990).
44. A. Sharon, D. Rosenblatt, A. A. Friesem, H. G. Weber, H. Engel, and R. Steingrueber, "Light modulation with resonant grating-waveguide structures," *Opt. Lett.* **21**, 1564-1566 (1996).
45. W. Ha, V. Gambin, M. Wistey, S. Bank, S. Kim, and J. S. Harris Jr, "Multiple-quantum-well GaInNAs-GaNAs ridge-waveguide laser diodes operating out to 1.4 $\mu$ m," *IEEE Photonics Technol. Lett.* **14**, 591-593 (2002).
46. R. Ben-Michael, U. Koren, B. I. Miller, M. G. Young, M. Chien, and G. Raybon, "InP-based multiple quantum well lasers with an integrated tapered beam expander waveguide," *IEEE Photonics Technol. Lett.* **6**, 1412-1414 (1994).
47. P. W. Juodawlkis, J. J. Plant, R. K. Huang, L. J. Missaggia, and J. P. Donnelly, "High-power 1.5- $\mu$ m InGaAsP-InP slab-coupled optical waveguide amplifier," *IEEE Photonics Technol. Lett.* **17**, 279-281 (2005).
48. Z. Bian, B. Liu, and A. Shakouri, "InP-based passive ring-resonator-coupled lasers," *IEEE J. Quantum Electron.* **39**, 859-865 (2003).
49. L. A. Coldren, S. C. Nicholes, L. Johansson, S. Ristic, R. S. Guzzon, E. J. Norberg, and U. Krishnamachari, "High Performance InP-Based Photonic ICs-A Tutorial," *J. Lightwave Technol.* **29**, 554-570 (2011).
50. S. C. Nicholes, M. L. Masanovic, B. Jevremovic, E. Lively, L. A. Coldren, and D. J. Blumenthal, "An 8x8 InP Monolithic Tunable Optical Router (MOTOR) Packet Forwarding Chip," *J. Lightwave Technol.* **28**, 641-650 (2010).
51. V. G. Ta'eed, M. Shokooh-Saremi, L. Fu, D. J. Moss, M. Rochette, I. C. M. Littler, B. J. Eggleton, Y. Ruan, and B. Luther-Davies, "Integrated all-optical pulse regenerator in chalcogenide waveguides," *Opt. Lett.* **30**, 2900-2902 (2005).
52. S. J. Madden, D. Y. Choi, D. A. Bulla, A. V. Rode, B. Luther-Davies, V. G. Ta'eed, M. D. Pelusi, and B. J. Eggleton, "Long, low loss etched As<sub>2</sub>S<sub>3</sub> chalcogenide waveguides for all-optical signal regeneration," *Opt. Express* **15**, 14414-14421 (2007).
53. M. D. Pelusi, V. G. Ta'eed, L. Fu, E. Magi, M. R. E. Lamont, S. Madden, D.-Y. Choi, D. A. P. Bulla, B. Luther-Davies, and B. J. Eggleton, "Applications of highly-nonlinear chalcogenide glass devices tailored for high-speed all-optical signal processing," *IEEE J. Sel. Top. Quantum Electron.* **14**, 529-539 (2008).
54. M. Galili, J. Xu, H. C. Mulvad, L. K. Oxenløwe, A. T. Clausen, P. Jeppesen, B. Luther-Davies, S. Madden, A. Rode, D.-Y. Choi, M. Pelusi, F. Luan, and B. J. Eggleton, "Breakthrough switching speed with an all-optical chalcogenide glass chip: 640 Gbit/s demultiplexing," *Opt. Express* **17**, 2182-2187 (2009).
55. B. Luther-Davies, A. Prasad, S. Madden, D. Y. Choi, D. Bulla, X. Gai, and K. Vu, "Supercontinuum generation and four wave mixing in Ge<sub>11</sub>As<sub>22</sub>Se<sub>67</sub> rib waveguides with a nonlinear parameter  $>26000\text{W}^{-1}\text{km}^{-1}$ ," in *CLEO/Europe - EQEC 2009 - European Conference on Lasers and Electro-Optics and the European Quantum Electronics Conference*, 2009).
56. X. Gai, T. Han, A. Prasad, S. Madden, D.-Y. Choi, R. Wang, D. Bulla, and B. Luther-Davies, "Progress in optical waveguides fabricated from chalcogenide glasses," *Opt. Express* **18**, 26635-26646 (2010).
57. H. Yildirim, "Dispersion parameters and nonlinear optical properties of silicon nitride rib waveguides," *Opt. Commun.* **284**, 2031-2035 (2011).
58. D. Olaosebikan, S. Yerci, A. Gondarenko, K. Preston, R. Li, L. D. Negro, and M. Lipson, "Absorption bleaching by stimulated emission in erbium-doped silicon-rich silicon nitride waveguides," *Opt. Lett.* **36**, 4-6 (2011).

59. J. S. Chang, I. Y. Kim, G. Y. Sung, and J. H. Shin, "Population inversion and low cooperative upconversion in Er-doped silicon-rich silicon nitride waveguide," *Opt. Express* **19**, 8406-8412 (2011).
60. E. Celasco, M. Quaglio, A. Chiodoni, C. Ricciardi, C. F. Pirri, L. Dominici, F. Michelotti, F. De Angelis, E. Di Fabrizio, and F. Giorgis, "Amorphous silicon and silicon nitride channel optical waveguides," *Phys. Status Solidi C* **7**, 836-839 (2011).
61. H. Y. Chen and K. C. Yang, "High efficiency broadband waveguide grating coupler with silicon nitride overlay," in *Optoelectronics and Communications Conference (OECC), 2010 15th*, 2010), 864-865.
62. J. S. Levy, A. Gondarenko, A. C. Turner-Foster, M. A. Foster, A. L. Gaeta, and M. Lipson, "Four-wave mixing in integrated silicon nitride waveguides," in *2009 Conference on Lasers and Electro-Optics and 2009 Conference on Quantum Electronics and Laser Science Conference, CLEO/QELS 2009*, 2009).
63. A. Gondarenko, J. S. Levy, and M. Lipson, "High confinement micron-scale silicon nitride high Q ring resonator," *Opt. Express* **17**, 11366-11370 (2009).
64. M. Fadel, M. Balters, M. Niemand, E. Voges, and P. M. Krummrich, "Low-loss and low-birefringence high-contrast silicon-oxynitride waveguides for optical communication," *J. Lightwave Technol.* **27**, 698-705 (2009).
65. C. K. Wong, H. Wong, M. Chan, Y. T. Chow, and H. P. Chan, "Silicon oxynitride integrated waveguide for on-chip optical interconnects applications," *Microelectron. Reliab.* **48**, 212-218 (2008).
66. G. Maire, L. Vivien, G. Sattler, A. Kaamierczak, B. Sanchez, K. B. Gylfason, A. Griol, D. Marris-Morini, E. Cassan, D. Giannone, H. Sohlstram, and D. Hill, "High efficiency silicon nitride surface grating couplers," *Opt. Express* **16**, 328-333 (2008).
67. K. Ikeda, R. E. Saperstein, N. Alic, and Y. Fainman, "Thermal and Kerr nonlinear properties of plasma-deposited silicon nitride/ silicon dioxide waveguides," *Opt. Express* **16**, 12987-12994 (2008).
68. D. Celo, R. Vandusen, T. Smy, J. Albert, N. G. Tarr, and P. D. Waldron, "Low temperature plasma etching for Si<sub>3</sub>N<sub>4</sub> waveguide applications," *J. Vac. Sci. Technol., A* **26**, 253-258 (2008).
69. L. Vivien, G. Maire, G. Sattler, D. Marris-Morini, E. Cassan, S. Laval, A. Kaamierczak, D. Giannone, B. Sanchez, A. Griol, D. Hill, K. B. Gylfason, and H. Sohlstram, "A high efficiency silicon nitride grating coupler," in *IEEE International Conference on Group IV Photonics GFP*, 2007), 162-164.
70. G. Pandraud, P. J. French, and P. M. Sarro, "PECVD silicon carbide waveguides for multichannel sensors," in *Proceedings of IEEE Sensors*, 2007), 395-398.
71. R. K. Pandey, L. S. Patil, J. P. Bange, and D. K. Gautam, "Growth and characterization of silicon nitride films for optoelectronics applications," *Opt. Mater.* **27**, 139-146 (2004).
72. G. L. Bona, R. Germann, and B. J. Offrein, "SiON high-refractive-index waveguide and planar lightwave circuits," *IBM J. Res. Dev.* **47**, 239-249 (2003).
73. Y.-T. Ren, "Nonlinear effect induced in thermally poled glass waveguides," *Journal of Zhejiang University: Science* **7**, 105-108 (2006).
74. S. Shen, A. Jha, X. Liu, M. Naftaly, K. Bindra, H. J. Bookey, and A. K. Kar, "Tellurite glasses for broadband amplifiers and integrated optics," *J. Amer. Cer. Soc.* **85**, 1391-1395 (2002).
75. K. Tanaka, A. Narazaki, and K. Hirao, "Large optical second-order nonlinearity of poled WO<sub>3</sub>-TeO<sub>2</sub> glass," *Opt. Lett.* **25**, 251-253 (2000).
76. B. Jeansannetas, S. Blanchandin, P. Thomas, P. Marchet, J. C. Champarnaud-Mesjard, T. Merle-Mejean, B. Frit, V. Nazabal, E. Fargin, G. Le Flem, M. O. Martin, B. Bousquet, L. Canioni, S. Le Boiteux, P. Segonds, and L. Sarger, "Glass structure and optical nonlinearities in thallium(I) Tellurium(IV) oxide glasses," *J. Solid State Chem.* **146**, 335 (1999).



77. J. S. Wang, E. M. Vogel, and E. Snitzer, "Tellurite glass: a new candidate for fiber devices," *Opt. Mater.* **3**, 187-203 (1994).
78. E. Chierici, M. C. Didavide, A. Moro, O. Rossotto, L. Tallone, and E. Monchiero, "Direct writing of waveguide on a tellurite glass using a focused ultraviolet laser beam," in *IEEE/LEOS Workshop on Fibre and Optical Passive Components*, (IEEE Press, 2002), 29-33.
79. E. Monchiero, D. Milanese, M. Ferraris, L. Tallone, and E. Chierici, "Direct writing of waveguides on tellurite glasses," in *19th Congress of the International Commission for Optics: Optics for the Quality of Life*, (SPIE, 2003), 135.
80. M. Martino, A. P. Caricato, M. Fernandez, G. Leggieri, A. Jha, M. Ferrari, and M. Mattarelli, "Pulsed laser deposition of active waveguides," *Thin Solid Films* **433**, 39-44 (2003).
81. Y. Tokuda, M. Saito, M. Takahashi, K. Yamada, W. Watanabe, K. Itoh, and T. Yoko, "Waveguide formation in niobium tellurite glasses by pico- and femtosecond laser pulses," *J. Non-Cryst. Solids* **326**, 472-475 (2003).
82. G. Nunzi Conti, V. K. Tikhomirov, M. Bettinelli, S. Berneschi, M. Brenci, B. Chen, S. Pelli, and A. Speghini, "Characterization of ion-exchanged waveguides in tungsten tellurite and zinc tellurite  $\text{Er}^{3+}$ -doped glasses," *Opt. Eng.* **42**, 2805-2811 (2003).
83. Y. Ding, S. Jiang, T. Luo, Y. Hu, and N. Peyghambarian, "Optical waveguides prepared in  $\text{Er}_3$  doped tellurite glass by  $\text{Ag}^+ - \text{Na}^+$  ion-exchange," in *Rare-Earth-Doped Materials and Devices V*, (Society of Photo-Optical Instrumentation Engineers, 2001), 23.
84. R. Ayres and L. Ayres, *A handbook of industrial ecology* (Edward Elgar Publishing, 2002).
85. R. D. Lide, *CRC Handbook of Chemistry and Physics*, 88 ed. (CRC Press, 2007).
86. W. A. Dutton and W. C. Cooper, "The oxides and oxyacids of Tellurium," *Chem. Rev.* **66**, 657-675 (1966).
87. J. Leciejewicz, "The crystal structure of Tellurium dioxide: a redetermination by neutron diffraction," (Polish Academy of Sciences. Inst. of Nuclear Research, Warsaw, 1961), p. Pages: 14.
88. R. A. H. El-Mallawany, *Tellurite glasses handbook: physical properties and data* (CRC Press, US, 2002).
89. A. P. Mirgorodsky, T. Merle-Mejean, J. C. Champarnaud, P. Thomas, and B. Frit, "Dynamics and structure of  $\text{TeO}_2$  polymorphs: model treatment of paratellurite and tellurite; Raman scattering evidence for new gamma - and delta-phases," *J. Phys. Chem. Solids* **61**, 509 (2000).
90. M. Ceriotti, F. Pietrucci, and M. Bernasconi, "Ab initio study of the vibrational properties of crystalline  $\text{TeO}_2$ : the alpha, beta, and gamma phases," *Phys. Rev. B: Condens. Matter* **73**, 17 (2006).
91. G. Arlt and H. Schweppe, "Paratellurite, a new piezoelectric material," *Solid State Commun.* **6**, 784 (1968).
92. S. Kumaragurubaran, D. Krishnamurthy, C. Subramanian, and P. Ramasamy, "Investigations on the growth of  $\text{Bi}_2\text{TeO}_5$  and  $\text{TeO}_2$  crystals," *J. Cryst. Growth* **197**, 215 (1999).
93. S. Miyazawa and H. Iwasaki, "Single Crystal Growth of Paratellurite  $\text{TeO}_2$ ," *Jpn. J. Appl. Phys.* **9**, 441-& (1970).
94. Y. Chu, Y. Li, Z. Ge, G. Wu, and H. Wang, "Growth of the high quality and large size paratellurite single crystals," *J. Cryst. Growth* **295**, 161 (2006).
95. P. Veber, J. Mangin, P. Strimer, P. Delarue, C. Josse, and L. Saviot, "Bridgman growth of paratellurite single crystals," *J. Cryst. Growth* **270**, 84 (2004).
96. S. Sakida, S. Hayakawa, and T. Yoko, "Part 1.  $^{125}\text{Te}$  NMR study of tellurite crystals," *J. Non-Cryst. Solids* **243**, 12 (1999).



97. S. Blanchandin, P. Marchet, P. Thomas, J. C. Champarnaud-Mesjard, B. Frit, and A. Chagraoui, "New investigations within the  $\text{TeO}_2$ - $\text{WO}_3$  system: phase equilibrium diagram and glass crystallization," *J. Mater. Sci.* **34**, 4292 (1999).
98. O. Noguera, T. Merle-Mejean, A. P. Mirgorodsky, M. B. Smirnov, P. Thomas, and J. C. Champarnaud-Mesjard, "Vibrational and structural properties of glass and crystalline phases of  $\text{TeO}_2$ ," *J. Non-Cryst. Solids* **330**, 60 (2003).
99. O. Noguera, M. Smirnov, A. P. Mirgorodsky, T. Merle-Méjean, P. Thomas, and J. C. Champarnaud-Mesjard, "Ab initio study of the polymer molecules  $(\text{TeO}_2)_n$  as model systems for the local structure in  $\text{TeO}_2$  glass," *Phys. Rev. B* **68**(2003).
100. O. Noguera, T. Merle-Mejean, A. P. Mirgorodsky, P. Thomas, and J. C. Champarnaud-Mesjard, "Dynamics and crystal chemistry of tellurites. II. Composition- and temperature-dependence of the Raman spectra of  $x(\text{Ti}_2\text{O}) + (1 - x) \text{Te}_2\text{O}$  glasses: Evidence for a phase separation?," *J. Phys. Chem. Solids* **65**, 993 (2004).
101. O. Noguera, M. Smirnov, A. P. Mirgorodsky, T. Merle-Mejean, P. Thomas, and J. C. Champarnaud-Mesjard, "Theoretical study of the polymer molecules  $(\text{TeO}_2)_n$  as model systems for the local structure in  $\text{TeO}_2$  glass," *J. Non-Cryst. Solids* **345-346**, 734 (2004).
102. G. Arlt and K. Reiber, "Ultrasonic amplification in Tellurium along the z-axis with longitudinal and transverse electric drift fields," *Solid State Commun.* **7**, 1157 (1969).
103. N. Uchida and Y. Ohmachi, "Elastic and photoelastic properties of  $\text{TeO}_2$  single crystal," *J. Appl. Phys.* **40**, 5 (1969).
104. N. Uchida, "Optical properties of single-crystal paratellurite  $\text{TeO}_2$ ," *Phys. Rev. B* **4**, 3736 (1971).
105. T. Yano, A. Fukumoto, and A. Watanabe, "Tellurite glass. A new acousto-optic material," *J. Appl. Phys.* **42**, 6 (1971).
106. C. W. Pitt, "Use of thin films in optical waveguiding devices - a case study," *Vacuum* **34**, 403 (1983).
107. O. Bazzi, M. G. Gazalet, J. C. Kastelik, and C. Bruneel, "Multi-channel  $\text{TeO}_2$  acousto-optic modulator: design and characteristics," in *IEEE Ultrasonics Symposium*, (IEEE, Piscataway, NJ, USA, 1994), 859.
108. I. Abdulhalim, C. N. Pannell, J. Wang, G. Wylangowski, and D. N. Payne, "Acoustooptic modulation using a new chlorotellurite glass," *J. Appl. Phys.* **75**, 519-521 (1994).
109. D. R. Pape and A. P. Goutzoulis, "New wavelength division multiplexing true-time-delay network for wideband phased array antennas," *J. Opt. A: Pure Appl. Opt.* **1**, 320-323 (1999).
110. W. Bonner, S. Singh, L. Van Uitert, and A. Warner, "High quality tellurium dioxide for acousto-optic and non-linear applications," *J. Electron. Mater.* **1**, 154-164 (1972).
111. G. W. Brady, "X-Ray study of Tellurium oxide glass," *J. Chem. Phys.* **24**, 477 (1956).
112. G. W. Brady, "Structure of Tellurium oxide glass," *J. Chem. Phys.* **27**, 300 (1957).
113. T. Uchino, S.-H. Kim, T. Yoko, and T. Fukunaga, "Medium-range structure of  $\text{TeO}_2$  glass from molecular orbital calculations," *J. Ceram. Soc. Jpn.* **105**, 205 (1997).
114. H. Niida, T. Uchino, J. Jin, S.-H. Kim, T. Fukunaga, and T. Yoko, "Structure of alkali tellurite glasses from neutron diffraction and molecular orbital calculations," *J. Chem. Phys.* **114**, 467 (2001).
115. R. Akagi, K. Handa, N. Ohtori, A. C. Hannon, M. Tatsumisago, and N. Umesaki, "High-temperature structure of  $\text{K}_2\text{O}$ - $\text{TeO}_2$  glasses," *J. Non-Cryst. Solids* **256-257**, 118 (1999).
116. R. El-Mallawany, A. Abdel-Kader, M. El-Hawary, and N. El-Khoshkhany, "UV-IR spectra of new tellurite glasses," *EPJ Applied Physics* **19**, 172 (2002).
117. A. Mori, "Tellurite-based fibers and their applications to optical communication networks," *J. Ceram. Soc. Jpn.* **116**, 1040-1051 (2008).
118. J. C. McLaughlin, S. L. Tagg, J. W. Zwanziger, D. R. Haefner, and S. D. Shastri, "The structure of tellurite glass: a combined NMR, neutron diffraction, and X-ray diffraction study," *J. Non-Cryst. Solids* **274**, 8 (2000).

119. N. Jiang, B. Jiang, R. Erni, N. D. Browning, and J. C. H. Spence, "Experimental and theoretical improvements on understanding of the OK-edge of TeO<sub>2</sub>," *Ultramicroscopy* **106**, 123-129 (2006).
120. S. Neov, I. Gerasimova, V. Kozhukharov, P. Mikula, and P. Lukas, "Structural study of complex tellurite glasses," *J. Non-Cryst. Solids* **192-193**(1995).
121. S. Neov, S. Ishmaev, and V. Kozhukharov, "High-resolution short-range order study of tellurite glasses," *J. Non-Cryst. Solids* **192-193**(1995).
122. S. Sakida, S. Hayakawa, and T. Yoko, "Part 2. <sup>125</sup>Te NMR study of M<sub>2</sub>O-TeO<sub>2</sub> (M = Li, Na, K, Rb and Cs) glasses," *J. Non-Cryst. Solids* **243**, 25 (1999).
123. I. Shaltout and T. A. Mohamed, "Raman spectrum, quantum mechanical calculations and vibrational assignments of (95% -TeO<sub>2</sub> 5% Sm<sub>2</sub>O<sub>3</sub>) glass," *Spectrochimica Acta Part A: Molecular and Biomolecular Spectroscopy* **67**, 454 (2007).
124. A. G. Kalampounias, G. N. Papatheodorou, and S. N. Yannopoulos, "A temperature-dependent Raman study of the xLiCl-(1-x)TeO<sub>2</sub> glasses and melts," *J. Phys. Chem. Solids* **68**, 1029-1034 (2007).
125. A. G. Kalampounias, S. N. Yannopoulos, and G. N. Papatheodorou, "Vibrational modes of sodium-tellurite glasses: Local structure and Boson peak changes," *J. Phys. Chem. Solids* **68**, 1035-1039 (2007).
126. V. O. Sokolov, V. G. Plotnichenko, and E. M. Dianov, "Structure of WO<sub>3</sub>-TeO<sub>2</sub> glasses," *Inorg. Mater.* **43**, 194-213 (2007).
127. V. O. Sokolov, V. G. Plotnichenko, V. V. Koltashev, and E. M. Dianov, "On the structure of tungstate-tellurite glasses," *J. Non-Cryst. Solids* **352**, 5618-5632 (2006).
128. T. Uchino and T. Yoko, "Ab initio cluster model calculations on the vibrational frequencies of TeO<sub>2</sub> glass," *J. Non-Cryst. Solids* **204**, 252 (1996).
129. F. Pietrucci, S. Caravati, and M. Bernasconi, "TeO<sub>2</sub> glass properties from first principles," *Phys. Rev. B* **78**, 16 (2008).
130. M. Soulis, A. P. Mirgorodsky, T. Merle-Mejean, and P. Thomas, "On the condensation mechanism of the dioxides of sixth- group elements: an ab initio approach," *Philos. Mag. Lett.* **87**, 979-988 (2007).
131. S. Suehara, S. Hishita, S. Inoue, and A. Nukui, "Cluster calculational approach to tellurite glasses," *Phys. Rev. B* **58**, 14124-14126 (1998).
132. B. E. Warren, "The basic principles involved in the glassy state," *J. Appl. Phys.* **13**, 610 (1942).
133. J. C. Champarnaud-Mesjard, S. Blanchandin, P. Thomas, A. Mirgorodsky, T. Merle-Mejean, and B. Frit, "Crystal structure, Raman spectrum and lattice dynamics of a new metastable form of Tellurium dioxide: [gamma]-TeO<sub>2</sub>," *J. Phys. Chem. Solids* **61**, 1507 (2000).
134. M. Mazzuca, J. Portier, B. Tanguy, and F. Romain, "Raman scattering in tellurium-metal oxyde glasses," *J. Mol. Struct.* **349**, 413-413 (1995).
135. R. El-Mallawany, "Optical properties of tellurite glasses," *J. Appl. Phys.* **72**(1992).
136. G. Ghosh, "Sellmeier coefficients and chromatic dispersions for some tellurite glasses," *J. Amer. Cer. Soc.* **78**, 2828-2830 (1995).
137. G. Agrawal, *Nonlinear Fiber Optics*, 3rd ed. (Academic Press, US, 2001).
138. D. A. Gaponov and A. S. Biryukov, "Optical properties of microstructure tellurite glass fibres," *Quantum Electron.* **36**, 343-348 (2006).
139. G. Qin, X. Yan, C. Kito, M. Liao, T. Suzuki, A. Mori, and Y. Ohishi, "Highly nonlinear tellurite microstructured fibers for broadband wavelength conversion and flattened supercontinuum generation," *J. Appl. Phys.* **107**(2010).
140. V. Kumar, A. K. George, J. C. Knight, and P. S. Russell, "Tellurite photonic crystal fiber," *Opt. Express* **11**, 2641-2645 (2003).

141. A. Ibrahim and S. K. J. Al-Ani, "Models of optical absorption in amorphous semiconductors at the absorption edge- A review and re-evaluation," *Czech. J. Phys.* **44**, 785-797 (1994).
142. M. Elahi and D. Souri, "Study of optical absorption and optical band gap determination of thin amorphous  $\text{TeO}_2\text{-V}_2\text{O}_5\text{-MoO}_3$  blown films," *Indian J. Pure Appl. Phys.* **44**, 468-472 (2006).
143. V. G. Plotnichenko, V. V. Koltashev, V. O. Sokolov, N. V. Popova, I. A. Grishin, and M. F. Churbanov, "Spectroscopic properties of new  $\text{BaCl}_2\text{-BaO-TeO}_2$  tellurite glasses for fibre and integrated optics applications," *J. Phys. D: Appl. Phys.* **41**(2008).
144. X. Feng, S. Tanabe, and T. Hanada, "Hydroxyl groups in Erbium-doped germanotellurite glasses," *J. Non-Cryst. Solids* **281**, 48-54 (2001).
145. M. D. O'Donnell, C. A. Miller, D. Furniss, V. K. Tikhomirov, and A. B. Seddon, "Fluorotellurite glasses with improved mid-infrared transmission," *J. Non-Cryst. Solids* **331**, 48-57 (2003).
146. S. X. Dai, J. J. Zhang, C. L. Yu, G. Zhou, G. N. Wang, and L. L. Hu, "Effect of hydroxyl groups on nonradiative decay of  $\text{Er}^{3+}$ :  $1\text{-}4(13/2) \rightarrow 1\text{-}4(15/2)$  transition in zinc tellurite glasses," *Mater. Lett.* **59**, 2333-2336 (2005).
147. N. Jaba, H. Ben Mansour, A. Kanoun, A. Brenier, and B. Champagnon, "Spectral broadening and luminescence quenching of  $1.53\text{ }\mu\text{m}$  emission in  $\text{Er}^{3+}$ -doped zinc tellurite glass," *J. Lumin.* **129**, 270-276 (2009).
148. E. R. Taylor, L. N. Ng, N. P. Sessions, and H. Buerger, "Spectroscopy of  $\text{Tm}^{3+}$ -doped tellurite glasses for  $1470\text{ nm}$  fiber amplifier," *J. Appl. Phys.* **92**, 112-117 (2002).
149. H. Burger, W. Vogel, and V. Kozhukharov, "IR transmission and properties of glasses in the  $\text{TeO}_2\text{-R}_n\text{O}_m$ ,  $\text{R}_n\text{X}_m$ ,  $\text{R}_n(\text{SO}_4)_m$ ,  $\text{R}_n(\text{PO}_3)_m$  and  $\text{B}_2\text{O}_3$  systems," *Infrared Physics* **25**, 395-409 (1985).
150. E. M. Vogel, M. J. Weber, and D. M. Krol, "Nonlinear optical phenomena in glass," *Phys. Chem. Glasses* **32**, 231-254 (1991).
151. T. M. Monro and H. Ebendorff-Heidepriem, "Progress in microstructured optical fibers," *Annual Review of Materials Research* **36**, 467-495 (2006).
152. R. Adair, L. L. Chase, and S. A. Payne, "Nonlinear Refractive-Index Measurements of Glasses Using 3-Wave Frequency Mixing," *Journal of the Optical Society of America B-Optical Physics* **4**, 875-881 (1987).
153. S. Montant, E. Freysz, and M. Couzi, "Nuclear and electronic contributions to the third-order nonlinearity in different glasses," *Opt. Commun.* **281**, 769-775 (2008).
154. A. Berthereau, E. Fargin, A. Villezusanne, and R. Olazcuaga, "Determination of local geometries around Tellurium in  $\text{TeO}_2\text{-Nb}_2\text{O}_5$  and  $\text{TeO}_2\text{-Al}_2\text{O}_3$  oxide glasses by XANES and EXAFS: investigation of electronic properties of evidenced Oxygen clusters by ab Initio calculations," *J. Solid State Chem.* **126**(1996).
155. E. Fargin, A. Berthereau, T. Cardinal, G. Le Flem, L. Ducasse, L. Canioni, P. Segonds, L. Sarger, and A. Ducasse, "Optical non-linearity in oxide glasses," *J. Non-Cryst. Solids* **203**, 101 (1996).
156. M. Dutreilh-Colas, P. Thomas, J. C. Champarnaud-Mesjard, and E. Fargin, "New  $\text{TeO}_2$  based glasses for nonlinear optical applications: study of the  $\text{Ti}_2\text{O-TeO}_2\text{-Bi}_2\text{O}_3\text{-Ti}_2\text{O-TeO}_2\text{-PbO}$  and  $\text{Ti}_2\text{O-TeO}_2\text{-Ga}_2\text{O}_3$  systems," *Phys. Chem. Glasses* **44**, 349-352 (2003).
157. R. Jose and Y. Ohishi, "Higher nonlinear indices, Raman gain coefficients, and bandwidths in the  $\text{TeO}_2\text{-ZnO-Nb}_2\text{O}_5\text{-MoO}_3$  quaternary glass system," *Appl. Phys. Lett.* **90**, 3 (2007).
158. R. Jose, G. Qin, Y. Arai, and Y. Ohishi, "Enhanced nonlinear susceptibility in  $\text{TeO}_2\text{-BaO-SrO-Nb}_2\text{O}_5$  tellurite glasses," *Jpn. J. Appl. Phys., Part 2* **46**(2007).
159. U. Osterberg and W. Margulis, "Efficient 2nd harmonic-generation in an optical fiber," *Journal of the Optical Society of America B-Optical Physics* **3**, P102-P103 (1986).

160. U. Osterberg and W. Margulis, "Dye-laser pumped by Nd-YAG laser-pulses frequency doubled in a glass optical fiber," *Opt. Lett.* **11**, 516-518 (1986).
161. R. A. Myers, N. Mukherjee, and S. R. J. Brueck, "Large 2nd-order nonlinearity in poled fused-silica," *Opt. Lett.* **16**, 1732-1734 (1991).
162. P. G. Kazansky, P. S. Russell, and H. Takebe, "Glass fiber poling and applications," *J. Lightwave Technol.* **15**, 1484-1493 (1997).
163. T. Fujiwara, T. Sawada, Y. Benino, T. Komatsu, M. Takahashi, T. Yoko, and J. Nishii, "Direct observation of second-harmonic generation from crystalline particles in Ge-doped SiO<sub>2</sub> glass films," *Opt. Express* **11**, 1598-1606 (2003).
164. T. Fujiwara, T. Sawada, T. Honma, Y. Benino, T. Komatsu, M. Takahashi, T. Yoko, and J. Nishi, "Origin of intrinsic second-harmonic generation in crystallized GeO<sub>2</sub>-SiO<sub>2</sub> glass films," *Jpn. J. Appl. Phys. Part 1 - Regul. Pap. Short Notes Rev. Pap.* **42**, 7326-7330 (2003).
165. T. Fujiwara, M. Takahashi, and A. J. Ikushima, "Second-harmonic generation in germanosilicate glass poled with ArF laser irradiation," *Appl. Phys. Lett.* **71**, 1032-1034 (1997).
166. A. Narazaki, K. Tanaka, K. Hirao, and N. Soga, "Effect of poling temperature on optical second harmonic intensity of sodium zinc tellurite glasses," *J. Appl. Phys.* **83**, 3986-3990 (1998).
167. K. Tanaka, K. Kashima, K. Hirao, N. Soga, A. Mito, and H. Nasu, "2nd-harmonic generation in poled tellurite glasses," *Jpn. J. Appl. Phys. Part 2 - Lett.* **32**, L843-L845 (1993).
168. K. Tanaka, K. Kashima, K. Hirao, N. Soga, A. Mito, and H. Nasu, "2nd-harmonic generation in electrically poled Li<sub>2</sub>O-Nb<sub>2</sub>O<sub>5</sub>-TeO<sub>2</sub> glasses," *J. Non-Cryst. Solids* **185**, 123-126 (1995).
169. K. Tanaka, A. Narazaki, Y. Yonezaki, and K. Hirao, "Poling-induced structural change and second-order nonlinearity of Na<sup>+</sup>-doped Nb<sub>2</sub>O<sub>5</sub>-TeO<sub>2</sub> glass," *J. Phys.-Condes. Matter* **12**, L513-L518 (2000).
170. T. Taniguchi, H. Tanaka, K. Nishimura, and M. Usami, "First observation of optical second-order nonlinearity of poled pure TeO<sub>2</sub> glass film prepared by novel fabrication process," in *Cleo(R)/Pacific Rim 2001, Vol II, Technical Digest* (Ieee, New York, 2001), pp. 458-459.
171. B. Ferreira, E. Fargin, B. Guillaume, G. Le Flem, V. Rodriguez, M. Couzi, T. Buffeteau, L. Canioni, L. Sarger, G. Martinelli, Y. Quiquempois, H. Zeglache, and L. Carpentier, "Second harmonic generation in poled tellurite glass," *J. Non-Cryst. Solids* **332**, 207-218 (2003).
172. G. Vrillet, P. Thomas, V. Couderc, A. Barthelemy, and J. C. Champarnaud-Mesjard, "Second harmonic generation in optically poled tellurite glasses doped with heavy metal oxides," *J. Non-Cryst. Solids* **345**, 417-421 (2004).
173. G. S. Murugan, E. Fargin, V. Rodriguez, F. Adamietz, M. Couzi, T. Buffeteau, and P. Le Coustumer, "Temperature-assisted electrical poling of TeO<sub>2</sub>-Bi<sub>2</sub>O<sub>3</sub>-ZnO glasses for non-linear optical applications," *J. Non-Cryst. Solids* **344**, 158-166 (2004).
174. C. Lasbrugnas, P. Thomas, O. Masson, J. C. Champarnaud-Mesjard, E. Fargin, and V. Rodriguez, "Second harmonic generation in poled tungsten tellurite glasses," *Glass Technol.* **46**, 71-75 (2005).
175. C. Lasbrugnas, P. Thomas, O. Masson, J. C. Champarnaud-Mesjard, E. Fargin, V. Rodriguez, and M. Lahaye, "Second harmonic generation of thermally poled tungsten tellurite glass," *Opt. Mater.* **31**, 775-780 (2009).
176. Y. Yonesaki, K. Tanaka, and K. Hirao, "Enhancement of optically encoded second-order nonlinearity in 15Nb<sub>2</sub>O<sub>5</sub>-85TeO<sub>2</sub> glass by doping with V and Tb," *J. Ceram. Soc. Jpn.* **114**, 110-113 (2006).

177. M. Qiu, F. Pi, and G. Orriols, "The role of lead component in second-harmonic generation in lead silica by electron-beam irradiation," *Appl. Phys. Lett.* **73**, 3040-3042 (1998).
178. L. R. P. Kassab, R. d. A. Pinto, R. A. Kobayashi, M. Piasecki, P. Bragiel, and I. V. Kityk, "Photoinduced second-order optical susceptibilities of Er<sub>2</sub>O<sub>3</sub> doped TeO<sub>2</sub>-GeO<sub>2</sub>-PbO glasses," *Opt. Commun.* **274**, 461-465 (2007).
179. X. Feng, W. H. Loh, J. C. Flanagan, A. Camerlingo, S. Dasgupta, P. Petropoulos, P. Horak, K. E. Frampton, N. M. White, J. H. V. Price, H. N. Rutt, and D. J. Richardson, "Single-mode tellurite glass holey fiber with extremely large mode area for infrared nonlinear applications," *Opt. Express* **16**, 13651-13656 (2008).
180. P. Domachuk, N. A. Wolchover, M. Cronin-Golomb, A. Wang, A. K. George, C. M. B. Cordeiro, J. C. Knight, and F. G. Omenetto, "Over 4000 nm bandwidth of Mid-IR supercontinuum generation in sub-centimeter segments of highly nonlinear tellurite PCFs," *Opt. Express* **16**, 7161-7168 (2008).
181. T. Delmonte, M. A. Watson, E. J. O'Driscoll, X. Feng, T. M. Monro, V. Finazzi, P. Petropoulos, J. H. V. Price, J. C. Baggett, W. Loh, D. J. Richardson, and D. P. Hand, "Generation of mid-IR continuum using tellurite microstructured fiber," in *Lasers and Electro-Optics and 2006 Quantum Electronics and Laser Science*, (Inst. of Elec. and Elec. Eng. Computer Society, 2006).
182. X. Feng, W. H. Loh, A. Camerlingo, S. Dasgupta, J. C. Flanagan, P. Petropoulos, K. E. Frampton, N. M. White, H. N. Rutt, and D. J. Richardson, "Broadband supercontinuum using single-mode/dual-mode tellurite glass holey fibers with large mode area," in *2008 Conference on Quantum Electronics and Laser Science Conference on Lasers and Electro-Optics, CLEO/QELS*, (Inst. of Elec. and Elec. Eng. Computer Society, 2008).
183. M. Liao, X. Yan, G. Qin, C. Chaudhari, T. Suzuki, and Y. Ohishi, "A highly non-linear tellurite microstructure fiber with multi-ring holes for supercontinuum generation," *Opt. Express* **17**, 15481-15490 (2009).
184. M. Liao, C. Chaudhari, G. Qin, X. Yan, C. Kito, T. Suzuki, Y. Ohishi, M. Matsumoto, and T. Misumi, "Fabrication and characterization of a chalcogenide-tellurite composite microstructure fiber with high nonlinearity," *Opt. Express* **17**, 21608-21614 (2009).
185. G. Qin, M. Liao, C. Chaudhari, Y. Arai, T. Suzuki, and Y. Ohishi, "Flat supercontinuum generation in a microstructure tellurite fiber," in *Lasers and Electro-Optics Society Annual Meeting*, (Institute of Electrical and Electronics Engineers Inc., 2008), 177-178.
186. M. Liao, C. Chaudhari, G. Qin, X. Yan, T. Suzuki, and Y. Ohishi, "Tellurite microstructure fibers with small hexagonal core for supercontinuum generation," *Opt. Express* **17**, 12174-12182 (2009).
187. G. Qin, X. Yan, C. Kito, M. Liao, T. Suzuki, A. Mori, and Y. Ohishi, "Zero-dispersion-wavelength-decreasing tellurite microstructured fiber for wide and flattened supercontinuum generation," *Opt. Lett.* **35**, 136-138 (2010).
188. A. J. Kenyon, "Recent developments in rare-earth doped materials for optoelectronics," *Prog. Quantum Electron.* **26**, 225-284 (2002).
189. S. Q. Man, E. Y. B. Pun, and P. S. Chung, "Tellurite glasses for 1.3 $\mu$ m optical amplifiers," *Opt. Commun.* **168**, 369 (1999).
190. P. C. Becker, N. A. Olsson, and J. R. Simpson, *Erbium-doped fiber amplifiers: fundamentals and technology* (Academic Press, San Diego, CA, 1997).
191. C. E. Chryssou, F. Di Pasquale, and C. W. Pitt, "Er<sup>3+</sup>-doped channel optical waveguide amplifiers for WDM systems: A comparison of tellurite, alumina and Al/P silicate materials," *IEEE J. Sel. Top. Quantum Electron.* **6**, 114-121 (2000).
192. G. N. van den Hoven, E. Snoeks, A. Polman, C. vanDam, J. W. M. vanUffelen, and M. K. Smit, "Upconversion in Er-implanted Al<sub>2</sub>O<sub>3</sub> waveguides," *J. Appl. Phys.* **79**, 1258-1266 (1996).

193. A. Mortensen, D. H. Christensen, O. F. Nielsen, and E. Pedersen, "Raman-Spectra of Amorphous  $\text{Al}_2\text{O}_3$  and  $\text{Al}_2\text{O}_3$   $\text{Moo}_3$  Obtained by Visible and Infrared Excitation," *J. Raman Spectrosc.* **22**, 47-49 (1991).
194. Y. Hu, S. Jiang, G. Sorbello, T. Luo, Y. Ding, B. C. Hwang, J. H. Kim, H. J. Seo, and N. Peyghambarian, "Numerical analyses of the population dynamics and determination of the upconversion coefficients in a new high Erbium-doped tellurite glass," *J. Opt. Soc. Am. B: Opt. Phys.* **18**, 1928-1934 (2001).
195. S. Brovelli, A. Galli, R. Lorenzi, F. Meinardi, G. Spinolo, S. Tavazzi, V. Sigaev, S. Sukhov, P. Pernice, A. Aronne, E. Fanelli, and A. Paleari, "Efficient  $1.53\mu\text{m}$  Erbium light emission in heavily Er-doped titania-modified aluminium tellurite glasses," *J. Non-Cryst. Solids* **353**, 2150-2156 (2007).
196. J. Fick, E. J. Knystautus, A. Villeneuve, F. Schiettekatte, S. Roorda, and K. A. Richardson, "High photoluminescence in Erbium-doped chalcogenide thin films," *J. Non-Cryst. Solids* **272**, 200-208 (2000).
197. L. Wetenkamp, G. F. West, and H. Többen, "Optical properties of rare earth-doped ZBLAN glasses," *J. Non-Cryst. Solids* **140**, 35-40 (1992).
198. R. Rolli, A. Chiasera, M. Montagna, E. Moser, S. Ronchin, S. Pelli, G. C. Righini, A. Jha, V. K. Tikhomirov, S. A. Tikhomirova, C. Duverger, P. Galinetto, and M. Ferrari, "Rare-earth-activated fluoride and tellurite glasses: Optical and spectroscopic properties," in *Rare-Earth-Doped Materials and Devices V*, (SPIE, 2001), 109-122.
199. A. Mori, Y. Ohishi, and S. Sudo, "Erbium-doped tellurite glass fibre laser and amplifier," *Electron. Lett.* **33**, 863-864 (1997).
200. S. Shen, L. Huang, P. Joshi, and A. Jha, "Gain characteristics of  $\text{Er}^{3+}/\text{Ce}^{3+}$  codoped tellurite short fibre amplifier pumped at 980 nm," *Electron. Lett.* **39**, 1797-1799 (2003).
201. G. Jose, P. Nandi, S. Shen, J. Zhang, and A. Jha, "Novel glass hosts for integrated planar amplifiers in the optical communication window (1200 -1700 nm)," in *2007 9th International Conference on Transparent Optical Networks*, (Inst. of Elec. and Elec. Eng. Computer Society, 2007), 284-287.
202. Y. G. Choi, K. H. Kim, S. H. Park, and J. Heo, "Comparative study of energy transfers from  $\text{Er}^{3+}$  to  $\text{Ce}^{3+}$  in tellurite and sulfide glasses under 980 nm excitation," *J. Appl. Phys.* **88**, 3832-3839 (2000).
203. S. Shen, B. Richards, and A. Jha, "Enhancement in pump inversion efficiency at 980 nm in  $\text{Er}^{3+}$ ,  $\text{Er}^{3+}/\text{Eu}^{3+}$  and  $\text{Er}^{3+}/\text{Ce}^{3+}$  doped tellurite glass fibers," *Opt. Express* **14**, 5050-5054 (2006).
204. H. Nii, K. Ozaki, M. Herren, and M. Morita, "Up-conversion fluorescence of  $\text{Er}^{3+}$ - and  $\text{Yb}^{3+}$ -doped  $\text{TeO}_2$ -based oxide glass and single crystals," *J. Lumin.* **76-77**, 116-119 (1998).
205. L. Lu, Q. Nie, T. Xu, S. Dai, X. Shen, and X. Zhang, "Up-conversion luminescence of  $\text{Er}^{3+}/\text{Yb}^{3+}/\text{Nd}^{3+}$ -codoped tellurite glasses," *J. Lumin.* **126**, 677-681 (2007).
206. S. Tanabe, T. Tamaoka, T. Hanada, Y. Kondo, N. Sugimoto, and S. Ito, "Spectral properties of  $\text{Tm}^{3+}$ -doped glasses for S-band amplifier," in *Optical Amplifiers and Their Applications*, N. E. Jolley, J. D. Minelly, and Y. Nakano, eds. (Optical Soc America, Washington, 2001), pp. 36-38.
207. S. Tanabe, "Design of rare-earth doped amplifiers for the WDM telecommunication," *Glass Sci Technol.-Glastech. Ber.* **74**, 67-81 (2001).
208. S. Tanabe, "Properties of  $\text{Tm}^{3+}$ -doped tellurite glasses for  $1.4\mu\text{m}$  amplifier," in *Rare-Earth-Doped Materials and Devices V*, S. Jiang, ed. (Spie-Int Soc Optical Engineering, Bellingham, 2001), pp. 85-92.
209. L. H. Huang, S. X. Shen, and A. Jha, "Near infrared spectroscopic investigation of  $\text{Tm}^{3+}$ - $\text{Yb}^{3+}$  co-doped tellurite glasses," *J. Non-Cryst. Solids* **345**, 349-353 (2004).
210. M. Naftaly, S. X. Shen, and A. Jha, " $\text{Tm}^{3+}$ -doped tellurite glass for a broadband amplifier at  $1.47\mu\text{m}$ ," *Appl. Opt.* **39**, 4979-4984 (2000).



211. E. R. M. Taylor, L. N. Ng, J. Nilsson, R. Caponi, A. Pagano, M. Potenza, and B. Sordo, "Thulium-doped tellurite fiber amplifier," *IEEE Photonics Technol. Lett.* **16**, 777 (2004).
212. J. S. Wang, E. Snitzer, E. M. Vogel, and G. H. Sigel Jr, "1.47, 1.88 and 2.8  $\mu\text{m}$  emissions of  $\text{Tm}^{3+}$  and  $\text{Tm}^{3+}$ - $\text{Ho}^{3+}$ -codoped tellurite glasses," *J. Lumin.* **60-61**, 145-149 (1994).
213. L. H. Huang, A. Jha, S. X. Shen, and X. B. Liu, "Broadband emission in  $\text{Er}^{3+}$ - $\text{Tm}^{3+}$  codoped tellurite fibre," *Opt. Express* **12**, 2429-2434 (2004).
214. J. S. Wang, E. M. Vogel, E. Snitzer, J. L. Jackel, V. L. da Silva, and Y. Silberberg, "1.3  $\mu\text{m}$  emission of Neodymium and Praseodymium in tellurite-based glasses," *J. Non-Cryst. Solids* **178**, 109-113 (1994).
215. S. Q. Man, E. Y. B. Pun, and P. S. Chung, "Tellurite glasses for 1.3 $\mu\text{m}$  optical amplifiers," *Opt. Commun.* **168**, 369-373 (1999).
216. J. S. Wang, D. P. Machewirth, F. Wu, E. Snitzer, and E. M. Vogel, "Neodymium-doped tellurite single-mode fiber laser," *Opt. Lett.* **19**, 1448-1450 (1994).
217. Y. Tsang, B. Richards, D. Binks, J. Lousteau, and A. Jha, "A  $\text{Yb}^{3+}$ / $\text{Tm}^{3+}$ / $\text{Ho}^{3+}$  triply-doped tellurite fibre laser," *Opt. Express* **16**, 10690-10695 (2008).
218. B. Richards, Y. Tsang, D. Binks, J. Lousteau, and A. Jha, "Efficient similar to 2  $\mu\text{m}$   $\text{Tm}^{3+}$ -doped tellurite fiber laser," *Opt. Lett.* **33**, 402-404 (2008).
219. S. Dai, C. Yu, G. Zhou, J. Zhang, and G. Wang, "Effect of  $\text{OH}^-$  content on emission properties in  $\text{Er}^{3+}$ -doped tellurite glasses," *J. Non-Cryst. Solids* **354**, 1357-1360 (2008).
220. B. Richards, A. Jha, Y. Tsang, D. Binks, J. Lousteau, F. Fusari, A. Lagatsky, C. Brown, and W. Sibbett, "Tellurite glass lasers operating close to 2.1 $\mu\text{m}$ ," *Laser Phys. Lett.* **7**, 177-193 (2010).
221. S. Dai, C. Yu, G. Zhou, J. Zhang, G. Wang, and L. Hu, "Concentration quenching in Erbium-doped tellurite glasses," *J. Lumin.* **117**, 39-45 (2006).
222. M. Yamada, A. Mori, K. Kobayashi, H. Ono, T. Kanamori, K. Oikawa, Y. Nishida, and Y. Ohishi, "Gain-flattened tellurite-based EDFA with a flat amplification bandwidth of 76 nm," *IEEE Photonics Technol. Lett.* **10**, 1244-1246 (1998).
223. M. Yamada, A. Mori, H. Ono, K. Kobayashi, T. Kanamori, and Y. Ohishi, "Broadband and gain-flattened  $\text{Er}^{3+}$ -doped tellurite fibre amplifier constructed using a gain equalizer," *Electron. Lett.* **34**, 370-371 (1998).
224. A. Mori, T. Sakamoto, K. Kobayashi, K. Shikano, K. Oikawa, K. Hoshino, T. Kanamori, Y. Ohishi, and M. Shimizu, "1.58- $\mu\text{m}$  Broad-band Erbium-doped tellurite fiber amplifier," *J. Lightwave Technol.* **20**, 822-827 (2002).
225. A. Mori, H. Ono, K. Shikano, and M. Shimizu, "980 nm band pumped  $\text{Er}^{3+}$ -doped tellurite-based fibre amplifier with low-noise figure of less than 4.5 dB," *Electron. Lett.* **38**, 1419-1420 (2002).
226. A. Mori, K. Kobayashi, M. Yamada, T. Kanamori, K. Oikawa, Y. Nishida, and Y. Ohishi, "Low noise broadband tellurite-based  $\text{Er}^{3+}$ -doped fibre amplifiers," *Electron. Lett.* **34**, 887-888 (1998).
227. C. E. Chryssou, F. Di Pasquale, and C. W. Pitt, " $\text{Er}^{3+}$ -doped channel optical waveguide amplifiers for WDM systems: A comparison of tellurite, alumina and Al/P silicate materials," *IEEE J. Sel. Top. Quantum Electron.* **6**, 114-121 (2000).
228. T. Makino, H. Sotobayashi, and W. Chujo, "1.5 Tbit/s (75-20 Gbit/s) DWDM transmission using  $\text{Er}^{3+}$ -doped tellurite fibre amplifiers with 63 nm continuous signal band," *Electron. Lett.* **38**, 1502-1504 (2002).
229. H. Ono, T. Sakamoto, A. Mori, J. Kani, and M. Fukutoku, "An Erbium-doped tellurite fiber amplifier for WDM systems with dispersion-shifted fibers," *IEEE Photonics Technol. Lett.* **14**, 1070-1072 (2002).
230. Y. Varaksa, G. Sinitsyn, and M. Khodasevich, "Transmission capacity of Erbium-doped fiber amplifiers as a criterion for quality of Erbium-doped optical fibers," *Opt. Spectrosc.* **104**, 130-134 (2008).



231. A. Mori and H. Masuda, "Tellurite fiber Raman amplifiers," *NTT Technical Review* **2**, 51-55 (2004).
232. A. Mori, H. Masuda, K. Shikano, K. Oikawa, K. Kato, and M. Shimizu, "Ultra-wideband tellurite-based Raman fibre amplifier," *Electron. Lett.* **37**, 1442-1443 (2001).
233. H. Takara, H. Masuda, K. Mori, K. Sato, Y. Inoue, T. Ohara, A. Mori, M. Kohtoku, Y. Miyamoto, T. Morioka, and S. Kawanishi, "Ultra-wideband tellurite/silica fiber Raman amplifier and supercontinuum lightwave source for 124-nm seamless bandwidth DWDM transmission," in *Optical Fiber Communication*, (Institute of Electrical and Electronics Engineers Inc., 2002), FB11-FB13.
234. H. Masuda, A. Mori, K. Shikano, K. Oikawa, K. Kato, and M. Shimizu, "Ultra-wide-band Raman amplifier using tellurite and silica fibres," *Electron. Lett.* **38**, 867-868 (2002).
235. G. Qin, R. Jose, and Y. Ohishi, "Design of ultimate gain-flattened O-, E-, and S+ C+ L ultrabroadband fiber amplifiers using a new fiber Raman gain medium," *J. Lightwave Technol.* **25**, 2727-2738 (2007).
236. R. Jose, G. Qin, Y. Arai, and Y. Ohishi, "Tailoring of Raman gain bandwidth of tellurite glasses for designing gain-flattened fiber Raman amplifiers," *J. Opt. Soc. Am. B: Opt. Phys.* **25**, 373-382 (2008).
237. R. Stegeman, L. Jankovic, H. Kim, C. Rivero, G. Stegeman, K. Richardson, P. Delfyett, Y. Guo, A. Schulte, and T. Cardinal, "Tellurite glasses with peak absolute Raman gain coefficients up to 30 times that of fused silica," *Opt. Lett.* **28**, 1128 (2003).
238. Y. Ohishi and R. Jose, "Raman scattering characteristics of WO<sub>3</sub> and P<sub>2</sub>O<sub>5</sub> doped TBSN glasses: A new gain medium for broadband fiber Raman amplifiers," in *Active and Passive Optical Components for Communications VI*, (International Society for Optical Engineering, Bellingham WA, WA 98227-0010, United States, 2006), 638906.
239. R. Jose and Y. Ohishi, "Enhanced Raman gain coefficients and bandwidths in P<sub>2</sub>O<sub>5</sub> and WO added tellurite glasses for Raman gain media," *Appl. Phys. Lett.* **89**(2006).
240. G. S. Murugan, T. Suzuki, and Y. Ohishi, "Phospho-tellurite glasses containing heavy metal oxides for ultrabroad band fiber Raman amplifiers," *Appl. Phys. Lett.* **86**, 221109 (2005).
241. M. D. O'Donnell, K. Richardson, R. Stolen, A. B. Seddon, D. Furniss, V. K. Tikhomirov, C. Rivero, M. Ramme, R. Stegeman, G. Stegeman, M. Couzi, and T. Cardinal, "Tellurite and fluorotellurite glasses for fiberoptic Raman amplifiers: Glass characterization, optical properties, Raman gain, preliminary fiberization, and fiber characterization," *J. Amer. Cer. Soc.* **90**, 1457 (2007).
242. R. Jose, Y. Arai, and Y. Ohishi, "Raman scattering characteristics of the TBSN-based tellurite glass system as a new Raman gain medium," *J. Opt. Soc. Am. B: Opt. Phys.* **24**, 1526 (2007).
243. R. Stegeman, C. Rivero, K. Richardson, G. Stegeman, P. Delfyett Jr, Y. Guo, A. Pope, A. Schulte, T. Cardinal, P. Thomas, and J.-C. Champarnaud-Mesjard, "Raman gain measurements of thallium-Tellurium oxide glasses," *Opt. Express* **13**, 1149 (2005).
244. S. Berneschi, G. Nunzi Conti, and G. C. Righini, "Planar waveguide amplifiers," *Ceramist: Jnl Korean Ceram. Soc.* **10**, 75-85 (2007).
245. S. K. Sundaram, C. B. Schaffer, and E. Mazur, "Microexplosions in tellurite glasses," *Appl. Phys. A* **76**, 379-384 (2003).
246. G. C. Righini, I. Banyasz, S. Berneschi, M. Brenci, A. Chiasera, M. Cremona, D. Ehrt, M. Ferrari, R. M. Montecore, G. Nunzi Conti, S. Pelli, S. Sebastiani, and C. Tosello, "Laser irradiation, ion implantation and e-beam writing of integrated optical structures," in *Photonic Materials, Devices, and Applications*, (SPIE, 2005), 649-657.
247. P. Nandi, G. Jose, C. Jayakrishnan, S. Debbarma, K. Chalapathi, K. Alti, A. K. Dharmadhikari, J. A. Dharmadhikari, and D. Mathur, "Femtosecond laser written channel waveguides in tellurite glass," *Opt. Express* **14**, 12145-12150 (2006).

248. T. T. Fernandez, G. Della Valle, R. Osellame, G. Jose, N. Chiodo, A. Jha, and P. Laporta, "Active waveguides written by femtosecond laser irradiation in an Erbium-doped phospho-tellurite glass," *Opt. Express* **16**, 15198-15205 (2008).
249. S. Berneschi, G. N. Conti, I. Banyasz, A. Watterich, N. Q. Khanh, M. Fried, F. Paszti, M. Brenci, S. Pelli, and G. C. Righini, "Ion beam irradiated channel waveguides in  $\text{Er}^{3+}$ -doped tellurite glass," *Appl. Phys. Lett.* **90**(2007).
250. N. Q. Khanh, S. Berneschi, I. Banyasz, M. Brenci, M. Fried, G. Nunzi Conti, F. Paszti, S. Pelli, G. C. Righini, and A. Watterich, "Fabrication of channel waveguides in  $\text{Er}^{3+}$ -doped tellurite glass via N+ ion implantation," *Nucl. Instrum. Methods Phys. Res., Sect. B* **267**, 2327-2330 (2009).
251. G. Della Valle, S. Taccheo, P. Laporta, G. Sorbello, E. Cianci, and V. Foglietti, "Compact high gain Erbium-ytterbium doped waveguide amplifier fabricated by Ag-Na ion exchange," *Electron. Lett.* **42**, 632-633 (2006).
252. G. Della Valle, A. Festa, G. Sorbello, K. Ennser, C. Cassagnetes, D. Barbier, and S. Taccheo, "Single-mode and high power waveguide lasers fabricated by ion-exchange," *Opt. Express* **16**, 12334-12341 (2008).
253. G. N. Conti, V. K. Tikhomirov, M. Bettinelli, S. Berneschi, M. Brenci, B. Chen, S. Pelli, and A. Speghini, "Characterization of ion-exchanged waveguides in tungsten tellurite and zinc tellurite  $\text{Er}^{3+}$ -doped glasses," *Opt. Eng.* **42**, 2805-2811 (2003).
254. V. A. G. Rivera, E. F. Chillece, E. Rodriguez, C. L. Cesar, and L. C. Barbosa, "Planar waveguides by ion exchange in  $\text{Er}^{3+}$ -doped tellurite glass," *J. Non-Cryst. Solids* **352**, 363-367 (2006).
255. S. Sakida, T. Nanba, and Y. Miura, "Refractive-index profiles and propagation losses of  $\text{Er}^{3+}$ -doped tungsten tellurite glass waveguide by  $\text{Ag}^{+}$ - $\text{Na}^{+}$  ion-exchange," *Mater. Lett.* **60**, 3413-3415 (2006).
256. M. Lanata, M. Fere, D. Piccinin, S. M. Pietralunga, and M. Martinelli, "Sputtered tellurite glass thin films for planar optical devices," in *2008 10th Anniversary International Conference on Transparent Optical Networks, ICTON*, (Inst. of Elec. and Elec. Eng. Computer Society, 2008), 227-230.
257. S. M. Pietralunga, M. Lanata, M. Fere, D. Piccinin, G. Cusmai, M. Torregiani, and M. Martinelli, "High-contrast waveguides in sputtered pure  $\text{TeO}_2$  glass thin films," *Opt. Express* **16**, 21662-21670 (2008).
258. M. D. O'Donnell, D. Furniss, V. K. Tikhomirov, D. Briggs, E. F. Smith, and A. B. Seddon, "Surface properties of tellurite and fluorotellurite glasses," *J. Mater. Res.* **22**, 1673-1684 (2007).
259. T. M. Benson, A. Vukovic, P. Sewell, A. Loni, Y. Zhang, W. Pan, D. Zhang, M. D. O'Donnell, J. Lousteau, D. Furniss, and A. B. Seddon, "Novel glass compositions and fabrication technologies for photonic integrated circuits," in *2005 7th International Conference on Transparent Optical Networks*, (IEEE, 2005), 296.
260. V. A. G. Rivera, E. Rodriguez, E. F. Chillece, C. L. Cesar, and L. C. Barbosa, "Waveguide produced by fiber on glass method using  $\text{Er}^{3+}$ -doped tellurite glass," *J. Non-Cryst. Solids* **353**, 339-343 (2007).
261. N. Chopra, A. Mansingh, and G. K. Chadha, "Electrical, optical and structural properties of amorphous  $\text{V}_2\text{O}_5$ - $\text{TeO}_2$  blown films," *J. Non-Cryst. Solids* **126**, 194-201 (1990).
262. M. A. Hassan and C. A. Hogarth, "A study of the structural, electrical and optical properties of copper Tellurium oxide glasses," *J. Mater. Sci.* **23**, 2500-2504 (1988).
263. M. A. Hassan, W. I. Khleif, and C. A. Hogarth, "A comparison of the optical properties of glass and of evaporated amorphous thin films of  $\text{BaO-TeO}_2$ ," *J. Mater. Sci.* **24**, 1607-1611 (1989).
264. L. Weng, S. N. B. Hodgson, and J. Ma, "Preparation of  $\text{TeO}_2$ - $\text{TiO}_2$  thin films by sol-gel process," *J. Mater. Sci. Lett.* **18**, 2037-2039 (1999).

265. S. N. B. Hodgson and L. Weng, "Chemical and sol-gel processing of tellurite glasses for optoelectronics," *J. Mater. Sci. - Mater. Electron.* **17**, 723-733 (2006).
266. S. N. B. Hodgson and L. Weng, "Preparation of tellurite thin films from Tellurium isopropoxide precursor by sol-gel processing," *J. Non-Cryst. Solids* **276**, 195-200 (2000).
267. S. Coste, A. Lecomte, P. Thomas, T. Merle-Mejean, and J. C. Champarnaud-Mesjard, "Sol-gel synthesis of  $\text{TeO}_2$ -based materials using citric acid as hydrolysis modifier," *J. Sol-Gel Sci. Technol.* **41**, 79-86 (2007).
268. A. Singh, E. J. Knystautas, and R. Lapointe, "Synthesis of Tellurium oxide by high dose Oxygen ion-implantation," *Appl. Surf. Sci.* **22-23**, 2-681 (1984).
269. M. F. Al-Kuhaili, S. M. A. Durrani, E. E. Khawaja, and J. Shirokoff, "Effects of preparation conditions on the optical properties of thin films of Tellurium oxide," *J. Phys. D: Appl. Phys.* **35**, 910-915 (2002).
270. S. Kumar and A. Mansingh, "Annealing-induced structural changes in Tellurium dioxide thin films," *J. Phys. D: Appl. Phys.* **23**, 1252-1255 (1990).
271. K. Arshak and O. Korostynska, "Gamma radiation-induced changes in the electrical and optical properties of Tellurium dioxide thin films," *IEEE Sens. J.* **3**, 717-721 (2003).
272. N. Lakshminarayan, M. Radhakrishnan, and C. Balasubramanian, "Dielectric studies on Tellurium oxide thin-films," *J. Mater. Sci.* **17**, 1623-1626 (1982).
273. N. Lakshminarayan, M. Radhakrishnan, and C. Balasubramanian, "Formation, structural and optical properties of Tellurium oxide films deposited by a plasma process (PARBAD)," *J. Mater. Sci.* **19**, 2368-2372 (1984).
274. M. Di Giulio, D. Manno, M. Concetta Nicotra, and M. Re, "Structural and morphological analysis of reactively sputtered Tellurium suboxide thin films," *J. Non-Cryst. Solids* **155**, 67-76 (1993).
275. M. Di Giulio, M. C. Nicotra, M. Re, R. Rella, and P. Siciliano, "Optical absorption and structural characterization of reactively sputtered Tellurium suboxide thin films," *Appl. Surf. Sci.* **65-66**, 313-318 (1993).
276. M. Di Giulio, A. Zappettini, L. Nasi, and S. M. Pietralunga, "Rf-sputtering growth of stoichiometric amorphous  $\text{TeO}_2$  thin films," *Cryst. Res. Technol.* **40**, 1023-1027 (2005).
277. F. D'Amore, M. Di Giulio, S. M. Pietralunga, A. Zappettini, L. Nasi, V. Rigato, and M. Martinelli, "Sputtered stoichiometric  $\text{TeO}_2$  glass films: Dispersion of linear and nonlinear optical properties," *J. Appl. Phys.* **94**, 1654-1661 (2003).
278. R. Nayak, V. Gupta, A. L. Dawar, and K. Sreenivas, "Optical waveguiding in amorphous Tellurium oxide thin films," *Thin Solid Films* **445**, 118-126 (2003).
279. S. M. Pietralunga, F. D'Amore, and A. Zappettini, "Optical properties of reactively sputtered  $\text{TeO}_x$  amorphous films," *Appl. Opt.* **44**, 534-537 (2005).
280. N. Dewan, K. Sreenivas, and V. Gupta, "Properties of crystalline gamma- $\text{TeO}_2$  thin film," *J. Cryst. Growth* **305**, 237-241 (2007).
281. N. Dewan, V. Gupta, K. Sreenivas, and R. S. Katiyar, "Growth of amorphous  $\text{TeO}_x$  ( $2 \leq x \leq 3$ ) thin film by radio frequency sputtering," *J. Appl. Phys.* **101**, 084910 (2007).
282. A. P. Caricato, M. Fernandez, M. Ferrari, G. Leggieri, M. Martino, M. Mattarelli, M. Montagna, V. Resta, L. Zampedri, R. M. Almeida, M. C. Concalves, L. Fortes, and L. F. Santos, "Er<sup>3+</sup> doped tellurite waveguides deposited by excimer laser ablation," *Mater. Sci. Eng., B* **105**, 65-69 (2003).
283. M. Martino, A. P. Caricato, M. Fernandez, G. Leggieri, A. Jha, M. Ferrari, and M. Mattarelli, "Pulsed laser deposition of active waveguides," *Thin Solid Films* **433**, 39-44 (2003).
284. M. Bouazaoui, B. Capoen, A. P. Caricato, A. Chiasera, A. Fazzi, M. Ferrari, G. Leggieri, M. Martino, M. Mattarelli, M. Montagna, F. Romano, T. Tunno, S. Turrel, and K. Vishnubhatla, "Pulsed Laser Deposition of Er doped tellurite films on large area," *J. Phys. Conf. Ser.* **59**, 475 (2007).

285. L. Weng and S. N. B. Hodgson, "Multicomponent tellurite thin film materials with high refractive index," *Opt. Mater.* **19**, 313-317 (2002).
286. M. Takenaga, N. Yamada, K. Nishiuchi, N. Akahira, T. Ohta, S. Nakamura, and T. Yamashita, "TeO<sub>x</sub> Thin films for an optical disc memory," *J. Appl. Phys.* **54**, 5376-5380 (1983).
287. A. Singh and R. A. Lessard, "Stoichiometry changes in Tellurium oxide films," *Solid State Commun.* **51**, 845-848 (1984).
288. A. Singh and R. A. Lessard, "Characterization of evaporated Tellurium oxide films," *J. Mater. Sci.* **19**, 3844-3848 (1984).
289. M. Irannejad, G. Jose, A. Jha, and D. P. Steenson, "A parametric study of Er<sup>3+</sup> ions doped Phospho-tellurite glass thin films by pulsed laser deposition," *Opt. Mater.* (2010).
290. M. Irannejad, G. Jose, A. Jha, and P. Steenson, "Pulsed laser deposition of phospho-tellurite glass thin film Waveguides," in *Transparent Optical Networks (ICTON), 2010 12th International Conference on*, (2010), 1-4.
291. G. Jose, D. P. Steenson, M. Irannejad, and A. Jha, "High quality erbium doped tellurite glass films using ultrafast laser deposition," in *ICTON 2009: 11th International Conference on Transparent Optical Networks*, (2009).
292. B. N. Chichkov, C. Momma, S. Nolte, F. Von Alvensleben, and A. TÄ¼nnermann, "Femtosecond, picosecond and nanosecond laser ablation of solids," *Appl. Phys. A* **63**, 109-115 (1997).
293. B. C. Stuart, M. D. Feit, S. Herman, A. M. Rubenchik, B. W. Shore, and M. D. Perry, "Nanosecond-to-femtosecond laser-induced breakdown in dielectrics," *Phys. Rev. B: Condens. Matter* **53**, 1749-1761 (1996).
294. S. Kumar and A. Mansingh, "Fabrication and characterization of tetragonal and orthorhombic TeO<sub>2</sub> films," in *1990 IEEE 7th International Symposium on Applications of Ferroelectrics*, (Publ by IEEE, 1992), 717-719.
295. M. Ohring, *The Materials Science of Thin Film* (Academic Press, 1993).
296. H. L. Hartnagel, A. L. Dawar, A. K. Jain, and C. Jagadish, *Semiconductor transparent thin films* (Institute of Physics Publishing, Bristol, UK, 1995).
297. S. Harsha, *Principle of vapor deposition of thin film* (Elsevier Science, 2006).
298. F.-m. Zhou, Z. Li, L. Fan, S.-y. Zhang, X.-j. Shui, and K. Wasa, "Effects of TeO<sub>x</sub> films on temperature coefficients of delay of Love-type wave devices based on TeO<sub>x</sub>/36YX-LiTaO<sub>3</sub> structures," *Vacuum* **84**, 986-991 (2010).
299. SCI, retrieved 27 Jan, 2010, <http://www.sci-soft.com/FilmTek%204000.htm>.
300. H. K. Pulker, "Characterization of optical thin films," *Appl. Opt.* **18**, 1969-1977 (1979).
301. M. H. Brodsky, R. J. Gambino, J. E. Smith, Jr., and Y. Yacoby, "Raman spectrum of amorphous Tellurium," *Phys. Status Solidi B* **52**, 609-614 (1972).
302. A. Jha, S. Shaoxiong, H. Li Hui, and P. Joshi, "Spectroscopic properties of rare earth metal ion doped Tellurium oxide glasses and fibres," *J. Opt.* **33**, 157 (2004).
303. P. K. Tien, "Light Waves in Thin Films and Integrated Optics," *Appl. Opt.* **10**, 2395-2413 (1971).
304. R. Ulrich and R. Torge, "Measurement of Thin Film Parameters with A Prism Coupler," *Appl. Opt.* **12**, 2901 (1973).
305. C. D. W. Wilkinson and M. Rahman, "Dry etching and sputtering," *Phil. Trans. R. Soc. Lond. A* **362**, 125-138 (2004).
306. N. Layadi, J. I. Colonell, and J. T.-C. Lee, "An introduction to plasma etching for VLSI circuit technology," *Bell Labs Tech. J.* **4**, 155-171 (1999).
307. N. Hosokawa, R. Matsuzaki, and T. Asamaki, "Rf sputter-etching by fluoro-chloro-hydrocarbon gases," *Jpn. J. Appl. Phys.*, 435-438 (1974).
308. L. Su, C. J. Rowlands, T. H. Lee, and S. R. Elliott, "Fabrication of photonic waveguides in sulfide chalcogenide glasses by selective wet-etching," *Electron. Lett.* **44**, 472-474 (2008).

309. F. P. Payne and J. P. R. Lacey, "Theoretical analysis of scattering loss from planar optical waveguides," *Opt. Quantum Electron.* **26**, 977-986 (1994).
310. K. K. Lee, D. R. Lim, H.-C. Luan, A. Agarwal, J. Foresi, and L. C. Kimerling, "Effect of size and roughness on light transmission in a Si/SiO<sub>2</sub> waveguide: Experiments and model," *Appl. Phys. Lett.* **77**, 1617-1619 (2000).
311. D. L. Flamm and V. M. Donnelly, "The design of plasma etchants," *Plasma Chem. Plasma Process.* **1**, 317-363 (1981).
312. J. H. Keller, "Inductive plasmas for plasma processing," *Plasma Sources Sci. Technol.* **5**, 166-172 (1996).
313. C. D. W. Wilkinson and M. Rahman, "Dry etching and sputtering," *Phil. Trans. R. Soc. Lond. A* **362**, 125-138 (2004).
314. D. L. Flamm, V. M. Donnelly, and D. E. Ibbotson, "Basic chemistry and mechanisms of plasma etching," *J. Vac. Sci. Technol., B* **1**, 23-30 (1983).
315. M. A. Foad, C. D. W. Wilkinson, C. Dunscomb, and R. H. Williams, "CH<sub>4</sub>/H<sub>2</sub>: A universal reactive ion etch for II-VI semiconductors?," *Appl. Phys. Lett.* **60**, 2531-2531 (1992).
316. S. J. Pearton and F. Ren, "Review science of dry etching of III-V materials," *J. Mater. Sci. - Mater. Electron.* **5**, 1-12 (1994).
317. R. Cheung, S. Thoms, S. P. Beamont, S. P. Doughty, V. Law, and C. D. W. Wilkinson, "Reactive ion etching of GaAs using a mixture of Methane and Hydrogen," *Electron. Lett.* **23**, 857-859 (1987).
318. A. Semu and P. Silverberg, "Methane-hydrogen III-V metal-organic reactive ion etching," *Semicond. Sci. Technol.* **6**, 287-289 (1991).
319. L. Henry, C. Vaudry, and P. Granjoux, "Novel process for integration of optoelectronic devices using reactive ion etching without chlorinated gas," *Electron. Lett.* **23**, 1253-1254 (1987).
320. T. Schwarzl, W. Heiss, G. Kocher-Oberlehner, and G. Springholz, "CH<sub>4</sub>/H<sub>2</sub> plasma etching of IV-VI semiconductor nanostructures," *Semicond. Sci. Technol.* **14**, L11-L14 (1999).
321. H. Toyoda, H. Kojima, and H. Sugai, "Mass spectroscopic investigation of the CH<sub>3</sub>\* radicals in a methane rf discharge," *Appl. Phys. Lett.* **54**, 1507-1509 (1989).
322. Y. Feurprier, C. Cardinaud, B. Grolleau, and G. Turban, "Etch product identification during CH<sub>4</sub>-H<sub>2</sub> RIE of InP using mass spectrometry," *Plasma Sources Sci. Technol.* **6**, 561-568 (1997).
323. R. C. Keller, M. Seelmann-Eggebert, and H. J. Richter, "Addition of N<sub>2</sub> as a polymer deposition inhibitor in CH<sub>4</sub>/H<sub>2</sub> electrocyclotron resonance plasma etching of Hg<sub>1-x</sub>Cd<sub>x</sub>Te," *Appl. Phys. Lett.* **67**, 3750-3750 (1995).
324. S. Shen, L. Huang, P. Joshi, and A. Jha, "A short fibre amplifier based on Er<sup>3+</sup> doped tellurite glass," in *OSA Trends in Optics and Photonics Series*, (OSA, 2004), 387-389.
325. A. Mori and Y. Ohishi, "Tellurite-based EDFAs for broadband communication," in *Optical Fiber Communication*, (IEEE, 1998), 97-98.
326. G. N. Conti, S. Berneschi, M. Bettinelli, M. Brenci, B. Chen, S. Pelli, A. Speghini, and G. C. Righini, "Rare-earth doped tungsten tellurite glasses and waveguides: fabrication and characterization," *J. Non-Cryst. Solids* **345-346**, 343 (2004).
327. S. Berneschi, G. N. Conti, I. Banyasz, A. Watterich, N. Q. Khanh, M. Fried, F. Paszti, M. Brenci, S. Pelli, and G. C. Righini, "Ion beam irradiated channel waveguides in Er<sup>3+</sup> -doped tellurite glass," *Appl. Phys. Lett.* **90**, 121136 (2007).
328. D.-Y. Choi, S. Madden, A. Rode, R. Wang, and B. Luther-Davies, "Dry etching characteristics of amorphous As<sub>2</sub>S<sub>3</sub> film in CHF<sub>3</sub> plasma," *J. Appl. Phys.* **104**, 113305 (2008).
329. D.-Y. Choi, S. Maden, A. Rode, R. Wang, and B. Luther-Davies, "Plasma etching of As<sub>2</sub>S<sub>3</sub> films for optical waveguides," *J. Non-Cryst. Solids* **354**, 3179-3183 (2008).

330. H. Gerung, C. J. Brinker, S. R. J. Brueck, and S. M. Han, "In situ real-time monitoring of profile evolution during plasma etching of mesoporous low-dielectric-constant  $\text{SiO}_2$ ," *J. Vac. Sci. Technol. A* **23**, 347-354 (2005).
331. G. Cunge and J. P. Booth, " $\text{CF}_2$  production and loss mechanisms in fluorocarbon discharges: Fluorine-poor conditions and polymerization," *J. Appl. Phys.* **85**, 3952-3959 (1999).
332. J. Werking, J. Schramm, C. Nguyen, E. L. Hu, and H. Kroemer, "Methane/hydrogen-based reactive ion etching of InAs, InP, GaAs, and GaSb," *Appl. Phys. Lett.* **58**, 2003-2005 (1991).
333. Q. Guo, N. Uesugi, T. Tanaka, M. Nishio, and H. Ogawa, "Reactive ion etching of zinc oxide using methane and hydrogen," *Jpn. J. Appl. Phys., Part 1* **45**, 8597-8599 (2006).
334. Y. Yamashita, H. Toyoda, and H. Sugai, "Formation of CH radical by surface bombardment in a methane/argon DC discharge," *Jpn. J. Appl. Phys., Part 1* **28**, 1647-1650 (1989).
335. M. A. Foad, M. Watt, A. P. Smart, C. M. Sotomayor Torres, C. D. W. Wilkinson, W. Kuhn, H. P. Wagner, S. Bauer, H. Leiderer, and W. Gebhardt, "High-resolution dry etching of zinc telluride. Characterization of etched surfaces by x-ray photoelectron spectroscopy, photoluminescence and Raman scattering," *Semicond. Sci. Technol.* **6**, A115-A122 (1991).
336. StatSoft, retrieved 26/07/2009, <http://www.statsoft.com/textbook/experimental-design/>.
337. M. A. Foad, A. P. Smart, M. Watt, C. M. Sotomayor Torres, and C. D. W. Wilkinson, "Reactive ion etching of II-VI semiconductors using a mixture of methane and hydrogen," *Electron. Lett.* **27**, 73-75 (1991).
338. B. Prince, "Trends in scaled and nanotechnology memories," in *2005 Non-Volatile Memory Technology Symposium*, (IEEE Computer Society, 2005), 55-61.
339. B. J. Eggleton, B. Luther-Davies, and K. Richardson, "Chalcogenide photonics," *Nat Photon* **5**, 141-148 (2011).
340. Y. Ruan, W. Li, R. Jarvis, N. Madsen, A. Rode, and B. Luther-Davies, "Fabrication and characterization of low loss rib chalcogenide waveguides made by dry etching," *Opt. Express* **12**, 5140-5145 (2004).
341. R. A. Jarvis, R. P. Wang, A. V. Rode, C. Zha, and B. Luther-Davies, "Thin film deposition of  $\text{Ge}_{33}\text{As}_{12}\text{Se}_{55}$  by pulsed laser deposition and thermal evaporation: Comparison of properties," *J. Non-Cryst. Solids* **353**, 947-949 (2007).
342. C. J. Mogab, "The loading effect in plasma etching," *J. Electrochem. Soc.* **124**, 1262-1268 (1977).
343. B. Gorowitz and R. Saia, "Reactive ion etching," in *VLSI electronics microstructure Science*, N. G. Einspruch and D. M. Brown, eds. (Academic Press, 1984).
344. J. Schmit, J. Reed, E. Novak, and J. K. Gimzewski, "Performance advances in interferometric optical profilers for imaging and testing," *J. Opt. A: Pure Appl. Opt.* **10**, 064001 (2008).
345. S. Di Nardo, L. Lozzi, M. Passacantando, P. Picozzi, and S. Santucci, "Reactivity towards oxygen of Te/Si(100) surfaces investigated by ultraviolet photoelectron spectroscopy, X-ray photoelectron spectroscopy and low energy electron diffraction spectroscopy," *J. Electron. Spectrosc. Relat. Phenom.* **74**, 129-134 (1995).
346. M. K. Bahl, R. L. Watson, and K. J. Irgolic, "X-ray photoemission studies of tellurium and some of its compounds," *J. Chem. Phys.* **66**, 5526-5535 (1977).
347. W. E. Swartz, K. J. Wynne, and D. M. Hercules, "X-ray photoelectron spectroscopic investigation of Group VIA elements," *Anal. Chem.* **43**, 1884-1887 (1971).
348. H. Hayashi, N. Shigemoto, S. Sugiyama, N. Masaoka, and K. Saitoh, "X-ray photoelectron spectra for the oxidation state of  $\text{TeO}_2\text{-MoO}_3$ ; catalyst in the vapor-phase selective oxidation of ethyl lactate to pyruvate," *Catal. Lett.* **19**, 273-277 (1993).



349. R. Scarmozzino, A. Gopinath, R. Pregla, and S. Helfert, "Numerical techniques for modeling guided-wave photonic devices," *IEEE J. Sel. Top. Quantum Electron.* **6**, 150-162 (2000).
350. H. Dong, A. Chronopoulos, J. Zou, and A. Gopinath, "Vectorial integrated finite-difference analysis of dielectric waveguides," *J. Lightwave Technol.* **11**, 1559-1564 (1993).
351. Z.-E. Abid, K. L. Johnson, and A. Gopinath, "Analysis of dielectric guides by vector transverse magnetic field finite elements," *J. Lightwave Technol.* **11**, 1545-1549 (1993).
352. C. Koos, L. Jacome, C. Poulton, J. Leuthold, and W. Freude, "Nonlinear silicon-on-insulator waveguides for all-optical signal processing," *Opt. Express* **15**, 5976-5990 (2007).
353. A. W. Snyder and J. Love, *Optical waveguide theory* (Kluwer Academic, London, 2000).
354. Z. Wang, B. Mikkelsen, B. Pedersen, K. E. Stubkjaer, and D. S. Olesen, "Coupling between angled-facet amplifiers and tapered lens-ended fibers," *J. Lightwave Technol.* **9**, 49-55 (1991).
355. A. Fallahkhair, K. S. Li, and T. E. Murphy, "Vector finite difference modesolver for anisotropic dielectric waveguides," *J. Lightwave Technol.* **26**, 1423-1431 (2008).
356. H. Takebe, S. Fujino, and K. Morinaga, "Refractive-index dispersion of tellurite glasses in the region from 0.40 to 1.71  $\mu\text{m}$ ," *J. Amer. Cer. Soc.* **77**, 2455-2457 (1994).
357. E. A. J. Marcatili, "Slab-coupled waveguides," *Bell Syst. Tech. J.* **53**, 645 (1974).
358. D. A. Stocker, E. F. Schubert, W. Grieshaber, K. S. Boutros, and J. M. Redwing, "Facet roughness analysis for InGaN/GaN lasers with cleaved facets," *Appl. Phys. Lett.* **73**, 1925-1927 (1998).
359. J. Xu, D. Yevick, and M. Gallant, "Approximate methods for modal reflectivity at optical waveguide facets," *J. Opt. Soc. Am. A* **12**, 725-728 (1995).
360. T. Feuchter and C. Thistrup, "Low-loss waveguide propagation characterization by high accuracy interferometric measurement technique," in *Lasers and Electro-Optics Europe*, (IEEE, 1994), EPS-Quantum Electronics and Optics Division; IEEE; Optical Society of America.
361. S. Taebi, M. Khorasaninejad, and S. S. Saini, "Modified Fabry-Perot interferometric method for waveguide loss measurement," *Appl. Opt.* **47**, 6625-6630 (2008).
362. G. Tittelbach, B. Richter, and W. Karthe, "Comparison of three transmission methods for integrated optical waveguide propagation loss measurement," *J. Opt. A: Pure Appl. Opt.* **2**, 683 (1993).
363. R. H. Hardin and F. D. Tappert, "Applications of the split-step Fourier method to the numerical solution of nonlinear and variable coefficient wave equations," *SIM Rev. Chronicle* **15**, 423 (1973).
364. S. Watanabe and M. Shirasaki, "Exact compensation for both chromatic dispersion and Kerr effect in a transmission fiber using optical phase conjugation," *J. Lightwave Technol.* **14**, 243-248 (1996).
365. G. P. Agrawal, "Phase detection in optical communication systems through phase conjugation," *J. Opt. B: Quantum Semiclassical Opt.* **8**, 383 (1996).
366. G. D. Bartolini, D. K. Serkland, P. Kumar, and W. L. Kath, "All-optical storage of a picosecond-pulse packet using parametric amplification," *IEEE Photonics Technol. Lett.* **9**, 1020-1022 (1997).
367. S. Chi and S. Wen, "Recovery of the soliton self-frequency shift by optical phase conjugation," *Opt. Lett.* **19**, 1705-1707 (1994).
368. C. G. Goedde, W. L. Kath, and P. Kumar, "Periodic amplification and conjugation of optical solitons," *Opt. Lett.* **20**, 1365-1367 (1995).
369. W. Ge, A. Lin, C. Guinand, and J. Toulouse, "Detention of dispersion and nonlinear coefficient of photonic crystal fibers by degenerated FWM method," in *Conference on Lasers and Electro Optics 2010*, (OSA, 2010).



370. R. H. Stolen, "Phase-matched-stimulated four-photon mixing in silica-fiber waveguides," *IEEE J. Quantum Electron.* **QE-11**, 100-103 (1975).
371. R. H. Stolen and J. E. Bjorkholm, "Parametric amplification and frequency conversion in optical fibers," *IEEE J. Quantum Electron.* **QE-18**, 1062-1072 (1982).
372. O. Aso, M. Tadakuma, and S. Namiki, "Four-Wave Mixing in Optical Fibers and its Applications," *Furukawa Rev.* **19**, 63-68 (2000).
373. D. E. McCumber, "Theory of phonon-terminated optical masers," *Phys. Rev.* **134**, A299 (1964).
374. W. J. Miniscalco and R. S. Quimby, "General procedure for the analysis of  $\text{Er}^{3+}$  cross sections," *Opt. Lett.* **16**, 258-260 (1991).
375. B. R. Judd, "Optical absorption intensities of rare-earth ions," *Phys. Rev.* **127**, 750-761 (1962).
376. G. S. Ofelt, "Intensities of crystal spectra of rare-earth ions," *J. Chem. Phys.* **37**, 511-520 (1962).
377. J. Garcia Sole, I. E. Bausa, and D. Jaque, *An introduction to the optical spectroscopy of inorganic solids* (John Wiley & Sons, Padstow, Cornwall, 2005).
378. M. J. F. Digonnet, ed., *Rare-earth doped fiber lasers and amplifiers*, Second ed., Optical Engineering (CRC Press, New York, 2001).
379. W. T. Carnall, P. R. Fields, and K. Rajnak, "Spectral Intensities of the trivalent Lanthanides and Actinides in solution. II.  $\text{Pm}^{3+}$ ,  $\text{Sm}^{3+}$ ,  $\text{Eu}^{3+}$ ,  $\text{Gd}^{3+}$ ,  $\text{Tb}^{3+}$ ,  $\text{Dy}^{3+}$ , and  $\text{Ho}^{3+}$ ," *J. Chem. Phys.* **49**, 4412-4423 (1968).
380. W. T. Carnall, P. R. Fields, and K. Rajnak, "Electronic energy levels of the trivalent Lanthanide aquo ions. IV.  $\text{Eu}^{3+}$ ," *J. Chem. Phys.* **49**, 4450-4455 (1968).
381. W. T. Carnall, P. R. Fields, and K. Rajnak, "Electronic energy levels of the trivalent Lanthanide aquo ions. III.  $\text{Tb}^{3+}$ ," *J. Chem. Phys.* **49**, 4447-4449 (1968).
382. W. T. Carnall, P. R. Fields, and K. Rajnak, "Electronic energy levels of the trivalent Lanthanide aquo ions. II.  $\text{Gd}^{3+}$ ," *J. Chem. Phys.* **49**, 4443-4446 (1968).
383. W. T. Carnall, P. R. Fields, and K. Rajnak, "Electronic energy levels in the trivalent Lanthanide aquo ions. I.  $\text{Pr}^{3+}$ ,  $\text{Nd}^{3+}$ ,  $\text{Pm}^{3+}$ ,  $\text{Sm}^{3+}$ ,  $\text{Dy}^{3+}$ ,  $\text{Ho}^{3+}$ ,  $\text{Er}^{3+}$ , and  $\text{Tm}^{3+}$ ," *J. Chem. Phys.* **49**, 4424-4442 (1968).
384. M. J. Weber, "Probabilities for Radiative and Nonradiative Decay of  $\text{Er}^{3+}$  in  $\text{LaF}_3$ ," *Phys. Rev.* **157**, 262 (1967).
385. S. Tanabe, "Optical transitions of rare-earth ions for amplifiers: how the local structure works in glass," *J. Non-Cryst. Solids* **259**, 1-9 (1999).
386. R. S. Grew, H. Ebendorff-Heidepriem, P. J. Veitch, and T. M. Monro, "Concentration effects in Erbium doped tellurite glass," in *Optoelectronic and Microelectronic Materials and Devices, Proceedings, COMMAD*, (Institute of Electrical and Electronics Engineers Inc., 2006), 196-199.
387. A. Laliotis, "Analysis and fabrication of homogenous high concentration erbium doped waveguide amplifiers," (Imperial College, London, 2005).
388. A. Laliotis, E. M. Yeatman, M. M. Ahmad, and W. Huang, "Molecular homogeneity in erbium-doped sol-gel waveguide amplifiers," *IEEE J. Quantum Electron.* **40**, 805-814 (2004).
389. Y. Yan, A. J. Faber, and H. de Waal, "Luminescence quenching by OH groups in highly Er-doped phosphate glasses," *J. Non-Cryst. Solids* **181**, 283-283 (1995).
390. H. Longerich, D. Günther, and S. Jackson, "Elemental fractionation in laser ablation inductively coupled plasma mass spectrometry," *Fresenius J. Anal. Chem.* **355**, 538-542 (1996).
391. S. X. Dai, T. F. Xu, Q. H. Nie, S. Xiang, J. J. Zhang, and L. L. Hu, "Effect of radiation trapping on spectroscopic properties of  $\text{Er}^{3+}$ -doped oxide glasses," *Acta Phys. Sin.* **55**, 1479-1485 (2006).

392. P. Nandi and G. Jose, "Erbium doped phospho-tellurite glasses for 1.5  $\mu\text{m}$  optical amplifiers," *Opt. Commun.* **265**, 588-593 (2006).
393. R. Rolli, M. Montagna, S. Chausseant, A. Monteil, V. K. Tikhomirov, and M. Ferrari, "Erbium-doped tellurite glasses with high quantum efficiency and broadband stimulated emission cross section at 1.5  $\mu\text{m}$ ," *Opt. Mater.* **21**, 743-748 (2003).
394. S. L. Zhao, X. L. Wang, D. W. Fang, S. Q. Xu, and L. L. Hu, "Spectroscopic properties and thermal stability of Er<sup>3+</sup>-doped tungsten-tellurite glass for waveguide amplifier application," *J. Alloy. Compd.* **424**, 243-246 (2006).
395. A. Jha, S. Shen, and M. Naftaly, "Structural origin of spectral broadening of 1.5- $\mu\text{m}$  emission in Er<sup>3+</sup>-doped tellurite glasses," *Phys. Rev. B* **62**, 6215-6227 (2000).
396. A. A. Rieznik and G. Rigolin, "Spontaneous decay rates in active waveguides," *Opt. Lett.* **30**, 1108-1110 (2005).
397. Q. Nie, L. Lu, T. Xu, S. Dai, X. Shen, X. Liang, X. Zhang, and X. Zhang, "Effect of hydroxyl groups on Er<sup>3+</sup> doped Bi<sub>2</sub>O<sub>3</sub>-B<sub>2</sub>O<sub>3</sub>-SiO<sub>2</sub> glasses," *J. Phys. Chem. Solids* **68**, 477-481 (2007).
398. O. Humbach, H. Fabian, U. Grzesik, U. Haken, and W. Heitmann, "Analysis of OH absorption bands in synthetic silica," *J. Non-Cryst. Solids* **203**, 19-26 (1996).
399. E. Stolper, "Water in silicate glasses: An infrared spectroscopic study," *Contrib. Mineral. Petrol.* **81**, 1-17 (1982).
400. L. Nemec and J. Gotz, "Infrared Absorption of OH- in E Glass," *J. Amer. Cer. Soc.* **53**, 526-526 (1970).
401. J. Leuthold, C. Koos, and W. Freude, "Nonlinear silicon photonics," *Nat. Photonics* **4**, 535-544 (2010).
402. M. R. Lamont, B. Luther-Davies, D.-Y. Choi, S. Madden, X. Gai, and B. J. Eggleton, "Net-gain from a parametric amplifier on a chalcogenide optical chip," *Opt. Express* **16**, 20374-20381 (2008).
403. X. Gai, S. Madden, D.-Y. Choi, D. Bulla, and B. Luther-Davies, "Dispersion engineered Ge<sub>11.5</sub>As<sub>24</sub>Se<sub>64.5</sub> nanowires with a nonlinear parameter of 136W<sup>-1</sup>m<sup>-1</sup> at 1550nm," *Opt. Express* **18**, 18866-18874 (2010).
404. G. N. van den Hoven, R. J. I. M. Koper, A. Polman, C. van Dam, J. W. M. van Uffelen, and M. K. Smit, "Net optical gain at 1.53  $\mu\text{m}$  in Er-doped Al<sub>2</sub>O<sub>3</sub> waveguides on silicon," *Appl. Phys. Lett.* **68**, 1886-1888 (1996).
405. Y. C. Yan, A. J. Faber, H. de Waal, P. G. Kik, and A. Polman, "Erbium-doped phosphate glass waveguide on silicon with 4.1 dB/cm gain at 1.535  $\mu\text{m}$ ," *Appl. Phys. Lett.* **71**, 2922-2922 (1997).
406. F. D. Patel, S. DiCarolis, P. Lum, S. Venkatesh, and J. N. Miller, "A compact high-performance optical waveguide amplifier," *IEEE Photonics Technol. Lett.* **16**, 2607-2609 (2004).
407. P. G. Kik and A. Polman, "Erbium-doped optical-waveguide amplifiers on silicon," *MRS Bull.* **23**, 48-54 (1998).
408. A. Polman, "Exciting Erbium-doped planar optical amplifier materials," in *Thin Films for Optical Waveguide Devices and Materials for Optical Limiting*, (Materials Research Society, 2000), 3-14.
409. G. Nykolak, M. Haner, P. C. Becker, J. Shmulovich, and Y. H. Wong, "Systems evaluation of an Er<sup>3+</sup>-doped planar waveguide amplifier," *IEEE Photonics Technol. Lett.* **5**, 1185-1187 (1993).
410. R. N. Ghosh, J. Shmulovich, C. F. Kane, M. R. X. d. Barros, G. Nykolak, A. J. Bruce, and P. C. Becker, "8-mV threshold Er<sup>3+</sup>-doped planar waveguide amplifier," *IEEE Photonics Technol. Lett.* **8**, 518-520 (1996).
411. G. N. van den Hoven, R. Koper, A. Polman, C. vanDam, J. W. M. vanUffelen, and M. K. Smit, "Net optical gain at 1.53  $\mu\text{m}$  in Er-doped Al<sub>2</sub>O<sub>3</sub> waveguides on silicon," *Appl. Phys. Lett.* **68**, 1886-1888 (1996).

- 412. P. Camy, J. E. Roman, F. W. Willems, M. Hempstead, J. C. Van Der Plaats, C. Prel, A. Beguin, A. M. J. Koonen, J. S. Wilkinson, and C. Lermينياux, "Ion-exchanged planar lossless splitter at 1.5 $\mu$ m," *Electron. Lett.* **32**, 321-323 (1996).
- 413. C. C. Li, H. K. Kim, and M. Migliuolo, "Er-doped glass ridge-waveguide amplifiers fabricated with a collimated sputter deposition technique," *IEEE Photonics Technol. Lett.* **9**, 1223-1225 (1997).
- 414. S. F. Wong, E. Y. B. Pun, and P. S. Chung, "Er<sup>3+</sup>-Yb<sup>3+</sup> codoped phosphate glass waveguide amplifier using Ag<sup>+</sup>-Li<sup>+</sup> ion exchange," *IEEE Photonics Technol. Lett.* **14**, 80-82 (2002).
- 415. G. Della Valle, R. Osellame, N. Chiodo, S. Taccheo, G. Cerullo, P. Laporta, A. Killi, U. Morgner, M. Lederer, and D. Kopf, "C-band waveguide amplifier produced by femtosecond laser writing," *Opt. Express* **13**, 5976-5982 (2005).
- 416. J. D. B. Bradley, L. Agazzi, D. Gekus, F. Ay, K. Worhoff, and M. Pollnau, "2.0 dB/cm gain in an Al<sub>2</sub>O<sub>3</sub>:Er<sup>3+</sup> waveguide on silicon," in *2009 Conference on Lasers and Electro-Optics and 2009 Conference on Quantum Electronics and Laser Science Conference, CLEO/QELS 2009*, 2009).
- 417. M. Khodasevich, G. Sinitsyn, and Y. Varaksa, "Glasses for Erbium-doped fiber amplifiers: A comparison based on the ultimate spectral efficiency of information transmission," *Opt. Spectrosc.* **101**, 757-761 (2006).
- 418. Y. A. Varaksa, G. V. Sinitsyn, and M. A. Khodasevich, "Transmission capacity of erbium-doped fiber amplifiers as a criterion for quality of erbium-doped optical fibers," *Opt. Spectrosc.* **104**, 130-134 (2008).
- 419. S. J. Madden and K. T. Vu, "Very low loss reactively ion etched Tellurium Dioxide planar rib waveguides for linear and non-linear optics," *Opt. Express* **17**, 17645-17651 (2009).
- 420. T. T. Fernandez, S. M. Eaton, G. Della Valle, R. M. Vazquez, M. Irannejad, G. Jose, A. Jha, G. Cerullo, R. Osellame, and P. Laporta, "Femtosecond laser written optical waveguide amplifier in phospho-tellurite glass," *Opt. Express* **18**, 20289-20297 (2010).
- 421. P. D. Townsend, "Ion implanted waveguides and waveguide lasers," *Nucl. Instrum. Methods Phys. Res., Sect. B* **65**, 243-250 (1992).
- 422. F. Chen, X.-L. Wang, and K.-M. Wang, "Development of ion-implanted optical waveguides in optical materials: A review," *Opt. Mater.* **29**, 1523-1542 (2007).
- 423. P. D. Townsend, "Development of ion implantation for optical applications," *Vacuum* **51**, 301-304 (1998).
- 424. S. Berneschi, I. Cacciari, G. Nunzi Conti, S. Pelli, G. C. Righini, I. Banyasz, N. Q. Khanh, T. Lohner, P. Petrik, Z. Zolnai, M. Bettinelli, A. Speghini, L. Mescia, and F. Prudenzano, "Annealing effect on optical barrier in ion-implanted tellurite glass waveguides," in *Integrated Optics: Devices, Materials, and Technologies XIII*, 2009).
- 425. C. R. Tewell and S. H. King, "Observation of metastable Erbium trihydride," *Appl. Surf. Sci.* **253**, 2597-2602 (2006).
- 426. J. A. Grimshaw, F. J. Spooner, C. G. Wilson, and A. D. McQuillan, "The growth of crystals of erbium hydride," *J. Mater. Sci.* **16**, 2855-2859 (1981).
- 427. S. Peng and R. M. Reano, "Cantilever couplers for intra-chip coupling to silicon photonic integrated circuits," *Opt. Express* **17**, 4565-4574 (2009).
- 428. W. J. Miniscalco, "Erbium-doped glasses for fiber amplifiers at 1500 nm," *J. Lightwave Technol.* **9**, 234-250 (1991).
- 429. N. Jaba, A. Kanoun, H. Mejri, A. Selmi, S. Alaya, and H. Maaref, "Infrared to visible up-conversion study for Erbium-doped zinc tellurite glasses," *J. Phys. Condens. Matter* **12**, 4523-4534 (2000).
- 430. A. P. Lopez-Barbero, W. A. Arellano-Espinoza, H. L. Fragnito, and H. E. Hernandez-Figueroa, "Tellurite-based optical fiber amplifier analysis using the finite-element method," *Microwave Opt. Technol. Lett.* **25**, 103-107 (2000).

431. Y. G. Choi, D. S. Lim, K. H. Kim, D. H. Cho, and H. K. Lee, "Enhanced  $^4I_{11/2} \rightarrow ^4I_{13/2}$  transition rate in  $\text{Er}^{3+}/\text{Ce}^{3+}$ -codoped tellurite glasses," *Electron. Lett.* **35**, 1765-1767 (1999).
432. A. Polman, "Exciting Erbium-doped planar optical amplifier materials," in *Thin Films for Optical Waveguide Devices and Materials for Optical Limiting*, (Society of Photo-Optical Instrumentation Engineers, 2000), 2-13.
433. L. H. Huang, A. Jha, S. X. Shen, and W. J. Chung, "Visible emissions at 592 and 613 nm in  $\text{Er}^{3+}$ - $\text{Eu}^{3+}$ -codoped tellurite fibers," *Opt. Commun.* **239**, 403-408 (2004).
434. M. Mattarelli, M. Montagna, L. Zampedri, M. Bouazaoui, B. Capoen, S. Turrell, M. Ferrari, and G. C. Righini, "Effect of  $\text{Eu}^{3+}$  and  $\text{Ce}^{3+}$  codoping on the relaxation of  $\text{Er}^{3+}$  in silica-hafnia and tellurite glasses," *Phys. Status Solidi C* **4**, 793-796 (2007).
435. Y. Q. Wei, A. Harsh, R. V. Penty, I. H. White, S. Shen, and A. Jha, "Er/Ce codoped tellurite fibre amplifier for high-gain and low-noise operation," in *OFC/NFOEC 2008 - 2008 Conference on Optical Fiber Communication/National Fiber Optic Engineers Conference*, (2008).
436. J. Yang, L. Zhang, L. Wen, S. Dai, L. Hu, and Z. Jiang, "Comparative investigation on energy transfer mechanisms between  $\text{Er}^{3+}$  and  $\text{Ce}^{3+}$  ( $\text{Eu}^{3+}$ ,  $\text{Tb}^{3+}$ ) in tellurite glasses," *Chem. Phys. Lett.* **384**, 295-298 (2004).
437. G. Della Valle, R. Osellame, S. Taccheo, N. Chiodo, G. Galzerano, G. Cerullo, P. Laporta, R. Ramponi, U. Morgner, and A. C. Ferrari, "Waveguide lasers in Er:Yb-doped phosphate glass fabricated by femtosecond laser writing," in *9th International Conference on Transparent Optical Networks*, (2007), 289-292.
438. G. Della Valle, S. Taccheo, R. Osellame, A. Festa, G. Cerullo, and P. Laporta, "1.5  $\mu\text{m}$  single longitudinal mode waveguide laser fabricated by femtosecond laser writing," *Opt. Express* **15**, 3190-3194 (2007).
439. J. D. B. Bradley, R. Stoffer, L. Agazzi, F. Ay, K. Worhoff, and M. Pollnau, "Widely wavelength-selective integrated ring laser in  $\text{Al}_2\text{O}_3:\text{Er}^{3+}$ ," in *Lasers and Electro-Optics/Quantum Electronics and Laser Science Conference: 2010 Laser Science to Photonic Applications, CLEO/QELS 2010*, (2010).
440. G. Della Valle, R. Osellame, G. Galzerano, N. Chiodo, G. Cerullo, P. Laporta, O. Svelto, U. Morgner, A. G. Rozhin, V. Scardaci, and A. C. Ferrari, "Passive mode locking by carbon nanotubes in a femtosecond laser written waveguide laser," *Appl. Phys. Lett.* **89**(2006).
441. R. Osellame, G. Della Valle, N. Chiodo, S. Taccheo, P. Laporta, O. Svelto, and G. Cerullo, "Lasing in femtosecond laser written optical waveguides," *Appl. Phys. A* **93**, 17-26 (2008).
442. H. Zhang, Q. Bao, D. Tang, L. Zhao, and K. Loh, "Large energy soliton erbium-doped fiber laser with a graphene-polymer composite mode locker," *Appl. Phys. Lett.* **95**, 141103-141103 (2009).
443. Q. Bao, H. Zhang, Y. Wang, Z. Ni, Y. Yan, Z. X. Shen, K. P. Loh, and D. Y. Tang, "Atomic-layer Graphene as a saturable absorber for ultrafast pulsed lasers," *Adv. Funct. Mater.* **19**, 3077-3083 (2009).
444. Z. Han, B. Qiaoliang, T. Dingyuan, Z. Luming, and L. Kianping, "Large energy soliton erbium-doped fiber laser with a graphene-polymer composite mode locker," *Appl. Phys. Lett.* **95**, 141103 (2009).
445. W. B. Cho, H. W. Lee, S. Y. Choi, J. W. Kim, D. I. Yeom, F. Rotermund, J. Kim, and B. H. Hong, "Monolayer graphene saturable absorber for bulk laser mode-locking," in *Lasers and Electro-Optics/Quantum Electronics and Laser Science Conference: 2010 Laser Science to Photonic Applications, CLEO/QELS 2010*, (2010).
446. Z. Sun, T. Hasan, D. Popa, F. Torrisi, F. Wang, F. Bonaccorso, and A. C. Ferrari, "Ultrafast fiber laser mode-locked by graphene based saturable absorber," in *Lasers and*

- Electro-Optics/Quantum Electronics and Laser Science Conference: 2010 Laser Science to Photonic Applications, CLEO/QELS 2010*, 2010).
447. Z. Sun, D. Popa, T. Hasan, F. Torrisi, F. Wang, E. J. R. Kelleher, J. C. Travers, V. Nicolosi, and A. C. Ferrari, "A stable, wideband tunable, near transform-limited, graphene-mode-locked, ultrafast laser," *Nano Res.* **3**, 653-660 (2010).
  448. G. Xing, H. Guo, X. Zhang, T. C. Sum, and C. H. A. Huan, "The physics of ultrafast saturable absorption in graphene," *Opt. Express* **18**, 4564-4573 (2010).
  449. H. Zhang, D. Y. Tang, L. M. Zhao, Q. L. Bao, and K. P. Loh, "Large energy mode locking of an erbium-doped fiber laser with atomic layer graphene," *Opt. Express* **17**, 17630-17635 (2009).
  450. G. N. Conti, S. Berneschi, M. Bettinelli, M. Brenci, B. Chen, S. Pelli, A. Speghini, and G. C. Righini, "Rare-earth doped tungsten tellurite glasses and waveguides: fabrication and characterization," **345-346**, 343 (2004).
  451. E. B. Intyushin and V. A. Novikov, "Tungsten-tellurite glasses and thin films doped with rare-earth elements produced by radio frequency magnetron deposition," *Thin Solid Films* **516**, 4194-4200 (2008).